Types and origin of quartz and quartz-hosted fluid inclusions in mineralised porphyries

by

Olga Vasyukova

B.Sc. Hons (Moscow State University, Russia)

Submitted in fulfilment of the requirements for the degree

of Doctor of Philosophy

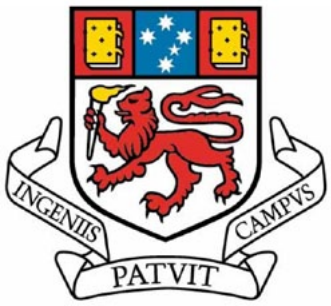

University of Tasmania

ARC Centre of Excellence in Ore Deposits

June, 2011

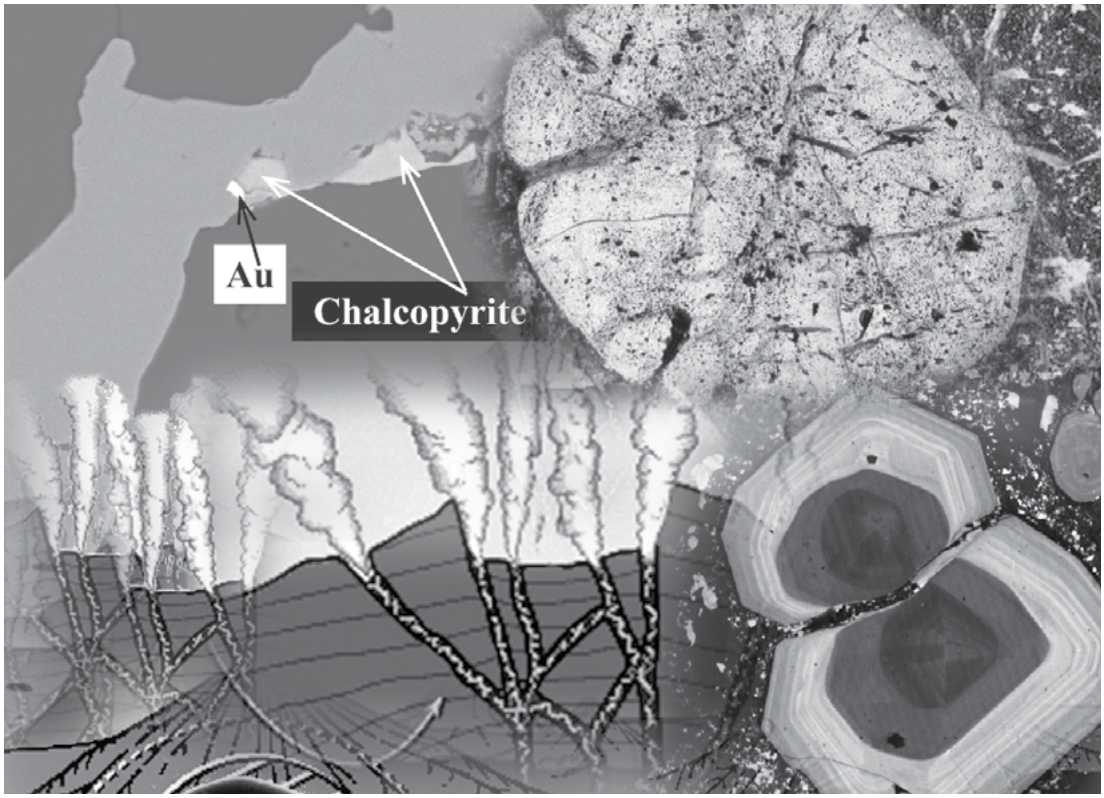

Declaration

This thesis contains no material which has been accepted for the award of any other degree or diploma in any tertiary institution, and to the best of my knowledge and belief, contains no material previously published or written by another person, except where due reference is made in the text of the thesis.

Date:

Signature:

Authority of Access

This thesis may be made available for loan and limited copying in accordance with the Copyright Act 1968.

Abstract

The formation of porphyry deposits is related to the intrusion of intermediate to felsic magmas, its cooling and crystallisation, followed by exsolution of a metal-rich magmatic vapour phase (MVP), its accumulation under the intrusion cupola and escape into country rocks. A ubiquitous phenomenon of the deposit-related intrusions is a porphyritic texture that is typically defined by feldspar and quartz crystals. It is believed that porphyry textures can be formed as a result of temperature quenching during intrusion of hot magma into cold country rocks, or pressure quenching after fluid escape. In spite of extensive research on porphyry deposits there is still uncertainty about when and where quartz eyes crystallise. Do they crystallise in deep magma chambers and travel with magma to a place of intrusion? Do quartz eyes crystallise after magma emplacement? How is crystallisation of quartz eyes related to mineralisation in time and space? Is it coeval with exsolution of mineralising fluid and its accumulation under the intrusion carapace? If they are coeval then study of quartz eyes may be highly beneficial for our knowledge of porphyry systems. The term 'quartz eyes' is used in preference to other terms (e.g. phenocrysts, porphyroblasts or clasts) to emphasise that their origin is yet to be established.

Quartz eyes from seven porphyry deposits were studied. These are Antapaccay (Peru), Batu Hijau (Indonesia), Climax (USA), Panguna (PNG), Far Southeast porphyry (Philippines), Rio Blanco (Chile) and Omsukchan (Russia). The research was focused on the internal textures of the quartz eyes and inclusions they contain. To study quartz textures SEM-based cathodoluminescence (CL) and hyperspectral CL mapping were applied. Both techniques were combined with Electron Probe Microanalysis (EPMA). For inclusion study optical and electron microscopy, LA-ICP-MS, Raman spectroscopy and microthermometry were applied.

Quartz eyes commonly showed strongly contrasted CL patterns, in many grains core and rim zones were revealed. CL study showed significant diversity of internal patterns of quartz eyes within a single thin section; grains with CL-dark cores and CL-bright rims were sometimes next to grains with reverse zoning or grains showing irregular or no zonation. Clusters of quartz grains were often found; diversity of CL patterns within grains of a single cluster was found typical. Quartz eyes with a distinct rim-and-core pattern often demonstrated enrichment of cores in Al, Li and OH-, whereas rims were Ti-rich and contained variable Al. CL-dark cores often showed sector zoning.

Fluid inclusion studies showed that inclusion assemblages in quartz eyes are unique; feldspar phenocrysts in the same thin sections contained only melt inclusions whereas adjacent quartz eyes were sponge-textured due to the abundance of fluid inclusions in them. Fluid inclusions in quartz eyes were found distributed along healed fractures, and often had halos of secondary quartz around them, indicating that they were most likely partially decrepitated. Such fractures were distributed only within quartz eyes and did not extend into the matrix. Inclusions displayed extreme diversity in composition that could be caused by a combination of processes upon cooling, such as precipitation of daughter crystals, necking down, leakage of the fluid components, etc. implying that inclusions underwent post-entrapment modification and cannot be used as characteristic fluid during conditions of crystallisation of quartz eyes.

According to LA-ICP-MS analyses fluid inclusions in the quartz eyes and veins contained Al, Na, K, Fe, Mn, Cl, S, W, Pb, Cu, Zn, Ca, Ag, Sn, Bi and Rb above their detection limits. The element ratios varied significantly within adjacent inclusions. Liquid-rich inclusions are usually chlorine-rich, and sometimes are B-rich. Vapour-rich inclusions are often Al- and S-bearing with higher Cu/Zn, Cu/Rb and Cu/Sr ratios than those in liquid-rich and multiphase inclusions. Multiphase inclusions are enriched in metals (Cu, Zn, Rb, Sr, Ag, Pb, Mo and W) and showed very low Al concentrations.

Microthermometry experiments demonstrated atypical behaviour of the fluid upon heating and cooling: some phases swirl (shrink in some parts while growing and coalescing in others without general changes in a size) upon heating, showing that those phases are more like immiscible liquids than solids. Upon cooling multiple episodes of fluid immiscibility were observed. Every immiscibility event led to separation of a phase, which appeared to be initially liquid-like and later could gradually reshape to form crystals. Fluid inclusion study showed that behaviour of such complex fluid is significantly different from that of model (NaCl) fluid and thus, using the NaCl-equivalent fluid properties to reconstruct conditions of formation of porphyry deposits can lead to erroneous results.

Distribution of metal-bearing phases (MBP) and trace metals in quartz eyes showed that the sulphides are secondary, that their distribution is confined by quartz eyes and that they are closely related to secondary CL-dark quartz. MBP in quartz veins are interstitial between quartz grains and are also related to late CL-dark quartz. MBP also form separate globules, which are associated with non-metal phases such as apatite, biotite and fluorite. Non-metal phases are also associated with MBP within quartz eyes and veins.

Although it is traditionally assumed that quartz eyes from porphyries are phenocrysts, comparison with quartz phenocrysts from lava samples showed significant difference. Quartz phenocrysts from lavas are often fragments of crystals, they show low contrast CL pattern (often oscillatory zoning only) with no healed fractures and they usually contain melt inclusions of rhyolitic compositions but no fluid inclusions. The difference in shapes, internal textures and inclusion assemblages can indicate different origin. Porphyry systems are related to intermediate intrusions. In such systems quartz will crystallise as the last magmatic phase when necessary silica saturation occurs (for crystallisation). Thus, quartz eyes should crystallise after magma emplacement during late magmatic stages. Preserved quartz clusters in the studied porphyry samples is consistent with late crystallisation. Abundance of oscillatory zonation together with preserved clusters can also indicate crystallisation in stagnant magma. Abundance of fluid inclusions in quartz eyes and their distribution indicate that they crystallised in an extremely fluid-rich environment. The absence of similar fluid inclusion assemblages in adjacent crystals (other than quartz) implies that quartz eye crystallisation was related to a unique event.

A new model for crystallisation of quartz eyes was proposed in this study, which accounts for the marked differences between quartz phenocrysts and quartz eyes. As a result of fractional crystallisation residual melt became enriched in silica, alkali, volatile and metal components. Cooling and/or further crystallisation induced liquid-liquid immiscibility within the melt, dividing it into peraluminous water-poor melt and peralkaline water- and silica-rich melt (heavy fluid). As a result of silica oversaturation during further cooling, heavy fluid underwent immiscibility with formation of silica-rich globules (>90wt% SiO_2+Na(K, Li, Al)$_2$O, H_2O and metals); from these globules quartz eyes crystallised. Crystallisation of quartz eyes could take place inwards when firstly Ti-rich rims (high temperature) formed and then high Al, Li and OH- cores with sector zoning crystallised. During the quartz crystallisation the other components (Na (K, Li, Al)$_2$O, H_2O and metals) were expelled from the crystal lattice and formed abundant fluid inclusions in quartz. Further cooling and fracturing of the pluton caused massive (partial) decrepitation of fluid inclusions. The released fluid healed multiple fractures. This scenario of formation of quartz eyes is in a good agreement with obtained CL and fluid inclusion data.

The residual phase (left after separation of silica-rich globules) was extremely mobile and easily migrated along fractures. The alkali-, volatile- and metal-rich phase was chemically aggressive, and probably very unstable under cooling conditions. It precipitated the remaining silica as veinlets, and then metal-bearing and alkali-bearing

phases in interstitial spaces between quartz grains or as late veinlets. This residual fluid may have colloidal nature; as soon as the fluid became oversaturated relative to any of its components, multiple centres of crystallisation formed, turning it into colloid (solid phase suspended in liquid phase). If the excess of this component was removed from the system (precipitated) the fluid could convert back into solution.

This mechanism of evolution of the residual melts and eventual formation of mineralising fluids from heavy fluid through a series of immiscibility events has significant advantages in terms of efficiency of metal extraction over the transition melt/aqueous fluid through the fluid exsolution. High efficiency of metal extraction allows formation of an economically significant deposit from a rather small porphyry stocks without necessity to invoke magma reservoirs of batholithic size. This scenario of formation of mineralised fluid is consistent with obtained CL data as well as with the observed fluid behaviour upon cooling. Suggested mechanism of the evolution of the fluid is also in a good agreement with co-deposition of quartz and sulphides, so typical for porphyry-type deposits.

Acknowledgments

It has been a great pleasure working in the friendly and supportive environment of Centre of Excellence in Ore Deposits. I would like to thank those people who contributed greatly to this thesis and without whom it would have been impossible to complete this thesis.

First and foremost I thank my family, without their love and support I could not have begun this project. To my parents, Vitislav and Nina, my sisters Anna and Alina, and my brothers Roman, Semen and Artem, many thanks. I was lucky to meet amazing people here in Hobart who became my close friends and my family. They did their best to support me, without them my life here would be much more difficult and less enjoyable. Many thanks to Irina, Alexey, Marie and Gareth.

Particular thanks must go to my thesis supervisors Dima Kamenetsky, Paul Davidson and Leonid Danyushevsky, and also my research supervisor Karsten Gömann. I am very grateful to Dima who has been my guide throughout these years in a field of geology new for me. Dima's door has always been open for me and he was always ready to answer any of my questions. Working with Dima was a great adventure; not only has his enthusiasm inspired confidence in myself for all these years, but he also taught me to 'think outside the box'. This has opened a whole new world of science for me, with new and exciting opportunities to apply my knowledge, that has, I believe, made me a better scientist and will benefit my future researches. Dima and his wife Maya have been extremely supportive and helped not only with my research but with any other problems I encountered. Almost all work of reviewing my thesis and correcting my English fell on Paul who has been extremely patient and helpful, which I will always appreciate. Thank to Leonid who always provided me with wise advice; whether about the LA-ICP-MS analyses for this thesis, writing chapters, or buying a car. I am also grateful to Karsten who has always been extremely helpful and supportive.

I am grateful to the CODES and School of Earth Science staff and students who created the friendliest and most encouraging atmosphere. Thank to the CODES support staff; their efforts make CODES function as a single well-oiled machine and contribute greatly to healthy environment; they always provided me with expert advice regarding information technology, poster printing, field equipment and sample preparation or financial reporting.

Table of Content

Chapter 1. Introduction

1.1. Porphyry-type deposits: characteristics and models

1.1.1. General description

Porphyry-type (porphyry copper) deposits are a major source of Cu, Mo, Au, Ag, and Sn. Nearly 60% of the world's Cu and approximately 95% of the world's Mo are produced by porphyries (Sinclair, 2007). Porphyry deposit may also contain by-products such as Re, W, In, Pt, Pd, and Se.

Deposits of this type are found in North and South America, Europe, Asia, and Pacific islands. The largest examples are found in the Andes, such as El Teniente (Chile) and Rio Blanco (Peru). Numerous publications have been dedicated to describing the geology, geochemistry, petrology, fluid and melt inclusions of porphyry type deposits and to modelling the formation of such deposits.

Porphyry deposits are large and typically contain hundreds of millions tonnes of ore, although they range in size from tens of millions to billions of tonnes. Grades for the different metals vary considerably, but generally average less than 1% (Sinclair, 2007).

Porphyry deposits are characterised by Cu sulphides occurring as disseminated grains in numerous tiny veinlets, within stockworks or breccia zones associated with shallow intermediate to felsic porphyritic intrusions. The stockworks typically occur as a shell surrounding the intrusion and penetrating its carapace. Porphyry type deposits also show characteristic alteration halos stepping out from the intrusion.

1.1.2. Formation of porphyry deposits: genetic model

The most accepted model for the formation of porphyry-type deposits is the 'orthomagmatic' model (Burnham, 1979; Burnham and Ohmoto, 1980; Hedenquist and Lowenstern, 1994; Lowell and Guilbert, 1970; Sinclair, 2007; White et al., 1971; Whitney, 1975). This model (Fig 1-1) involves the intrusion of intermediate to felsic magma at a subvolcanic level, following by cooling and crystallisation. This eventually results in the separation of a metal-rich magmatic vapour phase (MVP) and accumulation of the MVP within the cupola of the magma body. Accumulated fluid expands and increases in volume, and when the fluid pressure exceeds lithostatic pressure the intrusion carapace fails. This allows migration and evolution of such

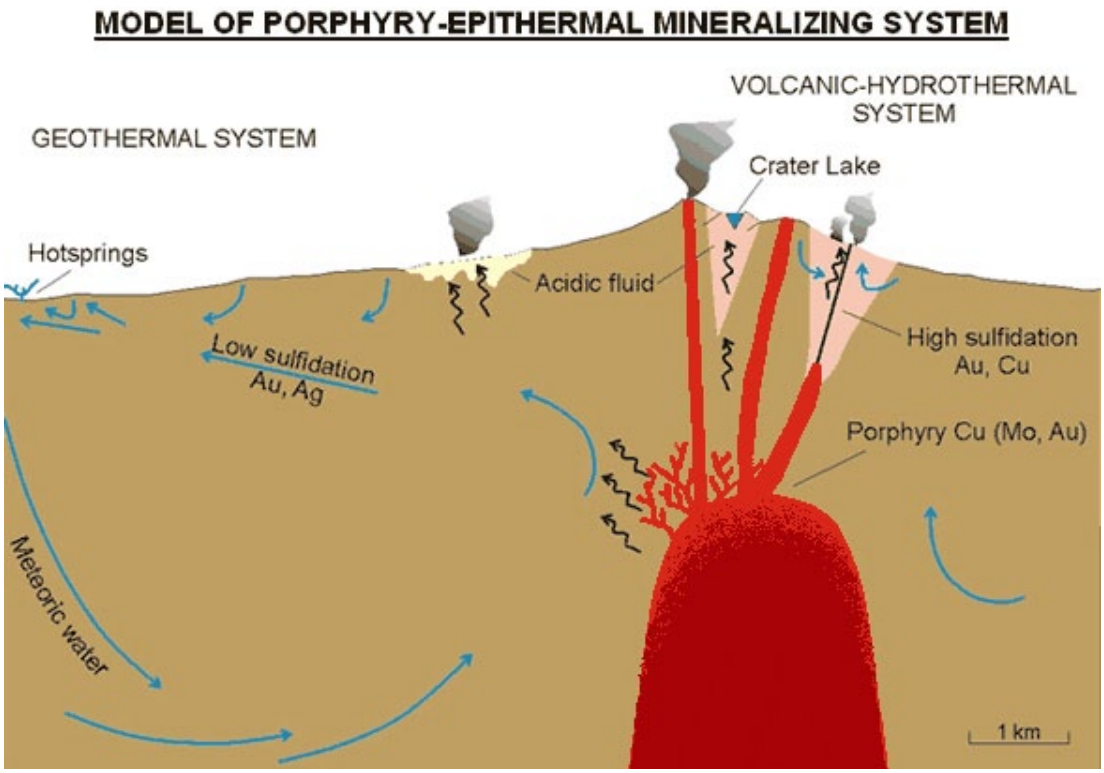

Figure 1-1 Model for porphyry-epithermal mineralising system
Figure after Hedenquist (1994).

fluids which may precipitate ore minerals within the host rocks surrounding the carapace (Burnham, 1979; Burnham and Ohmoto, 1980). Repeated episodes of such fluid escape produce the stockworks of mineralised fractures, veinlets and breccias around cupolas. It is believed that the deposit-specific geochemical signatures (e.g., metal ratios) are inherited from earlier stage of system evolution, i.e. from the fluid exsolved from the crystallising magma (Audetat et al., 2008). Incursion of meteoric water can contribute to late alteration of the host rocks after the intrusions have cooled below about 350°C (Gustafson, 1978).

However, in its current form the orthomagmatic model cannot fully explain the diversity of features observed in many porphyry deposits and requires some modification (Sinclair, 2007). Such modifications are mostly in regard to the size of the pluton and configuration of porphyry systems. Some authors believe that the amount of the fluid generated by small porphyry-style intrusion is sufficient to produce a deposit (Cline and Bodnar, 1991). Other authors believe that small porphyry stocks are unable to produce the amount of the MVP required to form a deposit, they either invoke multiple intrusions within a single deposit (Carten et al., 1988) or consider porphyry stocks as conduits for the fluid derived from significantly larger magma

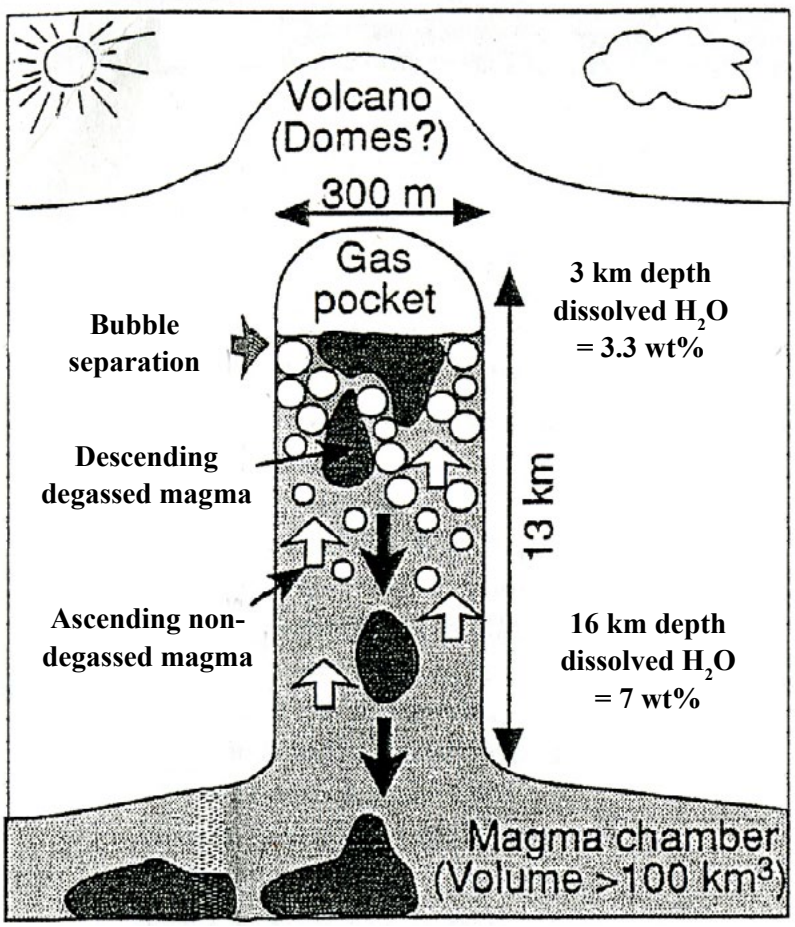

Figure 1-2 Schematic diagram of convecting magma column
Figure after Shinohara {, 1995 #138}.

reservoirs (10-150 times) at depth (Cloos, 2001; Lowenstern, 1994; Shinohara et al., 1995). The latter models require the establishment of magma convection within the magma column. Shinohara's model (Shinohara et al., 1995) suggests that sidewall magma flows upward because it is degassed hence less dense (Fig 1-2), though Cloos (2001) assumed that the direction of convection changes through time: during early stages sidewall magma sinks and magma in the middle of the column rises; during later stages sidewall magma becomes bubble-rich and buoyant enough to rise (Fig 1-3).

In spite of the long history of exploration and intensive study there is still no complete agreement on the mechanisms of formation of porphyry-type deposits, and there are still some significant discrepancies between models, including the sources of metals and sulphur, the size of magma body needed to account for formation of deposits, the mechanism of fluid accumulation under the carapace and the duration of formation for a porphyry deposit.

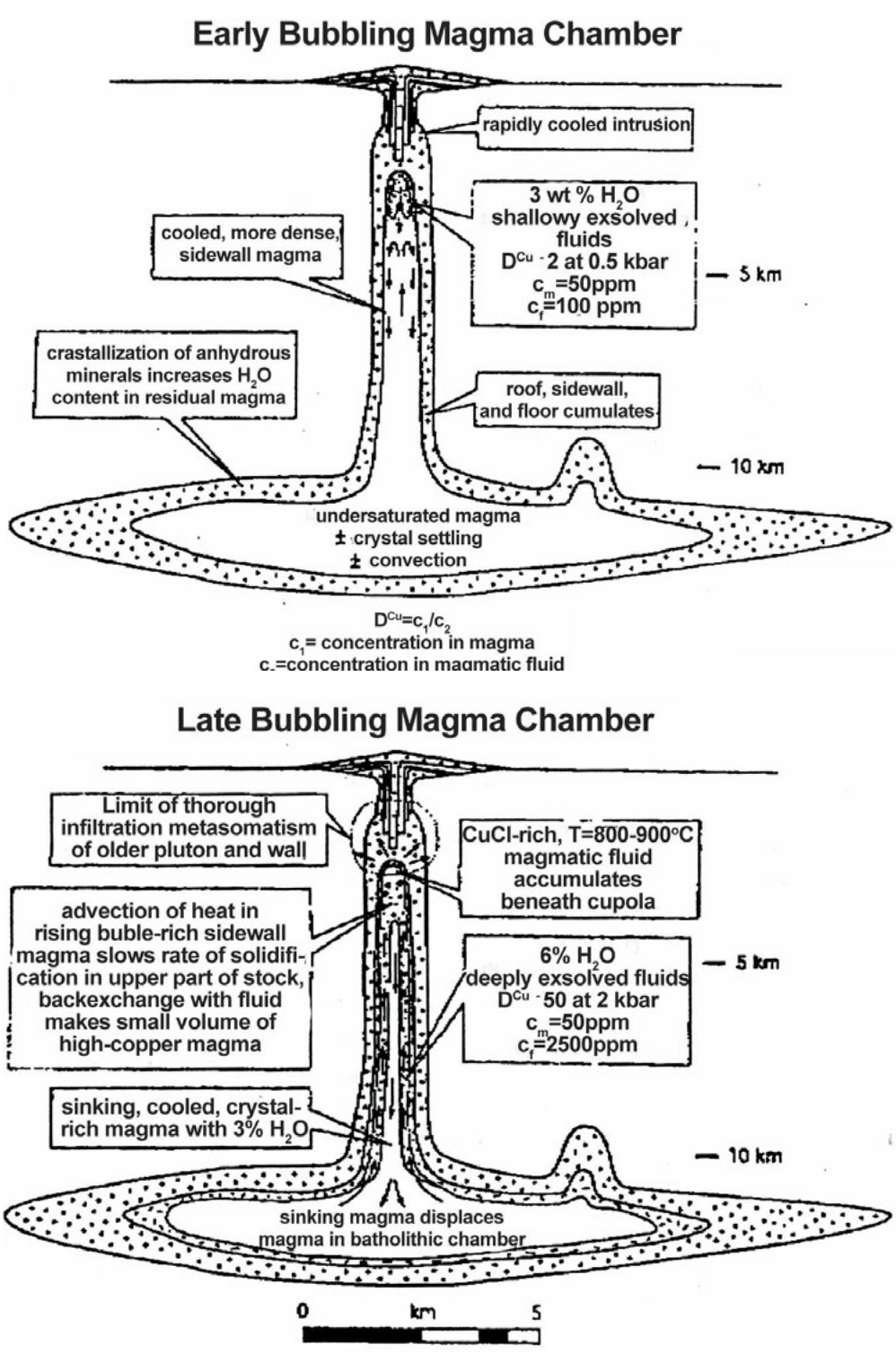

Figure 1-3 Different stages of magma bubbling chamber

The early stage is characterised by exolusion of copper-poor fluid and rising of magma in the middle of the column; sidewall magma is cool and dense. When the saturation front propagates inward and downward the fluid exsolved becomes richer and the direction of magma convection changes. Figure after Cloos {, 2001 #124}.

1.2. Mineralising fluid in the genetic model: problematic issues

According to the orthomagmatic model, hydrothermal fluid in porphyry environments forms when MVP exsolves from a crystallising magma. At this stage, however, such a fluid it is not capable of mineralisation even if it is metal-rich. There are a number of conditions required to turn a hydrothermal fluid into a mineralising fluid. The conditions favourable for the formation of a fluid with high ore-forming capacity come under three categories:

► Pre-saturation conditions are responsible for the enrichment of the residual melt in ore metals, water and other volatiles before the MVP exsolution occurs.

► Favourable separation and accumulation conditions are then required to provide an effective mechanism for fluid transport in magma towards the intrusion top, and its accumulation under a carapace.

► Efficient transport and precipitation mechanisms are required to transport ore metals to a deposition site, and precipitation of metal sulphides.

Every category contains a number of pre-requisite conditions, which are always interrelated and are sometimes controversial. Figure 1-4 shows schematically relationships between different conditions; favourable for mineralisation conditions are shown by green colour; unfavourable conditions are in red colour. Green arrows in the figure imply that conditions are fulfilled and mineralisation is possible, provided that next stages are also favourable for ore formation. Red arrows show that mineralisation is only possible if additional conditions are met, i.e. larger volume of fluid or magma reservoir are required.

1.2.1. Formation of mineralising fluid: pre-separation conditions

Pre-separation conditions are responsible for the concentration of metals, water, chlorine, sulphur, and other volatiles in residual melt (Fig 1-4). Favourable pre-saturation conditions include sufficient water content in parental magmas, high degree of fractional crystallisation before volatile saturation and sufficient initial concentrations of metals, chlorine and sulphur in parental magmas (Fig 1-4).

1.2.1.1. H_2O content in magma

Constraints on water content in parental magmas are mainly based on the following assumptions:

► Magma is unsaturated until after emplacement at subvolcanic levels; since the

ascent of volatile saturated magmas often results in explosions, which destruct any potential porphyry systems (Cloos, 2001).

► The amount of water should be enough to cause extensive fracturing of roof rocks as a result of expansion of accumulated fluid (Burnham and Ohmoto, 1980).

Water content in the range of 2-5 wt% in parental magmas is considered to be the most favourable for formation of porphyry deposit (Burnham and Ohmoto, 1980). Magmas with low water content (<2 wt%) have neither the capacity to exsolve a sufficient amount of fluid to provide extensive fracturing of roof rocks after fluid accumulation. High water content in parental magmas (>5 wt%) leads to water saturation at deeper levels than inferred for porphyry deposits (Cline and Bodnar,

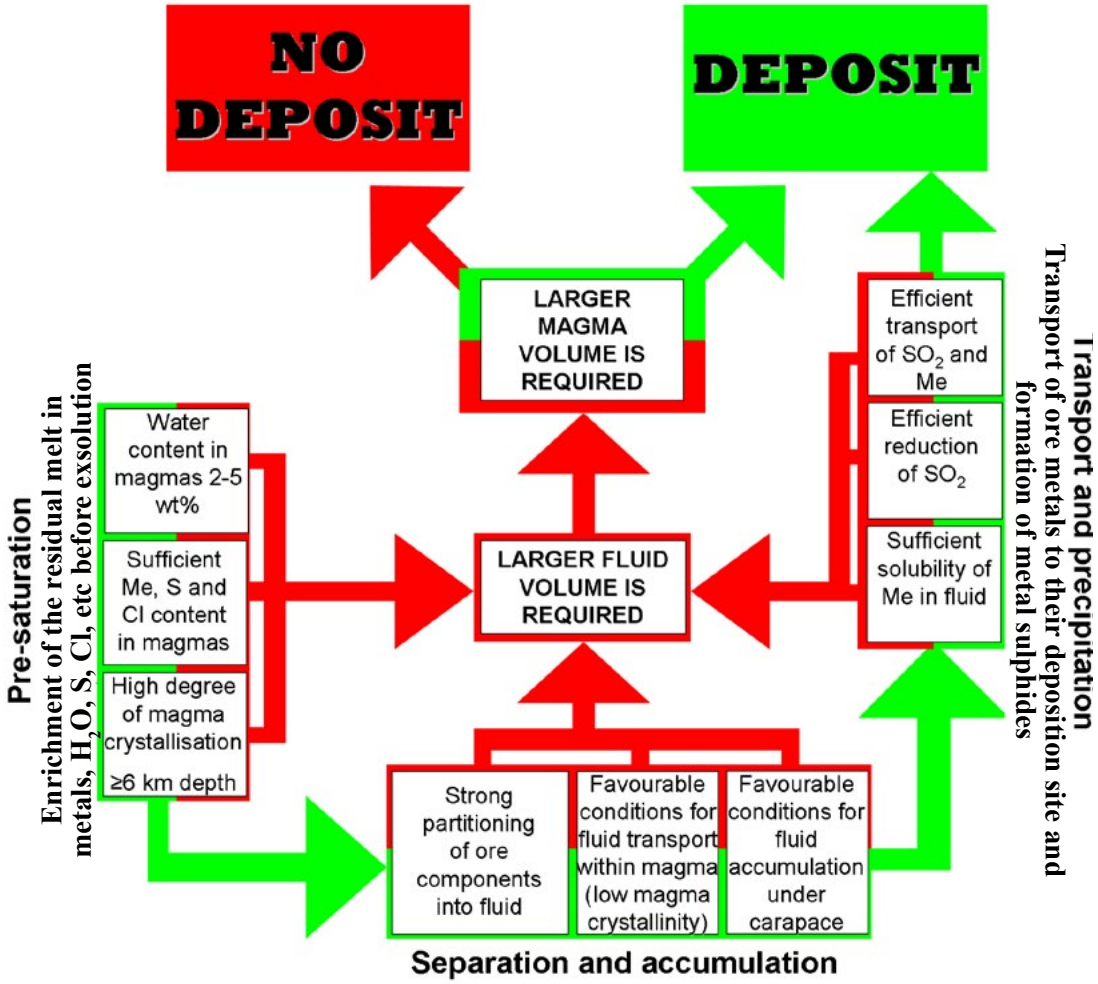

Figure 1-4 Conditions necessary for formations of porphyry-type deposits
Green fields are favourable conditions, red fields are less favourable conditions.

1991). Estimations of favourable water content in magmas are also based on the fact that crystallisation of hornblende (common in most porphyry intrusions) requires a minimum water content of 2-4 wt% (Cloos, 2001).

1.2.1.2. Degree of crystallisation and depth of emplacement

Fractional crystallisation increases concentrations of chlorine, water and ore metals in the residual melt. Therefore, the more crystallised the magma, the richer the residual melt, and thus, the higher ore-forming capacity of the exsolved fluid.

Emplacement depth has an effect on the chlorine partitioning coefficient. For example, at pressures greater than 1.3 kbar the first fluid to exsolve is the most Cl-rich and subsequent portions of the fluid are progressively poorer in chlorine. However, at pressures less than 1.3 kbar the reverse is true (Cline and Bodnar, 1991). Given that copper partitioning is known to be parallel to chlorine partitioning (Cline and Bodnar, 1991) the depth of fluid exsolution and the degree of crystallisation can play a crucial role in the formation of a potential ore-forming fluid. For instance, the fluid exsolved from a typical haplogranite melt at 0.5 kbar after 10% of crystallisation will contain only 5 wt% chlorine and will be very poor in copper, whereas at nearly 90% crystallisation the same melt will produce a fluid with a salinity of approximately 80 wt% and a copper concentration >2 wt% (Figs 1-5 and 1-6).

Thus, the favourable depth for the generation of a mineralising fluid is about 6 km or more (Cloos, 2001). This is the depth at which:

► The amount of water needed for saturation is greater than that at shallower levels (a greater amount of ore-forming fluid can be produced with smaller magma volumes);

► The degree of crystallisation is higher (the residual melt is richer in chlorine and metals);

► The chlorine partitioning coefficient is greater (the fluid is more chlorine- and metal-rich).

1.2.1.3. Concentrations of metals, chlorine and sulphur in magma

The orthomagmatic model does not require unusually metal-rich parental magmas (Cline and Bodnar, 1991; Cloos, 2001). Magmas with 50-70 ppm of Cu can be capable of forming a deposit, provided that chlorine and sulphur concentrations are sufficient (Cloos, 2001). However, the actual amount of metals required can vary and depends on magma volume, efficiency of metal extraction and the configuration of hydrothermal system (Burnham and Ohmoto, 1980).

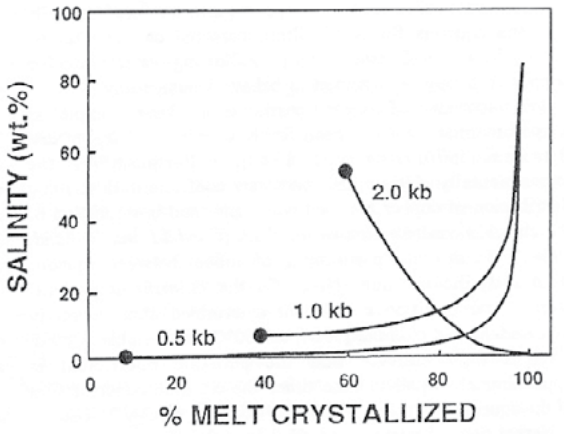

Figure 1-5 Salinity of an aqueous fluid exsolving from a crystallising magma at various pressures

Salinity of fluids was calculated for magmas with 2.5 wt% H_2O and Cl/H_2O ratio 0.1 at 0.5, 1 and 2 kbar pressure. Fgure after Cline and Bodnar (1991).

Nevertheless, simple estimations assume that the higher the initial concentrations of metals, chlorine and sulphur, the smaller the volume of the magma is required. Chlorine is essential for complexing metals (Cloos, 2001); high chlorine content enhances the efficiency of metal extraction (Burnham and Ohmoto, 1980). Sufficient concentration of sulphate (SO_2) in magmas is also required to enhance sulphur transport in the fluid (Cloos, 2001) and sulphur supply for sulphide precipitation. On the other hand, chlorine, SO_2 and CO_2 (and other volatile species) decrease the amount of water needed for saturation (Webster, 1997).

Although the chlorine content has a major effect on the water content required for magma saturation, it is not usually considered in the models. For example, Cline & Bodnar (1991) modelled formation of a porphyry deposit on a magma with Cl/H_2O=0.1 and water content 2.5 wt%; therefore, the Cl content was 0.25 wt%. They estimated the H_2O content necessary for the magma saturation at 2 kbar as 6 wt%. However, according to Webster (1997)e²», chlorine decreases the saturation point to 3 wt% (even 1 wt% in several experiments, Fig 1-6). Such decrease means that saturation occurs earlier, when magma is less crystallised. For example, magma with the initial 2.5 wt% H_2O and 0.25 wt% Cl would need to be 17% crystallised to reach saturation point at 2 kbar; whereas magma with the same H_2O content but without Cl would need to be 59% crystallised at the same conditions to reach saturation. Therefore, the presence of Cl significantly changes conditions.

It should also be kept in mind that porphyry copper deposits contain large

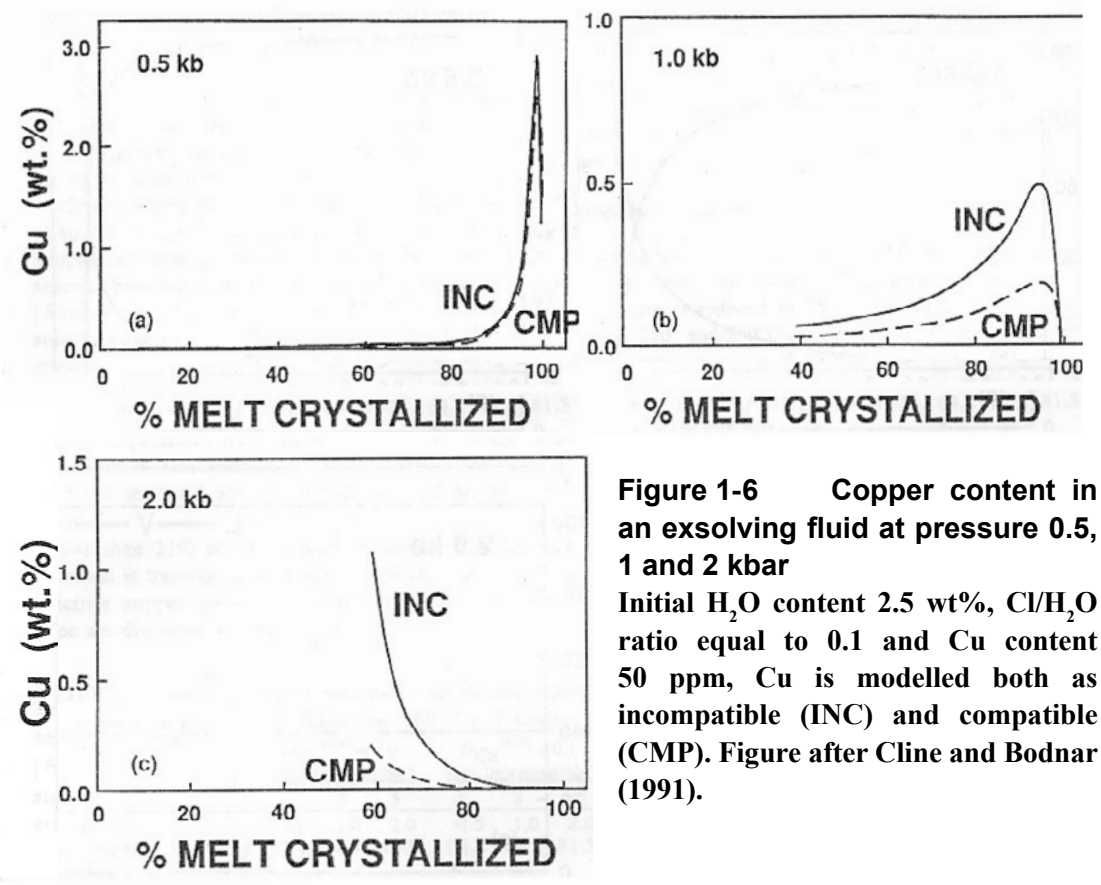

Figure 1-6 Copper content in an exsolving fluid at pressure 0.5, 1 and 2 kbar
Initial H_2O content 2.5 wt%, Cl/H_2O ratio equal to 0.1 and Cu content 50 ppm, Cu is modelled both as incompatible (INC) and compatible (CMP). Figure after Cline and Bodnar (1991).

quantities of sulphur as copper sulphides, significant anhydrite and even larger quantities of pyrite in alteration halos (Hattori and Keith, 2001) and thus, they are rather sulphur than copper anomalies (Cloos, 2001). In many cases eruptions of felsic magmas of similar to porphyry magmas compositions are accompanied by massive discharge of SO_2 (Andres et al., 1991; Gerlach et al., 1994; Hattori, 1993; Wallace and Gerlach, 1994). Mass-balance considerations showed that the entire amount of sulphur (SO_2) released during such eruptions could not have been dissolved in the magma reservoir (Pasteris, 1996). This is because felsic melts have low solubility for sulphur (Wallace and Carmichael, 1992) and melt inclusion data indicate that the sulphur content in melt is *'far too low (by one to two orders of magnitude) to account for the large mass of SO_2 released simply by exsolution of sulphur from melt during eruption'* (Wallace and Gerlach, 1994). It is believed that mafic magmas are injected into the bottom of dacitic magma reservoirs and contribute significantly to sulphur (as well as copper and other metals) supplies in volcanic systems (Hattori and Keith, 2001; Maughan et al., 2002). Similar mechanism of sulphur and metal input was offered to explain sulphur anomalies for porphyries (Maughan et al., 2002). At the same time, injections of mafic magmas into dacitic magma reservoirs are considered

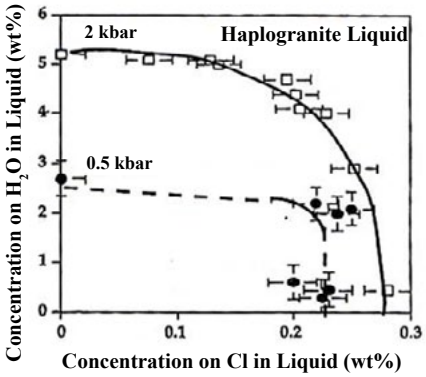

Figure 1-7 H_2O and Cl concentrations required for magma saturation
Figure after Webster (1997).

as triggers for eruptions (Hattori and Keith, 2001), which destroy porphyry systems and thus, are highly unfavourable for the formation of porphyry deposits (Cloos, 2001). Even if we assume that mingling of sulphur- and metal-rich mafic and felsic magmas occurred without eruptions, then the presence of large amounts of SO_2 will dramatically decrease the water content needed for saturation (Fig 1-7), because exsolution of the MVP from silicate magma is a direct function of the sum of the partial pressures of all volatiles in the system (Webster, 1997).

Another possible source of sulphur is magmatic sulphide globules, which form during immiscibility in parental magma. Such globules become unstable at shallow crustal levels, then oxidise and release sulphur and metals (Keith et al., 1997). This is in a good agreement with the data of Nadeau (2010) and Halter (2002) who concluded that the sulphide liquid may sequester 95% of the Cu and Au from the alumosilicate melt, and that this sulphide phase can react with saline aqueous fluid later releasing appreciable quantities of the ore metals.

1.2.2. Separation and accumulation of the mineralising fluid

Once magma has been emplaced and started cooling and crystallising there will be a point at which the MVP is exsolved from the magma. Provided that the pre-saturation conditions promoted formation of metal-rich residual melt, the probability that a deposit will form depends on how favourable the next stage, i.e. separation and accumulation, is. Favourable conditions for separation and accumulation stage include strong partitioning of ore components into a fluid phase, effective fluid transport within the magma and its accumulation under the intrusion carapace (Fig 1-4). For successful accumulation of the fluid, the magma-fluid system should either

be closed, or the rates of generation of the fluid should be greater than the rates of the fluids loss into surrounding rocks. Moreover, wallrocks should be strong enough to sustain increasing pressure during fluid accumulation. However, fluid pressure must eventually exceed lithostatic pressure and allow fluid to flow and precipitate sulphides along the fractures to form stockworks.

1.2.2.1. Fluid transport in magma

The ability of the exsolved fluid to coalesce into the large fluid-rich pocket under the intrusion carapace depends largely on efficiency of fluid transport in the magma. Several mechanisms of fluid transport in the magma have been proposed:

► Diffusion of fluid through magma (Shinohara et al., 1995).

► Migration of fluid bubbles (Shinohara et al., 1995).

► Rise of bubble-laden melt plumes (±crystals) in magma with < 20% crystallinity and formation of interconnected spanning fluid clusters in immobile crust (~20% of crystallisation) through which fluid can move (Candela, 1991).

► Rise of bubbles enlarged by coalescence due to buoyancy within convecting (upwelling) magma (Cloos, 2001; Shinohara et al., 1995).

Transport of magma-derived fluid by diffusion and via migration of small bubbles is considered to be too slow to be responsible for the accumulation of fluid: according to the data of Shinohara (1995), water can diffuse only 17 cm in 90 yr and a bubble with a 1 cm radius requires 500 yr to ascent 1 km.

Plume rise in a static magma is constrained by confining pressure (depth of emplacement), water content and the initial extent of magma crystallisation: this mechanism is only successful at a shallow level, within magmas of high water content and crystallinity less than 20% (Candela, 1991).

Formation of interconnected spanning fluid clusters is effective only within the apical part of intrusions where the bubble fraction is high (Shinohara et al., 1995). Magma convection or upwelling is an effective mechanism of fluid transport; however, magma convection occurs mostly within the ‘suspension zone’ where degree of crystallisation is less than 25% (Cloos, 2001) or 30% (Shinohara et al., 1995). Magma viscosity controls the rates of bubble separation from a convecting magma at the top of the magma body. Magma convection would cease if bubble separation was not fast enough to make the upper layers of magma denser to start sinking (Shinohara et al., 1995). In this case, the absence of convection and, thus, ascent of new batches of

bubble-rich magma would prevent further fluid accumulation.

Thus, high magma crystallinity (>25-30%), although favourable for formation of metal-rich fluids, is a negative factor in the ultimate formation of ore deposits, as the fluid transport through highly crystallised ductile environment is hindered. However, although favourable for fluid transport, a lower degree of magma crystallisation (<25-30%) does not allow sufficient enrichment of residual magmas and related aqueous fluids in metals and metal-complexing ligands.

1.2.2.2. Partitioning of ore components into fluid

Experimental data on chlorine and economic metals partitioning between aqueous fluid and melt indicate that partitioning coefficient of chlorine (D(Cl)=wt% Cl in aqueous phase/wt% Cl in granitic melt) increases strongly with increasing pressure (for pressures less than 6 kbar), with increasing of Cl content in the system and with decreasing temperatures (Kilinc and Burnham, 1972; Shinohara et al., 1989; Webster, 1992a, b). Kilinc (1972) found that the molal partition coefficient of chloride ($m_{Cl\ in\ melt}$ / $m_{Cl\ in\ fluid}$) is 0.023 at 2 kbar, 0.012 at 6 kbar and 0.077 at 8 kbar.

Partitioning of the most ore metals was found to be stronly dependant on the chloride concentration in the fluid (Candela and Holland, 1984; Hu et al., 2008; Zajacz et al., 2008). For example, Zajacz (2008) studied fluid/melt partitioning analysing coeval melt and fluid inclusions. According to the data, partition coefficients for Pb, Zn, Ag and Fe are the highest in brines; they are proportional to the chlorine molinity (mCl) in the melt and are about 6, 8, 4 and 1.4*mCl respectively. The authors concluded that such strong dependence indicate that they are dissolved primarily as Cl-complexes. On the contrary, partition coefficients for Mo, B, As, Sb and Bi are highest in low concentrated solutions; they are about 20, 15, 13, 8 and 15 mCl respectively. Fluid/melt partition coefficients of Cu, Sn and W were found highly variable; D_{Cu} reaches 2700 between melt and vapour indicating an important role for ligands other than Cl (Zajacz et al., 2008). Other data indicate that Cu partition coefficient between water and melt is approximately equal to nine times the chloride concentration of the aqueous fluid (Candela and Holland, 1984). Though it was found recently that Cu partitioning depends on the sulphur content in the fluid (Williams-Jones et al., 2005; Zajacz et al., 2008).

Exsolution of fluids with the highest metal-carrying capacity occurs at depths of 6 km or more after significant (up to 60%) crystallisation (Cline and Bodnar, 1991; Cloos, 2001). However, to form a porphyry-style deposit such fluids must move up '*at least several kilometres from where they are exsolved from the parent magma*' (Cloos,

2001) because the most common depth for porphyry copper ores is from 1 to 3 km. It follows from the experimental data for melt-fluid equilibria at different pressures (Cline and Bodnar, 1991), at 1-3 km depths the amount of chlorine and copper partitioning to the aqueous fluid is significantly reduced. Thus, fluids rich in Cl and Cu at the depth 6 km or more will re-equilibrate with the magma at shallow levels and inevitably lose significant amount of Cl and Cu to surrounding melt.

1.2.2.3. Duration of fluid accumulation

The orthomagmatic model implies that accumulation of the mineralising fluid under the intrusion carapace occurs prior to significant crystallisation, because for successful fluid transport magma viscosity must be low (Candela, 1991; Carten et al., 1988; Cloos, 2001; Shinohara et al., 1995; Sinclair, 2007). Analysis of the mechanisms of fluid transport in magmas (section 1.2.2.1) shows that fluid is able to move up towards the intrusion cupola and accumulate under the carapace until the degree of magma crystallisation reaches 25-30%. In magmas with crystallinity higher than 25-30% fluid mobility is restricted and fluid accumulation is hindered. We should also keep in mind that an intruding magma is partially crystallised; some authors (Shinohara et al., 1995) imply that the crystallinity of magma during emplacement can be up to 30%. Thus, there is not much time (if any) between emplacement and the state of the system when the magma is more than 30% crystallised.

Cooling time of an intrusion (without magma convection and input of the external heat) with a diameter of 300 m was estimated as 90 years (Shinohara et al., 1995). At these conditions there is very little chance that accumulation of the MVP would succeed simply because rapid crystallisation of the emplaced magma would hinder fluid transport within the magma. Accumulation of magma-derived fluid within the cupola of the intrusion can only continue while the magma is convecting; as soon as magma convection ceases the fluid exsolved from the magma would not be able to migrate, and probably remains within magma volume. According to Shinohara's model (1995) 390-960 km^3 of magma with crystallinity about 30% is able to degas due to magma convection within 30 years. In this model, however, it is implied that crystallinity of the magma increases by only 0.7% (from 30% to 30.7%) during that period, whereas in other variations of the model it is considered that conditions in a 'bubbling' convecting magma favour significant phenocryst growth (Cloos, 2001). If crystallinity of the magma increases further than 0.7%, then increasing viscosity of the magma would hinder and eventually terminate magma convection (Shinohara et al., 1995). Although a high degree of magma crystallinity favours exsolution of metal-rich fluid, it hinders fluid transport and put a significant constraint on a porphyry system

lifetime, and thus the efficiency of metal extraction.

1.2.2.4. Is the system closed?

Another question is whether the magma reservoir – porphyry stock system is closed or open. The condition that the system should be effectively isolated from surrounding rocks with the respect '*…to the transfer of matter (except hydrogen) either in or out*' (Burnham and Ohmoto, 1980) is essential for porphyry systems in the orthomagmatic model. However, in other variations of the model the combination of magma convection and open-system degassing is assumed (Cloos, 2001; Lowenstern, 1994). For initial accumulation of fluid either the rate of fluid generation should greatly exceed the rate of draining or the system should be closed; otherwise, accumulation of fluid is improbable. At the same time continuous accumulation of the fluid under the carapace can eventually trigger an eruption, which precludes successful ore formation. '*Porphyry copper ore deposits can only form where the rate of fluid generation and the rate of draining of the fluid pocket beneath a cupola is sufficiently steady that a buoyant rise is not initiated while a large volume of magma is cycled through the system and stripped of its copper*' (Cloos, 2001).

1.2.3. Transport and precipitation

If we assume that pre-saturation, separation and accumulation conditions have been successful they will have led to accumulation of the ore forming fluid beneath an intrusion cupola. According to the model of Burnham (1980), as soon as a sufficient amount of the mineralising fluid has accumulated the fluid pressure increases and at some point the roof rocks will not able to sustain the pressure, fracturing occurs, and the fluid from the intrusion carapace will be released outwards in host rocks. The Cloos's model (2001) assumes steady drainage of the fluid pocket. Once the fluid has been released, though, a new transport and precipitation stage begins. This stage is governed by the solubility of the metals and metal-complexing ligands in the fluid and by the conditions favouring transport of sulphur and metals and precipitation of sulphides (Fig 1-4).

One of the most important factors for formation of a porphyry-style deposit and its metal speciation is state of a melt and fluid during exsolution, accumulation, transport and precipitation. Single phase liquid would have significantly different properties comparing to a liquid containing several immiscible phases.

Immiscibility is a widespread phenomenon; there are three major types of immiscibility: melt-melt, melt-fluid and fluid-fluid immiscibility. Phase separation occurs

due to 'fundamental differences in the nature of chemical bonds', i.e. components with different types of bonding (ionic, covalent, metallic or intermolecular) form immiscible phases (Veksler, 2004). For instance, melts are characterised by components bonded with covalent (Si^{4+} and Al^{3+}) and ionic (alkalis, alkaline earths and Fe^{2+}) bonds; most of salts are pure ionic, sulphides have metallic bonds and C-O-H liquids and vapours are typical molecular fluids (Veksler, 2004). Crystallisation and immiscibility have competitive relationships: components, which supress crystallisation, at the same time enhance immiscibility (Veksler, 2004).

During the magmatic-hydrothermal transition as a result of fractional crystallisation concentration of non-silicate anions (such as F^-, Cl^-, BO_3^{3-} or PO_4^{2}) occurs within the residual melt. These components supress crystallisation to significantly lower temperatures; in such systems immiscibility can play a crucial role in their further evolution. Immiscible phases are typically of contrast composition and density (Audetat et al., 2008; Veksler, 2004; Veksler et al., 2004). The former is provided by different partitioning of elements between immiscible phases, the latter can provide spatial separation of newly formed phases. For example, gaseous components such as HCl, H_2S and SO_2 partition preferentially into the vapour (Proffett, 2009), whereas alkalis and the elements which can complex with Cl, partition mainly into the brine (Proffett, 2009). In this case due to the density contrast between vapour and melt can account for effective separation of vapour phase from the parent melt, whereas low density contrast between brine and melt may lead to accumulation of the phase within the cupola (Proffett, 2009). Moreover, many ore-components are separated during liquid-vapour immiscibility in the fluid: Cu, Au, As and B have tendency to fractionate into the vapour phase, whereas Na, K, Fe, Mn, Zn and Pb partition into the brine phase (Audetat et al., 2008; Heinrich, 2007; Proffett, 2009; Williams-Jones et al., 2005). Thus, immiscibility is extremely important phenomenon, which must be taken in account during modelling.

The existing model for formation of porphyry-style deposits considers two major immiscibility events. Firstly, melt-fluid immiscibility occurs within the residual melt that leads to exsolution of MVP. Secondly, fluid-fluid immiscibility can occur within the exsolved fluid, which separates low density vapour phase from hydrosaline liquid phase. These two immiscibility events are considered as keys for ore-forming processes, and are the major constrains for modelling of porphyry-style ore formation (Cline and Bodnar, 1991; Cloos, 2001; Hedenquist and Lowenstern, 1994; Kamenetsky, 2006; Kamenetsky and Kamenetsky, 2010; Shinohara et al., 1995). Depending on the depth of magma emplacement and magma compositions, exsolved fluid can be a single-

phase fluid of low to intermediate salinity or two-phase fluid (vapour + hydrosaline liquid) (Audetat et al., 2008; Cline and Bodnar, 1991; Heinrich, 2007; Proffett, 2009). Further evolution of a fluid during cooling may include sublimation, contraction (transition from vapour to liquid without immiscibility), condensation and boiling; combination and sequence of these processes determines type of an ore deposition (Heinrich, 2007). For example, magma emplaced close to the surface provides exsolution of high-temperature low-density vapour, which during cooling sublimates and precipitates any salts; further cooling of such vapour provides acid leaching and formation of vuggy quartz. Magmatic fluid produced at 1 km or deeper exsolves as low-salinity low (intermediate)-density fluid, which undergone immiscibility later (or exsolves as two-phase fluid) resulting in condensation and separation of small amount of hypersaline liquid. At these conditions further cooling leads to expansion of vapour and finally relatively focused precipitation with formation of Cu-Au 'ore shell'; the residual hypersaline liquid can produce later Mo veinlets (Heinrich, 2007). When immiscibility occurs at higher pressures vapour phase can contract during further cooling to a low-salinity fluid. Provided that there is an excess of sulphur, low-pressure boiling can provide favourable conditions of gold precipitation from such fluid. Within the fluid exsolved at even higher pressures and temperatures immiscibility can never occur, and a single-phase fluid simply contracts isochemically in this case.

Generally, the exsolution of MVP and fluid-fluid immiscibility characterise the beginning and the end of the magmatic-hydrothermal transition. However, the processes operating at this stage are still poorly understood (Audetat et al., 2008). In fact, more than two immiscibility events can occur during magmatic-hydrothermal transition (Kotel'nikova and Kotel'nikov, 2010a, b; Thomas and Davidson, 2008). This can change our view on the evolution of mineralising fluids.

1.2.3.1. High temperature hydrolysis

It has been found recently (Kotel'nikova and Kotel'nikov, 2010a, b; Veksler, 2004; Webster and Mandeville, 2007) that high temperature hydrolysis can play an important role in evolution of hydrothermal fluid. In a schematic way, hydrolysis reactions may be expressed as follows (Veksler, 2004):

$NaCl\ (melt) + H_2O\ (vapour) = NaOH\ (melt) + HCl\ (vapour)$

$NaF\ (melt) + H_2O\ (vapour) = NaOH\ (melt) + HF\ (vapour)$

$Na_2CO_3\ (melt) + H_2O\ (vapour) = 2NaOH\ (melt) + CO_2\ (vapour)$

$LiBO_2\ (melt) + 2H_2O\ (vapour) = NaOH\ (melt) + H_3BO_3\ (vapour)$

Thus, hydrolysis reactions can provide separation of acid vapour from hydrooxides; the former can migrate easily, whereas the latter tend to stay in the melt. Due to the hydrolysis reactions even simple systems, such as NaCl-H_2O, at high temperatures cannot be considered as binary systems (Veksler, 2004). Moreover, hydrooxide components may react with surrounding minerals as it was found in experiments on fluid inclusions in H_2O-Na_2SO_4-SiO_2 and H_2O-NaF-SiO_2 systems at 700-800°C and 1-3 kbar (Kotel'nikova and Kotel'nikov, 2010a, b). With a few exceptions our knowledge about high temperature hydrolysis in other systems is limited, and although hydrolysis is an extremely important phenomenon it is not considered in the orthomagmatic model.

1.2.3.2. Transport of metals

The ability of fluid to transport metals is determined by the solubility of the components, which differ strongly between different fluid phases, and vary with pressure, temperature, and/or bulk system composition. Aqueous vapours preferentially dissolve CO_2, SO_2, H_2S, S_2, HCl, HF, H_2, CO, CH_4, COS, whereas coexisting saline liquids transport alkali-enriched salts, which are mainly chlorides and

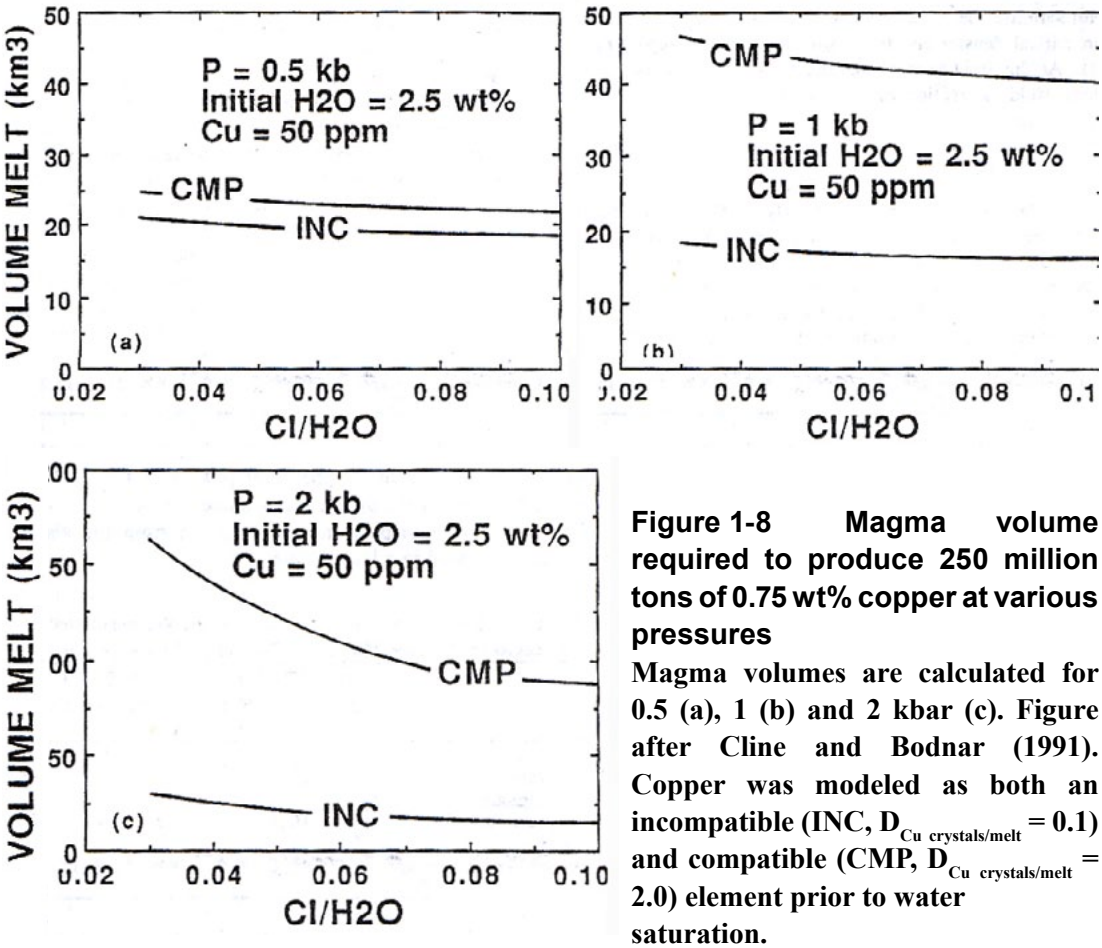

Figure 1-8 Magma volume required to produce 250 million tons of 0.75 wt% copper at various pressures

Magma volumes are calculated for 0.5 (a), 1 (b) and 2 kbar (c). Figure after Cline and Bodnar (1991). Copper was modeled as both an incompatible (INC, $D_{Cu\ crystals/melt} = 0.1$) and compatible (CMP, $D_{Cu\ crystals/melt} = 2.0$) element prior to water saturation.

sulphates, though fluorides, phosphates and carbonates may also occur (Hedenquist and Lowenstern, 1994; Webster and Mandeville, 2007).

In fact, the speciation of transition metals, heavy metals, and metalloids strictly depends on partitioning of complexing ligands, such as C, S, Cl, and F between fluid phases (Webster and Mandeville, 2007). For example, it was found that Cu can be transported as chloride complexes in highly concentrated brine, but it also preferentially partition in vapour phase in chlorine-free sulphur-bearing fluids (Williams-Jones and Heinrich, 2005). It was found that in volcanic vapours Ga, In, Tl, Fe, Co, Ni, Na, K, Zn, Pb and Cu are primarily dissolved as chloride species; Al and Ca in vapours dissolves as fluoride species; Ge, Bi, Sn, and Pb can be dissolve as sulphide or chloride species; Be, Al, and Si as fluoride and oxide species; Ti, Zr, V, Mo, W, and Re as oxyfluoride and oxychloride species, and Hg and Cd are transported as neutral species (Webster and Mandeville, 2007).

1.2.3.3. Transport of sulphur

There is no full agreement on how sulphur is transported in hydrothermal fluids. Cloos (2001) believes that *'magmas must be sufficiently oxidising that magmatic sulfur is partitioned into the fluid as SO_2, which is later reduced upon cooling to precipitate copper sulfides'*. Burnham thinks that sulphur is *'dissolved in hydrous melts principally as bisulfide ion (SH-)'*(Burnham and Ohmoto, 1980). Chlorine-rich fluid can contain low concentrations of reduced sulphur or higher concentrations of the sulphur in oxidised form (Skinner and Barton, 1973; Wilkinson, 2001). If a fluid contains reduced sulphur, precipitation of sulphides occurs only until the sulphide ions are consumed; further precipitation of sulphides requires external sources of reduced sulphur (Skinner, 1979). If a fluid contains oxidised sulphur then for extensive sulphide precipitation an effective mechanism of sulphate reduction is required (Skinner and Barton, 1973). A possible mechanism for sulphur reduction is hydrolysis of SO_2 during cooling via the reaction suggested by Holland (1965):

$$4SO_2 + 4H_2O = H_2S + 3H_2SO_4$$

However, only 1 mole of H_2S out of 4 moles of SO_2 can be provided by the reaction. Such inefficient mechanism for sulphide reduction lowers efficiency of metal transport and precipitation. If we assume that such a mechanism operates widely we must invoke larger sources of sulphur, e.g. larger volumes of mafic magmas. That would lower the chances of formation of a porphyry deposit because it increases the possibility of an eruption and thus destruction of a porphyry system.

Newton and Manning (2005) showed that solubility of anhydrite in concentrated NaCl fluid at near-magmatic temperatures (>750°C) is very high, which may indicate that a large proportion of magmatic sulphur will partition into an exsolving fluid as sulphate. On the other hand, the thermodynamic predictions that sulphur in ore fluids can exist either as sulphide or sulphate ions, is based on low T-P data (Pokrovski and Dubrovinsky, 2009). In contrast to those data it was found recently that the dominant species of sulphur at high P-T conditions can be polysulfide (e.g. $H_{0-2}S_3$) and/or polythionate (e.g. $H_{0-2}S_2O_5$) species, which are more abundant than believed (Pokrovski and Dubrovinsky, 2009). This fact may change significantly the model for the sulphur transfer to the deposit sites, however, it is not considered in the models yet.

The coexistence of quartz and sulphides, which is so typical for porphyry-type deposits, points to the important role of sulphur in the transport and deposition of metals. Some authors believe that sulphur and metals are transported by the same fluid (Burnham and Ohmoto, 1980; Cloos, 2001). Other authors consider that significant concentrations of sulphur and metals (apart from the cases when sulphur is transported in an oxidised form, most commonly as sulphate) are transported by separate fluids and ore formation can only occur where mixing of these two fluids occurs (Wilkinson, 2001). The significance of sulphur for metal transport was emphasised by a number of authors (Williams-Jones and Heinrich, 2005; Williams-Jones et al., 2005; Zajacz and Halter, 2009). For instance, it was shown that Cu and Au partition preferentially into the vapor provided that significant concentrations of sulfur is present, and that such strong preference of the metals for the the vapor phase may indicate the formation of sulfur-bearing metallic gas species (Williams-Jones and Heinrich, 2005).

1.2.3.4. Transport of silica

Quartz is closely associated with ore bodies in porphyry environments. Vein quartz as stockworks, comb quartz and quartz eyes are typical; massive quartz sometimes underlies ore bodies (Wallace et al., 1968). Moreover, silicification is a common type of alteration, which is also associated with ore fluids in porphyry environments. Occurrence of quartz and sulphides together indicate that silica may play a significant role in transport and precipitation of sulphides, and thus it should be reflected in the genetic model. Although quartz and sulphides crystallise from the same fluid, there is no model that consider possible influence of dissolved silica on the ability of a fluid to transfer metals, or simultaneous precipitation silica with ore minerals.

Silica is transported as H_4SiO_4 or $H_3SiO_4^-$ (Rimstidt, 1997). However, quartz solubility in both pure water and chlorine solution is relatively low (Kennedy, 1950; Rimstidt, 1997; Shmulovich et al., 2006). There is no experimental data on quartz solubility in complex fluids including chlorides, metals and sulphur. It is known though that dissolved silica 'behaves in a rather intriguing way' in complex systems (Akinfiev and Diamond, 2009). The presence of CO_2 in aqueous fluids lowers silica solubility, and the presence of salts can cause both a decrease (salting-out effect) and increase (salting-in effect) in silica solubility (Kennedy, 1950; Shmulovich et al., 2006). At 700°C the salting-out effect is maximal at high pressures (15 kbar) and weakens with a decrease in pressure (Akinfiev and Diamond, 2009), therefore, in porphyry environments it can be significant. Nevertheless, the abundance of quartz typically associated with porphyry-type deposits can only be precipitated as a result of the flow of '*unreasonably large volumes of fluid*' (Wilkinson et al., 1996) or unreasonably high silica solubility. Large fluid volumes are not an issue for formation of the hydrothermal deposits, where large circulation cells can be implied, in which fluids can circulate for prolong periods and scavenge ore components from large volumes of rocks. It is believed though, that porphyry fluids are magma-derived (Burnham and Ohmoto, 1980; Cloos, 2001) and external fluids do not contribute significantly to formation of deposits of the type until the systems are cooled below 350°C (Gustafson, 1978). Therefore, if magmatic fluids do not contain sufficient amounts of metals then additional volumes of magma are required. External fluids in porphyry systems are only invoked to provide effective means of precipitation of ore minerals, e.g. as a result of fluids mixing (Wilkinson, 2001). Thus, in porphyry environments low solubility of metals, sulphur or silica in aqueous fluid can only indicate that the efficiency of metal extraction from magma is low and larger magma volumes must be involved.

1.2.4. Magma volume

The volume of magma required to generate an amount of mineralising fluid sufficient to form a deposit depends on the compatibility of ore metals, initial water content, depth of emplacement and initial chlorine/water ratio (Cline and Bodnar, 1991), as well as the efficiency of fluid transport, accumulation and precipitation.

According to the Cline & Bodnar model (1991) the formation of approximately 2 million tons of copper (250 million tons with 0.75 wt% copper) requires 15-20 km^3 of magma if copper behaves incompatibly, whereas 20-90 km^3 of magma are required to produce a deposit of the same tonnage if copper is compatible with the magma (Fig 1-8).

The model implies that after copper has partitioned into the fluid phase the next stages such as fluid transport in the magma, its accumulation under the carapace, transport in the host rocks and precipitation from hydrothermal fluid, have efficiency 100%. However, this is unrealistic, as not all the exsolved fluid is able to reach the intrusive cupola, and not all the fluid that has accumulated within the cupola is able to contribute to the focused fluid flow required for ore formation. Furthermore, the fluid can lose metals in transit to the cupola owing to fluid-magma re-equilibration. Moreover, the total metal content in a porphyry deposit is often underestimated; for example, estimations of copper content in porphyry systems are commonly restricted by 0.3 wt% grade zones (Cloos, 2001) and ignore the metals in the inevitable large low-grade halo. Taking into consideration that efficiency of metal extraction is significantly less than 100% during the mentioned stages, much larger than 20-90 km^3 magma is required. For the formation of super-giant (>10,000,000 tons of copper) porphyry-type deposits magma volumes on the order of 1000-2000 km^3 or even more are required (Cloos, 2001), which is the equivalent of a large batholitic chamber.

Finally, any changes towards less favourable conditions during the pre-saturation, separation and accumulation, and transport and precipitation stages exacerbate this decrease in efficiency and the formation of a deposit is only possible provided that magma volume increases proportionately (Fig 1-4).

1.3. What is missing?

What do we actually know about fluids that exsolve from magmas? Generally, almost all processes leading to mineralisation (including fluid exsolution) of the type are related to magmatic-hydrothermal transition, which is still poorly understood (Audetat et al., 2008). This period is characterised by features inferred to have existed for only a short period of time and which have generally left no evidence of their existence. Minerals stable at magmatic conditions become unstable, for example, magmatic sulphides decompose, magmatic biotite and amphibole are replaced by hydrothermal varieties (Audetat et al., 2008).

The orthomagmatic model has evolved over many years and now it is probably the most acceptable model for the formation of porphyry-type deposits (Sinclair, 2007). Every new modification of the orthomagmatic model has attempted to address some of the inconsistencies from previous models, yet in spite of much effort there are still many unanswered questions.

Variations of the orthomagmatic model involve scavenging of the metals from

small stocks (Cline and Bodnar, 1991), batholithic chambers (Cloos, 2001), or from static (Burnham and Ohmoto, 1980), convecting (Cloos, 2001; Shinohara et al., 1995) or rising magmas (Lowenstern, 1994). Between different examples of porphyry deposits, the depth of emplacement varies, as does the configuration of the system, varying from isolated small stocks (Cline and Bodnar, 1991) to small stocks linked to large, underlying mafic magma chambers (Cloos, 2001; Shinohara et al., 1995). Different mechanisms of fluid transport in magmas have been suggested (Candela, 1991; Shinohara et al., 1995).

Nevertheless, the detailed analysis of the model indicates that there are still many mutual contradictions. For example, conditions that favour the enrichment of residual melt also cause early separation of an MVP that actually reduces the chances of formation of porphyry deposits (Fig 1-8). Favourable conditions for the formation of a fluid of high metal-carrying capacity in most cases reduce the potential for fluid transport (Fig 1-8). Moreover, even if we assume that transport of a metal-rich fluid within the magma proceeds successfully, the fluid will probably lose a significant part of its metal content in transit as a result of fluid-magma re-equilibration. Such re-equilibration occurs because the partition coefficients of chlorine and copper between fluid and melt decrease dramatically with decreasing pressure (Cloos, 2001). Thus, re-equilibration of fluid with melt at shallower depth generally depletes the fluid and enriches the melt in chlorine and copper. According to the model, depleted fluid separates from the magma at the top of magma column and accumulates under the carapace and the enriched magma sinks. So, the final efficiency of stripping metals from melt is rather low. Thus, formation of even small porphyry deposits requires rather large magma reservoirs at depth. Moreover, mass-balance calculations show that the magma that generates porphyries cannot provide enough sulphur even for the formation of a small deposit; injections of mafic magmas, although they can contribute to sulphur supplies, would most likely destroy the porphyry system by causing an eruption. There is no convincing explanation for co-precipitation of sulphides and silica. Furthermore, there is still no answer to the simple question: what makes the difference between barren and mineralised plutons? The fertile vs infertile magma debate has gone on for decades, and remains unresolved. The major control factors (fluid focusing, immiscibility, structural control, geochemical signatures or magmas, etc) responsible for porphyry mineralisation are still unknown (Audetat et al., 2008).

Presumably something must be missing in the model because there is no model to fit everything. We would suggest that whatever has been missed is most likely transient (brief and unstable at the conditions of magmatic-hydrothermal transition)

and fugitive, since it leaves little or no evidence (turns into something else, for instance, recrystallise to a more stable mineral).

1.4. Fluid inclusions as the source of our knowledge about mineralising fluid

Our knowledge about mineralising fluids is heavily reliant on fluid inclusion data. Fluid inclusions can indeed be a useful tool for deciphering fluid compositions, origin of fluids and precipitation mechanisms of hydrothermal minerals. This is conditional on fluid inclusions being representative of the original fluid present at the time of precipitation with no post-entrapment modification. Unfortunately, this underlying assumption is not always correct. Re-equilibration of fluid inclusions after entrapment is a very common phenomenon (Roedder, 1984; Vasyukova and Fonarev, 2006; Vityk and Bodnar, 1995; Vityk et al., 2000; Vityk et al., 1995). Such re-equilibration can include leakage of fluid in or out of inclusions, diffusion of the fluid components (water and hydrogen), precipitation of daughter phases and necking down. In some cases revealing post-entrapment modification is not an easy task. Moreover, it was shown for epithermal (Sanders and Black, 1988) and mesothermal (Herrington and Wilkinson, 1993) quartz veins that in rare instances fluid inclusions form as a result of recrystallisation of water-rich quartz precursor into water-poor quartz plus liquid water. Although in those cases inclusions show primary distribution, they do not represent a media from which a host mineral grows. Evidence for such origins of fluid inclusions are preserved extremely rarely. Thus, fluid inclusion data are not always applicable for reconstruction of conditions of host-mineral crystallisation and we should be extremely careful interpreting fluid inclusion data.

Roedder (1984) defines three main fluid characteristics for a fluid from porphyry environments on a base of fluid inclusion data:

1. High temperature (400-800°C).
2. High salinity (40-60 wt% NaCl equivalent or even higher)
3. Boiling assemblages.

In many cases fluid boiling is considered to be the main precipitation mechanism. However, boiling assemblages are also often observed in barren plutons (Audetat et al., 2008; Roedder, 1984). Other reports of fluid inclusions in porphyries indicate even wider ranges in temperatures and salinities (Wilkinson, 2001) from 200-700°C and 0-70 wt%. NaCl equivalent. Such diversity in the composition of coeval inclusions is

believed to occur because of evolving conditions during entrapment (such as pressure variations, boiling, condensation or entrapment in the liquid+solid+vapour field) and/or post-entrapment modification (leakage of fluid, hydrogen diffusion or necking down).

The number of techniques that allow us to identify fluid compositions is limited. In fact, in many cases the composition of fluid inclusions is only approximately determined: salinity is measured as NaCl equivalent, and compositions of daughter phases are often speculated based on optical properties and shapes. Eutectic temperatures are usually used to identify composition of salts. However, this technique is based on experimental data, e.g. data of Borisenko (1977), and thus applicable to the limited number of the salt systems, whereas in nature fluid of much more complex compositions (multi-component system) are usually trapped. Moreover, eutectic temperatures are difficult to observe and because of this in most case are not reported. Even when the fluid data are reliable and the fluid composition is identified it should be kept in mind that fluid inclusions can be significantly different from the fluid which was initially trapped. In fact, entrapped fluid may *'bear only slight resemblance'* of *'the solution first expelled from a crystallising magma'* (Ingerson, 1954). Experimental data is another source of knowledge on the fluids which exsolves from magmas. Experimental studies on fluids contribute significantly to our knowledge about fluif-fluid, fluid-melt and fluid-rock interactions, as well as about re-equilibration of fluid after entrappment (Heinrich, 2007; Liebscher and Heinrich, 2007; Sterner et al., 1988; Vityk and Bodnar, 1995; Vityk et al., 2000; Vityk et al., 1995; Webster and Mandeville, 2007). However, experimental modelling always simplifies the fluid composition, so that experimental results not always can be applied to natural fluid systems. The majority of experiments on fluid inclusions are carried out on binary or sometimes ternary fluid systems, whereas a composition of natural fluids is much more complicated. We should always remember that '*primary fluid inclusions from ore deposits provide almost all we know about the nature of the ore fluids, but they generally provide almost nothing as to their origin' (Roedder, 1992).*

1.5. New ideas on hydrothermal fluids

It has been proposed that high temperature hydrothermal fluids may be represented by a viscous, dense and highly metal-charged substance, namely 'silicothermal fluid' (Sirbescu and Nabelek, 2003; Wilkinson et al., 1996; Williamson et al., 1997; Williamson et al., 2002). Such fluid was observed in synthetic fluid

inclusions (Wilkinson et al., 1996), in natural inclusions in topaz from the Hensbarrow granite (Williamson et al., 1997) and in Tin Mountain pegmatite Hills in South Dakota (Sirbescu and Nabelek, 2003). Thomas (2000) reported 'type-B melts' from central Erzgebirge pegmatite in Germany, which contain up to 50 wt% of silica. A 'silicothermal fluid' may contain up to 90 wt% silica, which apparently crystallises to quartz over time (Wilkinson et al., 1996) and can have a very high metal-charge capacity (Williamson et al., 1997; Williamson et al., 2002).

Moreover, it was confirmed experimentally that the system SiO_2-Na_2O-H_2O belongs to p-Q topology type, which with either stable or metastable immiscibility between dilute (about 1 wt% of solute) and concentrated solutions with about 20 wt% H_2O, 60 wt% SiO_2 and 20 wt% Na_2O (Veksler, 2004).

Although the formation of hydrosilicate liquids as a late stage phase at the magmatic-hydrothermal transition was discussed by many researches (Kotel'nikova and Kotel'nikov, 2010a, b; Thomas and Davidson, 2008; Thomas et al., 2010; Tuttle and Friedman, 1948; Veksler, 2004; Wilkinson et al., 1996; Williamson et al., 1997; Williamson et al., 2002), the significance of such phases for the fluid-melt evolution and ore formation is not fully understood. However, such fluids can play a crucial role in metal transport and metallogenesis even if it represents a transient, thermodynamically unstable phase (Wilkinson et al., 1996). Since the 'silicothermal' fluid can be very concentrated there is no need to invoke unreasonably large volumes of fluid required for hydrothermal fluid transport (Wilkinson et al., 1996) and duration of formation of ore deposits can be much shorter (Williamson et al., 2002).

1.6. Aims of the study

The discovery of the 'silicothermal fluid' changes the conventional view on hydrothermal fluids. It raises many questions, for instance, how and where does it form? Is the exsolving fluid actually a 'silicothermal' one? If not then when and how does the fluid turn into a dense and highly metal-charged substance? How can the new data on the nature of fluids change our view on porphyry-type deposit formation? And whether the 'silicothermal fluid' is the missing piece of the puzzle of porphyry formation?

This study aims to verify whether 'silicothermal fluid' participates in porphyry formation, and to what extent. Since 'silicothermal fluid' can be very rich in silica, quartz must be the most abundant product to precipitate from it. This is consistent with geological observations in many deposits: many varieties of quartz are observed within

ore bodies such as quartz veins, comb quartz, quartz stockworks, and sometimes massive quartz and silicification products. The ‘classic’ hydrothermal origin for quartz explains neither the association of quartz and sulphides nor the abundance of quartz in porphyry systems. If the quartz from porphyries has ‘silicothermal’ precursors then high silica contents and co-precipitation of silica with sulphides should be a common feature.

Porphyry-related intrusions are typically characterised by porphyritic textures, which is determined mostly by feldspar and quartz crystals. Both of them are believed to crystallise within convecting magma at significant depth (Burnham and Ohmoto, 1980; Cloos, 2001). However, magmas of intermediate composition are silica undersaturated and thus, in porphyry systems quartz must be the last phenocrystic phase to crystallise, because silica saturation required to begin crystallisation of quartz occurs relatively late. Therefore, quartz crystals in porphyry environments may crystallise during the late magmatic stage or even during the magmatic-hydrothermal transition. Such late crystallisation was suggested for vermicular quartz eyes from the Empire Mine in Idaho (Chang and Meinert, 2004) and the Bajo de la Alumbrera porphyry Cu-Au deposit (Harris et al., 2004). These late conditions are significantly different from those of crystallisation of normal quartz phenocrysts in volcanic rocks. Moreover, quartz crystals can also be porphyroblasts or clasts (Hopwood, 1976). Quartz in porphyry deposits commonly occurs as rounded to irregular grains, usually classed as phenocrysts, although often with anhedral shapes. The term ‘quartz eyes’ does not imply a certain origin and is used here in preference to other terms (e.g. phenocrysts, porphyroblasts or clasts) to emphasise that their origin is yet to be established.

Quartz is a mineral of simple and constant composition, and it had not been studied in much detail until about two decades ago when cathodoluminescence (CL) technique became available. This method has proved to be an excellent tool for visualising internal growth textures in quartz invisible by any other means (Götze, 2009; Götze et al., 2001; Müller, 2000). CL reveals variations in quartz textures based on the distribution of trace elements and lattice defects in the crystal, which is believed to reflect the changes of physico-chemical conditions of crystal growth (Müller, 2000). CL has been successfully used in reconstructing the growth history of quartz (Allan and Yardley, 2007; D’Lemos et al., 1997; Götze, 2009; Landtwing and Pettke, 2005; Monecke et al., 2002; Müller, 2000; Penniston-Dorland, 2001; Peppard et al., 2001; Rusk et al., 2008; Rusk and Reed, 2002; Rusk et al., 2006; Wark et al., 2007; Wiebe et al., 2007).

Here we use CL to reveal the internal growth patterns of quartz eyes and to reconstruct their growth history. Did they crystallise from the melt in the magma reservoir – magma column system during magma convection? Are quartz eyes crystallised in-situ after emplacement? Quartz eyes are often the only host mineral for fluid inclusions within a plutonic rock, which are usually the only source of the information on the mineralising fluid, and our knowledge about the internal structures of the quartz eyes can be crucial for determining their origin. This study concentrates on quartz eyes since it is our view that they are the concrete expression of 'silicothermal fluid' and thus a critical link in the origins of porphyry deposits.

This study focuses on internal structures of quartz eyes and veins from several porphyry deposits and inclusions they contain. The deposits are: Antapaccay (Peru), Batu Hijau (Indonesia), Climax (USA), Panguna (PNG), Far Southeast porphyry (Philippines), Rio Blanco (Chile) and Omsukchan (Russia). Cathodoluminescence, optic microscopy, backscattered scanning electron imaging, electron microprobe, Raman spectrometry, laser ablation ICMS and microthermometry are applied to identify quartz precursors and the origin of inclusions in quartz eyes in order to contribute to our knowledge about mechanisms of metal concentration and metal transport in porphyry environments.

The study of porphyry deposits has produced a lot of data and numerous variations of the orthomagmatic model, which have involved 'tweaking' of the original model (Burnham and Ohmoto, 1980). However this continual modification still has not produced a consistent model, or removed the mutual contradictions introduced by each new 'tweak'. In this study we investigate a paradigm shift but recognise that this is not without risk. We are conscious of almost a half-century of research and evolution of the Burnham model, however it is our view, and we will demonstrate that silicothermal fluid may provide the paradigm shift needed to porphyry deposit genetic models. Clearly a PhD thesis can only be a preliminary step in such an undertaking, but we are comforted by the old Chinese proverb 'A journey of a thousand miles starts with a single step'.

Chapter 2. Samples and Localities

2.1. Antapaccay

Antapaccay is a Cu-Au porphyry deposit (Table 2-1) of moderate size and grade, with zones of high grade skarn and epithermal mineralisation, located on the western edge of the Altiplano in southern Peru. The mineralisation is associated with the extensive Abancay Batholith, i.e. the Antapaccay intrusive suite, which is part of the Abancay batholith. Intrusives were emplaced at Antapaccay between 41.5 to 32.2 Ma (Jones, 2006).

Antapaccay intrusives are atypical, medium to high-K, calcalkaline rocks and contain intrusions with a wide composition ranging from hornblende gabbro cumulates, through quartz tonalites to trondhjemites. Mineralisation is associated with multiple intrusions and occurred as several mineralising events. Magmatic-hydrothermal evolution was accompanied by uplift and erosion, which resulted in the telescoping of the system and the superimposition of shallow epithermal system on porphyry and skarn formation. Mineralisation is developed around three intrusive centres: Antapaccay north, Atalaya and Antapaccay south.

Total resource were estimated as 470 Mt of ore at a grade 0.7 wt% Cu, 0.15 g/t Au and 0.006% Mo*.

Three samples from Antapaccay were studied (Table 2-2). Sample 092-29700 is from one of the trondhjemite dykes at Atalaya. The dike strikes NE-SW, and is 100-200 meters wide. It is homogeneous, medium-coarse grained and glomeroporphyritic. It contains plagioclase feldspar (30%; 0.5-7mm), hornblende (4%; 0.1-2.4 mm) and quartz eyes (5%; 0.2-3 mm) in a fine-grained groundmass of alkali and plagioclase feldspar and quartz. Fe-Ti oxides and apatite microphenocrysts (0.1-0.4 mm in size) comprise approximately 1% of the rock. Titanite, zircon and rare rutile are accessory phases. Ore minerals are pyrite, chalcopyrite and bornite associated with calcite and anhydrite.

Sample 334-53250 is from a crowded quartz porphyry from Antapaccay north, which is synchronous with main stage porphyry alteration and mineralisation at Antapaccay. It contains plagioclase feldspar (30%, 0.2-6 mm), hornblende (6%; 0.2-4 mm), biotite (3%; 0.2-2 mm) and quartz (2%; 0.2-4 mm) in a fine-grained groundmass

* Data on resources were collected from http://www.portergeo.com.au/ website

Table 2-1 Age, commodity and number of samples for studied deposits

Ore deposit	Age, Ma	Mineralisation type	Number of samples studied
Panguna, PNG	4.5-3.4	Cu	2
Far Southeast porphyry, Philippines	1.4	Cu-Au	1
Batu Hijau, Indonesia	5.9-3.7	Cu-Au	3
Antapaccay, Peru	41.5-32.5	Cu-Au	3
Rio Blanco, Chile	5.3-3.9	Cu-Mo	10
Climax, USA	33-18	Mo	5
Omsukchan, Russia	79±4	Sn	2

(plagioclase feldspar and quartz). There are also Fe-Ti oxide (1%) and rare anhydrite microphenocrysts. Titanite, apatite, Ce-bastnasite and zircon are accessory phases. Ore minerals are chalcopyrite and bornite associated with calcite, quartz, K-feldspar and anhydrite.

Sample 133-19920 is trondhjemite dyke, from Antapaccay south. The dyke is homogeneous with a medium grained glomeroporphyritic texture. It contains plagioclase feldspar (33%, 0.4-1.5 mm), biotite (1%; 0.2-1 mm) phenocrysts and quartz eyes (5%; 0.2-2 mm) in a devitrified glassy groundmass of alkali and plagioclase feldspar and quartz. There are rare hornblende and orthoclase phenocrysts and also rare titanite microphenocrysts (0.2-0.6 mm in size). Fe-Ti oxides, apatite, zircon and rutile are accessory phases (<1%).

2.2. Batu Hijau

The Batu Hijau porphyry copper-gold deposit (Table 2-1) is located on the south-western corner of the island of Sumbawa in central Indonesia. The deposit lies within the east-west trending Sunda-Banda magmatic arc at the convergent intersection of the Australian-Indian and the Eurasian plates.

Mineralisation is related to multiple tonalite porphyry intrusions (5.9-3.7 Ma , Table 2-1), which were emplaced along the contact between the andesitic volcaniclastics and the quartz diorite. These tonalites, around which the mineralisation is zoned, are divided into the Old, Intermediate and Young Tonalites. Each intrusion is associated

with quartz veining and Cu-Au mineralisation. The Old Tonalite has the highest grades and the two following phases have progressively lower grades, vein densities and alteration (Davidson and Crawford, 2006).

Total resources were estimated as 570 Mt of ore at a grade 0.55 wt% Cu and 0.37 g/t Au*.

Three samples from Batu Hijau were studied (Table 2-2). Sample SBD-69 is from the Batu Hijau Young Tonalite. It contains phenocrysts of plagioclase feldspar (40%, 0.5-4 mm), hornblende (2%, 0.5-3 mm) and quartz eyes (2-3%, 0.5-4 mm) in a coarse-grained groundmass of plagioclase, hornblende, biotite and quartz. Quartz eyes are from subhedral to anhedral (amoeboid or worm-like). Accessory phase include magnetite, apatite and rare ilmenite often associated with quartz and biotite.

Sample 138.2 is from mineralised zone of the Batu Hijau Young Tonalite. It contains phenocrysts of plagioclase feldspar (40%, 0.5-4 mm), hornblende (2%, 0.5-3 mm) and quartz eyes (5%, 0.5-3 mm) in a coarse-grained groundmass of plagioclase, hornblende, biotite and quartz. Quartz eyes are from subhedral to rounded. Accessory phase include magnetite, apatite and ilmenite often associated with quartz and biotite. Ore minerals are pyrite and chalcopyrite associated with quartz, calcite, K-feldspar and chlorite.

Sample SRD-02 is from the non-mineralised Arung Ara Tonalite. Porphyritic hornblende tonalite forms elongate stocks along the margins of equigranular quartz diorite plutons at Arung Ara, in the Batu Hijau district. The Arung Ara tonalite is light- to medium-gray, massive and strongly porphyritic. Phenocrysts are plagioclase (40%, 0.5-2 mm), amphibole (5%, 0.5-5 mm) and quartz eyes (5%, 0.5-1 mm) in a coarse-grained groundmass of plagioclase and quartz, locally with K-feldspar, minor biotite and rare amphibole. Fine-grained biotite and relics of orthopyroxene form minor phenocrysts. Accessory minerals include fine-grained magnetite, ilmenite and minor apatite. Minor chalcopyrite occurs within groundmass and is associated with biotite and K-feldspar.

2.3. Rio Blanco

The Río Blanco-Los Bronces Cu-Mo deposit (Table 2-1) is located in Central Chile. Mineralisation is related to a series of porphyry and breccia complexes, superimposed on a porphyry Cu deposit.

* Data on resources were collected from http://www.portergeo.com.au/ website

The Miocene San Francisco Batholith (200 km^2) hosts the Los Bronces-Rio Blanco ore deposit. The San Francisco Batholith is a multi-phase intrusive (20.1 to 7.4 Ma) with compositions including quartz-diorite, granodiorite, quartz-monzonite and quartz-monzodiorite with lesser granite and syenite. The Los Bronces-Rio Blanco deposit lies on the western margin of the San Francisco Batholith.

The first mineralisation phase is generally associated with stockworks and breccia matrix or is disseminated in host rocks surrounding the breccias. A second phase of mineralisation is related to younger, tourmaline rich breccia. Both phases of mineralisation are cut by late Miocene to early Pliocene porphyries. The Don Luis Porphyry and La Copa volcanic complex (5.3-3.9 Ma) erupted through the northern part of the deposit. A quartz monzonite porphyry stock (6.3 Ma) is probably the first unit of the Late Porphyries. The latest units of the late porphyries are the Don Luis Porphyry (5.23 ± 0.07 Ma), and the La Copa Volcanic (4.03 ± 0.19 Ma) Complex (Davidson, 2004).

The combined Los Bronces-Rio Blanco deposit is estimated to contain more than 5 Gt of ore at 1% Cu, 0.02% Mo*.

Ten samples from Rio Blanco porphyry deposit were studied (Table 2-2). The samples were collected and provided by Dave Cooke, Peter Fricken and Pete Hollings, and were collected from the La Copa Volcanic Complex and Don Luis Porphyry. The samples are spatially associated with, but postdate Cu-Mo mineralisation.

La Copa Volcanic Complex as a diatreme 1.5 km wide and 2 km long. It contains 17 mappable units, rhyolitic to dacitic intrusives capped by remnants of lavas, with some hydrothermal and contact breccias. The complex is thought to be subvolcanic intrusives that have intruded the base of their own volcanic pile. Alteration is sericite-dominated, with local silicification (Davidson et al., 2005).

Sample 9902 is a porphyritic breccia-textured rhyolite containing quartz eyes (10%, 0.5-3 mm), plagioclase (15%, 0.5-3 mm), and biotite phenocrysts (2%, 1-7 mm), with rare clasts of coarse- and fine-grained volcanics in a groundmass of glass and fine-grained quartz/feldspar. The phenocrysts are commonly broken and the clasts are angular to sub-rounded. Quartz eyes are from euhedral to rounded and show some fracturing. Accessory phases are magnetite, ilmenite and apatite.

Sample CA6 is a rhyolite containing feldspar (5%, 0.5-3 mm) phenocrysts and quartz eyes (10%, 0.5-2 mm) in a very fine-grained groundmass of quartz

* Data on resources were collected from http://www.portergeo.com.au/ website

Table 2-2 Main features of the studied samples

Locality	Sample	Rock type	Phenocryst and quartz eye composition	Groundmass	Accessory minerals
Antapacay	334-53250	Trondhjemite	Pplagioclase feldspar (30%, 0.2-6 mm), hornblende (6%; 0.2-4 mm), biotite (3%; 0.2-2 mm) and quartz (2%; 0.2-4 mm)	Fine-grained groundmass of plagioclase feldspar and quartz	Titanite, apatite, Ce-bastnasite and zircon, chalcopyrite and bornite associated with calcite, quartz, K-feldspar and anhydrite
	092-29700	Trondhjemite	Plagioclase feldspar (30%; 0.5-7mm), hornblende (4%; 0.1-2.4 mm) and quartz eyes (5%; 0.2-3 mm)	Fine-grained groundmass of alkali and plagioclase feldspar and quartz	Titanite, zircon and rare rutile, pyrite, chalcopyrite and bornite associated with calcite and anhydrite
	133 - 19920	Trondhjemite	Plagioclase feldspar (33%, 0.4-1.5 mm), biotite (1%; 0.2-1 mm) phenocrysts and quartz eyes (5%; 0.2-2 mm)	Devitrified glassy groundmass of alkali and plagioclase feldspar and quartz	Fe-Ti oxides, apatite, zircon and rutile
Batu Hijau	138.2	Tonalite	Plagioclase feldspar (40%, 0.5-4 mm), hornblende (2%, 0.5-3 mm) and quartz eyes (5%, 0.5-3 mm)	Coarse-grained groundmass of plagioclase, hornblende, biotite and quartz	Magnetite, apatite and ilmenite, pyrite and chalcopyrite associated with quartz, calcite, K-feldspar and chlorite
	SBD -69	Tonalite	Plagioclase feldspar (40%, 0.5-4 mm), hornblende (2%, 0.5-3 mm) and quartz eyes (2-3%, 0.5-4 mm)	Coarse-grained groundmass of plagioclase, hornblende, biotite and quartz	Magnetite, apatite and rare ilmenite often associated with quartz and biotite
	SRD -02	Tonalite	Pplagioclase (40%, 0.5-2 mm), amphibole (5%, 0.5-5 mm) and quartz eyes (5%, 0.5-1 mm)	Coarse-grained groundmass of plagioclase and quartz, locally with K-feldspar, minor biotite and rare amphibole	Magnetite, ilmenite and minor apatite, minor chalcopyrite occurs within groundmass and is associated with biotite and K-feldspar.
Rio Blanco	CA 6	Rhyolite	feldspar (5%, 0.5-3 mm) phenocrysts and quartz eyes (10%, 0.5-2 mm)	Very fine-grained groundmass of quartz and plagioclase feldspar	Rutile, pyrite, chalcopyrite, bornite and covellite associated with with biotite, apatite, quartz and anhydrite
	CA 8	Rhyolite	feldspar (5%, 0.5-3 mm) phenocrysts and quartz eyes (10%, 0.5-2 mm)	Fine-grained quartz – plagioclase feldspar groundmass	Pyrite and chalcopyrite associated with quartz and biotite
	CA 33	Breccia-textured glass-bearing rhyolite lava	plagioclase feldspar (15%, 0.5-2 mm), quartz eyes (7%, 0.5-2 mm), and biotite (2%, 0.5-1 mm)	Glassy and fine-grained quartz/feldspar	Accessory phases are minor magnetite and apatite

Locality	Sample	Rock type	Phenocryst and quartz eye composition	Groundmass	Accessory minerals
Rio Blanco	**9902**	Porphyritic breccia-textured rhyolite	quartz eyes (10%, 0.5-3 mm), plagioclase (15%, 0.5-3 mm), and biotite phenocrysts (2%, 1-7 mm) with rare clasts of coarse- and fine-grained volcanics	Glassy and fine-grained quartz/feldspar	Magnetite, ilmenite and apatite
	DC-DLP-1	Rhyolite	Plagioclase feldspar (40%, 1-7 mm) and quartz (10%, 0.5-3 mm)	Fine-grained groundmass of quartz and plagioclase feldspar.	rutile, hematite, pyrite, chalcopyrite and bornite often associated with apatite, biotite and chlorite.
	G1	Rhyolite	Plagioclase feldspar (30%, 0.5-2 mm) and quartz eyes (2%, 3-8 mm)	Coarse-grained groundmass of biotite, quartz and alkali and plagioclase feldspar	Magnetite and apatite, Pyrite and chalcopyrite are associated with quartz and calcite veinlets, chlorite and biotite
	DC-DP-1	Rhyolite	feldspar phenocrysts (15%, 0.5-5 mm) and quartz eyes (5-7%, 0.5-5 mm)	Fine-grained groundmass of quartz and plagioclase feldspar	Accessory phases are rutile, hematite and pyrite associated with biotite and chlorite.
	G2	Rhyolite	Plagioclase feldspar (30%, 1-5 mm) and quartz (5%, 0.5-3 mm)	Fine-grained groundmass of biotite, quartz and alkali and plagioclase feldspar	Minor magnetite and apatite associated with chlorite and biotite
	599-2	Rhyolite	Feldspar (10%, 0.5-5 mm) and biotite (1%, 0.1-1 mm) phenocrysts and quartz eyes (2%, 1-2 mm)	Very fine-grained groundmass of quartz and plagioclase feldspar	Rutile and apatite, pyrite and chalcopyrite, associated with apatite, quartz and biotite.
	599-5	Rhyolite	Feldspar phenocrysts (30%, 0.5-4 mm) and quartz eyes (7-10%, 0.5-2 mm)	Fine-grained groundmass of quartz and plagioclase feldspar.	Rutile, pyrite and chalcopyrite, associated with biotite.
Climax	109 643	Topaz-bearing equigranular granite	Alkali feldspar (50%), quartz (40%) and topaz (10%)	-	Magnetite, pyrite and molybdenite, associated with quartz, fluorite and topaz.
	109 644	Granite	Alkali feldspar phenocrysts (10%, 0.5-4 mm) and quartz eyes (7-10%, 0.5-4 mm)	Coarse-grained groundmass of quartz, alkali feldspar and topaz.	rutile, chlorite, pyrite and REE minerals associated with quartz and topaz.

Locality	Sample	Rock type	Phenocryst and quartz eye composition	Groundmass	Accessory minerals
Climax	**109 645**	Granite	Alkali feldspar phenocrysts (2%, 0.5-4 mm) and quartz eyes (2%, 1-3 mm)	Coarse-grained groundmass of alkali feldspar and quartz	Fluorite, topaz, pyrite and molybdenite, associated with quartz, K-feldspar, fluorite and topaz.
	109 646	Granite	Alkali feldspar phenocrysts (25%, 0.5-4 up to 9 mm) and quartz eyes (25%, 1-3 up to 8 mm)	Coarse-grained groundmass of alkali feldspar and quartz.	Fluorite, topaz, pyrite and chalcopyrite, associated with quartz, chlorite, fluorite and topaz.
	109 647	Biotite-bearing granite	Alkali and plagioclase feldspar (50%, 0.5-4 mm), biotite (4%, 0.5-2 mm) and quartz eyes (5%, 0.5-3 mm)	Medium-grained groundmass of alkali feldspar, biotite and quartz.	Magnetite and apatite; pyrite associated with apatite and magnetite.
Panguna	**109 607**	Diorite	Plagioclase feldspar (40%, 0.5-4 mm) and biotite phenocrysts (5%, 0.5-2 mm) and quartz eyes (5%, 0.5-2 mm)	Medium-grained groundmass of quartz, plagioclase feldspar and biotit	Magnetite, ilmenite and apatite associated with biotite.
	109 611	Diorite	Plagioclase feldspar phenocrysts (50%, 0.5-4 mm)	Very coarse-grained groundmass of quartz, chlorite and alkali feldspar.	Magnetite, apatite, pyrite and chalcopyrite, associated with chlorite, biotite and apatite.
SEP	**P13**	Quartz diorite	Feldspar phenocrysts (35%, 0.5-3 mm) and quartz eyes (7-10%, 0.5-2 mm)	very fine-grained groundmass of quartz, chlorite and alkali feldspar.	Magnetite, ilmenite and apatite, minor chalcopyrite is associated with magnetite
Omsukchan	**M2**	Granite	60% alkali feldspar, 10% quartz, 15% plagioclase feldspar and 10% amphibole.		Fluorite and apatite
	M10	Granite	65% alkali feldspar, 5-7% quartz, 20% plagioclase feldspar and 5% amphibole.		Fluorite and apatite

and plagioclase feldspar. Quartz eyes are from euhedral to anhedral and rounded, fragments of broken phenocrysts are rare. Accessory phases are rutile, pyrite, chalcopyrite, bornite and covellite associated with biotite, apatite, quartz and anhydrite.

Sample CA8 is a rhyolite containing feldspar (5%, 0.5-3 mm) phenocrysts and quartz eyes (10%, 0.5-2 mm) in fine-grained quartz – plagioclase feldspar groundmass. Quartz eyes are from euhedral to anhedral and rounded, fragments of broken phenocrysts are rare. Accessory phases are pyrite and chalcopyrite associated with quartz and biotite.

Sample CA33 is a breccia-textured glass-bearing rhyolite lava containing phenocrysts of plagioclase feldspar (15%, 0.5-2 mm), quartz eyes (7%, 0.5-2 mm), and biotite (2%, 0.5-1 mm) in a groundmass of glass and fine-grained quartz/feldspar. Most of the phenocrysts are broken. Quartz eyes are from euhedral to rounded, and show some fracturing. Accessory phases are minor magnetite and apatite.

Sample G1 is a rhyolite containing phenocrysts of plagioclase feldspar (30%, 0.5-2 mm) and quartz eyes (2%, 3-8 mm) in a coarse-grained groundmass of biotite, quartz and alkali and plagioclase feldspar. Quartz eyes are from subhedral to anhedral. Accessory phases are magnetite and apatite. Pyrite and chalcopyrite are associated with quartz (2 mm width) and calcite (0.5 mm width) veinlets and chlorite and biotite.

Sample G2 is a rhyolite with phenocrysts of plagioclase feldspar (30%, 1-5 mm) and quartz (5%, 0.5-3 mm) in a fine-grained groundmass of biotite, quartz and alkali and plagioclase feldspar. Quartz eyes are from subhedral to rounded and anhedral. Accessory phases are minor magnetite and apatite associated with chlorite and biotite.

Sample DC-DLP-1 is a rhyolite with phenocryst content up to 50%: plagioclase feldspar (40%, 1-7 mm) and quartz (10%, 0.5-3 mm) in a fine-grained groundmass of quartz and plagioclase feldspar. Quartz eyes are from subhedral to rounded and anhedral. Accessory phases are rutile, hematite, pyrite, chalcopyrite and bornite often associated with apatite, biotite and chlorite.

Sample DC-DP-1 is a rhyolite containing feldspar phenocrysts (15%, 0.5-5 mm) and quartz eyes (5-7%, 0.5-5 mm) in a fine-grained groundmass of quartz and plagioclase feldspar. Quartz eyes are from euhedral to anhedral and often are broken. Accessory phases are rutile, hematite and pyrite associated with biotite and chlorite.

Sample 599-2 is a rhyolite containing feldspar (10%, 0.5-5 mm) and biotite (1%, 0.1-1 mm) phenocrysts and quartz eyes (2%, 1-2 mm) in a very fine-grained

groundmass of quartz and plagioclase feldspar. Quartz eyes are from euhedral to subhedral and often are broken. Accessory phases are rutile and apatite, pyrite and chalcopyrite, associated with apatite, quartz and biotite.

Sample 599-5 is a rhyolite containing feldspar phenocrysts (30%, 0.5-4 mm) and quartz eyes (7-10%, 0.5-2 mm) in a fine-grained groundmass of quartz and plagioclase feldspar. Quartz eyes are from euhedral to anhedral and rounded, fragments of broken phenocrysts are rare. Accessory phases are rutile, pyrite and chalcopyrite, associated with biotite.

2.4. Panguna

The Panguna porphyry Cu-Au deposit is located on Bougainville Island (the Crown Prince Range) in eastern Papua New Guinea (Table 2-1). The Panguna ore deposit is related to the south-eastern margin of Kawerong Quartz Diorite, which is about 4 km in diameter and of 5 to 4 Ma age. The ore is developed where its multiphase apophysis intrudes the Late Miocene Panguna Andesite.

Biotite Diorite, Leucocratic Quartz Diorite, Biotite Granodiorite and Feldspar Porphyry carry most of mineralisation as stockworks and breccias. Intrusive, collapse and tectonic breccias cut most of the main intrusive phases (Eastoe, 1978). Intrusive breccias formed during the emplacement of the Biotite Diorite into the Panguna Andesite, and contains andesite fragments in a matrix of biotite, chalcopyrite, bornite and locally free gold.

The first stage of mineralisation is associated with the Kawerong Quartz Diorite. The second stage (chalcopyrite and gold) associated with hydrothermal biotite in the Biotite Diorite and Panguna Andesite. The third stage, quartz veins with chalcopyrite and bornite, were accompanied intrusion of Leucocratic Quartz Diorite (Eastoe, 1978). The fourth stage (chalcopyrite and pyrite) is associated with the intrusion of Biotite Granodiorite. Finally, pyrite precipitation occurs irregularly through all rocks in the system (Eastoe, 1978).

The original pre-mining ore reserve in 1969 was estimated as 994 Mt at 0.48 wt% Cu, 0.56 g/t Au and 3 g/t Ag*.

Two samples from Panguna porphyry were studied (Table 2-2). Sample 109607 is a diorite containing plagioclase feldspar (40%, 0.5-4 mm) and biotite phenocrysts (5%, 0.5-2 mm) and quartz eyes (5%, 0.5-2 mm) in a medium-grained groundmass of

* Data on resources were collected from http://www.portergeo.com.au/ website

quartz, plagioclase feldspar and biotite. Quartz eyes are from subhedral to anhedral and rounded. Accessory phases are magnetite, ilmenite and apatite associated with biotite.

Sample 109611 is a diorite containing plagioclase feldspar phenocrysts (50%, 0.5-4 mm) in a very coarse-grained groundmass of quartz, chlorite and alkali feldspar. Quartz only occurs in the groundmass. Accessory phases are magnetite, apatite, pyrite and chalcopyrite, associated with chlorite, biotite and apatite.

2.5. Climax

The Climax porphyry molybdenum deposit (Table 2-1) is located west of Denver, within the Colorado Mineral Belt in central Colorado, USA. It is related to the mid Oligocene to Miocene composite Climax Stock introduced as multiple pulses over the period from 33 to 18 Ma (Wallace et al., 1968). The mineralised stock is adjacent to the Mosquito Fault, which partly displaced the ore body by about 3000 m. The stock cuts early the Middle Proterozoic Idaho Springs Formation (1800 to 1700 Ma) and the Silver Plume Granite (1350 to 1480 Ma).

The Climax Stock was introduced in five main phases. The South-west Mass is biotite poor fine grained granite to aplite porphyry and contains the Ceresco Orebody. The Central Mass is biotite poor, foliated granite porphyry, spatially related to the Upper Orebody. The Lower Intrusive Series form a cupola beneath the Lower Orebody, and concentrically within and below the Central Mass. The Post-ore Intrusive phase is series of dykes of late rhyolite porphyry. The Seriate Granite is nearly equigranular and un-mineralised granite, spatially related to the Lower Orebody.

Molybdenum mineralisation is closely associated with silica distribution: it is present in thin quartz filled fractures (95% of the molybdenum in the Upper Orebody), in tabular quartz veins, in pegmatite pods and aplite dykes, in high silica rocks (as irregular clots and sparse scattered crystals) and as ‘paint’ on thin fractures.

Published reserve and production figures at Climax include: Production, 1918-87 - 421 Mt @ 0.41% MoS_2. Reserve 1987 - 310 Mt @ 0.30 to 0.35% MoS_2. Proven + probable Reserve, 1994 - 132 Mt @ 0.23% Mo*.

Five samples from Climax were studied (Table 2-2). Sample 109643 is a topaz-bearing equigranular granite containing alkali feldspar (50%), quartz (40%) and topaz

* Data on resources were collected from http://www.portergeo.com.au/ website

(10%). Accessory phase are magnetite, pyrite and molybdenite, associated with quartz, fluorite and topaz.

Sample 109644 is a granite containing alkali feldspar phenocrysts (10%, 0.5-4 mm) and quartz eyes (7-10%, 0.5-4 mm) in a coarse-grained groundmass of quartz, alkali feldspar and topaz. Quartz eyes are from euhedral to anhedral and rounded. Accessory phases are rutile, chlorite, pyrite and REE minerals associated with quartz and topaz.

Sample 109645 is a granite with alkali feldspar phenocrysts (2%, 0.5-4 mm) and quartz eyes (2%, 1-3 mm) in a coarse-grained groundmass of alkali feldspar and quartz. Quartz eyes are anhedral. Accessory phase are fluorite, topaz, pyrite and molybdenite, associated with quartz, K-feldspar, fluorite and topaz.

Sample 109646 is a granite containing alkali feldspar phenocrysts (25%, 0.5-4 up to 9 mm) and quartz eyes (25%, 1-3 up to 8 mm) in a coarse-grained groundmass of alkali feldspar and quartz. Quartz eyes are from euhedral to anhedral and rounded. Accessory phases are fluorite, topaz, pyrite and chalcopyrite, associated with quartz, chlorite, fluorite and topaz.

Sample 109647 is a biotite-bearing granite containing alkali and plagioclase feldspar (50%, 0.5-4 mm), biotite (4%, 0.5-2 mm) and quartz eyes (5%, 0.5-3 mm) in a medium-grained groundmass of alkali feldspar, biotite and quartz. Quartz eyes are from subhedral to anhedral and rounded. Accessory phases are magnetite and apatite. Ore mineral is pyrite, associated with apatite and magnetite.

2.6. Far Southeast Porphyry

The Far Southeast Porphyry Copper deposit (SEP, Table 2-1) is located in the Mankayan Mineral District in northern Luzon, the Philippines. The FSE porphyry copper deposit is a bell-shaped porphyry deposit deeply seated in host volcanoclastics. Mineralisation is related to a late Miocene quartz diorite intrusive complex, which has mineralisation localised in its dark coloured facies. Porphyry mineralisation is overprinted by a late stage hydrothermal breccia, which is also mineralised with Cu-Au (Hedenquist et al., 1998).

The resource at FSE is of the order of 140 mt at 0.85 wt% Cu and 1.9 g/t Au*.

One sample from the Far East Porphyry was studied (Table 2-2). Sample P13

* Data on resources were collected from http://www.portergeo.com.au/ website

is a quartz diorite containing feldspar phenocrysts (35%, 0.5-3 mm) and quartz eyes (7-10%, 0.5-2 mm) in a very fine-grained groundmass of quartz, chlorite and alkali feldspar. Quartz is from subhedral to rounded. Accessory phases are magnetite, ilmenite and apatite, minor chalcopyrite is associated with magnetite.

2.7. Omsukchan granite

The tin-bearing Omsukchan leucogranite massif (Table 2-1) is located within the Okhotsko-Chukotsky volcanic belt (Chukotka Peninsula, NE Russia). The intrusion is a flat-topped cupola with shallow dipping flanks, containing three concentric zones of texturally different granites (Kamenetsky et al., 2004). Mineralisation is related to the zones of metasomatic Na–Fe alteration and quartz-tourmaline veins within the roof of the cupola.

Two samples from Omsukchan granite were studied (Table 2-2). Sample M2 is granite containing about 60% alkali feldspar, 10% quartz, 15% plagioclase feldspar and 10% amphibole. Accessory phases are fluorite and apatite.

Sample M10 is granite containing about 65% alkali feldspar, 5-7% quartz, 20% plagioclase feldspar and 5% amphibole. Accessory phases are fluorite and apatite.

More detailed description of quartz eyes and metal-bearing phases are in the chapters 4 and 6.

Our choice of samples allows comparing conditions of formation of quartz eyes within a wide range of porphyry plutons (Table 2-1). For instance, one of the samples are from mineralised zone (138.2 from Batu Hijau) and contains quartz veinlets with ore minerals, whereas the other samples represent host porphyry rocks. Two of the Batu Hijau samples are from mineralised pluton (138.2 and SBD-69), whereas the third one (SRD-02) is from non-mineralised tonalite in the Batu Hijau district. The samples from Rio Blanco are from two plutons, which postdate main stage mineralisation. The chosen deposits also reflect the difference in age and type of mineralisation (from granites to diorites, see Table 2-2).

* Data on resources were collected from http://www.portergeo.com.au/ website

Chapter 3. Methods and Techniques

3.1. Cathodoluminescence background

The interest in cathodoluminescence (CL) of quartz has increased dramatically over the last two decades. Such a boost was caused by the fact that CL data provide us with information which cannot be obtained by other analytical methods. CL reveals primary (e.g. zonation, resorption, incrustation, cementation) and secondary textures (e.g. alteration halos along grain boundaries, healed microcracks formed and healing structures around fluid inclusions). Intensity of CL depends on the type of chemical bond, lattice defects (vacancies), and impurity elements (which can act as activators, sensitisers, and quenchers) which can be revealed by complementary microanalytical methods. Luminescence can be divided into intrinsic and extrinsic CL. The intrinsic luminescence characterises the host lattice (Si and O atoms and their linkages), and is caused by non-stoichiometry (vacancies) or structural imperfections (poor ordering, radiation damage, shock damage), which distort the crystal lattice and larger defects such as dislocations and clusters. The extrinsic luminescence results from impurities referred to as activators (Müller, 2000).

The number of ions which can substitute for the silicon atom in the quartz lattice is limited because of the small ionic radius of Si^{4+}. Typical substitutes are Al^{3+}, Ti^{4+}, Fe^{3+}, Ge^{4+}, P^{5+}, and Ga^{3+} (Götze, 2009; Müller, 2000). Large open channels thread through the quartz structure parallel to the c-axis and offer locations for interstitial cations such as H^{+}, Na^{+}, K^{+}, Li^{+}, Fe^{2+}, Cu^{+}, Co^{2+}, Ag^{+} (Müller, 2000). Bonded water in the quartz lattice is also very important impurity. Water can be incorporated into the quartz lattice as OH^{-} linked with silica atoms or as $4H^{+}$, which can substitute Si^{4+}. Hydrogen and hydroxyl may act as a charge compensator of Al^{3+} (Müller, 2000), thus Al content might influence on the solubility of water in the quartz lattice.

Changes in the quantity and quality of defects and impurities in quartz reflect the changes of physico-chemical conditions of crystal growth and therefore, can be used for their reconstruction. In this study we used CL technique for the interpretation of rock-forming processes related to formation of porphyries.

Firstly, BSE maps were made for every slide. Then quartz grains were chosen and CL imaging on the individual quartz grains were performed using Cameca SX100 EPMA (Central Science Laboratory at the University of Tasmania) equipped with CL detector. During the first runs CL images were captured parallel to BSE images,

which allowed comparing two different data sets. CL mapping of quartz veins and slides were performed on the SEM in automatic mode, using the Mineral Liberation Analysis (MLA) software package. The most interesting quartz grains were studied by hyperspectral cathodoluminescence mapping at SCIRO Minerals (Melbourne).

CL images are typically made up of a mosaic of smaller images as the sample was moved under the beam, which have been made with slightly different CL conditions, and this can produce 'checkerboard' patterns parallel to the photomicrograph border, and occasional mismatches.

3.2. Electron microscopy and electron probe microanalysis

The FEI Quanta 600 MLA environmental scanning electron microscope (Central Science Laboratory at the University of Tasmania) equipped with Secondary Electrons (SE), Backscattered Electrons (BSE) and cathodoluminescence (CL) detectors (Gatan PanaCLF) was used for SE, BSE and CL mapping and chemical analyses on individual crystals (EDS). Mapping and EDS analyses were carried out on polished and carbon coated samples at an accelerating voltage of 20 kV and beam current of 20 nA.

3.3. Hyperspectral cathodoluminescence mapping

Cathodoluminescence spectra and hyperspectral maps were collected using a JEOL field emission gun electron microprobe analyser (JXA 8500F) customised with quartz optics, and equipped with an Ocean Optics QE65000 grating CCD spectrometer (MacRae et al., 2005). The spectrometer employs a Hamamatsu S7031-1006 back-thinned CCD and was operated with the Peltier cooling set at -15°C. A 300µm diameter optical fibre was used to connect the spectrometer to the collection optics within the microprobe and the diameter of this fibre formed the entrance slit of the spectrometer. This resulted in a wavelength resolution of 10.0 nm. Spectra were collected with 1024 equal wavelength windows over the full spectrometer range of 199 to 998 nm. Spectra were not corrected for either detector efficiency or instrumental response. This means that the CL peak calibration is not transferrable to another instrument however this is normal for electron beam microanalysis where standards are measured on every element. All spectra are displayed in energy rather than wavelength as the CL peaks are symmetric in energy space and can be fitted using a series of Guassians.

Maps of the quartz samples were then collected with an accelerating voltage of 20 kV, beam current of 40 nA, dwell time of 40 ms, beam defocus of 1 µm and a step

size of 1 μm in X and Y. Stage scanning was used to step the sample beneath a fixed beam and maps of 1000 by 1000 pixels were collected, with at each pixel a full 1024 channel CL spectrum stored in parallel with WDS measurements of Ti, Si, to identify the bulk mineralogy and major-to-minor Ti levels.

To identify lines for quantification, both selected area and sum spectra from the map were examined, peaks identified and compared to known lines in quartz. The 2.72 eV line has been previously associated with the alkali compensated paramagnetic [TiO_4/M^+] centre with M being either Li^+ or Na^+ (Götze et al., 2005; Preusser et al., 2009). Götze (2005) has previously observed a peak at 450 nm (2.76 eV) but has not been able to associate it with the TiO_4/M^+ centre. Spear (2009) have postulated a 415 nm (2.99 eV) peak is correlated with Ti concentrations but have not been able to quantify the relationship.

We fitted three Gaussians to the spectra thus removing the overlaps and allowing the true peak centre of the TiO_4/M^+ to be determined as 2.72 eV (455 nm) and quantified following the procedure of Leeman (2008). Chimage software (Harrowfield et al., 1993) was then used to fit the series of Gaussians, in energy space, to the spectrum from each pixel within the CL map, with the peak positions and widths of the Gaussians being kept constant, and only the heights of the Gaussians being allowed to vary during the least squares fitting.

The electron microprobe was used to collect backscattered electron images in parallel to the x-ray and CL mapping. The backscattered electron images show the major structures within the quartz eye grains but do not reveal the fine detail or zoning that is revealed in the CL images.

To calibrate the fitted 2.72 eV peak intensity versus the Ti level a series of point analyses were performed across the mapped region using the electron microprobe. The point analyses were performed after the CL mapping as the long acquisition times associated with the point analyses damage the structure and lead to variable CL yields. The JEOL electron microprobe was operated with an accelerating voltage of 20 kV, a beam current of 200 nA and the beam was defocused to 20 μm. To improve the detection limits on Ti two spectrometers with PET crystals were operated in parallel. Total peak acquisition time on titanium, per spectrometer, was 80 seconds on the peak and 40 seconds on each of the backgrounds, the three sigma detection limit for titanium being 10 ppm (Ancey, 1978). To determine the titanium offset caused by slight variations in the x-ray background, a synthetic quartz sample was analysed. This gave an offset of 8 ppm, which is negligible compared to the Ti levels measured.

A series of points in each of the three samples were analysed and the measured Ti elemental levels were compared to the fitted peak height of the 2.72 eV line. A series of 20 μm regions equivalent to those analysed by point analysis were selected from the fitted 2.72 eV data and average. This data is presented in Figure 4-d, for sample DC-DLP -1. A least squares fit of the data shows a good agreement with an R^2 value of a 0.963 for a linear fit. Errors in the microanalysis are typically ±12 ppm.

The Cameca SX100 EPMA (Central Science Laboratory at the University of Tasmania) equipped with SE, BSE and CL detectors was also used for determination of melt inclusion composition and trace elements identification in quartz. Both studies were carried out on polished and carbon coated samples at an accelerating voltage of 20 kV and beam current of 20 nA. For melt inclusion analyses the beam current used was 15 nA with a beam diameter of 5 μm. Al, Ti, Fe, Zn, K, Ge and Mn were measured in quartz. Detection limits were calculated as 8-10 ppm for Al, 10-14 ppm for Ti, 23-28 ppm for Fe, 93 ppm for Zn, 11 ppm for K, 27 ppm for Ge and 21-23 for Mn.

3.4. Laser ablation-inductively coupled plasma-mass spectrometry (LA-ICP-MS)

Laser Ablation Inductively Coupled Plasma Mass Spectrometry (LA-ICP-MS) was used for determination of fluid inclusion compositions and for trace element mapping in quartz. This technique uses a laser beam to ablate material off a prepared sample inside a sealed chamber. A stream of carrier gas collects the ablated material, and is introduced into a Mass Spectrometer, which separates the ions in the plasma by mass, and counts them. This gives an analysis of the ablated material as a ratio of intensities for each atomic mass. The technique is capable of routinely detecting most elements down to a few ppm, and as it is possible to ablate to a depth of several tens of μms, it is possible to analyse inclusions below the surface of the sample.

Laser Ablation Inductively Coupled Plasma Mass Spectrometry was performed at the CODES, University of Tasmania, with a New Wave 213-nm solid-state laser microprobe coupled to an Agilent 4500 quadrupole ICPMS.

The analyses were performed by ablating spots and lines ranging in size from 35 to 100 μm with the laser repetition rate 5-10 Hz and laser beam energy 3-3.5 J/cm^2. The analysis time for each spectrum was 100 seconds, including a 30 second measurement of background (laser off) and a 70 second with laser on. The standards (NIST612 and BCR-2) were analysed twice every one and a half hours to account for the instrument drift, with a 100-μm beam and at 10 Hz.

Laser ablation imaging was performed by ablating sets of parallel lines in a grid across the quartz grains. Beam size of 50 μm was used with the same space between lines. Prior to imaging profiles were performed to determine the set of elements to measure. Intensities of Li^{7}, Mg^{24}, Al^{27}, Si^{29}, Ti^{49}, Mn^{55}, Fe^{57}, Ga^{69}, Ge^{70}, Rb^{85}, Sr^{88}, Pb^{208} were mapped. Depth of ablation during mapping was around 5 μm. Although single isotopes are measured the system software uses known isotopes ratios to convert to ppm.

3.5. Fourier-transform infrared (FTIR) spectroscopy

Transmission FTIR spectra of quartz were obtained using the Bruker Vertex 70 equipped with a Bruker Hyperion 2000 microscope at the University of Tasmania. FTIR spectroscopy was used for the determination of the distribution and specification of structural water in quartz crystals. The analyses were carried out on doubly polished wafers 150 μm in thickness cleaned with acetone and dried. The spectra were acquired in a range of wave lengths from 4000 to 2000 cm^{-1} with 128 scans in the transmission mode and the resolution of the measurements was 4 cm^{-1}. FT-IR mapping was carried out with the 25 μm aperture and increment of 25 μm. Background spectra were taken before and after each map. The baseline correction, sample thickness correction and converting of the transmission spectrum to the absorption spectrum was carried out on a PC using OPUS package.

3.6. Microthermometry

Individual quartz eye grains were prepared as doubly-polished wafers about 150 μm thick, and experiments were performed on a Linkam TS1500 heating stage, using an Olympus model BX 60 optical microscope fitted with a CCD camera. The heating stage contains an electric heating element, which allowed to heat samples at any predetermined rate up to 600°C. The accuracy was ± 5°C. A set of windows permitted microscope observation of inclusions during heating and cooling. A circulating-water cooling jacket permitted rapid cooling at a rate of ≈ 150°C/min or controlled cooling at any predetermined rate. This heating stage permits observation of temperature ranges of any phase changes. The stage is equipped with video output, which allows recording video files, which permits more detailed and accurate observations.

The microthermometry was applied to two samples, which contained both quartz eyes and vein quartz with fluid inclusions (SBD-69 from Batu Hijau and G1 from Rio Blanco).

3.7. Bulk homogenisation of melt inclusions

Quartz crystals were placed in a ceramic crucible in a furnace, and heated to 750°C for 24 hours. The crucible was then removed from the furnace, and quenched in air. Bulk heating technique produced large numbers of homogenised inclusions required for statistically valid analyses, at relatively little cost. Homogenised inclusion then were exposed and analysed by electron microprobe.

The bulk homogenisation was applied to the sample SBD-69 (from Batu Hijau); melt inclusions from Rio Blanco were studied in details by Davidson (2005; 2001), and the results on homogenisation were used in this study.

Chapter 4 Composition of quartz

4.1. General description

Three types of quartz were studied: quartz eyes, quartz veinlets and groundmass quartz. Quartz eye content within samples varies from 0 to 25% (Table 4-1) with an average of about 7%. The quartz eyes are usually large, 0.5 to 8 mm (1-2 mm typically) and of different shapes. Most quartz eyes are from subhedral to rounded and often appear to be highly corroded. Adjacent crystals may vary greatly in their shapes and degree of corrosion (Fig 4-1).

Quartz grains often cluster together, which is referred to as synneusis (Fig 4-1).

Table 4-1 Characteristic features of quartz eyes and groundmass quartz within the studied samples

Locality	Sample	Percentage of quartz eyes (%)	Quartz eye shapes	Quartz eye size (mm)	Groundmass quartz	Synneusis
Antapaccay	334-53250	2	Subhedral, anhedral, subrounded	1-5	fine grained	rare
	092-29700	2	Subhedral, anhedral, subrounded	1-3	fine grained	rare
	133-19920	5	Subhedral, anhedral, subrounded	0.5-2	fine grained	rare
Rio Blanco	CA6	10	Euhedral, subhedral, anhedral, rounded	0.5-2	very fine grained	rare
	CA8	10	Euhedral, subhedral, anhedral, rounded	0.5-2	fine grained	rare
	CA33	7	Euhedral, subhedral, anhedral, rounded	0.5-2	very fine grained	rare
	9902	10	Euhedral, subhedral, anhedral, rounded	0.5-3	very fine grained	rare
	DC-DP-1	5-7	Euhedral, subhedral, anhedral ('vitrous'), rounded	0.5-5	fine grained	rare
	DC-DLP-1	10	Euhedral, subhedral, anhedral, rounded	0.5-3	fine grained	common
	G1	2	Subhedral, anhedral	3-8	coarse grained	rare
	G2	5	Subhedral, anhedral, rounded	0.5-3	fine grained	common
	599-2	2	Subhedral, anhedral	1-2	very fine grained	rare

Locality	Sample	Percentage of quartz eyes (%)	Quartz eye shapes	Quartz eye size (mm)	Groundmass quartz	Synneusis
Rio Blanco	599-5	7-10	Subhedral, anhedral, rounded	0.5-2	fine grained	rare
Climax	109643	no quartz eyes				
	109644	7-10	Euhedral, subhedral, anhedral	0.5-4	coarse grained	abundant
	109645	2	Anhedral	1-3	coarse grained	abundant
	109646	25	Euhedral, subhedral, anhedral, rounded	1-3 up to 8	coarse grained	abundant
	109647	5	Subhedral, anhedral, rounded	0.5-3	medium grained	abundant
Panguna	109607	5	Subhedral, anhedral, rounded	0.5-2	medium grained	common
	109611	no quartz eyes				
Batu Hijau	138.2	5	Subhedral, anhedral, rounded	0.5-3	coarse grained	rare
	SBD-69	2-3	Subhedral, anhedral (amoeboid, vermiform), rounded	0.5-4	coarse grained	common
	SRD-02	5	Subhedral, anhedral (amoeboid, vermiform), rounded	0.5-1	coarse grained	rare
SEP	P13	7-10	Subhedral, rounded	0.5-2	fine grained	abundant
Omsuck chan	M2+M10	no quartz eyes				

Such clusters consist of two to six or more quartz grains. In crossed polars, several distinct optical orientations are commonly observed (Fig 4-1, insets in a and b). Such clusters may contain grains of different sizes and shapes (Fig 4-2).

The margins of quartz eyes are often embayed. Some of embayments are short, whereas others are long and sinuous and extend deep into the core of the grain; different styles of embayment may even be found in adjacent grains (Fig 4-2). All embayments have smooth and rounded edges. Separate grains fragments are in some cases have the same crystallographic orientations (Fig 4-3). In some cases the quartz eyes have the silica rims around them (Fig 4-1b and 4-3c, d), which have the same extinction as the quartz eyes, thus being crystallographically continuous.

Sugary aggregates of quartz form veinlets (1-2 mm in width), which were found in two samples (138-2 and G1). The studied veinlets crosscut porphritic rocks, and

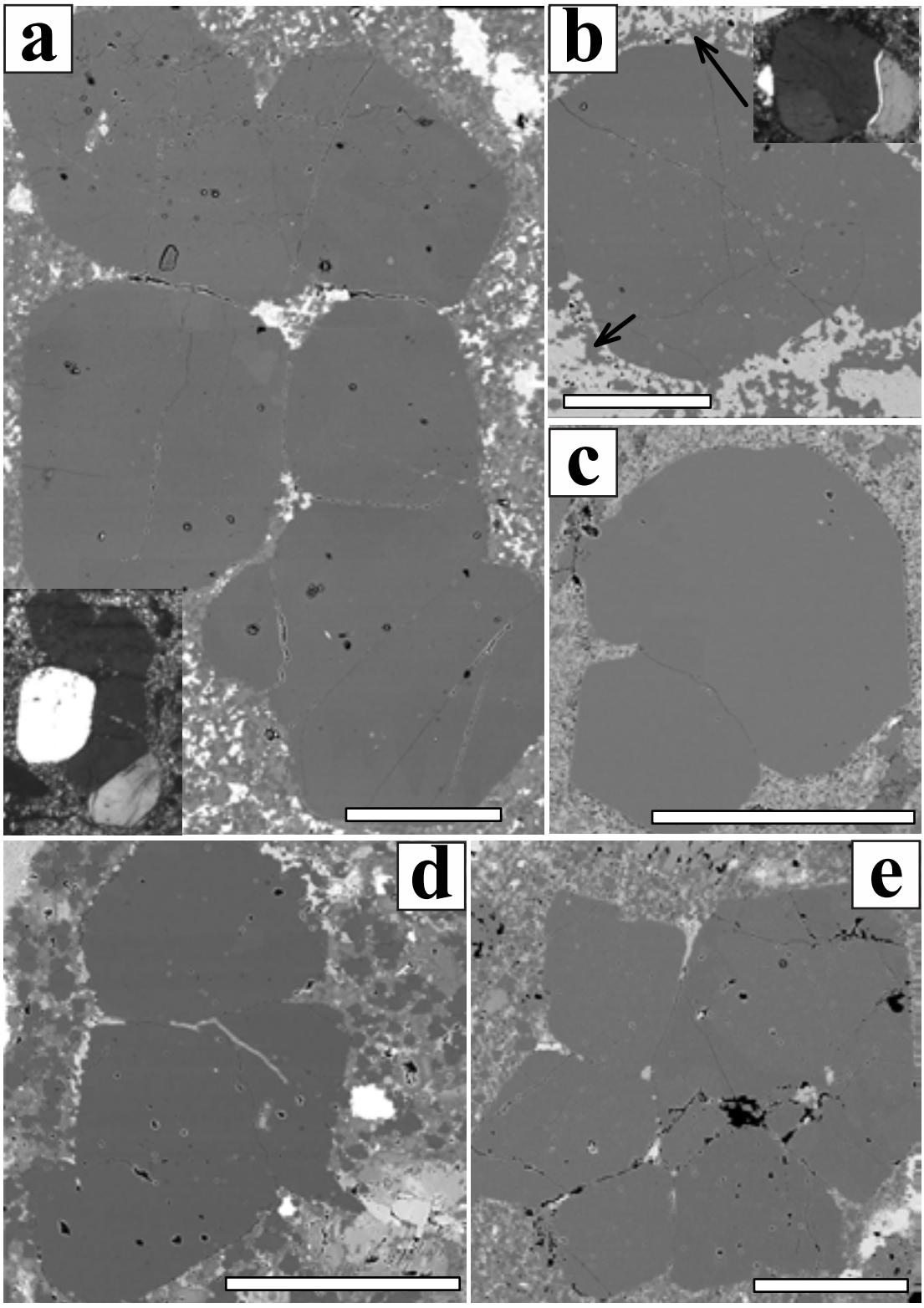

Figure 4-1 Quartz eye clusters (synneusis)
(a) – Climax, sample 109647; (b) – Climax, 109646; (c) – Rio Blanco, 599-5; (d) – Batu Hijau, SRD-02; (e) –South East Porphyry, p13. All are BSE images except for insets in (a) and (b), which are made in crossed polars and show different optical orientation of the grains in clusters. Arrows point out silica rim around the quartz eye in (b). Scale bars are 500µm.

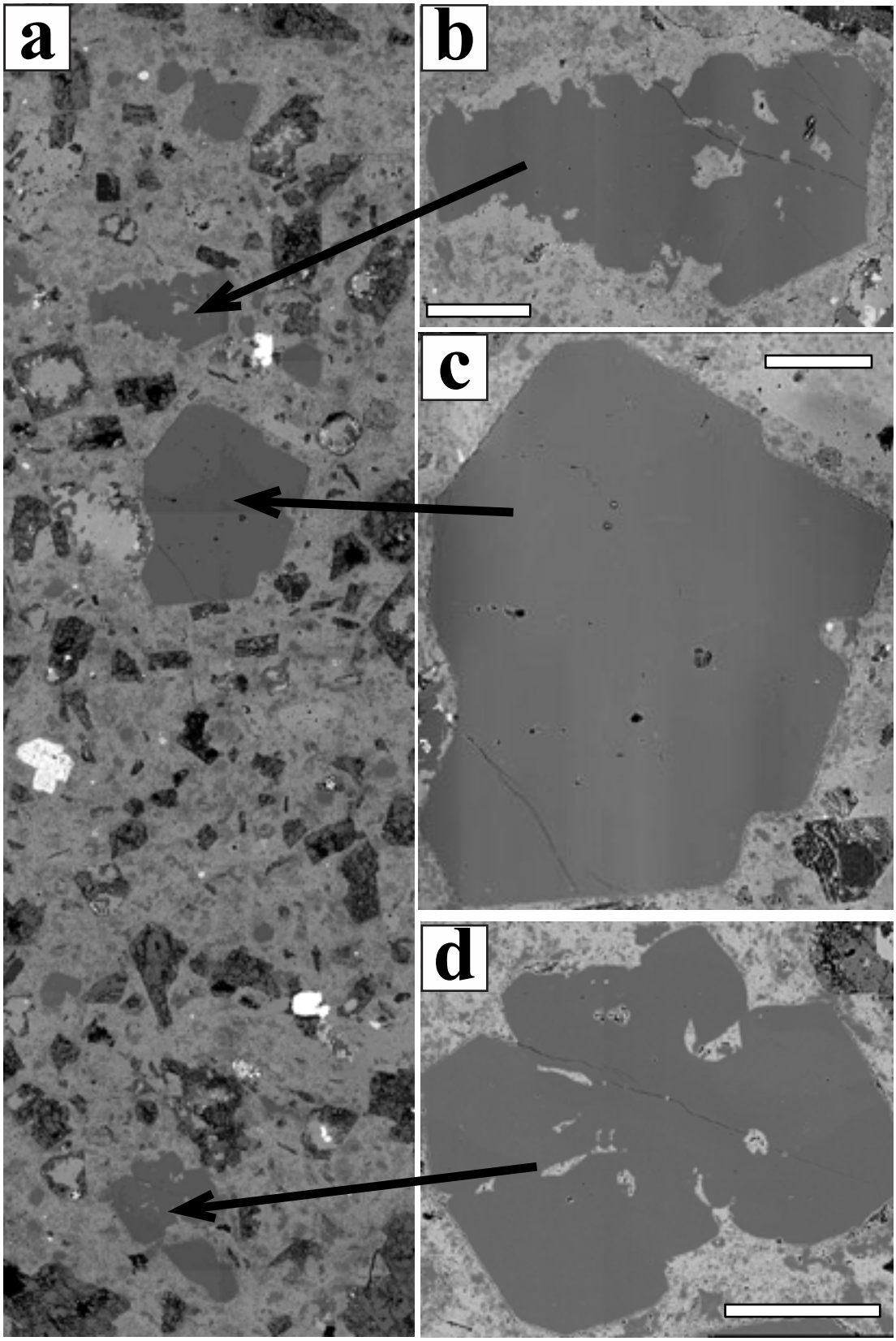

Figure 4-2 Different shapes of adjacent quartz eyes within a typical sample, DC-DP-1, Rio Blanco, Chile

(a) – general view. (b, c, d) – magnified views of three large grains shown in (a) by arrows. BSE images. Scale bars are 500 μm.

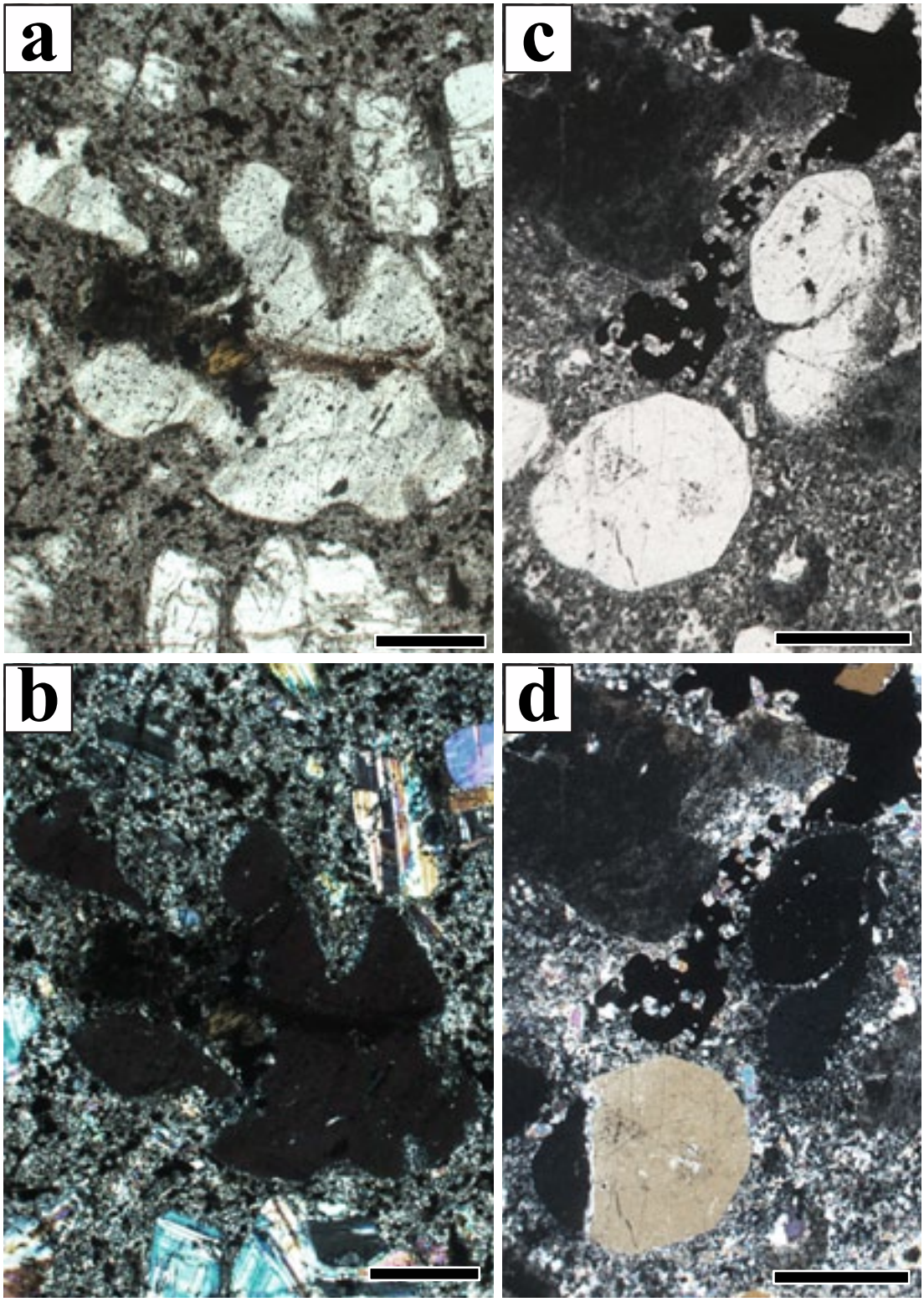

Figure 4-3 Crystallographic orientation within clusters and silica rims
Quartz grains from Batu Hijau (a, b) and Climax (c, d) show the same crystallographic orientation ofdifferent grains within a cluster (a, b) and surrounding silica rims. (a, c) – transmitted light; b, d – crossed polars, extinction position. Scale bars are 500 µm.

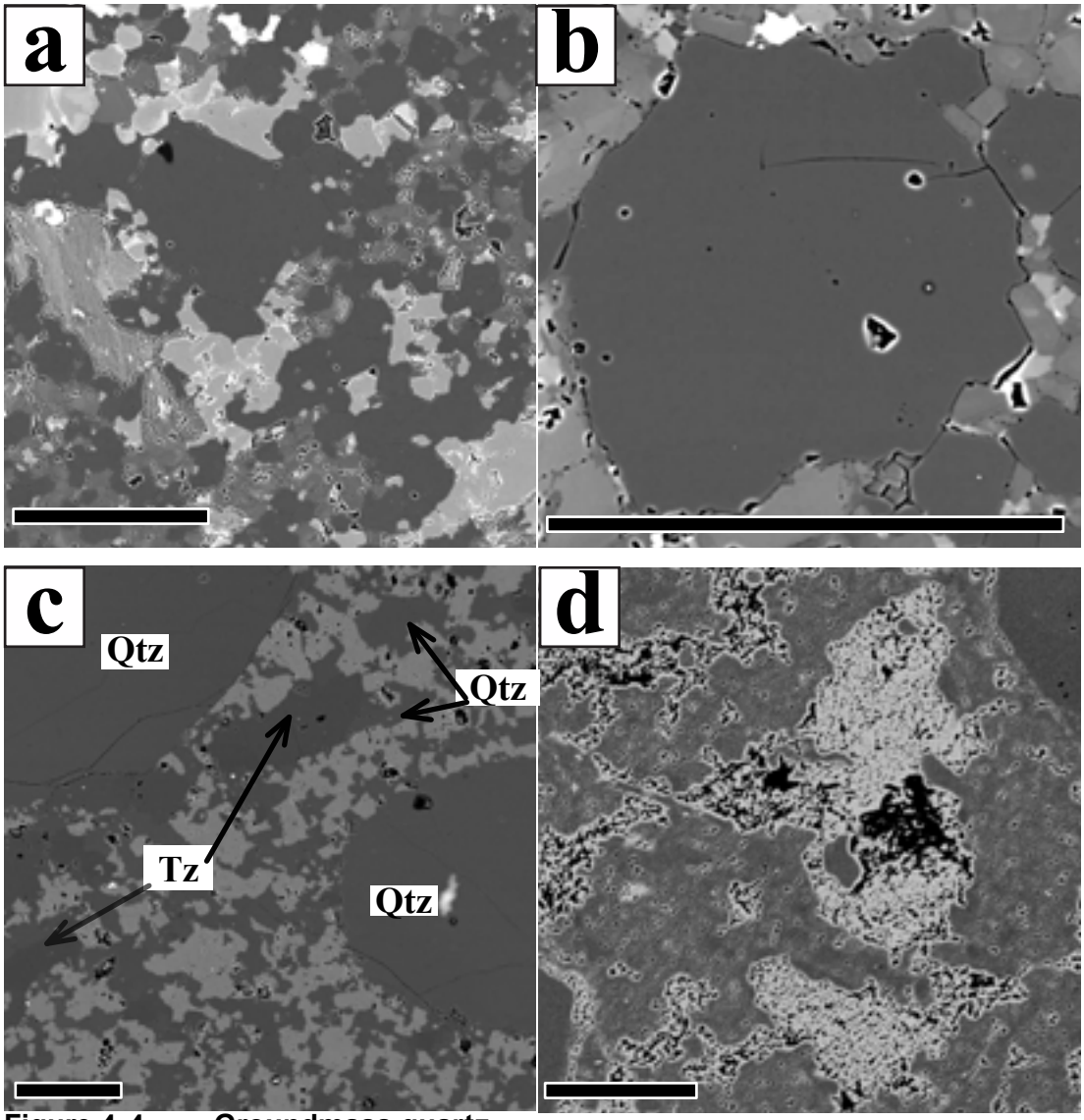

Figure 4-4 Groundmass quartz

(a, b) - typical groundmass quartz in Batu Hijau (a – 138-2, b – SBD-69), (c) – groundmass quartz intergrowth with topaz, Climax (109646), (d) – groundmass quartz in intergrowth with feldspar, Rio Blanco (CA6). Qtz – quartz, Tz – topaz. BSE images. Scale bars are 200 µm.

contain sulphides in interstitial spaces between quartz grains.

Matrix quartz within coarse to very fine grained groundmass (Table 4-1) exhibits variable shapes (from anhedral to euhedral and from elongated to isometric) and size (0.02±0.5 mm, Fig 4-4b). Within samples with fine grained groundmass, and in some cases with coarse grained matrix (Climax, USA) the groundmass quartz occurs as clusters or networks around quartz eyes (Fig 4-4). Crystals (<0.1 mm) are frequent in granophyric and micrographic intergrowths with feldspar. In some samples matrix quartz is in intergrowth with groundmass topaz (Fig 4-4c).

4.2. Results of SEM-CL

4.2.1. Quartz eyes

Cathodoluminescence technique (CL) revealed zoning in quartz eyes within all the studied samples. Primary CL features include major zoning, which usually referred to as 'compositional' or 'step' zoning (Müller, 2000) and oscillatory zoning. Compositional zoning is non-periodic and shows a significant change in cathodoluminescence intensities. In most cases quartz crystals have a core-and-rim CL pattern, where both the core and the rim usually has one (or sometimes more) compositional zones of 50 to 1000 μm. Oscillatory zones are usually fine (2 to 50 μm in width), and show minor alternations in intensity within the compositional zones. Adapting feldspar terminology, cathodoluminescence patterns with a bright core and a darker rim will be termed 'normal' in the descriptions below. Zoning with a core darker than the outer layers will be termed 'reverse'.

Secondary CL textures include fine intra-granular fractures healed by nearly non-luminescent CL-dark quartz, and patchy haloes of secondary quartz around fluid inclusions, which are often arranged along fractures.

4.2.1.1. Diversity of CL patterns

Quartz eyes within a single thin-section commonly appear to have very different cathodoluminescence zones, in terms of numbers and sequences (Figs 4-5 and 4-6). This diversity of CL patterns can usually be subdivided into the following CL pattern types (Table 4-2):

Type 1 Reversely zoned quartz eyes with a dark core overgrown by a bright mantle, often with oscillatory zoning ('1' in Figs 4-5 and 4-6). The cores are often rounded and mostly without oscillatory zoning. Sometimes, however, the cores show sector zoning (shown in Fig 4-5).

Type 2 Normally zoned quartz eyes with bright cores overgrown by darker mantles, which often contain oscillatory zoning. Sometimes cores also have oscillatory zoning ('2' in Figs 4-5 and 4-6). Unlike dark cores (type 1) bright cores are rarely rounded; they often show crystallographic shapes.

Type 3 Quartz grains with CL-bright and CL-dark alternating layers without distinct core-and-rim patterns or grains with features characteristic for both type 2 and type 1, such as a bright core with oscillatory zoning, dark mantle and a bright rim ('3' in Figs 4-5 and 4-6).

Table 4-2 Types of cathodoluminescence patterns in the studied samples

Locality	Sample	number of grains studied	Type 1	Type 2	Type 3	Type 4a	Type 4b	Type 4c	Type 5	Type 6	Number of clusters
Antapaccay	334-53250	14	2	5	-	2	2	1	-	2	-
	092-29700	6	2	1	-	-	3	-	-	-	-
	133-19920	20	5	2	-	3	4	4	2	-	2
Rio Blanco	CA6	54	17	6	2	8	13	6	1	1	7
	CA8	15	3	2	-	3	7	-	-	-	-
	CA33	18	8	-	-	-	6	1	3	-	-
	9902	16	5	-	-	1	7	2	1	-	2
	DC-DP-1	17	7	3	-	-	7	-	-	-	2
	DC-DLP-1	12	4	1	-	-	4	-	-	3	3
	G1	11	1	3	1	-	2	-	2	2	-
	G2	15	4	3	-	-	1	2	3	2	1
	599-2	10	5	-	1	-	1	-	-	3	1
	599-5	20	7	4	-	-	4	-	3	2	2
Climax	109644	18	-	5	-	-	3	-	2	-	13
	109645	1	1	-	-	-	-	-	-	-	1
	109646	16	2	5	-	-	4	1	4	1	5
	109647	14	6	4	1	1	2	1	-	-	6
Panguna	109607	17	3	3	7	-	1	-	2	1	4
	109611	2	-	-	-	-	-	-	-	2	-
Batu Hijau	138-2	7	-	-	1	-	1	-	2	2	-
	SBD-69	25	7	-	5	1	3	1	5	3	5
	SRD-02	15	6	1	-	-	1	-	2	5	1
South East Porphyry	P13	20	4	3	-	2	10	-	1	-	10
Omsuckchan	M2+M10	7	-	2	-	-	-	-	1	4	3
Total number of quartz grains studied		370	99	53	18	21	86	19	34	33	68

Type 4 Quartz grains with oscillatory zoning only (i.e. without strongly contrasting zones). The oscillatory layers are fine and usually bright; their numbers within different grains vary significantly ('4' in Fig 4-5).

Type 5 Quartz grains with irregular CL pattern ('5' in Fig 4-6).

Type 6 Indistinct CL zonation. Sometimes with secondary patchy quartz (Fig 4-8).

Every sample contains quartz eyes of three or more types of CL pattern (Table 4-2). Diversity of CL patterns within a single sample is illustrated in Figure 4-5 (sample CA6, Rio Blanco) and Figure 4-6 (sample 109607, Panguna). Diversity of CL patterns within the other samples are illustrated in the SUPPLEMENTARY section (pp 163-182).

Strong correlation between CL patterns and crystal shapes are sometimes observed. For example, in sample DC-DP-1 from Rio Blanco grains showing a large CL-dark core and a narrow CL-bright rim tend to have anhedral shapes with deeper sinuous embayments, whereas grains displaying no dark core or small dark core and a broad CL-bright rim have euhedral shapes (Fig 4-7).

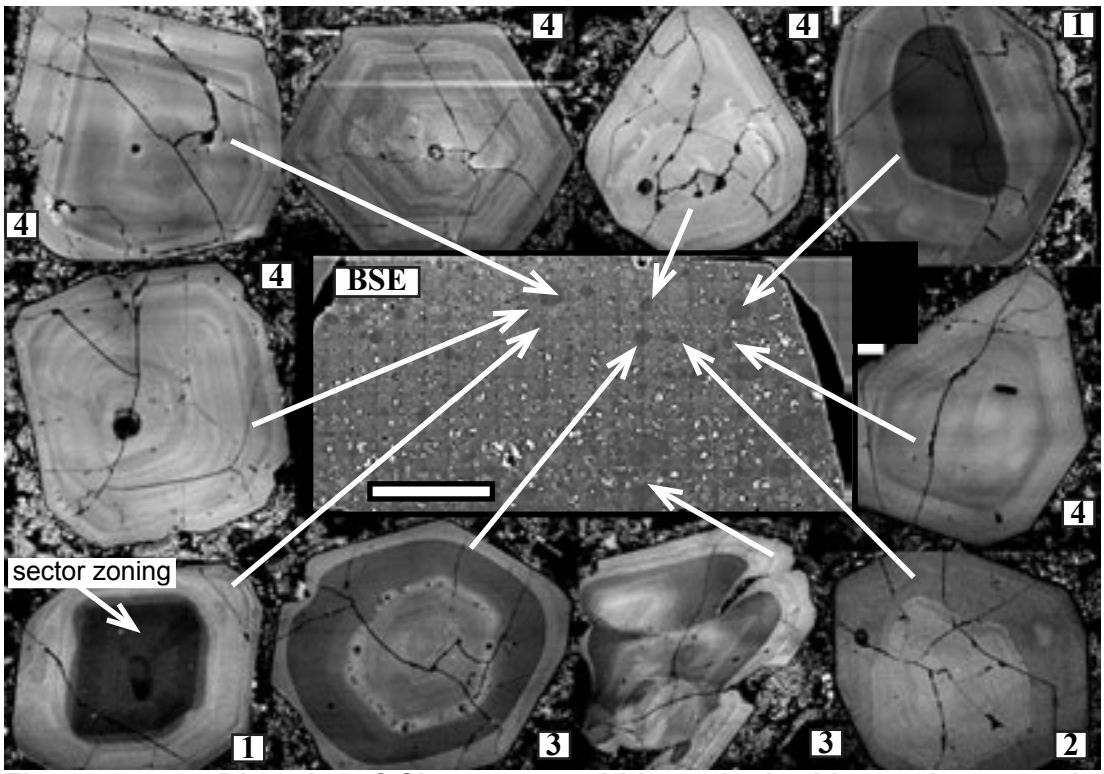

Figure 4-5 Diversity of CL patterns within a single thin section, sample CA6, Rio Blanco.
1-4 - types of CL patterns. Central image is BSE, the other images are SEM-CL. Scale bar is 1cm.

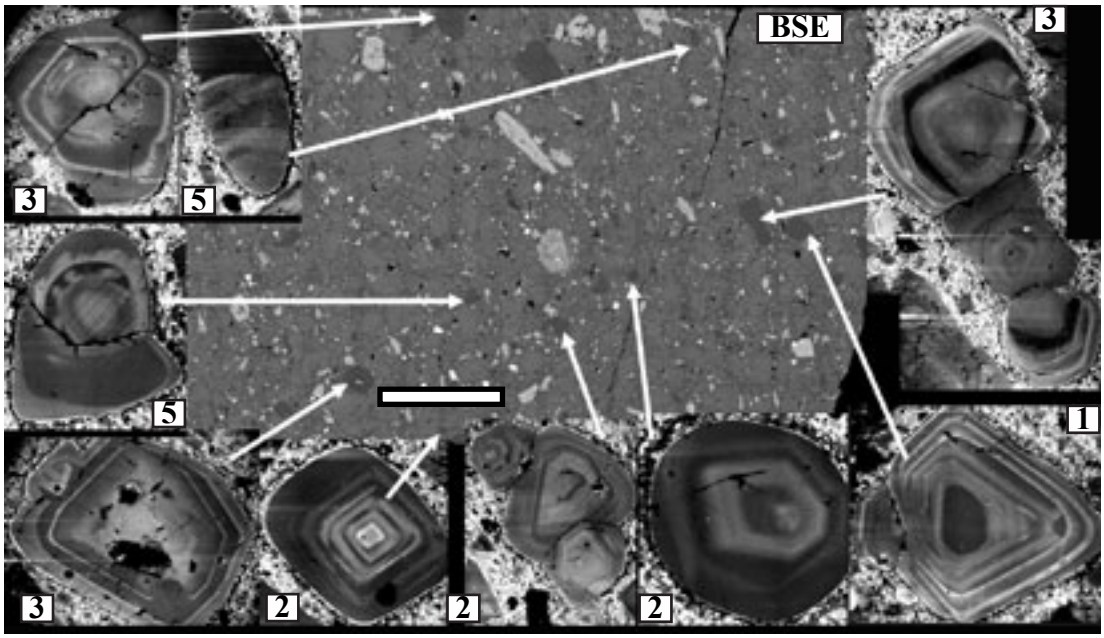

Figure 4-6 Diversity of CL patterns within a single thin section, sample 109607, Panguna

1-4 -types of CL patterns. Central image is BSE, the other images are SEM-CL. Scale bar is 1cm.

Quartz grains from the Omsukchan granite (M2 and M10) and sample 109611 from Panguna (where quartz fills interstices between large plagioclase crystals) show indistinct zonation with significant amount of patchy quartz (Fig 4-8). The quartz from samples 109643 and 109645 is mostly vein-like, and will be described in the section 4.2.3. Sample from Climax (109644) contains quartz grains with bright irregular cores and broad intermediate intensity mantles (sometimes with oscillatory zoning) and clusters of quartz that often contain grains with different CL patterns (Fig 4-9).

Both compositional and oscillatory layers are usually parallel to grain boundaries. Sometimes however, CL zones are cut by a grain boundary (Fig 4-10a) or CL layers cut other layers (Fig 4-10c). The outermost CL layers are mostly bright and often lace-like and have CL properties similar to those of the matrix quartz (Fig 4-10a). Sometimes lace-like layers are internal ones (Fig 4-10c). In some cases CL layers are very irregular and appear to be smoke-like (Fig 4-10b).

Secondary CL features are common in all the samples except for lava samples 9902 and CA30. Secondary CL features include fractures healed by nearly non-luminescent quartz (dotted arrows in Figs 4-9 and 4-11). Patchy haloes of non-luminescent quartz around fluid inclusions are also typical (solid arrows Figs 4-8, 4-9 and 4-11).

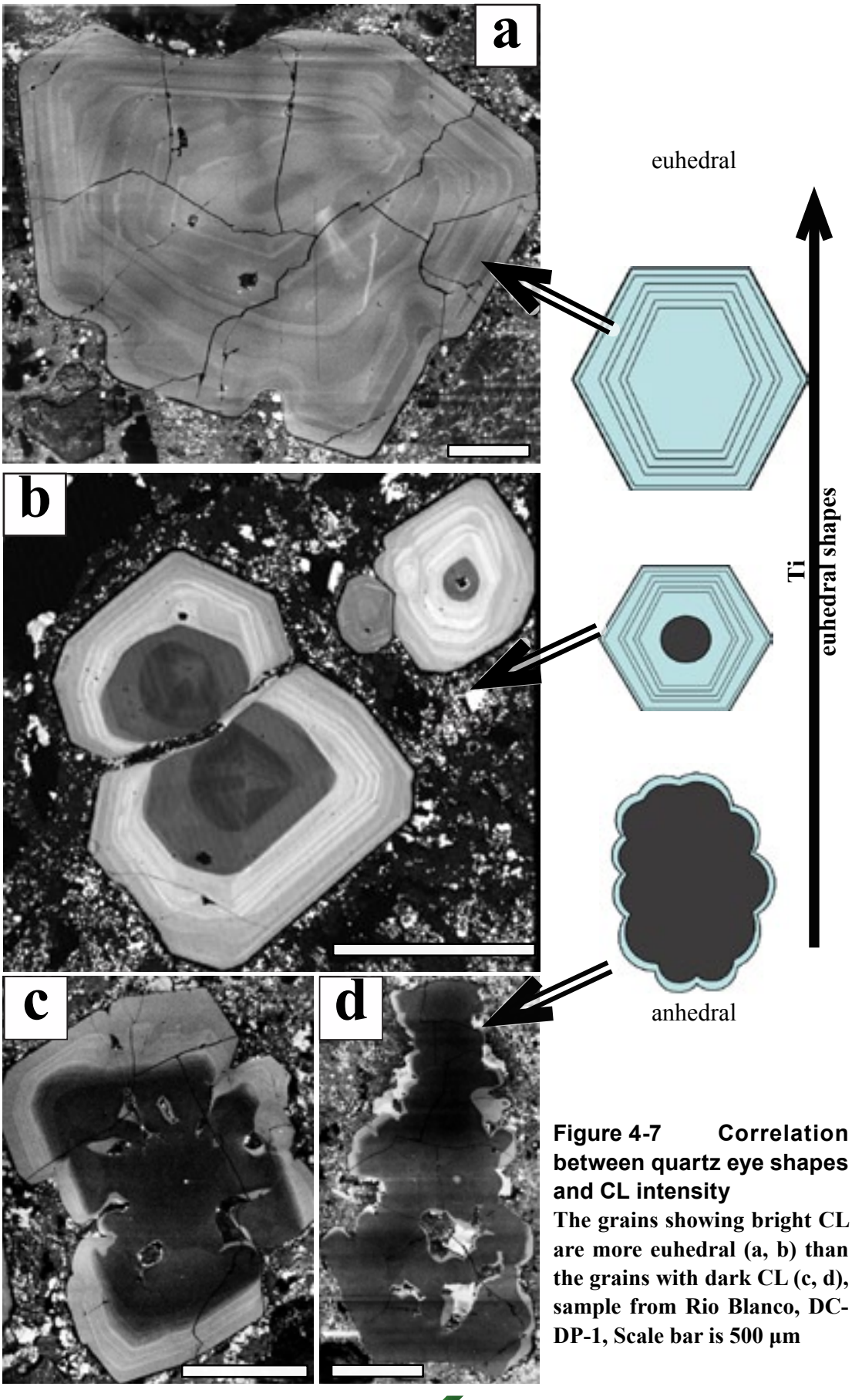

Figure 4-7 Correlation between quartz eye shapes and CL intensity
The grains showing bright CL are more euhedral (a, b) than the grains with dark CL (c, d), sample from Rio Blanco, DC-DP-1, Scale bar is 500 µm

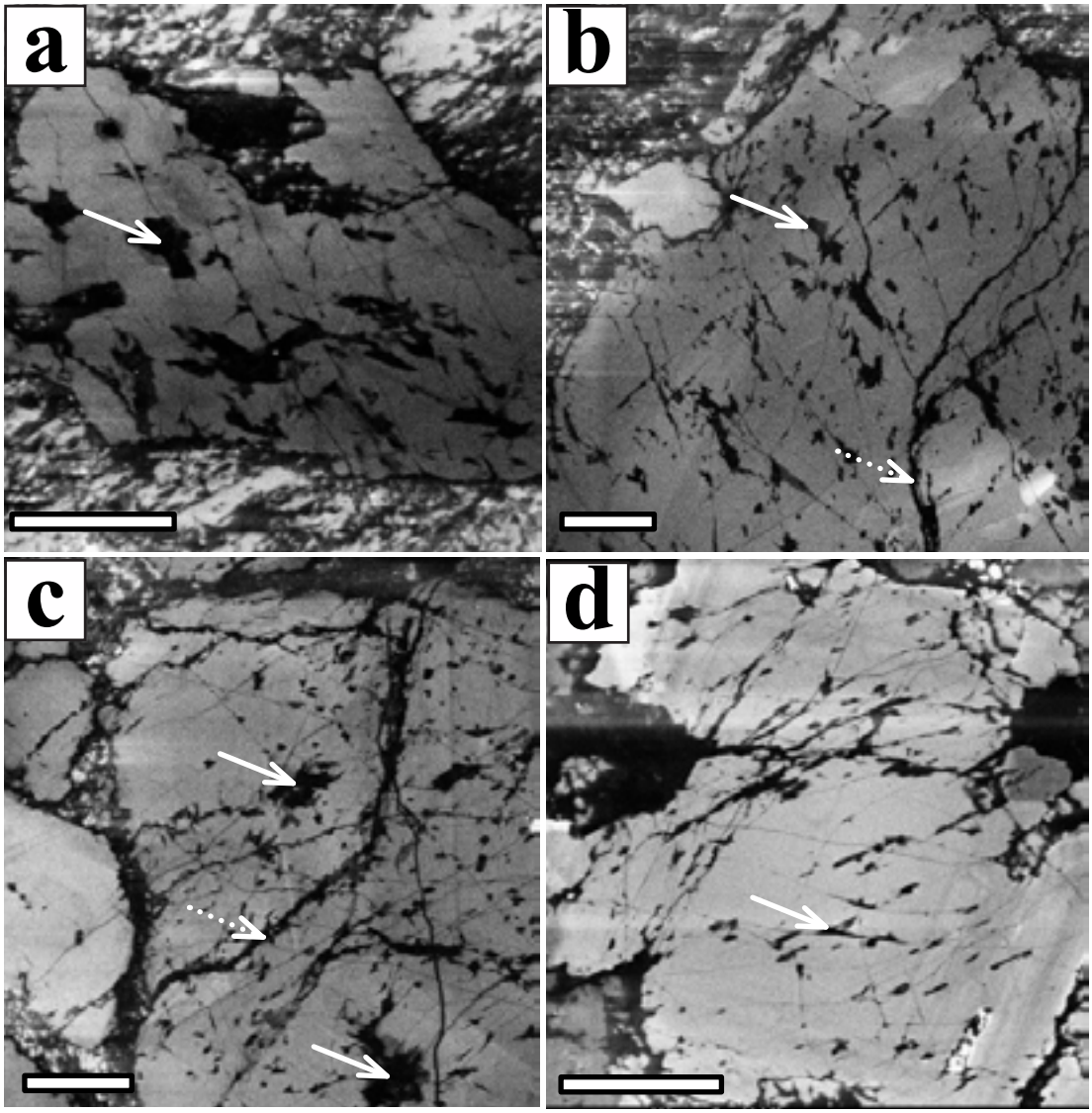

Figure 4-8 Patchy quartz in M10 (a, c), M2 (b) and 109611 (d)
Solid arrows point to patchy secondary quartz, dotted arrows show healed fractures. SEM-CL images. Scale bars are 200 µm.

4.2.1.2. Diversity of clusters

Quartz eye clusters also show diversity of shapes and internal textures within a single thin section (Fig 4-11). Clusters with bright rims can be next to those showing no rim zones (Fig 4-11a, b). Quartz crystals, which are attached within clusters, often show identical internal patterns with CL layers continuing from one grain to another (Fig 4-11d, f, g). Other clusters have attached grains with different patterns (Fig 4-11b, e). In many cases quartz grains are attached in such a way they form a single crystallographic shape (Fig 4-11e, f). Other attached grains are clustered to form an irregular cluster shape (Fig 4-11g). Secondary quartz is distributed within clusters only and do not continue in surrounding groundmass.

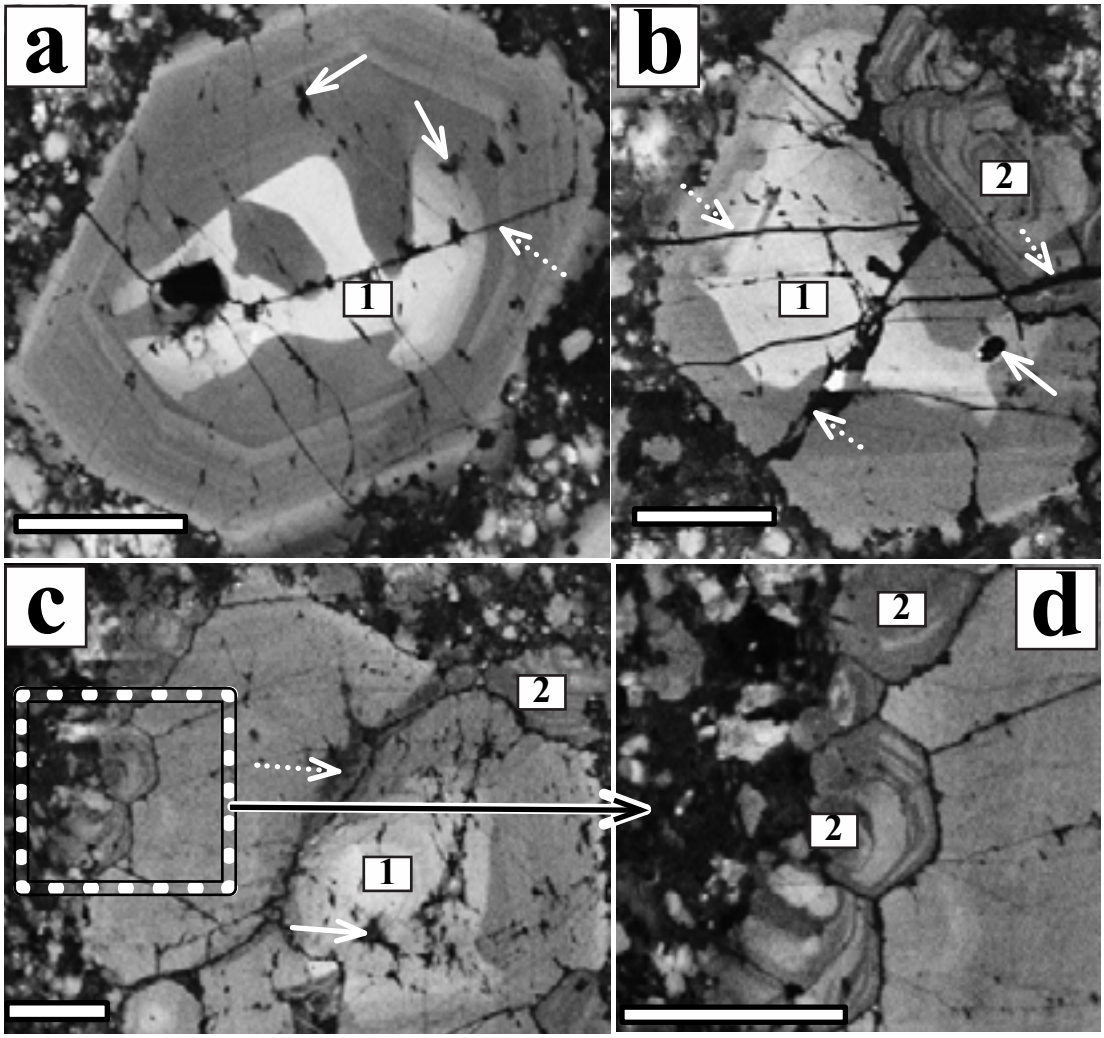

Figure 4-9 Cathodoluminescence pattern in the sample 109644
(a) – quartz grain with a bright irregular core and an CL-intermediate broad mantle with oscillatory zoning; (b, c) – clustered quartz grains with different CL patterns: some of the grains have bright irregular core (1), others grains in the clusters have CL pattern similar to oscillatory-type zoning but with much stronger contrast (2); (d) – enlarged area from (c). Solid arrows point to patchy secondary quartz, dotted arrows show healed fractures. SEM-CL images. Scale bars are 200 µm.

4.2.1.3. Relationships between primary and secondary CL features

Fractures are common in the studied samples. In most cases they are healed, but sometimes open fractures are present. Fractures often appear to separate grains within the clusters (Fig 4-12a-c). Fractures are secondary relatively to the growth zones; from BSE images it is apparent that some fractures continue from the quartz eyes into the groundmass (Fig 4-12b'), which indicates their very late origin. Nevertheless, fractures affect the geometry of growth zones: they are often inflected or smudged in the closest vicinity of fractures (Fig 4-12, arrows 1 and 3). In many cases growth layers are cut along one side of a fracture (Fig 4-12b, c, arrows 2) and inflected and

smudged along another side (Fig 4-12b, c, arrows 1). In other cases both straight and inflected layers are observed along a fracture (Fig 4-12d and e, arrows 2 and 3). Sometimes depressions in grain surfaces are observed where healed fractures break surfaces (Fig 4-12e, arrows 4).

Melt inclusions are rare in the samples, usually black in CL and do not have the layers around inflected (Fig 4-19). Unlike melt inclusions, groundmass and mineral inclusions in most instances have growth zones curved around them (Figs 4-13 - 4-15). Inflections and smudging of CL layers around the embayments are also very common (Fig 4-13c and 4-15). In many cases embayments are so deep and sinuous (closed embayments) that now they represent groundmass inclusions rather than embayments (Fig 4-15a). Such closed embayments often have channels which connects embayments with depressions in the surface relief (Fig 4-15).

4.2.2. Vein quartz

Vein quartz tends to display lower CL intensity (darker) than quartz eyes (Fig 4-16b). Cathodoluminescence pattern of the quartz veins is very complex. Euhedral crystals with well-defined concentric

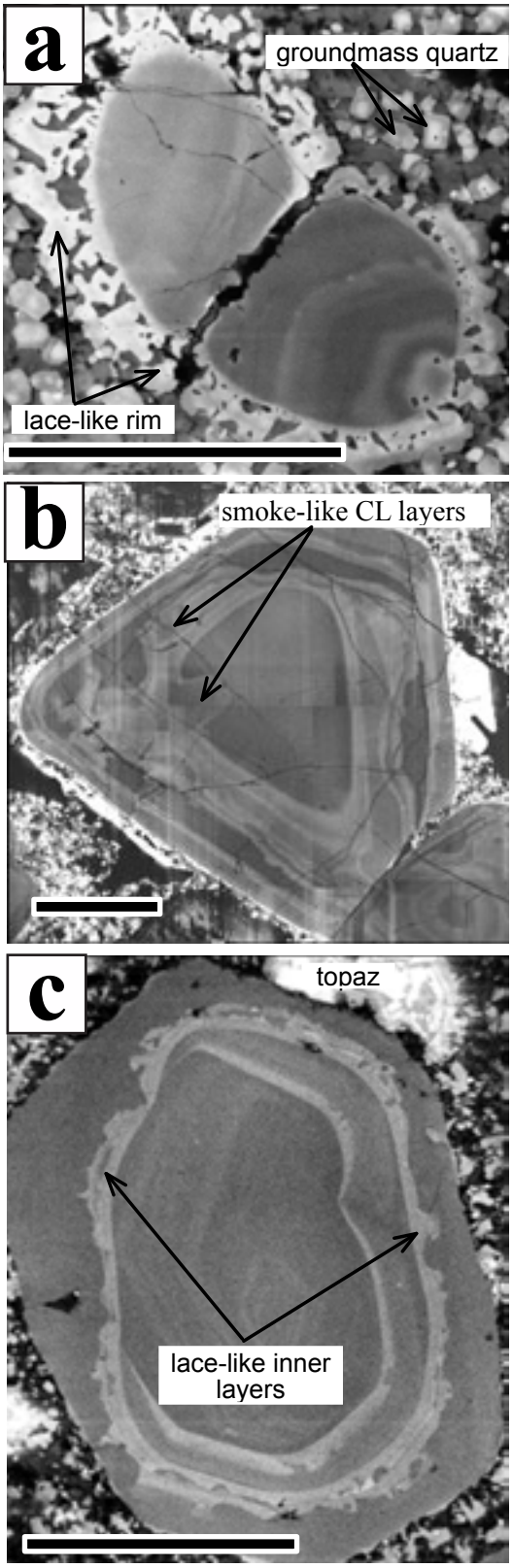

Figure 4-10 Lace-like and smoke-like CL zones
(a) – a bright lace-like outermost CL zone with CL properties similar to those of the groundmass quartz (sample SBD-69, Batu Hijau), (b) - smoke-like inner CL layers zones (sample G2, Rio Blanco), (c) - bright lace-like inner CL layers (sample 109646, Climax). SEM-CL images. Scale bars are 500 µm.

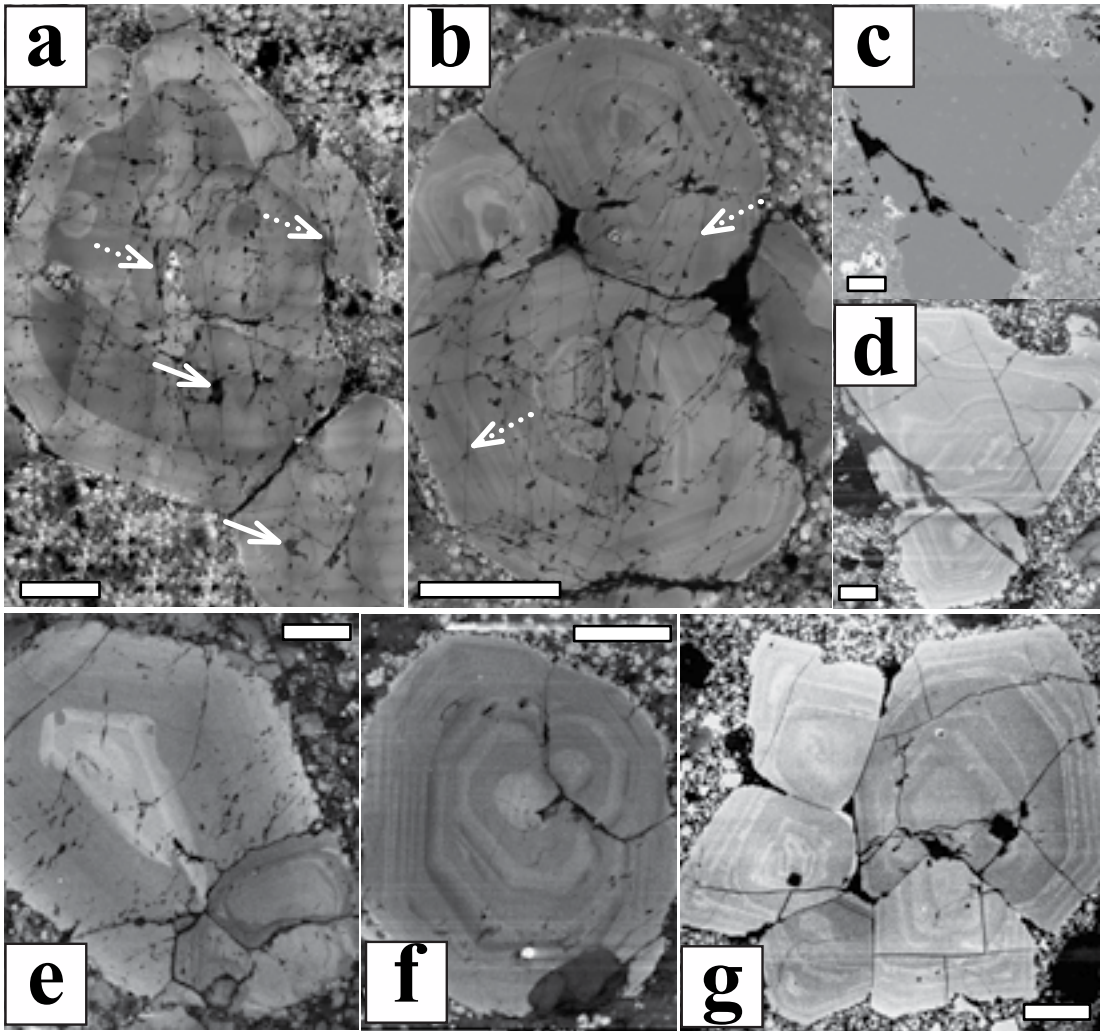

Figure 4-11 Internal CL and fracture patterns within quartz eye clusters
(a, b) - adjacent clusters from sample SBD-69; (a) shows high Ti rim and (b) shows absence of a rim. (c, d) - clusters with fractures that do not extend outside quartz, P13. (e) - cluster from sample 109644, Climax: attached grains show different CL patterns, (f) - sample 109647, Climax: attached grains show identical CL patterns. (g) - cluster from P13, SEP with similar attached grains where the rim continues from one grain to the others. Solid arrows point to patchy secondary quartz, dotted arrows show healed fractures. All images except for (c) are SEM-C. Scale bars are 200 µm.

bands of light and dark luminescence pointing generally toward the centre of the veins (Fig 4-16b1) are surrounded by weakly contrasted crystals with blurry CL zones (Fig 4-16b3). Sometimes crystals with high contrast alternating bands occupy interstitial position (Fig 4-16d2). Most of the grains, however, have combined CL pattern with blurry zoning surrounding and often truncating the euhedral zoning (Fig 4-16d4). Agate-like banding (Fig 4-16c5) is common and related mostly to the latest quartz, which is associated with sulphides. Several stages of brittle deformation are indicated by several generation of dark in CL secondary quartz (Fig 4-16b6).

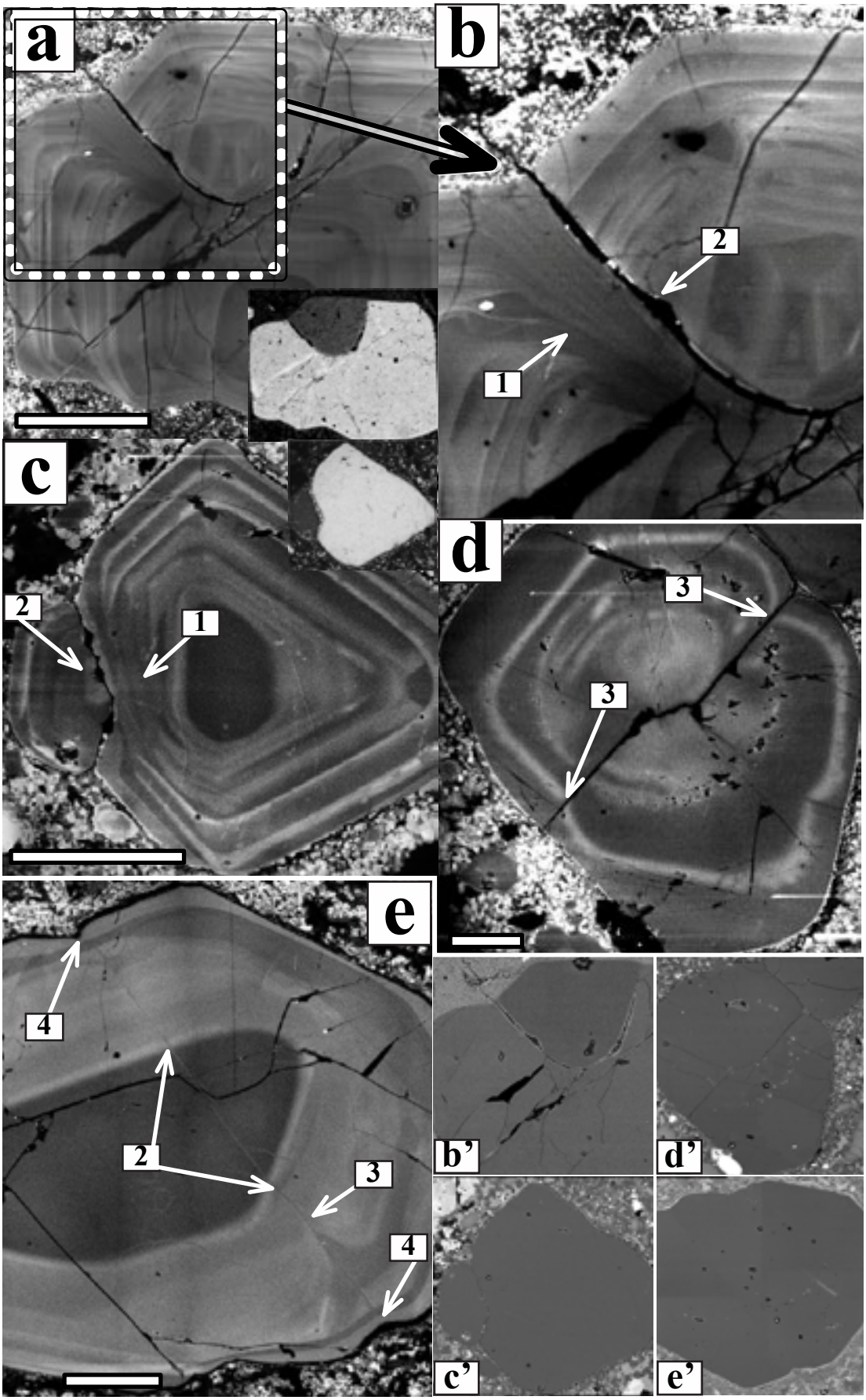
a
b
2
1
c
2
1
d
3
3
e
4
2
3
4
b'
d'
c'
e'

Figure 4-12 Interplay between fractures and CL bands

(a-e) – SEM-CL images, (b', c', d' and e') – BSE images of the grains in (b), (c), (d) and (e), the insets in (a) and (c) are an optic images, crossed polars, show different extinction of grains within clusters. (arrows 1-3) - different geometry of CL layers along fractures: 1 - CL layers are inflected and smudged, 2 - CL layers are cut, 3 - CL layers are inflected. Arrows 4 show depressions in grain surfaces associated with healed fractures. (a, b) - Antapaccay (133-19920), (b) – enlarged view of the dashed area in (a). (c, d) - Panguna (109607). (e) - Rio Blanco (CA6). Scale bars are 500 µm.

Quartz veinlets in Climax (samples 109643, 109645) show CL dull rims and CL dark centres (Fig 4-17). The veinlets' centres often show alternating layers of different CL contrast (darker than rims); sometimes there are crystals pointing towards the centre of a veinlet. Transitions between central part of a veinlet and its margins are gradual and diffusional in some cases (Fig 4-17c) and distinct in others (Fig 4-17b). CL layers continue from grain to grain without any disruption (Fig 4-17b, c).

4.2.3. Groundmass quartz

Groundmass quartz is always CL-brighter than quartz eyes (Fig 4-18a) and in most cases zoned (Fig 4-18b). Moreover, in most cases a sequence of CL layers within the groundmass quartz grains is different: the grains with normal and reverse

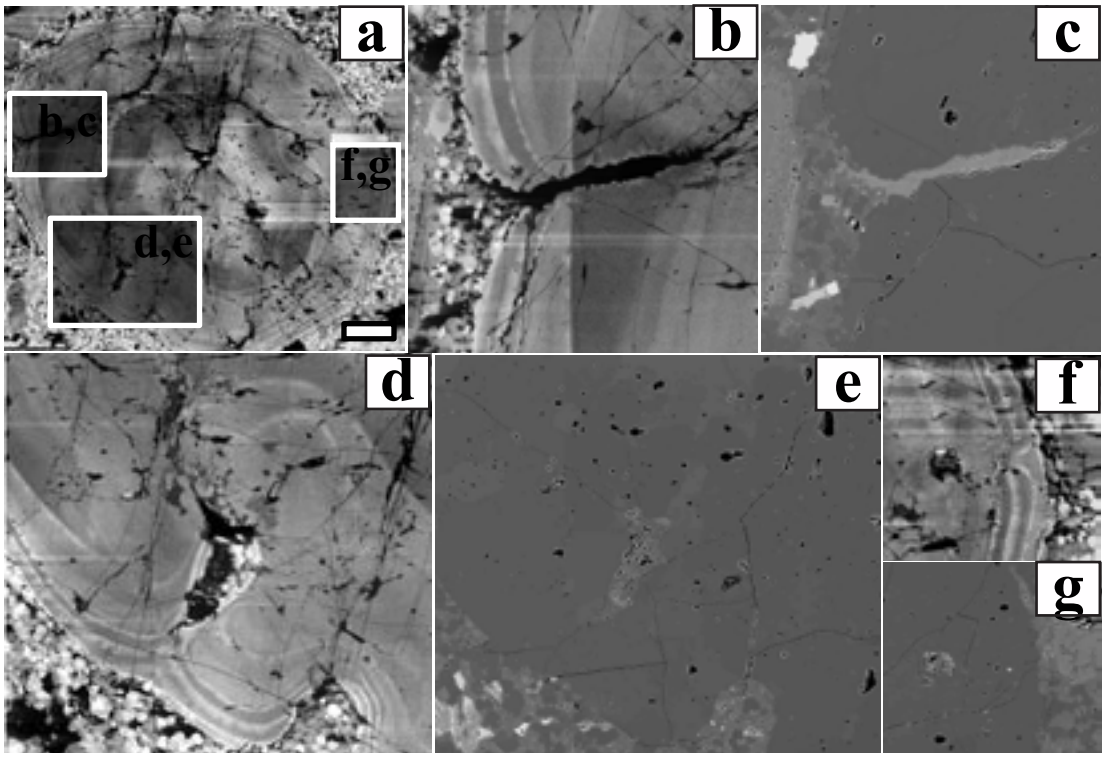

Figure 4-13 Interplay between CL layers and healed fractures, embayments and inclusions

Sample SBD-69, Batu Hijau (Indonesia). (a, b, d and f) - SEM-CL images, (c, e and g) - BSE images. Scale bar is 200 µm.

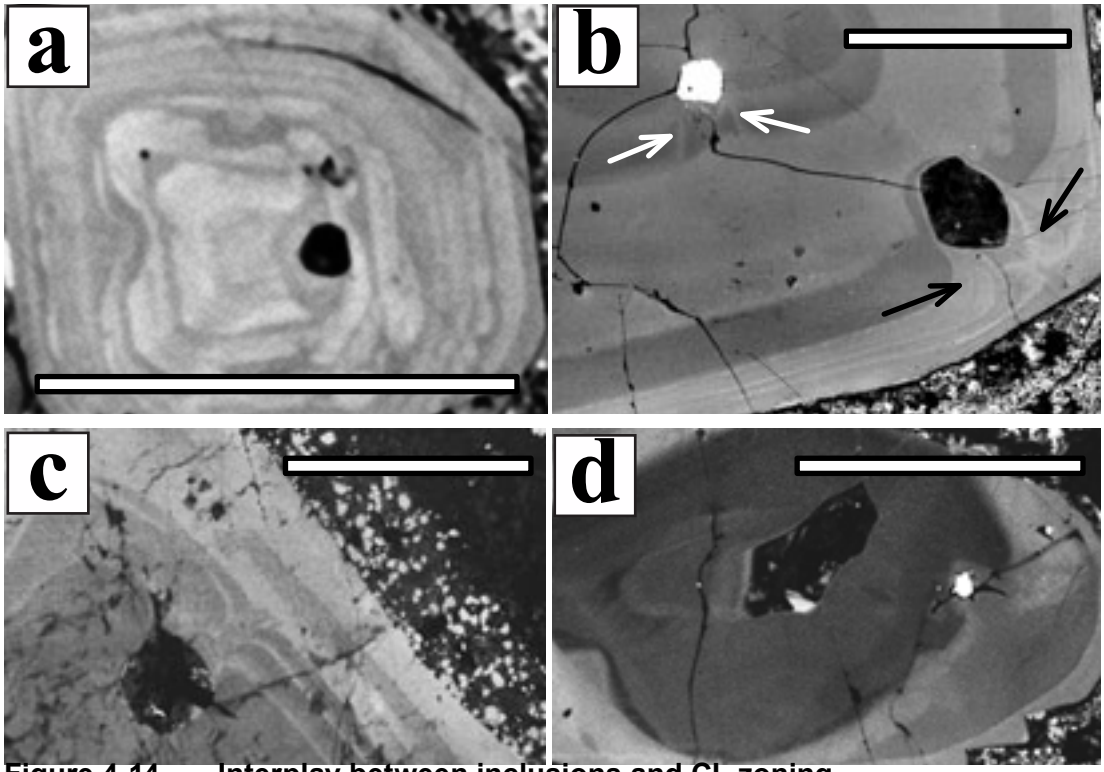

Figure 4-14 Interplay between inclusions and CL zoning.
(a) – melt inclusion (shown by arrow) without curved layers around it (Rio Blanco, CA8); (b)-(d) – groundmass inclusions and curved layers near it (arrowed); (b) and (d) – Rio Blanco, CA6; (c) – Climax, 109647. SEM-CL images. Scale bars are 200 µm.

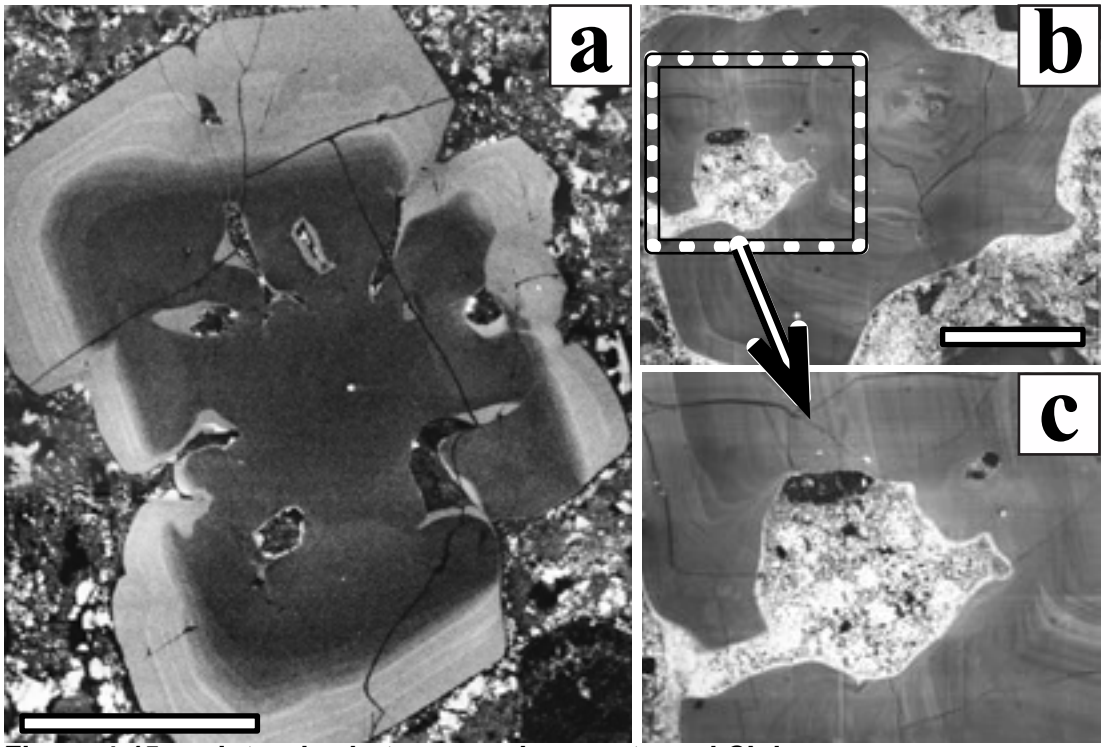

Figure 4-15 Interplay between embayments and CL layers
CL images of the quartz eyes from Rio Blanco (a – DC-DP-1) and Antapaccay (b – 133-19920, c – the enlarged area of the same grain). SEM-CL images. Scale bars are 500 µm.

CL growth pattern are observed next to each other (Fig 4-18b). In some samples groundmass shows dull CL no growth zoning (Fig 4-18c, d). It was found that groundmass quartz does not show any healed fractures, i.e. secondary quartz (Fig 4-18b).

4.2.4. Cathodoluminescence patterns in quartz phenocrysts from the Taupo Volcanic Zone

To compare CL pattern of rocks that underwent significant fractional crystallisation in-situ after emplacement, with CL pattern of the extrusive rocks that crystallised mostly in a magma chamber, two rhyolite samples from the Taupo Volcanic Zone (TVZ) were studied. Unlike quartz eyes, phenocrysts from TVZ are often crystal fragments, and display very faint CL patterns containing only oscillatory zoning (Fig 4-19). Another striking discrepancy is the absence of healed fractures in the Taupo samples; however, open cracks are abundant (Fig 4-19). Unlike healed fractures in porphyry samples, fractures visible in BSE images are not associated with inflected or smudged CL layers. The quartz crystals from Taupo do not contain fluid inclusions (Fig 4-19). Melt and groundmass inclusions do not disturb the CL layers in the Taupo samples (Fig 4-19) and there are no smudged layers around them (Fig 4-19). Melt inclusions are dark in CL and isolated; groundmass inclusions are always connected with the surface of the phenocrysts by fractures and embayments in most cases cut CL layers (Fig 4-19).

4.2.5. Surface damage from the electron beam

It was observed that points on quartz surfaces which have been subjected to electron beam of the electron microprobe analyses, show a permanent change in their relief and CL intensity (Fig 4-20 and 4-21). To study the influence of the damage quartz structure from the electron beam a series of spots were made with different electron beam current and beam size in two quartz grains from Rio Blanco (DC-DP-1) and Taupo (New Zealand Fig 4-21). Raman spectroscopy was also applied both to the spots and to the undamaged area next to the spots. The study has shown that:

Figure 4-16 Complex CL pattern of vein quartz from sample 138-2 (Batu Hijau)

(a) – cross section through the vein, (b-d) – enlarged parts of the cross section. Scarce euhedral crystal shapes pointed toward the centre of the veins (1) and can also occupy interstitial position (2). Some grains show dull CL (3); most grains, show combined CL patterns (dull in CL central zones surrounded and often truncated by euhedral zoning (4). Agate-like banding is related to the latest quartz associated with sulphides (5). Several generations of secondary quartz are revealed (6). SEM-CL images. Scale bar is 300 µm.

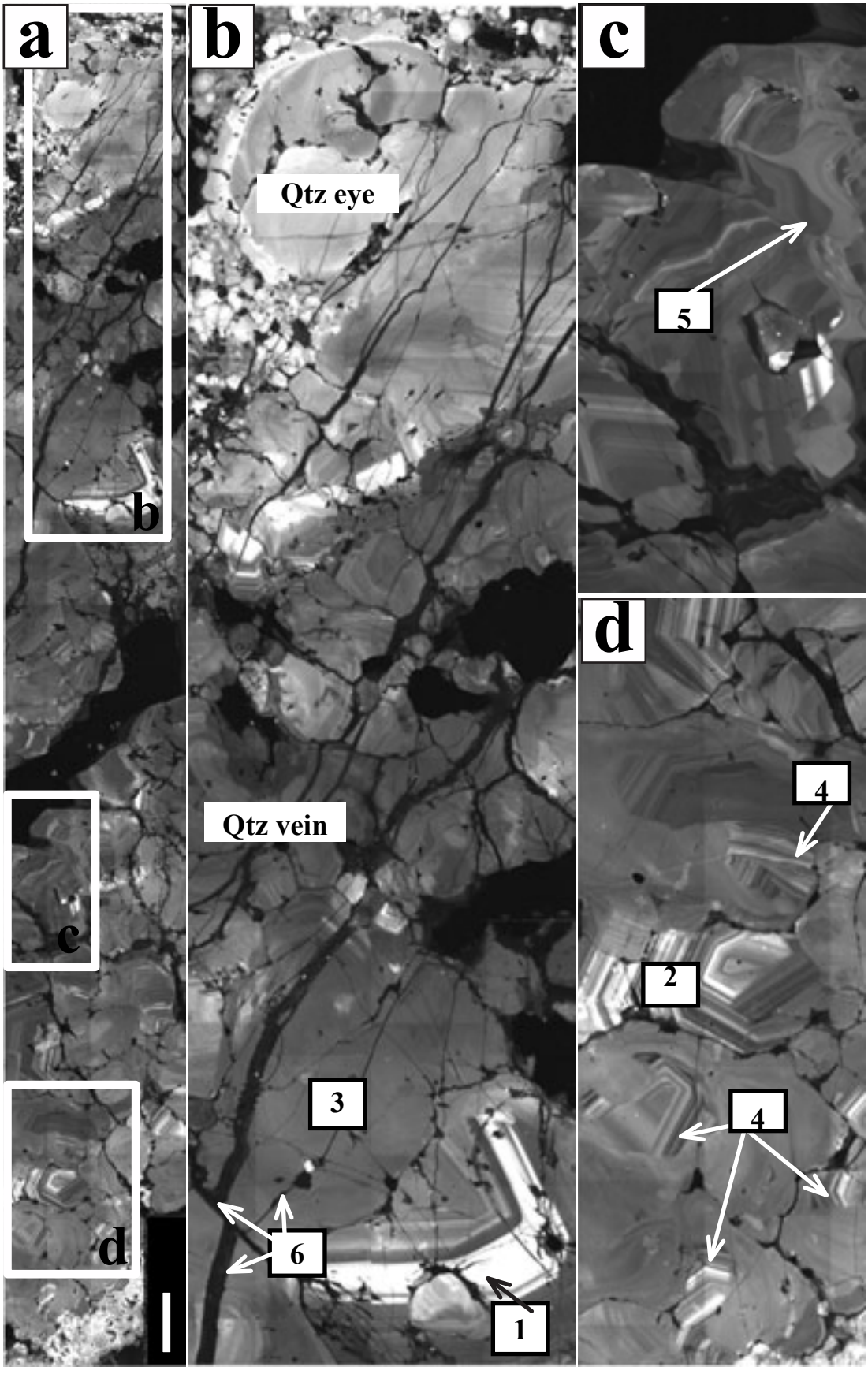
a
b
c
d
Qtz eye
Qtz vein
5
4
2
4
3
6
1

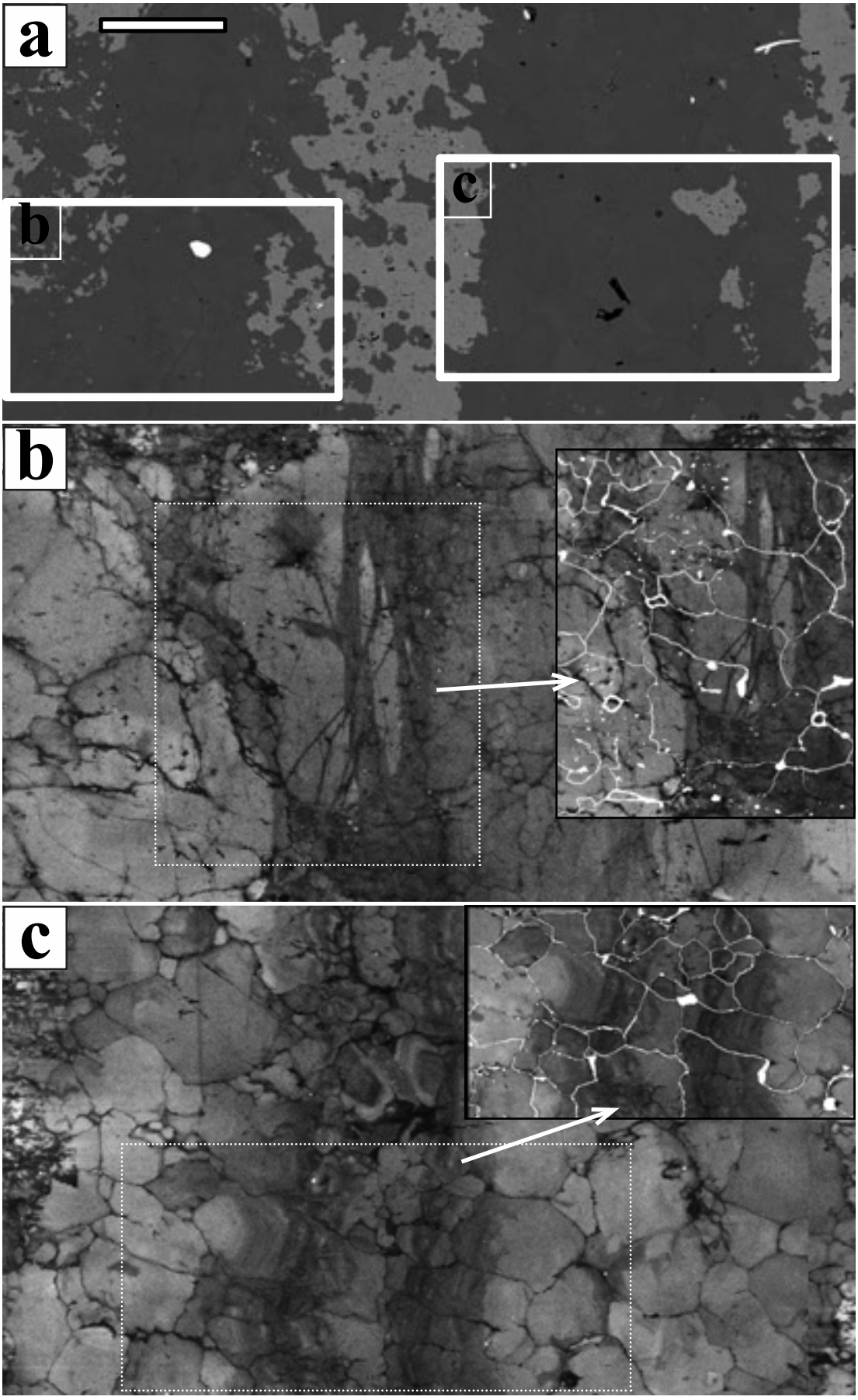
a
b
c
b
c

Figure 4-17 Cathodoluminescence pattern of quartz veinlets from Climax (109645)
(a) – BSE image, (b) and (c) – enlarged areas outlined in (a), SEM-CL images, with overlaid map of grain boundaries (white lines). Scale bar is 1000 µm.

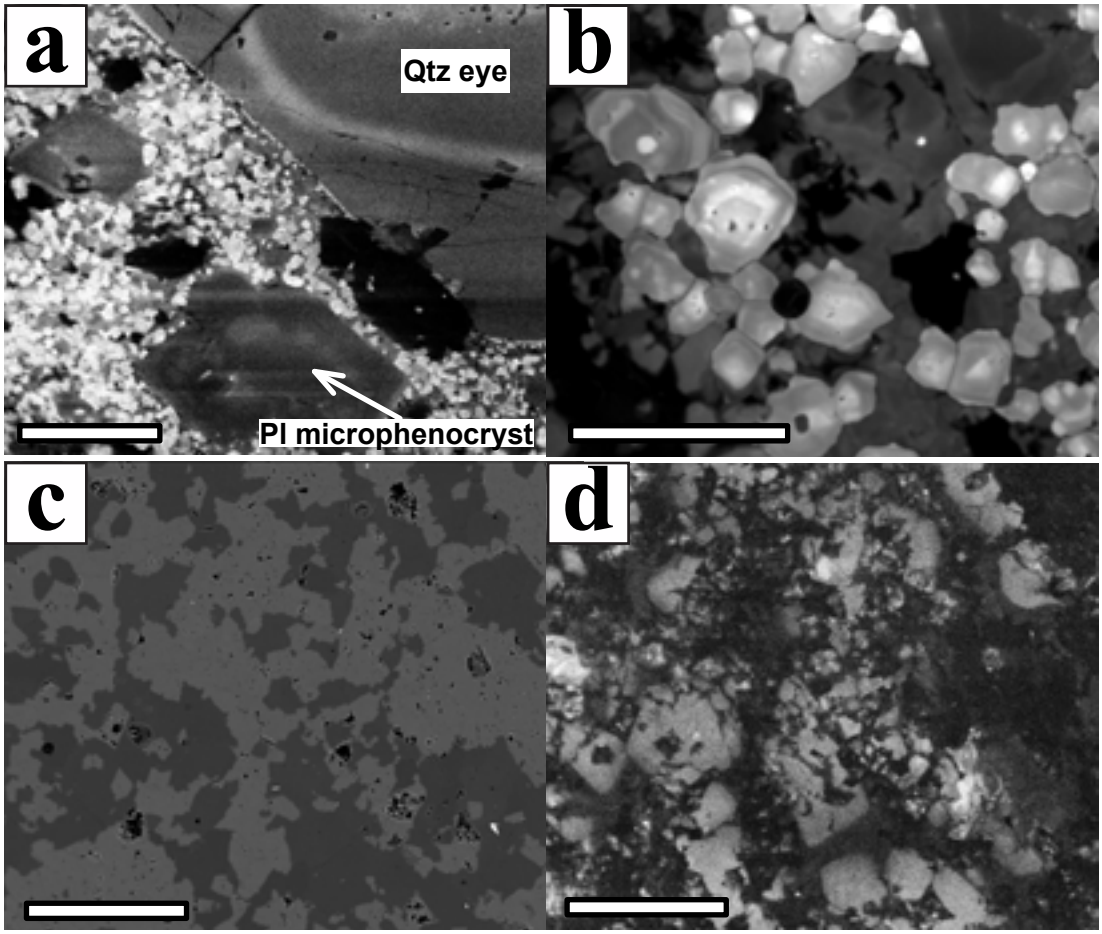

Figure 4-18 Cathodoluminescence of groundmass quartz
(a) – the sample 109607 (Panguna). Note that groundmass quartz is brighter than quartz eyes, (b) – the sample 138-2 (Batu Hijau); note that adjacent grains have normal and reverse CL growth pattern (shown by the arrows), (c, d) – the sample from Climax show dull in CL groundmass. (a, b and d) – SEM-CL images, (c) – BSE image. Scale bars are 200 µm.

1. Electron beam damaged the quartz structure, creating a domed area with vermiform-like surface outgrowth (Fig 4-20). Such a volume increase implies structural changes and indeed, the Raman spectrum in such spots show significant decrease in peak intensities comparing to the spectrum of undamaged quartz (Fig 4-20).

2. Electron beam damages quartz from the porphyry (Rio Blanco) and

phenocrystic quartz from Taupo in different ways. In reflected light (Figure 4-21a, b) it is clear that amorphous outgrowths in the sample from Taupo (Fig 4-21a) are shallow and smooth, whereas the outgrowths in sample from Rio Blanco are higher and have shagreen-like surfaces (Fig 4-21b).

3. As a result of the electron beam irradiation spot areas became lighter in BSE images (Fig 4-21c, d) that could be caused by a change in trace element content, because the intensity of the BSE signal is strongly related to the atomic number of the specimen.

4. CL image of the Taupo quartz shows more or less homogeneous dark grey – black spots, whereas the spots on the quartz grain from Rio Blanco are heterogeneous and have bright rims (Fig 4-21e, f).

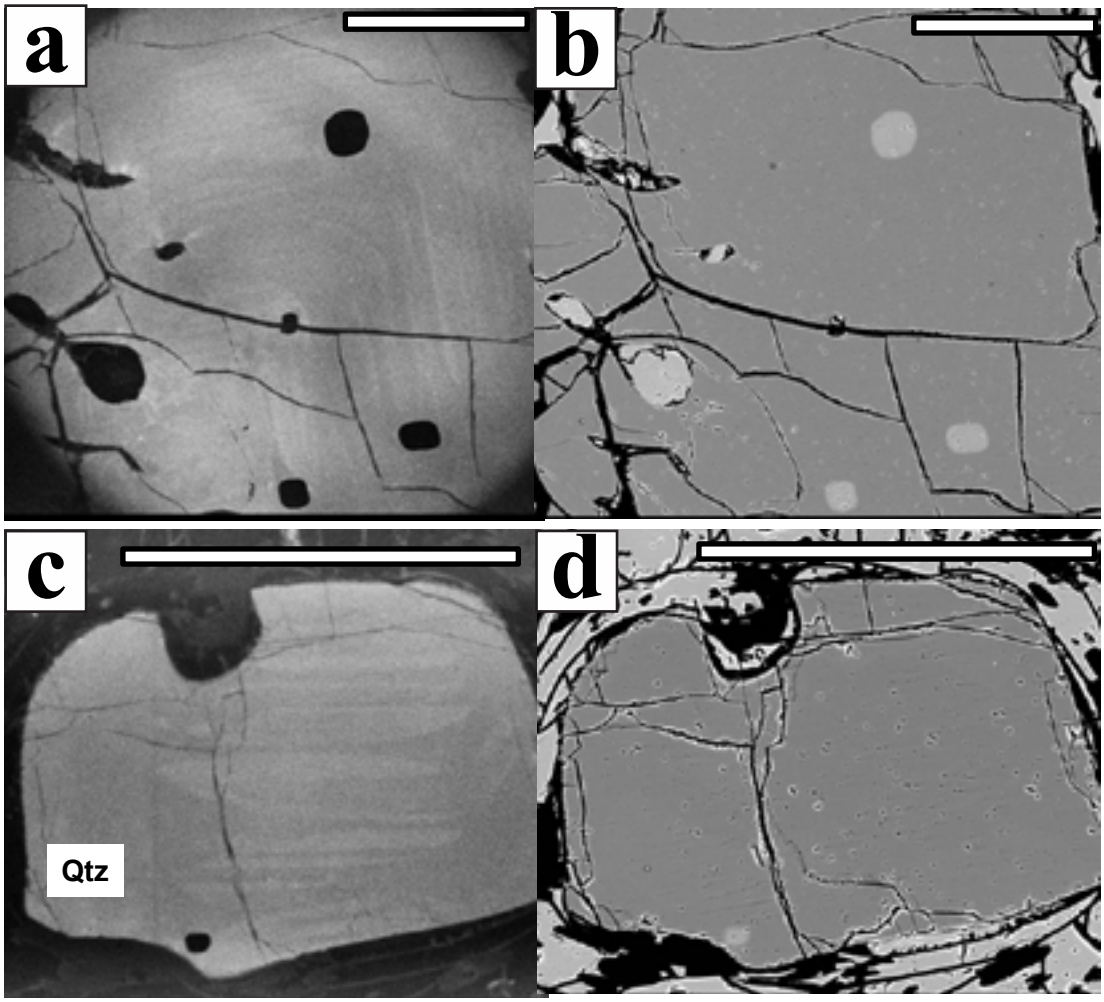

Figure 4-19 Cathodoluminescence images of the quartz phenocrysts from Taupo Volcanic zone (the sample nz27b)

(a, c) - SEM-CL images, black spots are melt inclusions (now glass), CL pattern is low contrast oscillatory zoning. Note that there are no healed fractures in the phenocrysts. (b, d) - BSE images of the same crystals. Scale bars are 200 µm.

4.3. Trace element composition (EPMA results)

4.3.1. Trace elements in quartz eyes

4.3.1.1. Trace elements in primary growth zones

Trace element analyses were performed on the quartz eyes from samples SBD-69 and SRD-02 from Batu Hijau (Indonesia), 109647 from Climax (USA), DC-DP-1, DC-DLP-1 and CA6 from Rio Blanco (Chile) and 092-29700 from Antapaccay (Peru).

Aluminium and titanium were well above detection limits, which are 8-10 ppm for Al and 10-14 ppm for Ti; Fe tends to be below detection limits (23-38 ppm) in the cores and to increase significantly above detection limits towards rims (Figs 4-22 - 4-24). Aluminium, titanium and iron contents vary both between different samples and different CL zones of a grain. Concentrations of Zn in quartz were measured in two samples (SRD-02, Batu Hijau and 092-29700, Antapaccay, the detection limit was 93 ppm). Other elements such as K, Ge and Mn were always below detection limits (11 ppm for K, 27 ppm for Ge and 21-23 for Mn). Our data show that there is a clear correlation between CL brightness and Ti concentrations.

In samples from Rio Blanco trace elements content varies significantly within samples. Within the quartz grains from sample DC-DP-1 and CA6 Al content varies within a range of 55-150 ppm within the grains of type 1 CL pattern. Al content is often

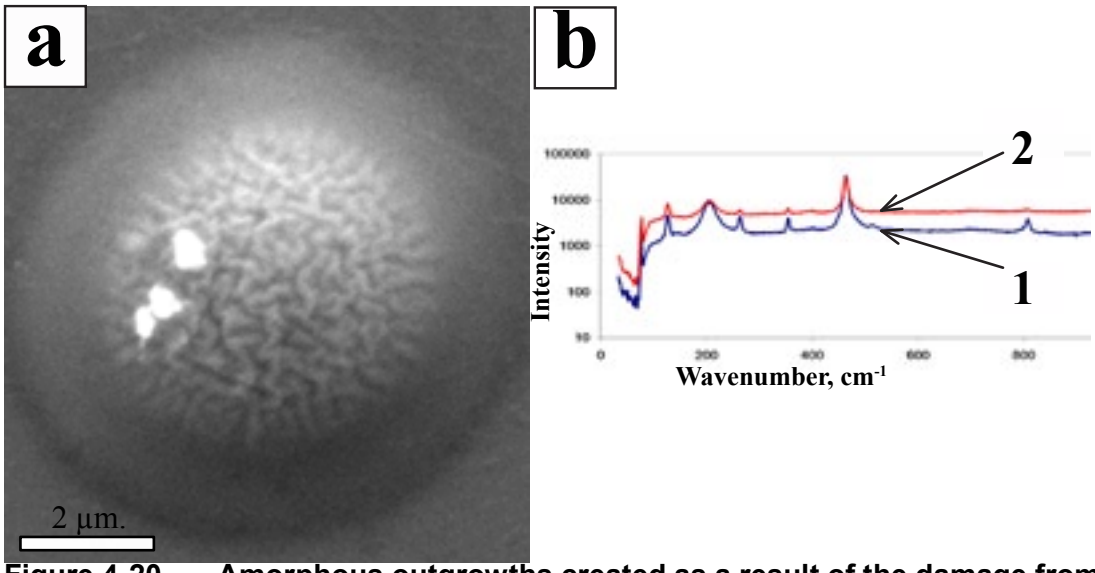

Figure 4-20 Amorphous outgrowths created as a result of the damage from electron beam (SE and Raman spectra)
(a) – an example of such outgrowths on the surface of the sample DC-DP-1 (SE image); (b) – Raman spectra of quartz (1) and amorphous outgrowths (2) of the sample DC-DP-1.

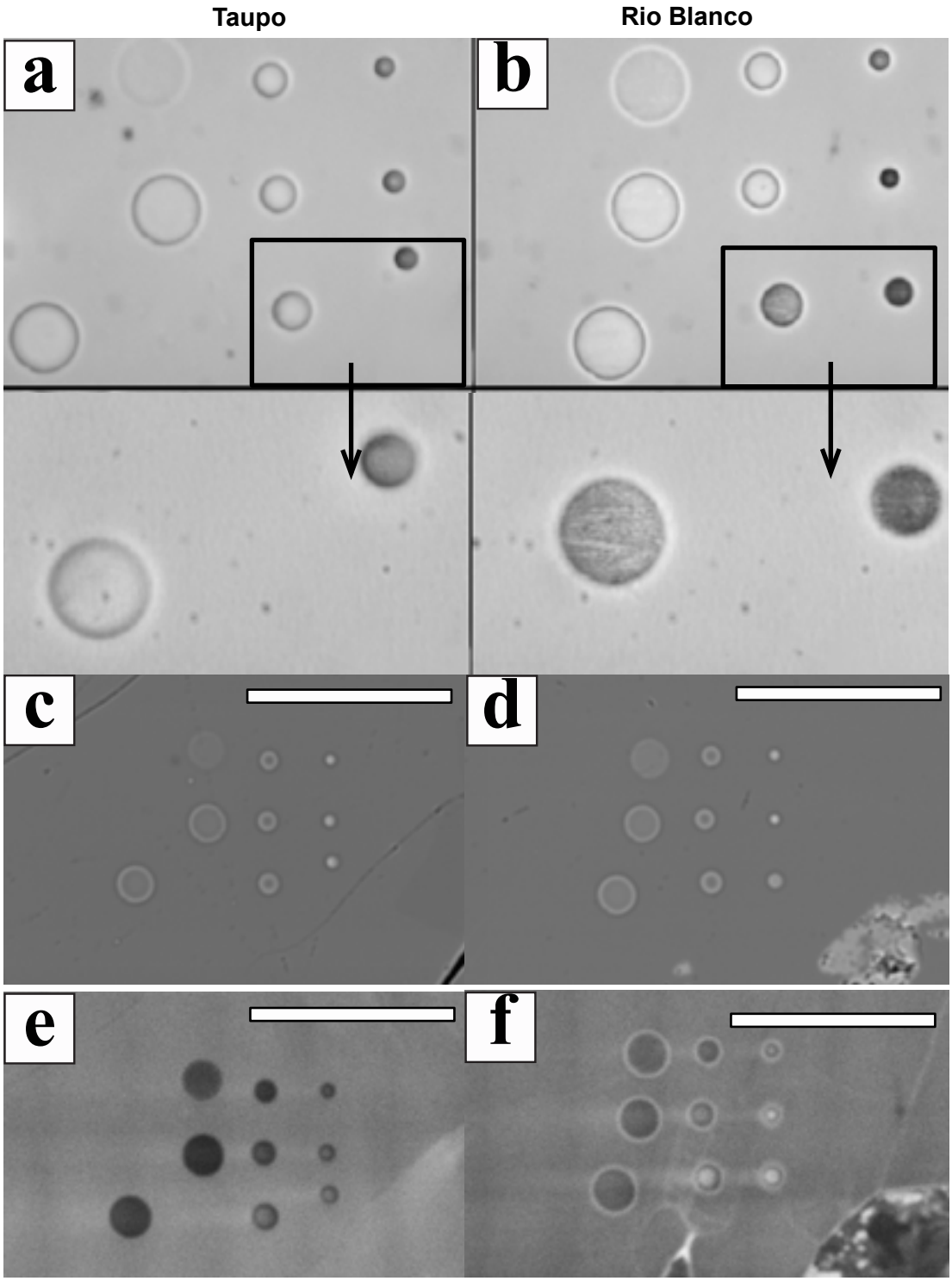

Figure 4-21 Amorphous outgrowths from electron beam damage (optical, BSE and CL images)

(a, b) - amorphous outgrouwths, reflected light. (c, d) – BSE images of electron beam spots with various parameters: beam current from 50 nA in the bottom row to 100 nA in the middle row and 200 nA in the upper row and beam size from 5 µm (left column) to 10 µm (middle column) and 20 µm (right column). (e) and (f)–CL images of the same spots. (a, c, e) - sample 27b from Taupo, (b, d, f) sample DC-DP-1, Rio Blanco. Scale bars are 100 µm.

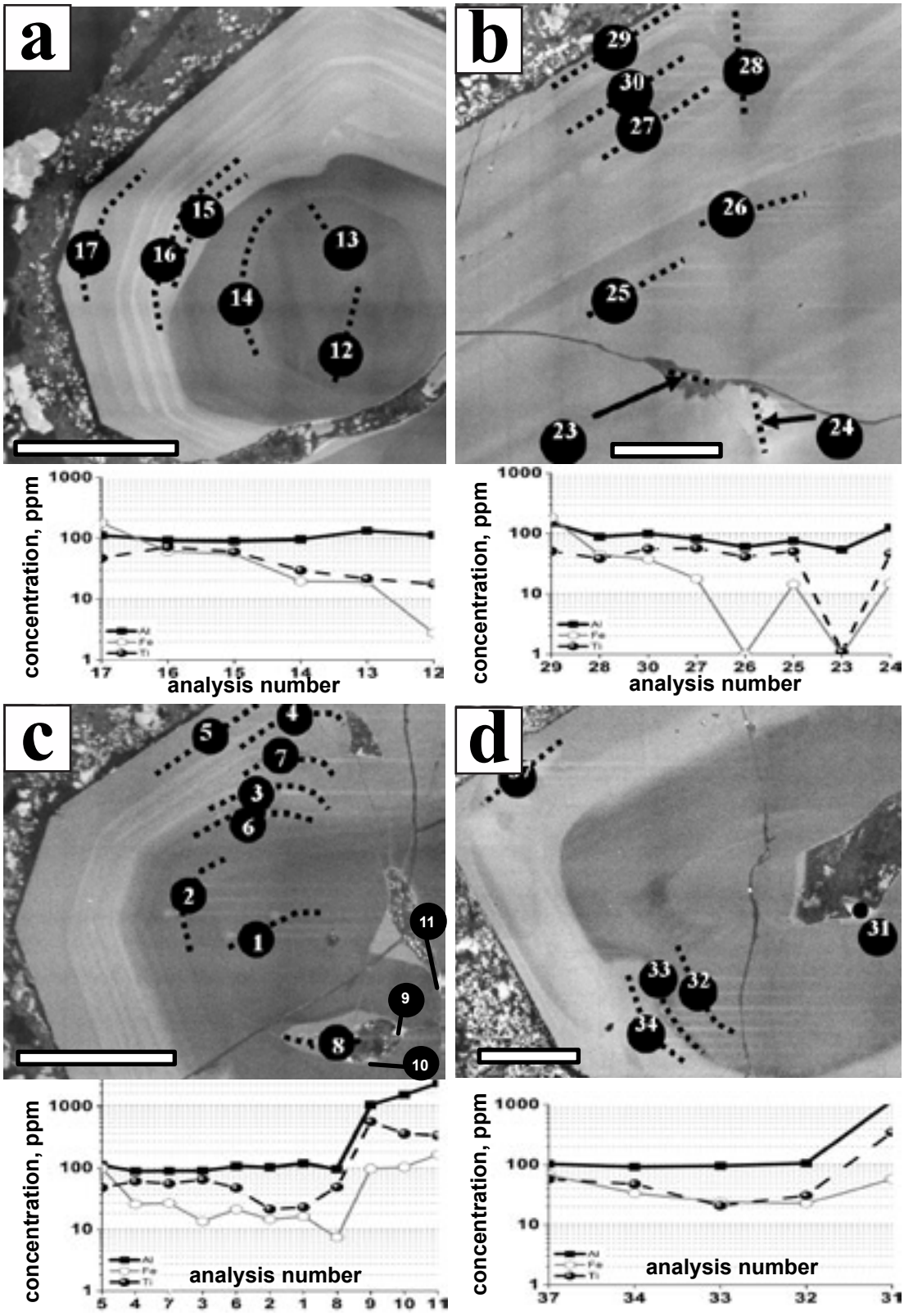

Figure 4-22 Trace element distribution within quartz grains from Rio Blanco (a-c) - DC-DP-1, (d) – CA6. Analyses arranged from rims to cores. SEM-CL images. Axis 'concentration' are logarithmic. Analyses were in three point along dotted lines; an average concentration from the analyses is plotted. Scale bars are 200 µm.

higher in the dark cores (95-131 ppm) than in the rims (89-103 ppm) and it tends to increase in the very outmost layers (Fig 4-22a, c and d) and reaches up to 1000-3000 ppm in very bright spots along the embayments (Fig 4-22c). Unlike Al, Ti content is the lowest within the dark cores (18-31 ppm) and increases in the rims (47-72 ppm); Ti content is higher in the fine oscillatory zones (60-72 ppm) and is highest in very bright spots along the embayments (up to 565 ppm, Fig 4-22c). Within type 3 grains Al and Ti trends are parallel: with an increase in Al there is an increase in Ti (Fig 4-22b). Both Al and Ti within the type 3 grains are lower that in the type 2 grains. Al varies within 60-100 ppm increasing to 149 in the outmost layers; Ti fluctuates between 39-57 ppm. Fe content in all the grains is always below detection limits within the cores and increases up to 163-184 ppm in outmost layers and in bright spots along the embayments.

Aluminium and titanium content within the quartz grain from sample DC-DLP-1 (Rio Blanco) is remarkably higher (Fig 4-23b). Al within zones that are bright in SEM-CL (Fig 4-23b) is extremely high (from 943-2796 ppm) and differ significantly between adjacent oscillatory zones (micron scale); the difference can vary from 146 to 1853 ppm. Aluminium drops dramatically from 1454 to 92 ppm within tens of microns of the transition from the bright zone to the darker part of the grain. Al content fluctuates in the range 83-103 ppm within the middle of the grain and then increases drastically up to 2146-4358 ppm in the darkest core and its nearest surroundings (Fig 4-23b). Similarly to Al, Ti content is anomalously high in the bright part of the grain (from 177 to 269 ppm) varying drastically on a micron scale within oscillatory zones. The Ti trend is sometimes opposite to that of Al, and Ti fluctuations between the adjacent zones are up to 122 ppm (Fig 4-23b). Ti content drops from 177 to 60 ppm within about 30 µm of the zone transition in the middle of the grain. Within the rest of the grain Ti content varies within 46-69 ppm decreasing in the darkest core to 31-47 ppm (Fig 4-23b). Fe is below its detection limit within the middle zone, it varies between 37-161 ppm in the bright zone, reaches 65-235 ppm in the darkest core and 41-52 ppm in the outmost layer adjacent to the core.

In the grain 109647 from Climax Al varies within 86-416 ppm in the dark core and 106-168 ppm in the rim zone of (Fig 4-23a). Ti content is 9-32 ppm in the core and 32-58 ppm in the rim. Al and Ti trends are roughly parallel. Fe is parallel to Al and Ti in the core and varies from below the detection limits to 75 ppm and increases in the rim from 44 ppm in the layer next to the core to 354 ppm in the outmost layer.

Generally, trace element content within the quartz grains from Batu Hijau is higher than that of the previously described grains (except for the grain DC-DLP-1). In the grain from SBD-69 maximum Al, Ti and Fe content is in the very bright spot

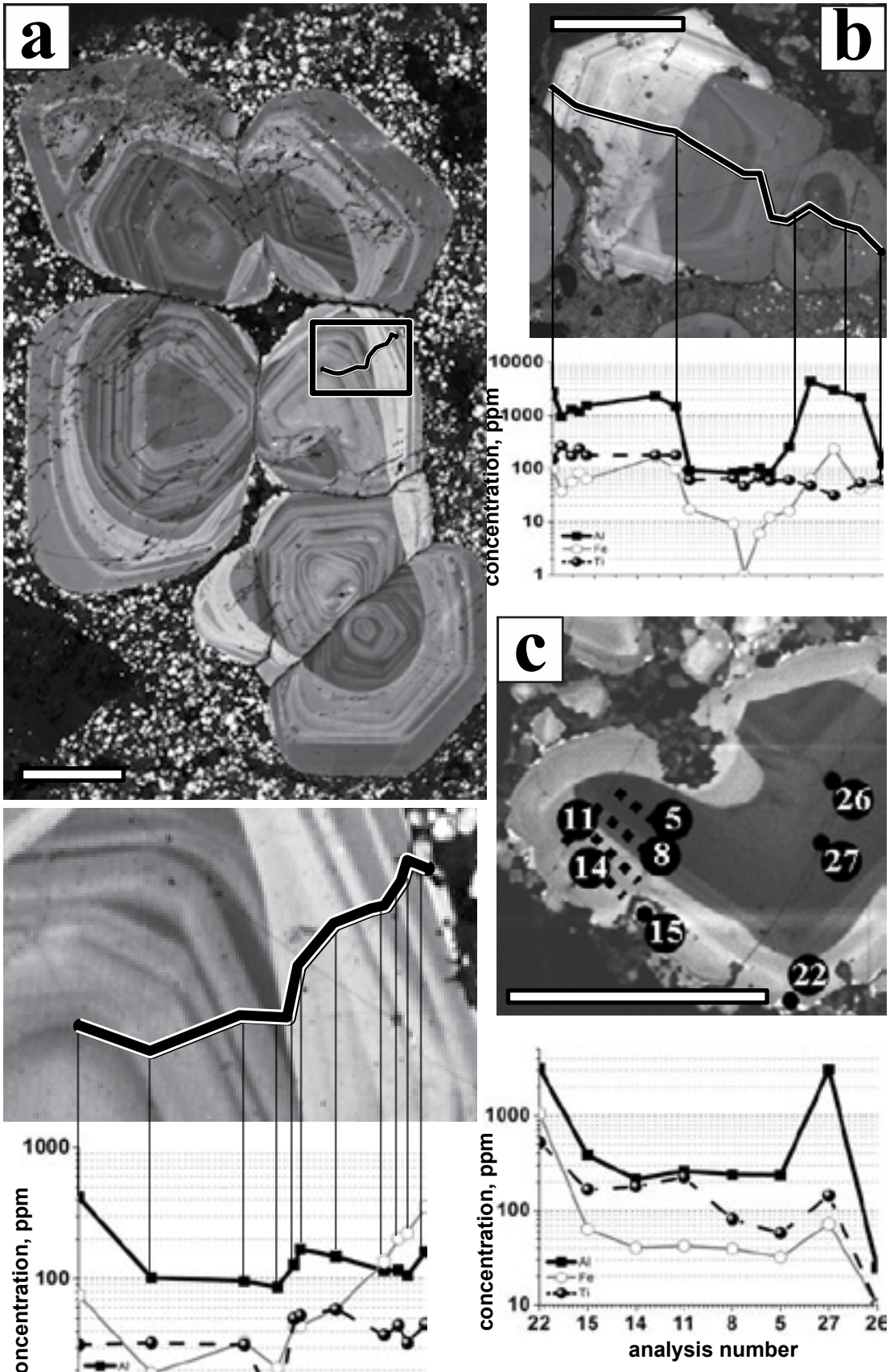
a
b
10000
1000
100
10
1
concentration, ppm
Al
Fe
Ti
c
11
5
26
8
14
27
15
22
1000
100
10
concentration, ppm
22
15
14
11
8
5
27
26
analysis number

Figure 4-23 Trace elements vs CL intensities in the samples from Climax, Batu Hijau and Rio Blanco
(a) - 109647 (Climax), (b) - DC-DLP-1 (Rio Blanco), lines in (a, b) lines of points which were analysed. (c) - SBD-69 (Batu Hijau). SEM-CL images. Axis 'concentration' are logarithmic. Scale bars are 500 µm.

along the grain boundary (up to 3167, 522 and 1048 ppm, respectively, Fig 4-23c) Al content varies within 212-384 ppm, Ti ranges between 166 and 224 ppm and Fe is quite low (40-63 ppm). Within the dark core (zones 5 and 8, Fig 4-23c) Al and Fe content is about the same (236-239 and 32-39 respectively) and Ti within the core is much lower: 58-80 ppm.

Within the grain from SRD-02 Al varies mostly in a range from 144 to 221 ppm (Fig 4-25a) reaching 4359 ppm in some spots within the outmost rim. Ti increases from the centre (76 ppm) towards the rim (225 ppm) and Fe varies from 28 to 515 ppm (Fig 4-25a).

Aluminium content within Antapaccay sample 092-27000 varies from 98 to 1427 ppm (Fig 4-6), Ti content is within 24-90 ppm and Fe is generally below the detection limit (Fig 4-24c). CL-bright zone in this quartz grain is very heterogeneous in trace element content: 153-370 ppm Al and 42-61 ppm Ti below the healed fracture and 101-114 ppm Al and 41-44 ppm Ti in the same CL zone above the fracture (Fig 4-24c). Zn content was also measured in this grain; it is very high and varies from 547 to 3278 ppm showing diffusional distribution (Fig 4-24c).

4.3.1.2. Trace elements in secondary quartz

Secondary CL-dark quartz shows different distribution of trace elements than that observed within primary growth zones. Trace elements in the secondary quartz are highly heterogeneous. For example, aluminium content within a single healed fracture in sample SBD-69 (Fig 4-23c) varies from 3071 ppm (spot 27) to 25 ppm (spot 26). As it is shown in Figure 4-24 (c) Al within secondary quartz concentrates along fine fractures, and ranges from 307 to 3361 ppm, whereas away from those fractures Al varies from 40 to 96 ppm.

Titanium in the secondary quartz is always below the detection limit except for one spot in sample SBD-69 from Batu Hijau (spot 27), where Ti is 143 ppm (Fig 4-23c). Iron within secondary quartz is in most cases below detection limit; only in sample 092-27000 (Antapaccay) it is above the detection limit, and varies from 39 to 69 ppm (Fig 4-24c).

a

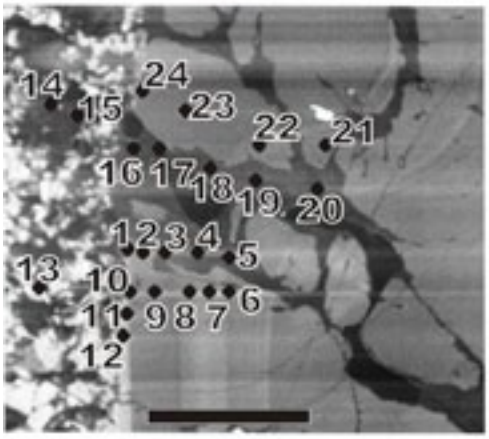

b

	Al	Fe	Ti	Zn		Al	Fe	Ti	Zn
1	96	19	17	1342	13	253	38	109	176
2	95	27	30	1661	14	1148	33		256
3	43	14		2538	15	816	36	4	417
4	47	36	3	4304	16	3361	51	2	3048
5	51	46		5691	17	911	39	10	3908
6	370	10	42	3278	18	49	69		5852
7	216	21	66	2637	19	40	41	5	3984
8	153	11	61	2217	20	307	40		3885
9	100	16	31	1364	21	101	15	44	1417
10	117	15	40	928	22	114		41	2078
11	154	22	63	740	23	98	11	24	1551
12	1427	63	90	547	24	174	30	49	855

c

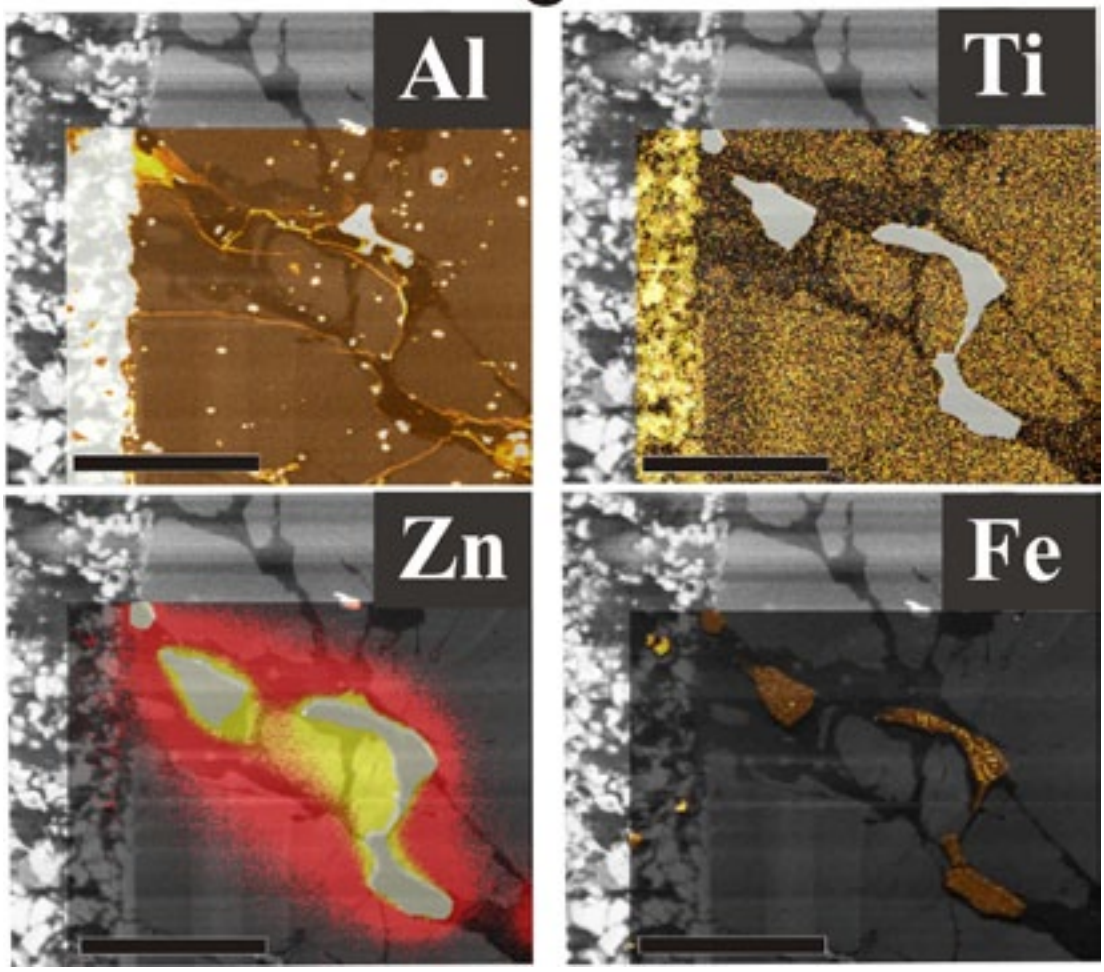

Figure 4-24 Point analyses and distribution maps for Al, Ti, Zn, Fe

Quartz eye from the sample 092-27000, Antapaccay. (a) - Analysed spots, SEM-CL image. (b) - trace element concentrations in spots from 1 to 24 from (a). (c) - Al, Ti, Zn, Fe distribution maps overlaid on SEM-CL images. Detection limits: Al - 10 ppm, Fe - 37ppm, Ti - 17 ppm, Zn - 93 ppm. Scale bars are 200 µm.

a

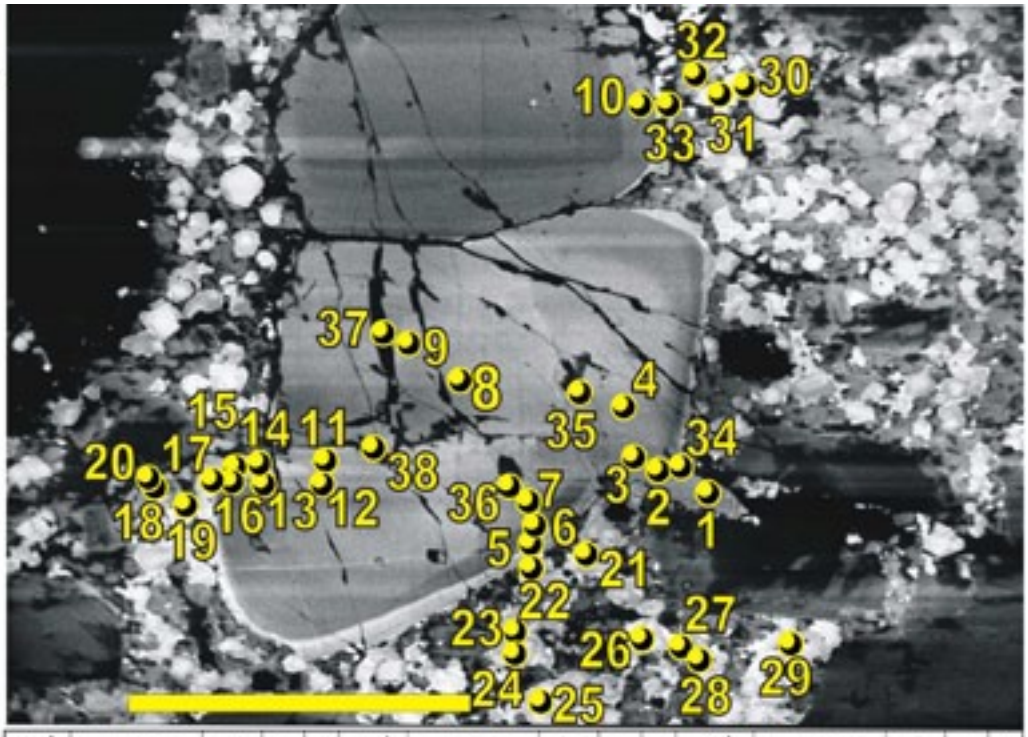

b

spot number	quartz type	Al	Fe	Ti	spot number	quartz type	Al	Fe	Ti	spot number	quartz type	Al	Fe	Ti
1	quartz eye	153	442	125	14	quartz eye	163	515	140	27	groundmass	181	140	162
2	quartz eye	159	450	123	15	quartz eye	179	284	138	28	groundmass	14712	263	154
3	quartz eye	129	337	113	16	quartz eye	176	153	76	29	groundmass	312	246	281
4	quartz eye	176	144	174	17	quartz eye	4359	182	225	30	groundmass	198	155	184
5	quartz eye	172	215	136	18	groundmass	168	237	137	31	groundmass	175	142	137
6	quartz eye	207	269	93	19	groundmass	300	95	115	32	groundmass	118039	1962	97
7	quartz eye	207	175	164	20	groundmass	453	403	12	33	groundmass	250	140	122
8	quartz eye	211	28	154	21	groundmass	190	462	183	34	secondary quartz	766	386	1
9	quartz eye	221	31	130	22	groundmass	175	343	172	35	secondary quartz	84665	169	0
10	quartz eye	197	117	94	23	groundmass	154	410	142	36	secondary quartz	84	88	0
11	quartz eye	144	112	114	24	groundmass	6197	744	289	37	secondary quartz	31	23	0
12	quartz eye	217	67	149	25	groundmass	213	505	180	38	secondary quartz	36	53	1
13	quartz eye	204	170	93	26	groundmass	256	247	236					

c

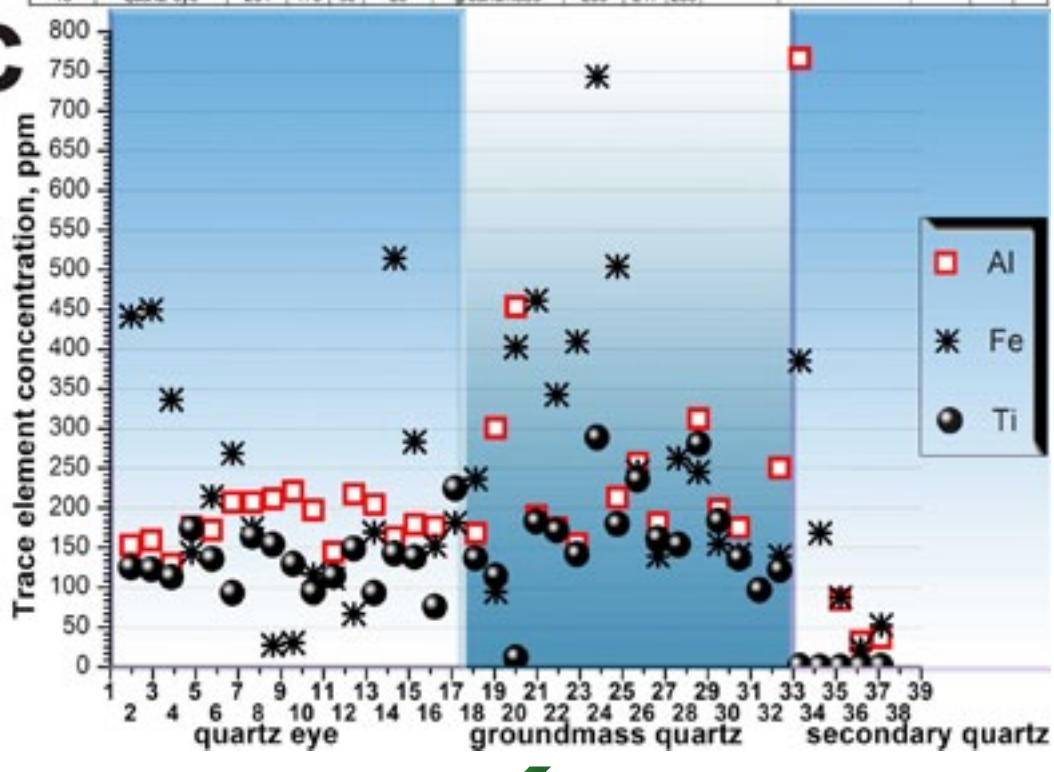

Figure 4-25 Trace element content within quartz eye and groundmass
Sample SRD-02 (Batu Hijau): (a) - Analysed spots, SEM-CL image. (b) - trace element concentrations in spots from (a). (c) – a graph with the same data set, spot numbers (axis X) correspond to those in (a). Detection limits: Al - 10 ppm, Fe - 37ppm, Ti - 17 ppm. Scale bar is 500 µm.

Extremely high Zn content (up to 5852 ppm) was observed in the secondary quartz within the quartz eye from sample 092-27000 (Fig 4-24c). Distribution of Zn was found to be completely different from Al, Ti and Fe distribution patterns. Firstly, it decreases gradually from the sphalerite without showing any abrupt changes on the boundary from secondary to primary quartz (Fig 4-24c). Secondly, Zn concentrates mostly within the quartz eye; Zn content in the groundmass quartz next to the quartz eye is from 176 to 417 ppm. Other trace elements such as K, Na and Cl are distributed within fine fractures in secondary quartz similar to Al.

4.3.2. Trace elements in groundmass quartz

Generally, trace element content in groundmass quartz is higher than that in growth zones and healed fractures and rather heterogeneous (probably due to microinclusions). For example, in sample SRD-02 from Batu Hijau (Fig 4-25) Al content in the groundmass quartz varies within 154-453 ppm, Ti content is in the range 12-280 ppm and Fe content is 96-744 ppm, whereas in the quartz eye Al is within 129-259 ppm, Ti 76-225 ppm, Fe 28-450 ppm. Within secondary quartz Al is within 31-84 ppm, Ti is below detection limit, Fe – within 23-53 ppm.

4.3.3. Al vs Ti

The Ti vs Al diagrams show very different distribution patterns of those elements (Fig 4-26). Ti content is always higher in rims, whereas Al content in rims can be either slightly higher than in cores (sample 109647) or much lower than in cores (sample DC-DP-1). In sample DC-DLP-1 the outer CL-bright zone is enriched in both Al and Ti (field I, Fig 4-26), CL-grey zone contain low Ti and Al (field II, Fig 4-26) and the core shows low Ti and high and variable Al content (field III, Fig 4-26).

Within grains, which do not show rim-and-core pattern, Al and Ti concentrations are distributed evenly, do not show any separate groups (samples DC-DP-1, SRD-02 and 092-29700). Outer rims demonstrate increased Al and Ti concentrations, especially in the CL-brightest areas (Fig 4-26).

Generally, secondary quartz shows Ti below detection limits and variable Al

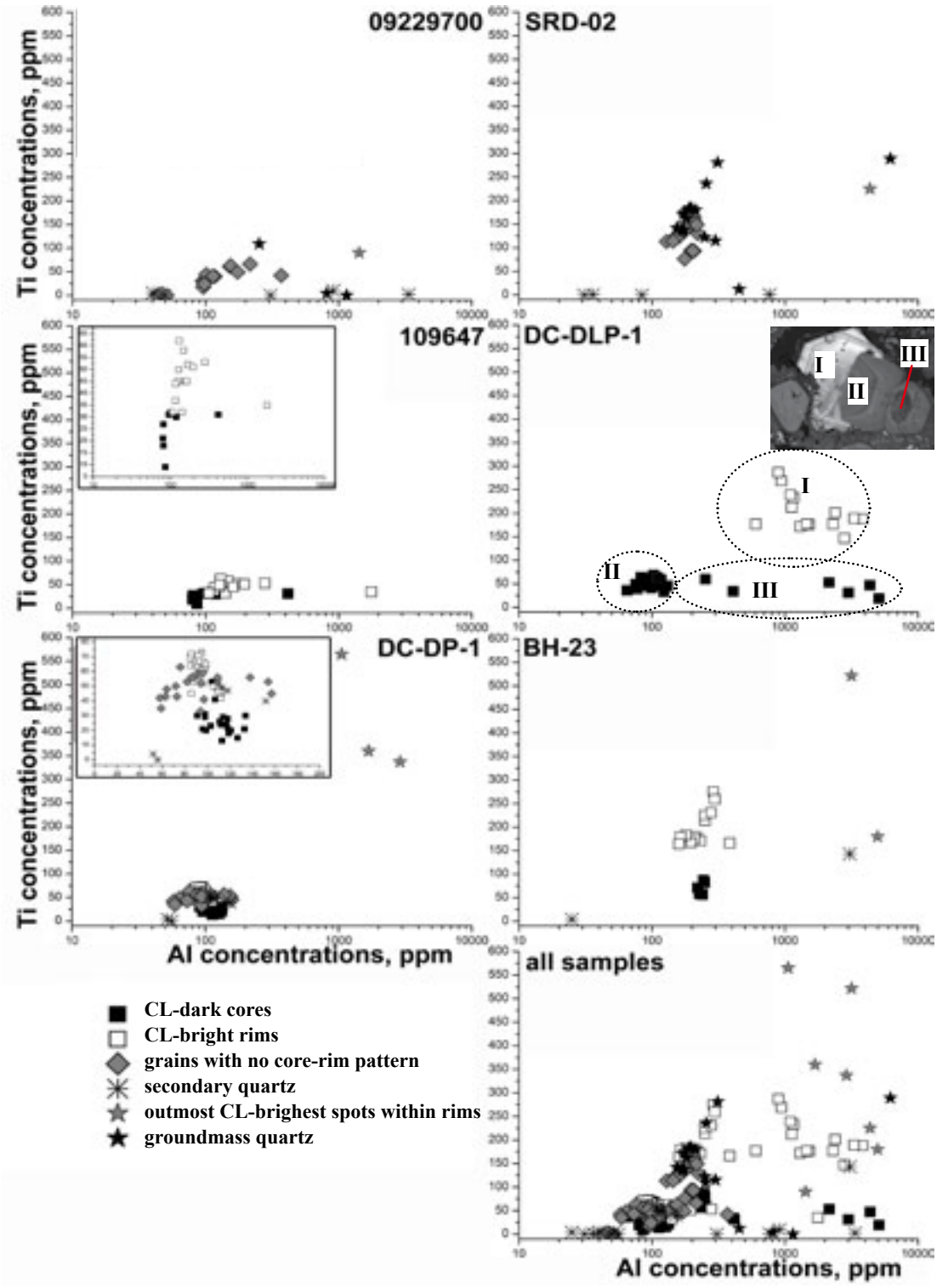

Figure 4-26 Al vs Ti distribution in the all studied samples
Insets are the same plots with different scales

content (Fig 4-26). Groundmass quartz demonstrates extremely variable Al vs Ti distribution, but in most cases groundmass quartz are enriched in both Al and Ti (Fig 4-26).

4.4. Spectral cathodoluminescence mapping

Hyperspectral cathodoluminescence mapping were performed on three grains from Climax (109647) and Rio Blanco (DC-DP-1 and DC-DLP-1). The data showed three principle contributors to the CL emission: the peaks centreed at 1.93 eV, 2.05 eV and 2.72 eV.

4.4.1. 2.72 eV emmision

The quartz grain from sample DC-DP-1 is a cluster of two subgrains, which are almost identical regarding their 2.72 eV intensity pattern (Fig 4-27a). This grain shows much more intense 2.72 eV emission in the rim than in the core with the most intense layers in the middle of the rim zone (Fig 4-27a). A boundary between the core and the rim is sharp showing no gradational transitions. The grain's core shows outer and inner zones, which are different in intensity. Both core zones have lower 2.72 eV band intensity than the rim zone, and the inner core zone shows the lowest 2.72 eV intensity. The core has oscillatory layers, and clearly shows sectoral and intrasectoral zonation (Fig 4-27a). All the transitions between different layers

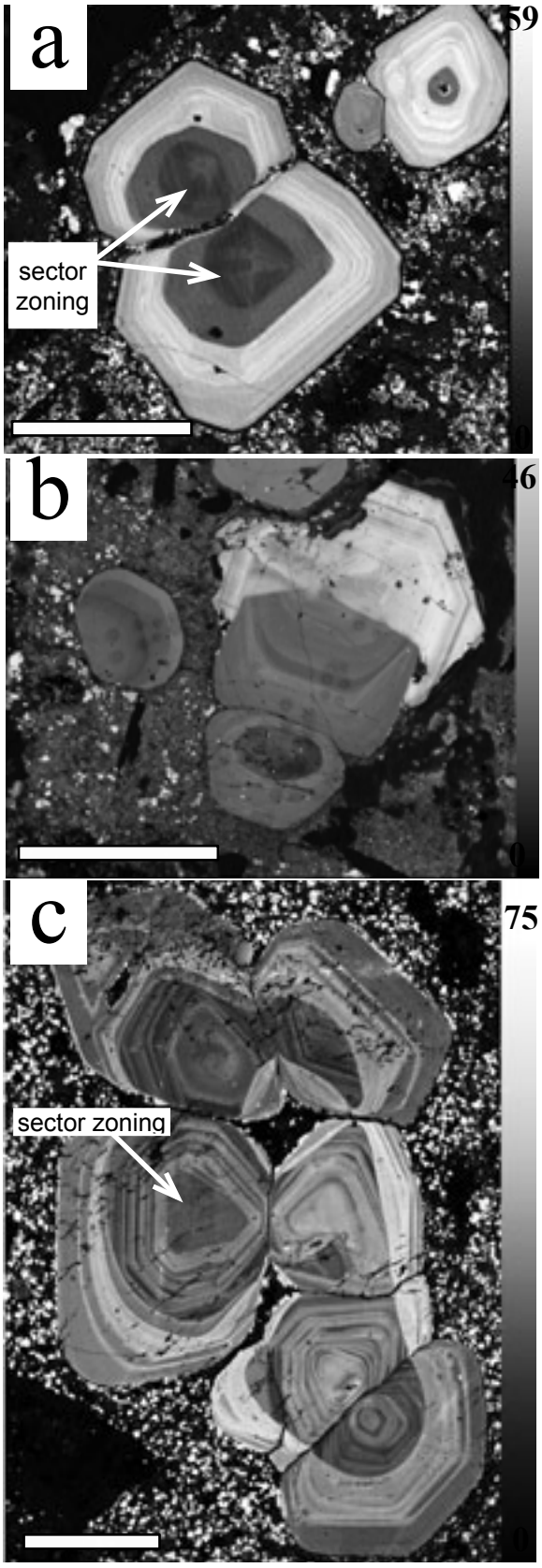

Figure 4-27 Distribution of 2.72 eV band emission in quartz grains
(a) - DC-DP-1 and (b) - DC-DLP-1, Rio Blanco, (c) - 109647, Climax. Hyperspectral CL maps. Scale bars are 500 µm.

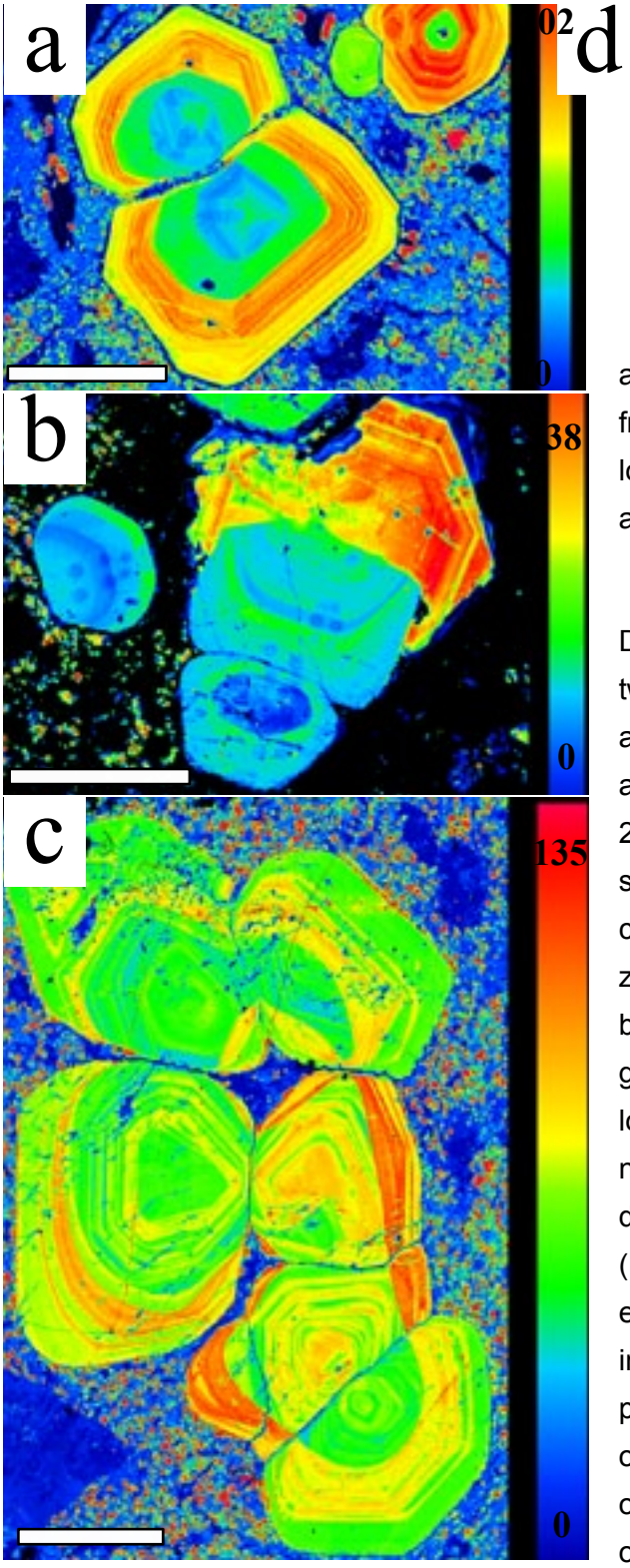

Figure 4-28 Ti distribution maps for the grains (a-c) and a calibration curve based on trace EPMA analyses (d)
(a) - DC-DP-1 and (b) - DC-DLP-1, Rio Blanco, (c) - 109647, Climax. Calibrated hyperspectral CL maps. Scale bars are 500 µm.

are sharp. There is only one healed fracture visible in the grain; it shows low 2.72 eV band intensity (Fig 4-27 a).

The quartz eye from sample DC-DPL-1 (Fig 4-27b) is a cluster of two subgrains. One of them shows a rather low 2.72 eV band intensity, and has a core, which has even lower 2.72 eV concentrations. The other subgrain consists of two extremely contrasting in 2.72 eV emission zones with a sharp transition between them in the middle of the grain (Fig 4-27b). One of them shows low 2.72 eV intensity, and has a narrow concentric zone in the middle displaying lower 2.72 eV intensity (Fig 4-27b). The other zone shows extremely high 2.72 eV intensity. The inner part of this zone has an irregular pattern resembling sector zoning; the outer part shows euhedral concentric oscillatory zones. There is a number of healed fractures distributed within the grain, which show low 2.72 eV band intensity.

The quartz grain from sample 109647 is a cluster of six grains. Each

of the grains show internal texture similar to that in grain DC-DP-1: the dark (low 2.72 eV band intensity) inner core with oscillatory zoning, and the bright rim zone (high in 2.72 eV band intensity), which also has oscillatory zoning. One of the cores shows sector zoning (Fig 4-27c). All the transitions between different layers are sharp. There is a number of healed fractures and star-like patches of secondary quartz showing low 2.72 eV band intensity.

4.4.2. Correlation between 2.72 eV emission and Ti content

Electron microprobe point analyses showed a strong positive correlation between 2.72 eV band intensity and Ti content (Fig 4-28). A line of best fit, shown in Figure 4-28d, has a R^2 of 0.9631 and this was used to calibrate the fitted 2.72 eV CL intensity maps. The resultant trace speciation map for Ti (Fig 4-28) reveals the following features:

- Titanium concentration is significantly higher in the rims than in cores (in samples 109647and DC-DP-1) or in particular zones (sample DC-DPL-1).

- Attached grains within a cluster can sometimes be significantly different in Ti concentrations. For instance, in sample 109647 two of the adjacent

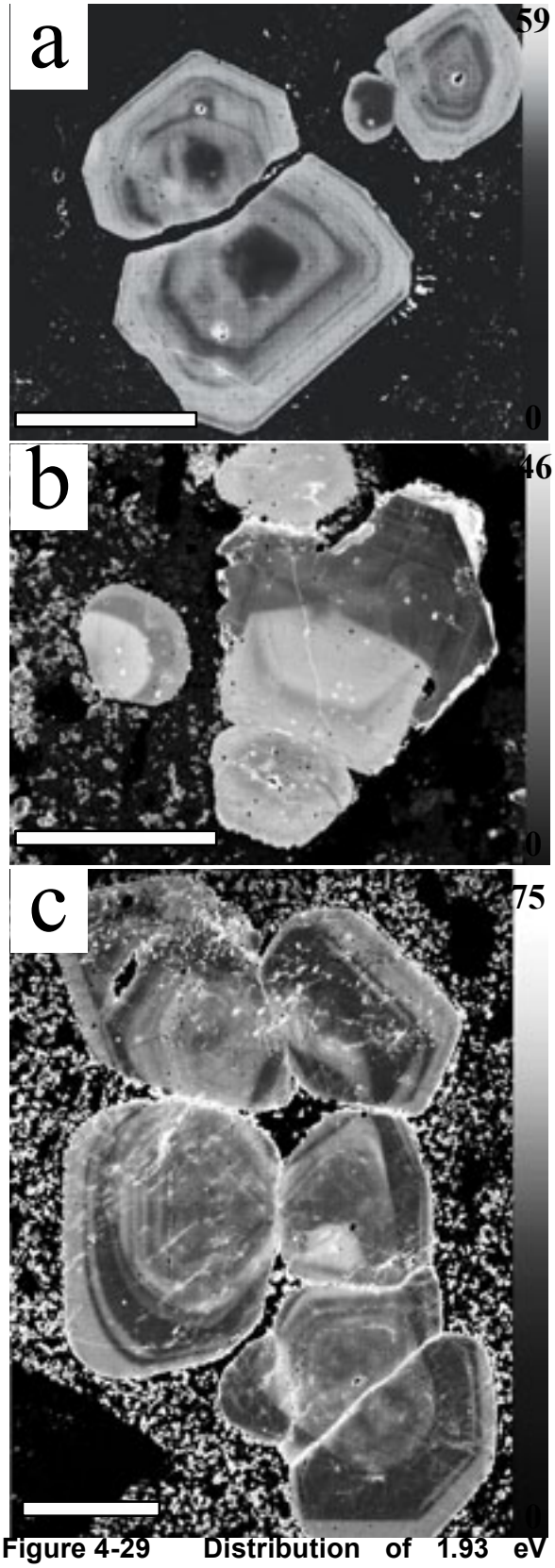

Figure 4-29 Distribution of 1.93 eV band emission in quartz grains
(a) - DC-DP-1 and (b) - DC-DLP-1, Rio Blanco, (c) - 109647, Climax. Hyperspectral CL maps. Scale bars are 500 µm.

grains within the cluster have Ti concentration almost twice as higher as the other clustered grains (Fig 4-28c).

• Titanium content changes abruptly within an extremely narrow transition areas between the rims and the cores. For example, Ti increases from 1 to 35 ppm within 10-15 μm transition zone in sample 109647 (Fig 4-28c). In sample DC-DPL-1 Ti concentrations rises from 45-48 to 162-186 ppm within ~10 μm transitions zone (Fig 4-28b). Finally, in sample DC-DP-1 Ti concentration increases from 30 ppm in the core to 60 ppm in the rim within 10 μm zone (Fig 4-28a).

• Titanium is responsible for sector zoning observed within grain cores where Ti concentrations are extremely low (10-20 sometimes 30 ppm, see Fig 4-28a).

4.4.3. 1.93 eV emission

Intensity of 1.93 eV band in the DC-DP-1 grain shows a distribution pattern different from that of 2.72 eV band intensity (Fig 4-29a). The 1.93 eV emission is intense in both the rim zone and the outer core, and shows the lowest intensity in the inner core and along the transition zone between the core and the rim. In the inner core a sector zoning is observed (Fig 4-29a). Low 1.93 eV intensities within sectors are correlated with high 2.72 eV intensities (higher Ti concentrations).

There are patches of extremely high 1.93 eV intensity within the inner core (Fig

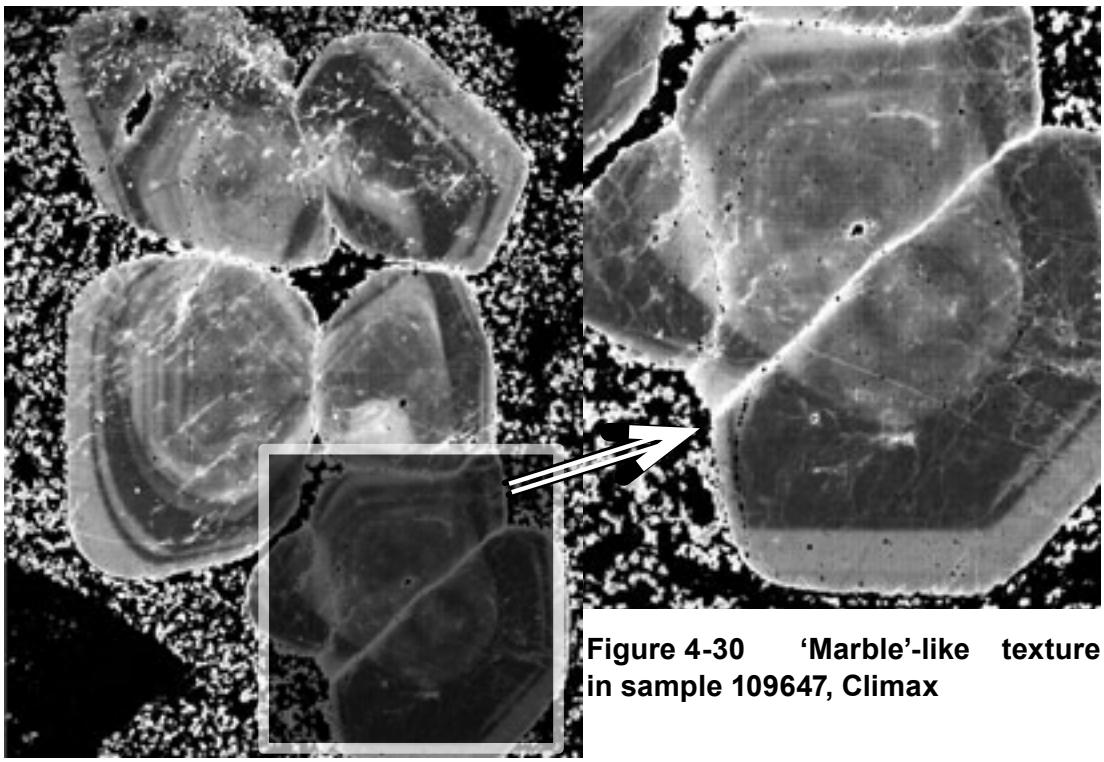

Figure 4-30 'Marble'-like texture in sample 109647, Climax

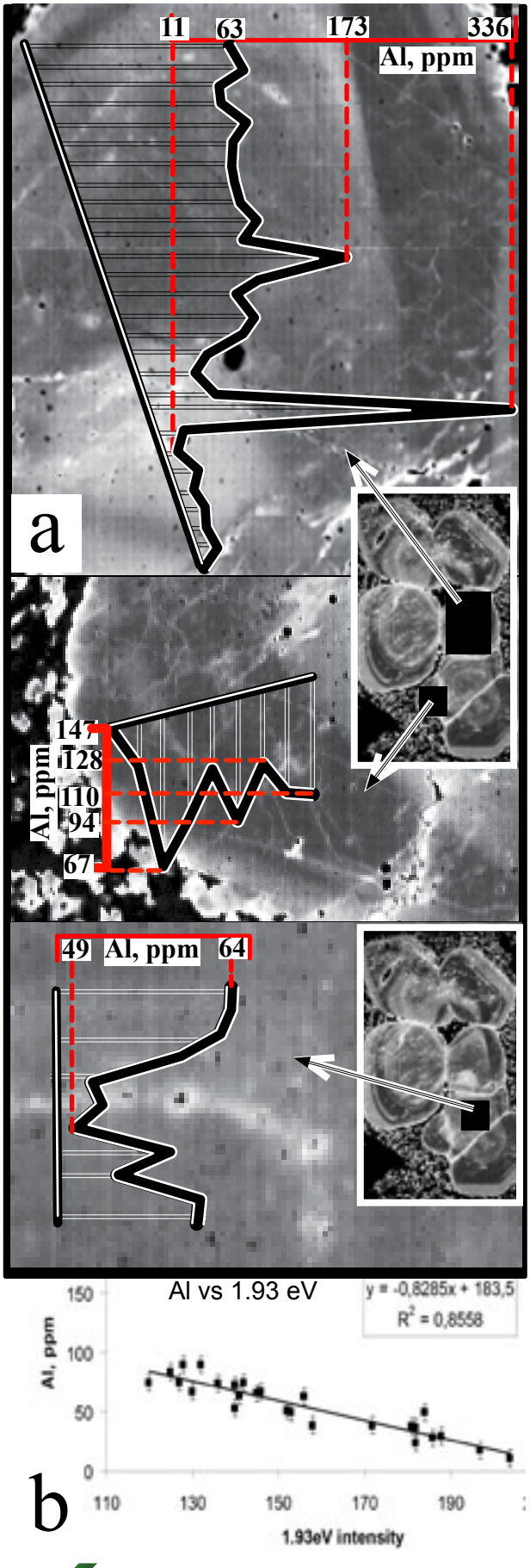

Figure 4-31 uminium distribution vs 1.93 eV intensity
(a) - distribution maps of 1.93 eV intensity with lines showing Al concentrations, (b) - Al concentrations plotted vs 1.93 eV intensity. Sample 109647. Spikes with 336 and 173 ppm are probably microinclusions, and werere not plotted in (b).

4-29a), which are not correlated with 2.72 eV intensities. Preliminary data show negative correlation between such areas and Al content (Fig 4-31). The core-to-rim transition is sharp along some faces and diffusional along the others (Fig 4-29a). The fracture shows high 1.93 eV intensity (Fig 4-29a).

Within the large subgrain of DC-DPL-1 grain low 1.93 eV intensity is correlated with high 2.72 eV emission (Fig 4-29b). Low 1.93 eV emission zone shows an irregular pattern in the middle and concentric euhedral oscillatory zones in its outer part.

The 1.93 eV pattern within the small subgrain is nether positively nor negatively correlated with 2.72 eV intensity pattern. The rim of DC-DPL-1 shows high 1.93 eV and medium 2.72 eV intensity, whereas the core displays low both 1.93 eV and 2.72 eV band intensity.

There are numerous healed fractures within the grain. All of them show different 1.93 eV band intensity.

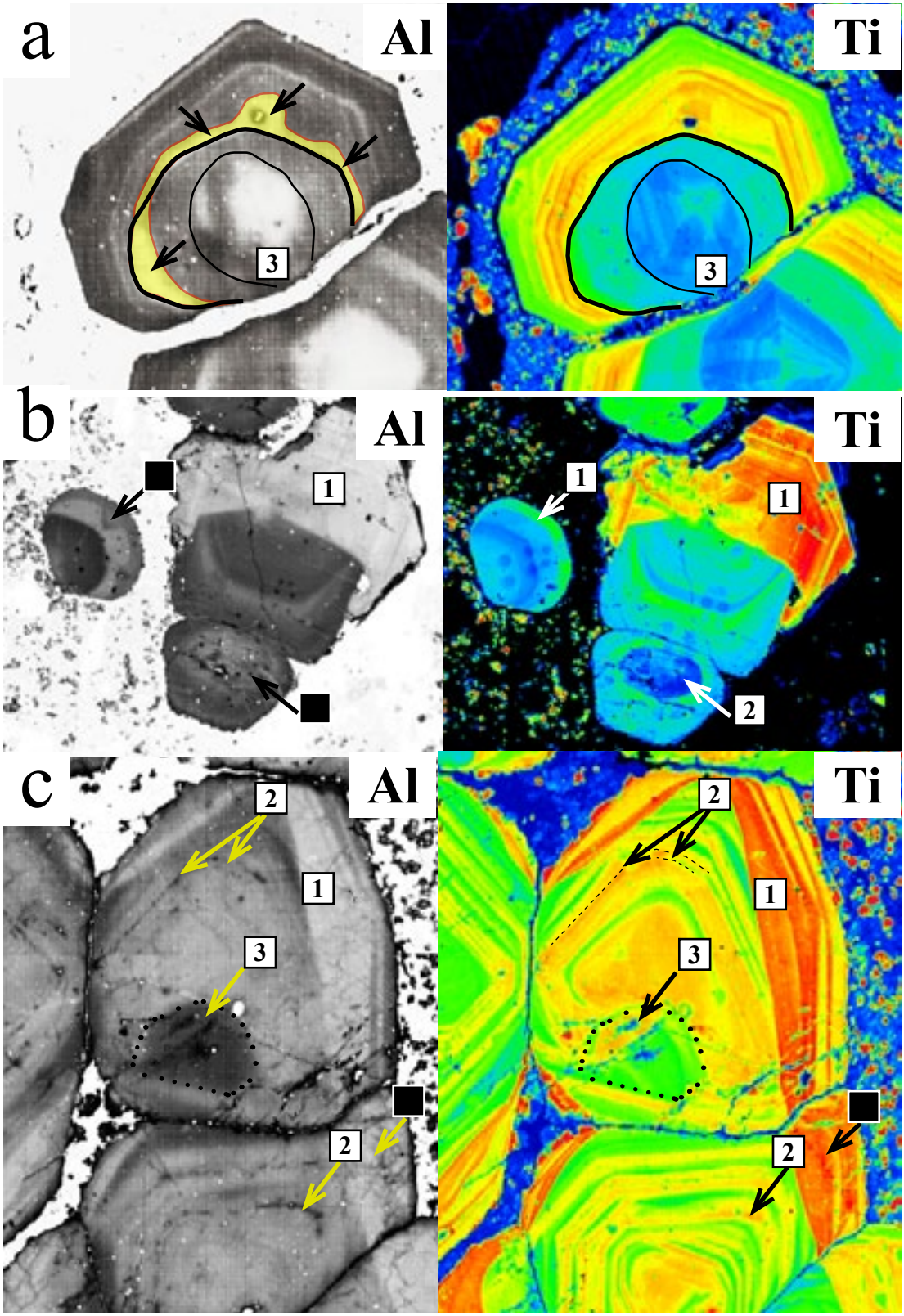

Figure 4-32 Correlation between Al and Ti content

Samples DC-DP-1 (a, d) and DC-DLP-1 (b, e) from Rio Blanco and 109647 (c, f) from Climax. (a-c) inverted 1.93 eV maps, which reflect Al distribution. (d-f) - Ti distribution maps. 1 - areas, which are positively correlated between Ti and Al content, 2 - areas, which are negatively correlated, 3 - areas, which are not correlated.

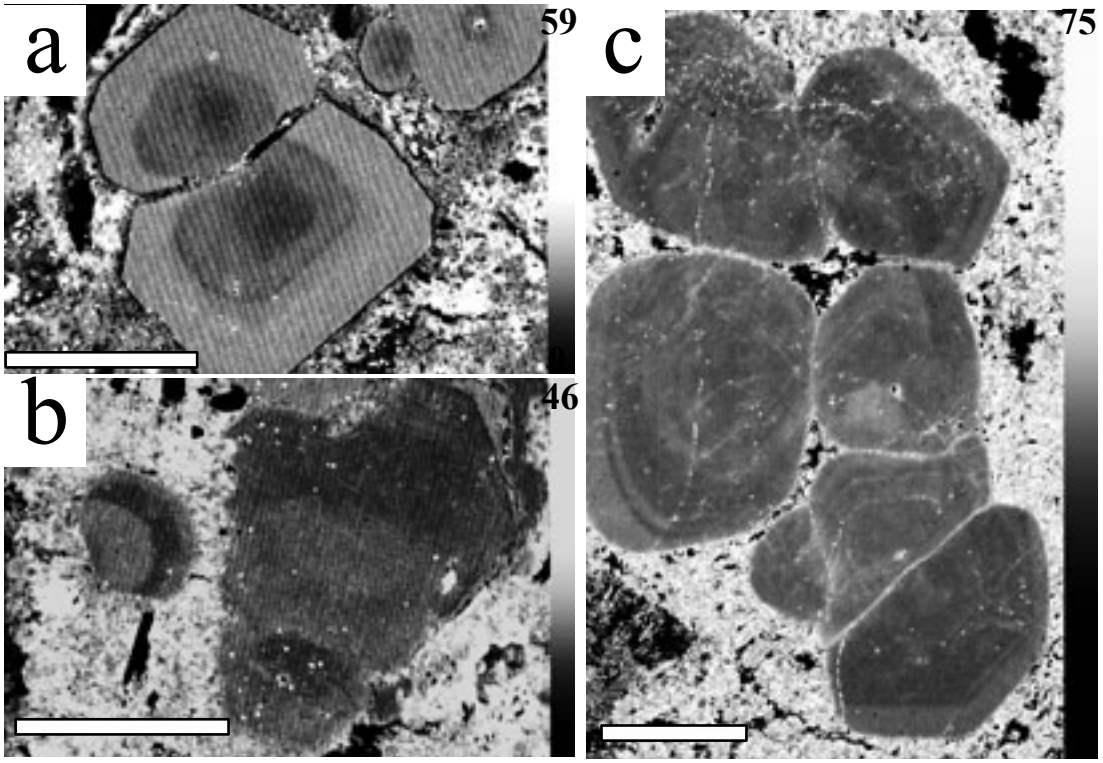

Figure 4-33 Distribution of 2.05 eV band emission in quartz grains
(a) - DC-DP-1 and (b) - DC-DLP-1, Rio Blanco (c) - 109647, Climax.Hyperspectral CL maps. Scale bars are 500 µm.

Only few of the healed fractures are visible in the 2.72 eV band map (Fig 4-29b).

Within sample 109647 the zones of low 1.93 eV bad shows higher intensity in the inner rim zone, where it is correlated with high 2.72 eV intensity (Fig 4-29c). Unlike 2.72 eV emission, 1.93 eV emission show almost no oscillatory layers in the inner rim zone. It shows marble-like texture due to numerous irregular healed fractures (Fig 4-30). Such fractures are different in 1.93 eV intensities ranging from extremely high to very low 1.93 eV emission. This marble-like texture is not visible in the 2.72 eV intensity map.

Transitions between the core and the rim zones are diffusional. The core is intermediate in 1.93 eV intensity with several distinct layers and irregular patches of high 1.93 eV intensity (Fig 4-29c), which are not correlated with 2.72 eV emission (Fig 4-27c). The inner core zones have lower 1.93 eV intensity than the outer core zones.

The healed fractures and star-like patches of secondary quartz visible in 2.72 eV map show extremely high 1.93 eV band intensity (Fig 4-29c).

4.4.4. Correlation between 1.93 eV emission and Al content

Electron microprobe point analyses showed a strong negative correlation between 1.93 eV intensity and Al content (Fig 4-31a). Analyses display that the quartz likely contain microinclusions (Al spikes on Fig 4-31a). A line of best fit (without Al content in spikes) has a R^2 =0.8558 (Fig 4-31b). A comparison of Al with Ti distribution was made on a base of 2.72 and 1.93 eV emission maps, which showed that:

High Al concentrations in some areas are positively correlated with high Ti content (areas '1' in Fig 4-32). Other areas are negatively correlated, for example, the inner core in sample DC-DLP-1 has lowest Ti concentrations and the highest Al content (areas '2' in Fig 4-32b). Another example of negative correlation between Al and Ti content is tiny zones in sample 109647, which have the lowest Al and the highest Ti concentrations (areas '2' in Fig 4-32c).

There are also zones which are not correlated in Al and Ti distributions. For example, in sample 109647 the marble-like texture visible in Al distribution is not reflected in Ti distribution map (area '3' in Fig 4-32c). An area within one of the inner cores in sample DC-DP-1 has patchy Al distribution, which is not correlated with Ti distribution (area '3' in Fig 4-32a). Moreover, a narrow high in Al zone crosscuts the boundary between the core and the rim visible in the Ti distribution map (yellow area shown by arrows in Fig 4-32a), thus determining the double zoning. Similar crosscutting relationships between Al and Ti distribution are observed in sample 109647 (Fig 4-32c). Therefore, double zoning is likely to be caused by different distribution of Al and Ti within the samples.

4.4.5. 2.05 eV emission

The fitted 2.05 eV emission map for DC-DP-1 grain shows intermediate 2.05 eV intensity rim zone, lower in 2.05 eV intensity outer core and the lowest 2.05 eV intensity inner core (Fig 4-33a). The core-rim transition is sharp; the transition between the outer and inner core zones is diffusive and similar to that observed in 1.93 eV map.

The 2.05 eV intensity pattern within DC-DPL-1 grain is similar to the 1.93 eV emission pattern, but shows more diffusional transitions (Fig 4-33b). It also displays higher 2.05 eV intensity within outer euhedral oscillatory layers (Fig 4-33b). The irregular pattern visible in 1.93 eV emission map is indistinguishable on 2.05 eV emission map.

Within the quartz from sample 109647 the 2.05 eV intensity pattern is the same as the pattern in 1.93 eV intensity map, but less contrasted and with all transitions

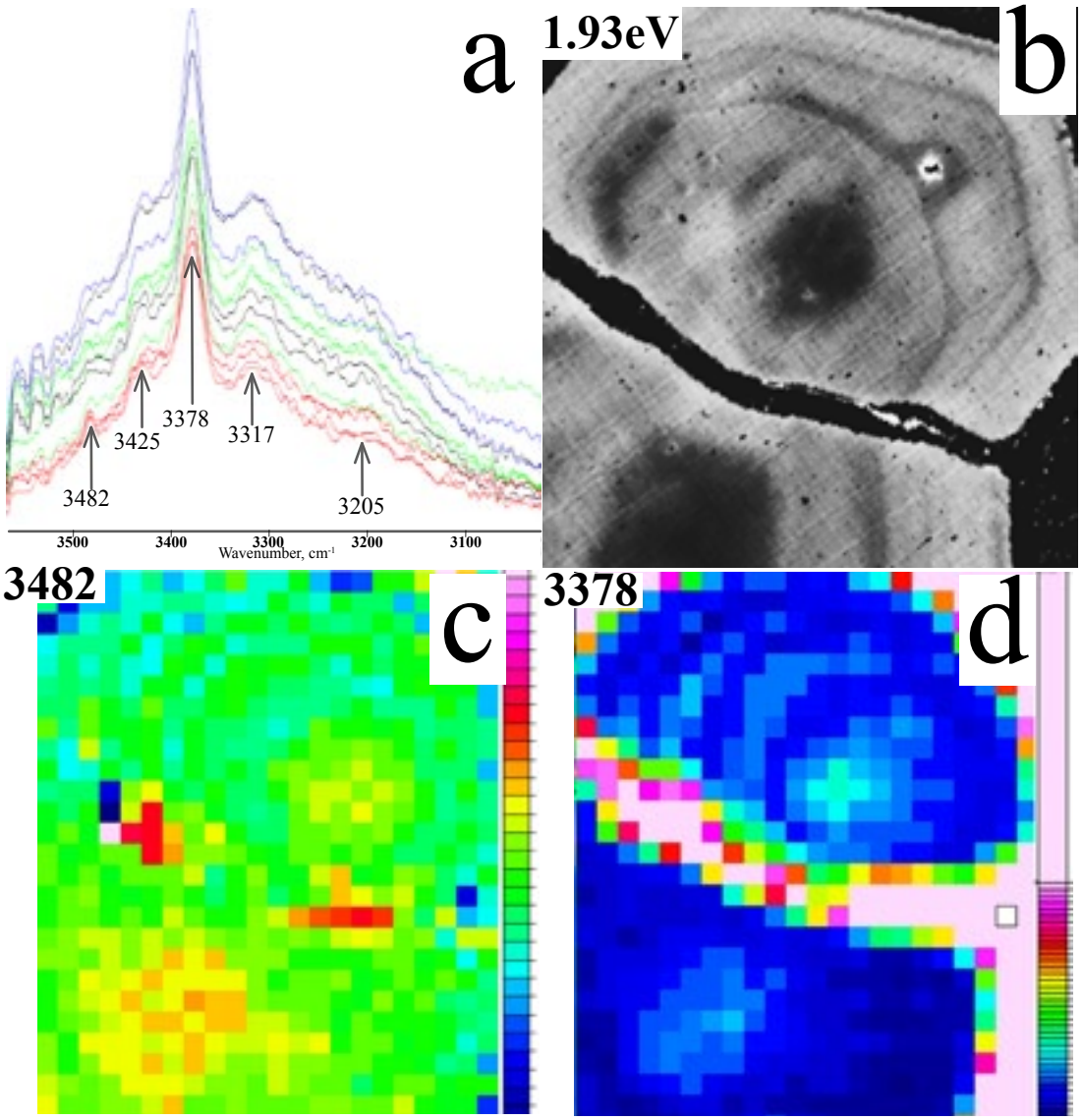

Figure 4-34 Infrared spectroscopy mapping, sample DC-DP-1, Rio Blanco (a) - examples of IR spectra with peaks at 3482, 3425, 3378, 3317 and 3205 cm-1. (b) - 1.9 eV map showing an area which was mapped by IR spectroscopy. (c) - 3482 cm-1 (Li-OH) map, (d) - 3378 cm-1 (Al-OH) map.

diffusional (Fig 4-33c).

4.5. Infrared spectroscopy

Two types of absorption were observed in the IR spectra within the grain DC-DP-1: the sharp absorption bands at 3482 and 3378 cm^{-1} and the broad absorption bands at 3425, 3317 and 3205 cm^{-1} (Fig 4-34a). The 3378 and 3482 cm^{-1} peaks are the most intensive. Distribution maps of those bands are shown in Figure 4-34 (c) and (d). Intensities of the both absorption bands are the highest in the inner cores and the

lowest in the rim, which is negatively correlated with 1.93 eV distribution map.

Bands at 3425, 3317 and 3205 show very low intensity and have no distribution patterns.

4.6. Summary

Quartz eyes and their clusters show significant diversity in shapes and CL patterns within a single thin section. Internal textures include different sequences of CL bands of different intensity; quartz eyes often demonstrate a distinct CL-dark core and a CL-bright rim. The main trace elements are Ti and Al, which together with crystal defects define CL intensity. Cores are either depleted in Al and Ti or depleted in Ti and enriched in Al. Bright rims are enriched in Ti. Al and Fe often display enrichment towards a crystal margins. Secondary quartz heals fractures and often contain higher Al. Some trace elements are concentrated in secondary quartz and only within quartz eyes (such as Zn in sample 092-29700). Groundmass quartz demonstrate more intense CL emission than quartz rims, which in turn are more intense than cores.

Hyperspectral CL mapping revealed three peaks responsible for the total CL emission: 1.93 eV, 2.05 eV and 2.72 eV. The first two peaks are intrinsic, i.e. caused by host Si and O atoms. The 2.72 eV peak is caused by Ti impurities in quartz. Al itself does not cause any intensive luminescence, but significantly suppresses 1.93 eV emission. As a result of such quenching the total emission is extremely weak in samples where intrinsic emission prevails. On the other hand, if extrinsic emission (caused by impurities) is much more intensive than intrinsic one then quenching of 1.93 eV emission is hardly reflected in the total luminescence. This explains why a correlation between Al and CL intensity was not found until now.

Hyperspectral mapping also showed that Al distribution pattern was not correlated with Ti distribution pattern within a single quartz grain: enriched in Ti zones could cross Al-rich zones and some features of Al distribution pattern were not reflected in Ti maps. Moreover, Al showed diffusional distribution in most cases, whereas transitions between different Ti zones are extremely narrow. Sector zoning is often found in quartz eye cores, which is also defined by different distribution of Al and Ti along different faces. According to infrared spectrometry, CL-dark cores show higher density of Al-OH and Li-OH defects. Ti content in attached grains within a single cluster can vary significantly, even in those with the same optical orientation. Al distribution is often patchy.

Quartz eye internal zoning is more similar to agates or hydrothermal quartz than

to quartz phenocrysts from lava samples (from Taupo). Quartz eyes and phenocrysts have distinctly different growth patterns, secondary features and probably crystal structure, i.e. spots exposed to the electron beam are damaged in different ways.

Chapter 5. Inclusions

5.1. What can inclusions tell us?

Fluid and melt inclusions are tiny ‘bottles’ with messages that can help us to constrain the chemistry of magmatic fluids, element partitioning, compositions of hydrothermal fluids and conditions of mineral deposition (Clemens, 2009). Those messages could be crucial for understanding ore forming processes. However, to decode the messages correctly, we should know what these inclusions are now, we also should be sure that they did not change their composition since their entrapment, and that they were representative of the bulk composition of that phase in the system. We also need to know their relationships to a host mineral, i.e. whether they are primary, pseudosecondary or secondary, and whether they were representative of the media from which a host mineral crystallised. Primary inclusions are trapped during crystallisation of a host mineral; pseudosecondary inclusions form as a result of healing fractures during mineral growth, and secondary inclusions may be trapped at some later time during healing of secondary fractures (Roedder, 1984). A textural criterion for primary origin is the inclusions’ spatial distribution, e.g. isolated occurrence or within a three-dimensional inclusion group, along a growth zone or a twin plane (Roedder, 1984). Inclusions that occur along fractures, which are visibly terminated at a growth plane within a crystal, are considered pseudosecondary (Roedder, 1984). Secondary inclusion trails usually crosscut minerals boundaries. Detailed description of empirical criteria for primary, pseudosecondary and secondary origin can be found in Roedder (1984, pp 43-45).

Before inclusion study we also need to establish the inclusions’ relation to the process of interest (in our case formation of a deposit). It is commonly assumed that primary and pseudosecondary inclusions in transparent gangue minerals associated with ore minerals (often sulphides) are related to the ore-forming fluid from which the precipitation of ore minerals occurs (Roedder, 1984; Wilkinson, 2001). In this case study of primary or pseudosecondary inclusions, which were trapped during growth of a host mineral at the time of formation of a ore deposit, and which represented the bulk fluid (and/or melt) at that time, can provide us with necessary information to constrain models for formation of deposits of the type. Unfortunately, it is almost impossible to obtain data that proves all of those points. Instead, assumptions are usually made suggesting that all the conditions mentioned above are fulfilled.

Inclusions that are assumed to be related to the process of interest do not

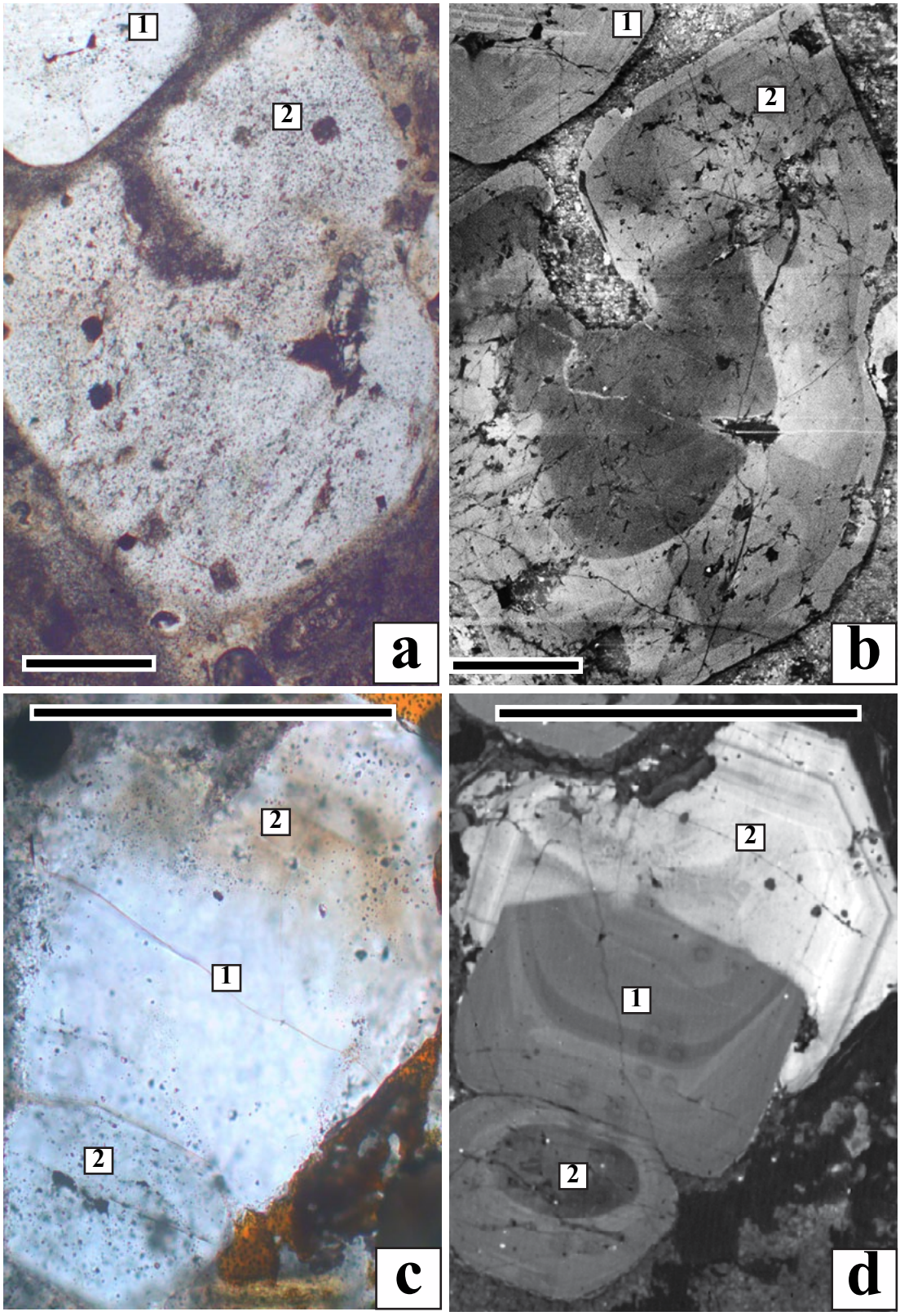

Figure 5-1 Distribution of fluid inclusions in adjacent quartz eyes and different quartz eye zones

(a, c) - optical images, (b, d) - CL images. 1 - areas with a few fluid inclusions, 2 - areas with abundant fluid inclusions. Scale bars are 500µm. (a, b)

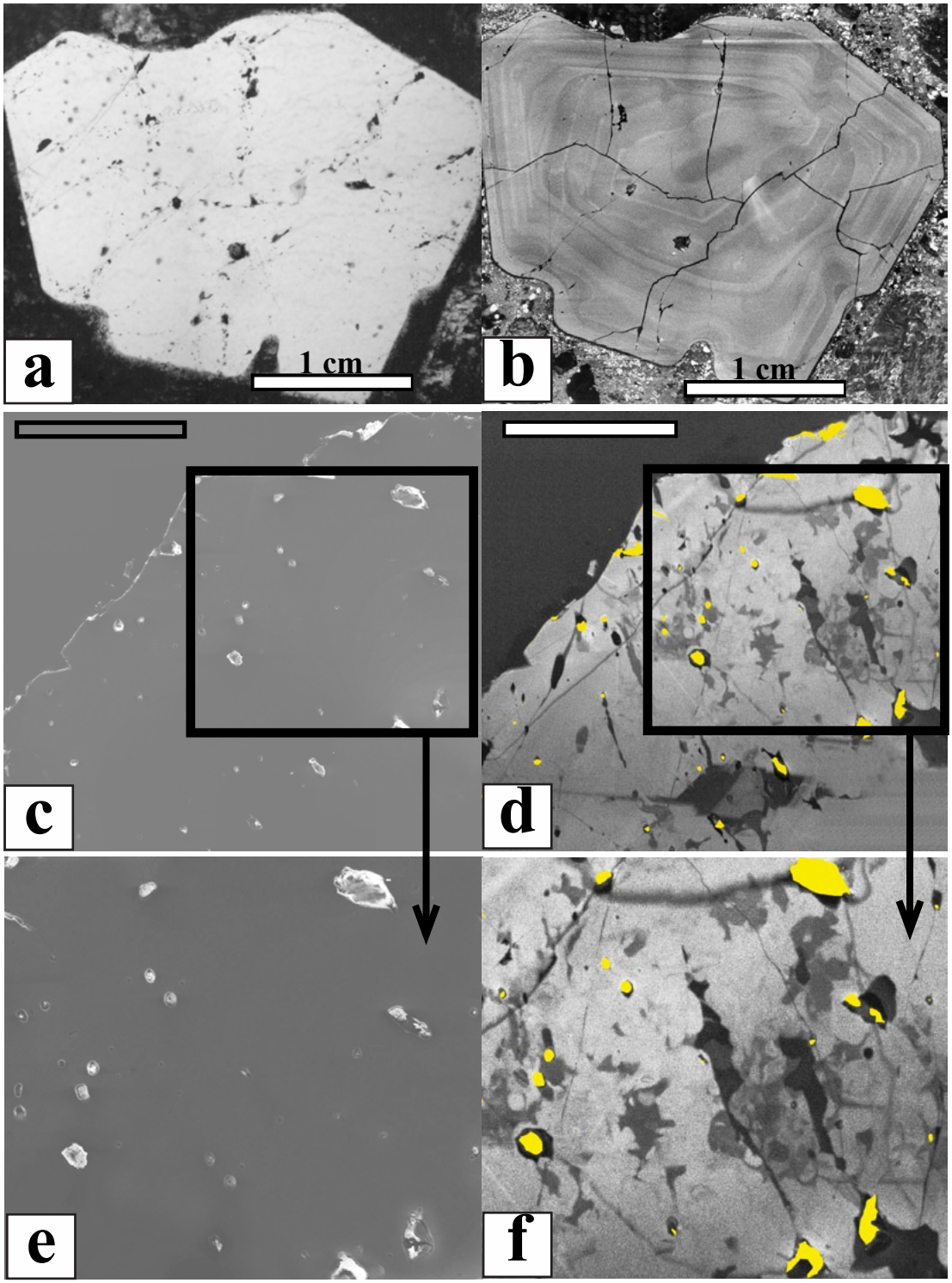

Figure 5-2 Distribution of inclusions according CL

(a, b) - quartz grain from Rio Blanco (DC-DP-1) in transmitted light (a) and a CL image (b); note that dark secondary quartz in (b) correlates with fluid inclusion trails in (a). (c, d) - quartz grain from Batu Hijau (SBD-69). (c) - SE image, bright spots are exposed inclusions. (d) - CL image, yellow spots mark exposed inclusions. (e, f) - are enlarged areas from (c) and (d). Note that there are thick halos of different generation of secondary quartz around fluid inclusions. Scale bars are 200µm.

necessarily reflect conditions of the host mineral growth, since their composition may change over time due to various post-entrapment modifications as a result of fluid re-equilibration in new confining conditions (Audetat and Gunther, 1999; Qin et al., 1992; Roedder, 1984; Van den Kerkhof and Hein, 2001; Vityk and Bodnar, 1995; Wilkinson, 2001). Post-entrapment modifications include:

- Crystallisation on inclusion walls;
- Leakage of a fluid in or out;
- Diffusion of fluid components (e.g. hydrogen or H_2O diffusion in or out inclusion);
- Change in inclusion shapes (for instance as a result of decrepitation or necking down);
- Migration away from pseudosecondary trails (which infer the recrystallisation of the host mineral, water loss, and thus often increase in salinity),
- Precipitation of daughter phases.

Generally, fluid inclusion techniques are used to characterise composition of the fluid that participated in precipitation (crystallisation) of host minerals, and to determine the temperature (T_t) and the pressure (P_t) during inclusion entrapment. In cases where fluid inclusions are studied in minerals of ore deposits, the parameters of ore formation can be determined. Fluid inclusion data usually include phase description (such as types, sizes and numbers) and temperatures of phase transitions (such as from liquid to vapour or from crystal to liquid) that depend on P-V-T-X (Pressure-Volume-Temperature-Composition) properties of fluids. Interpretation of the phase transition temperatures is based on experimental data, and only possible if the following basic principles and underlying assumptions are applied (Roedder, 1984):

1. Distinctions between trapping of homogeneous vs heterogeneous fluid are made. The term ‘homogeneous’ implies that the fluid existed as a single phase during the entrapment. The term ‘heterogeneous’ means that fluid either contained two or more immiscible fluids or solid particles were present in a fluid. By ‘immiscibility’ I imply any combination of different phases, which coexist in equilibrium in a fluid (of different or the same composition). If homogeneous fluid was trapped than the temperature of entrapment (T_t) can be estimated from the homogenisation temperature (T_h) only if the effect of pressure is either insignificant or known. Where two immiscible fluids are present in the same inclusions, and separate inclusions of each fluid individually were trapped

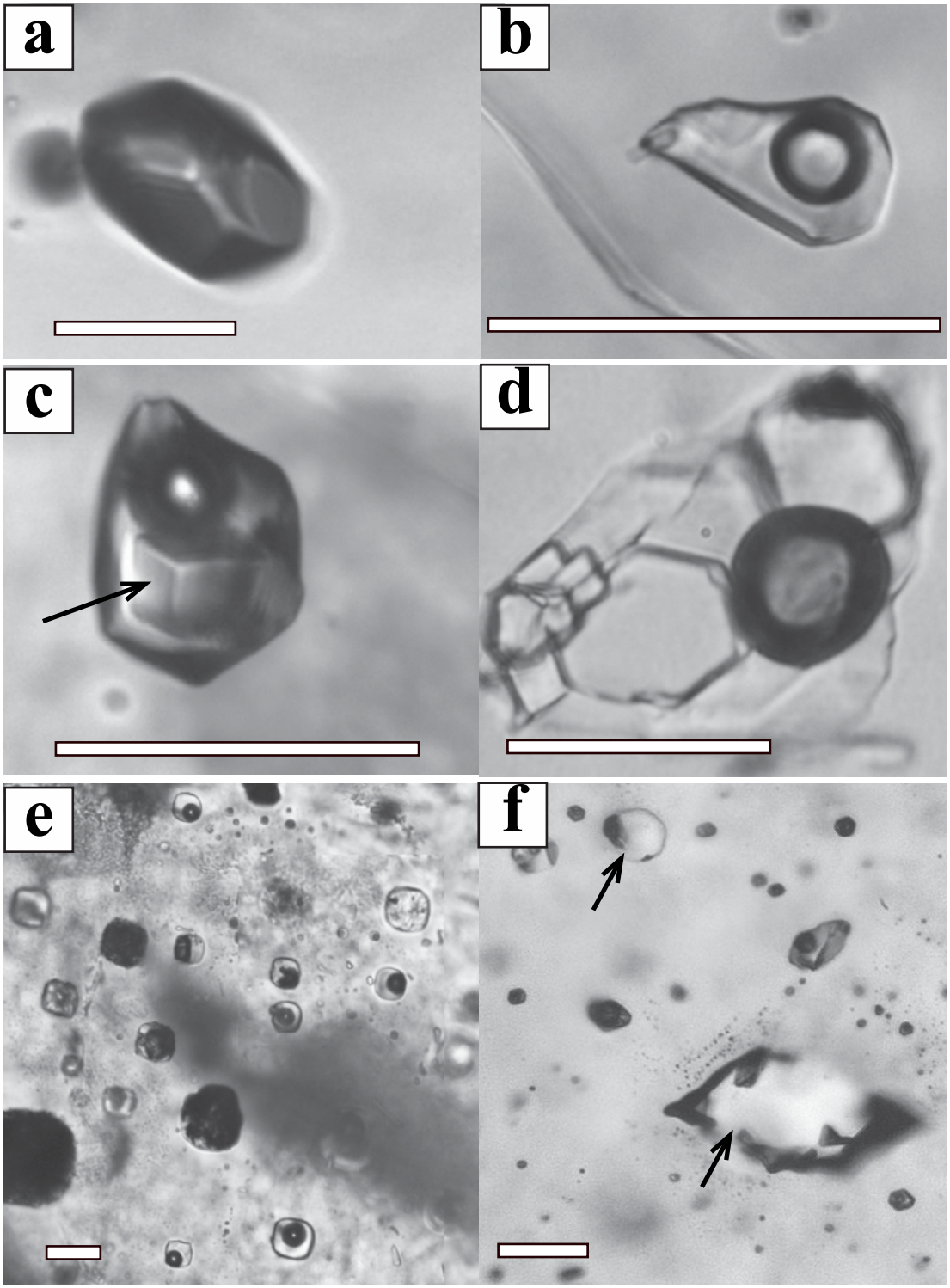

Figure 5-3 Types of inclusions in quartz in the studied samples

(a) – type 1, vapour inclusion from 138-2 (Batu Hijau), (b) – type 2, two-phase fluid inclusion from 109646 (Climax), (c) – type 3, halite-saturated fluid inclusion from SBD-69 (Batu Hijau, halite cube is shown by arrow), (d) – type 4, multiphase fluid inclusion from 138-2 (Batu Hijau), (e) – type 5, melt inclusions from 9902 (Rio Blanco); notice some of inclusions are crystalline and others are glassy with different gas bubble/melt volume ratios, (f) - type 6, mineral (K-Feldspar) inclusions (shown by arrows) decorated with a shrinkage bubble (or bubbles) from 109645 (Climax). Scale bars are 10 μm.

simultaneously, each with known P-V-T properties, then both T_t and P_t can be determined from homogenisation temperature. Finally, if a boiling fluid was trapped, then $T_t = T_h$ and no pressure correction is needed. Entrapment of a boiling fluid is assumed when liquid-rich end-member inclusions homogenise in liquid phase at the same temperature as vapour-rich end-member inclusions homogenise by evapouration of liquid;

2. Composition of inclusions is known and experimental data on thermodynamic properties (P-V-T) of the fluid of that composition are available. The exception is inclusions trapped along the boiling curve: in this case temperature of entrapment is the homogenisation temperature and does not depend on fluid composition;

3. Post-entrapment modifications did not occur, neither change in inclusions' volumes nor in their compositions.

Fluid inclusion techniques have been applied to porphyry-copper deposits for several decades (Bodnar, 1995; Eastoe, 1978; Roedder, 1971, 1984; Wilkinson, 2001). Data from numerous fluid inclusion studies provided most of constraints on the existing model for formation of porphyry-type deposits (see the chapter 1 'Introduction').

5.2. Fluid inclusion distribution

Fluid inclusions in the quartz eyes from the studied samples are usually abundant, often giving quartz grains a spongy texture (Table 5-1 and Fig 5-1a). Only in rare cases do quartz grains lack inclusions. Distribution of inclusions within a single sample, e.g. between different quartz eyes or different zones in a single quartz eye, is usually uniform. However, in some cases adjacent quartz eyes display different inclusion distribution, often related to different cathodoluminescence patterns or zones. As it is shown in Figure 5-1 (a, b) the crystal with oscillatory zoning (labelled '1') contains few fluid inclusions, whereas the adjacent quartz eye (labelled '2') with compositional zoning is sponge-textured due to the abundance fluid inclusions. Other crystals showed different distribution of fluid inclusions in different CL zones. For example, in Figure 5-1 (c, d) almost no fluid inclusions were found associated with the zone showing dull cathodoluminescence (labelled '1'), whereas both bright and dark in CL zones contain abundant inclusions (labelled '2').

Cathodoluminescence of quartz eyes revealed that fluid inclusion trails always correspond to healed fractures in CL images (Fig 5-2). CL images of sponge-textured quartz eyes showed that:

Exposed inclusions (yellow areas in Fig 5-2d, f) are connected to each other by tiny fractures healed with secondary (CL-dark) quartz. Inclusions, which localised within an intersection of healed fractures are often vapour (Fig 5-4a, b);

Exposed inclusions often show halos of secondary quartz around them (Fig 5-2d, f);

In some cases inclusion halos contain several generation of secondary quartz (Fig 5-2f).

Since all of the exposed inclusions showed a correlation with secondary quartz and were texturally related to fractures, the same correlation was assumed for inclusions under a surface. Thus, a secondary or pseudosecondary origin was established for the fluid inclusions.

5.3. General description of inclusions: size, phases, volume fractions

Six main inclusion types were observed in the studied samples. Using my nomenclature these are:

Type 1 Salt undersaturated single-phase inclusions (usually vapour), typically dark, 5 to 25 μm globular or sometimes negative crystal shaped (Fig 5-3a).

Type 2 Salt undersaturated two-phase fluid inclusions (5-25 μm) with variable volume fractions, globular or sometimes negative crystal shaped (Fig 5-3b).

Type 3 Salt-saturated fluid inclusions (± hematite) usually 10-30 μm often with negative crystal shape (Fig 5-3c).

Type 4 Multiphase crystal-rich inclusions (with a shrinkage bubble) 10-30 μm inclusions (Fig 5-3d).

Type 5 Melt inclusions in this study are mainly crystalline, though both glassy and crystalline were also found in two samples from Rio Blanco (9902 and CA33). Glassy melt inclusions often contain gas bubble with various gas/silicate phase ratios (Fig 5-3e). Crystalline melt inclusions are often larger than fluid inclusions (10-80 μm) and dark in transmitted light. Silicate melt inclusions are usually observed along growth zones or in three-dimensional clusters (Table 5-3). Silicate melt inclusions are the only varieties which are distributed along growth zones in quartz grains; they are also distributed along healed fractures

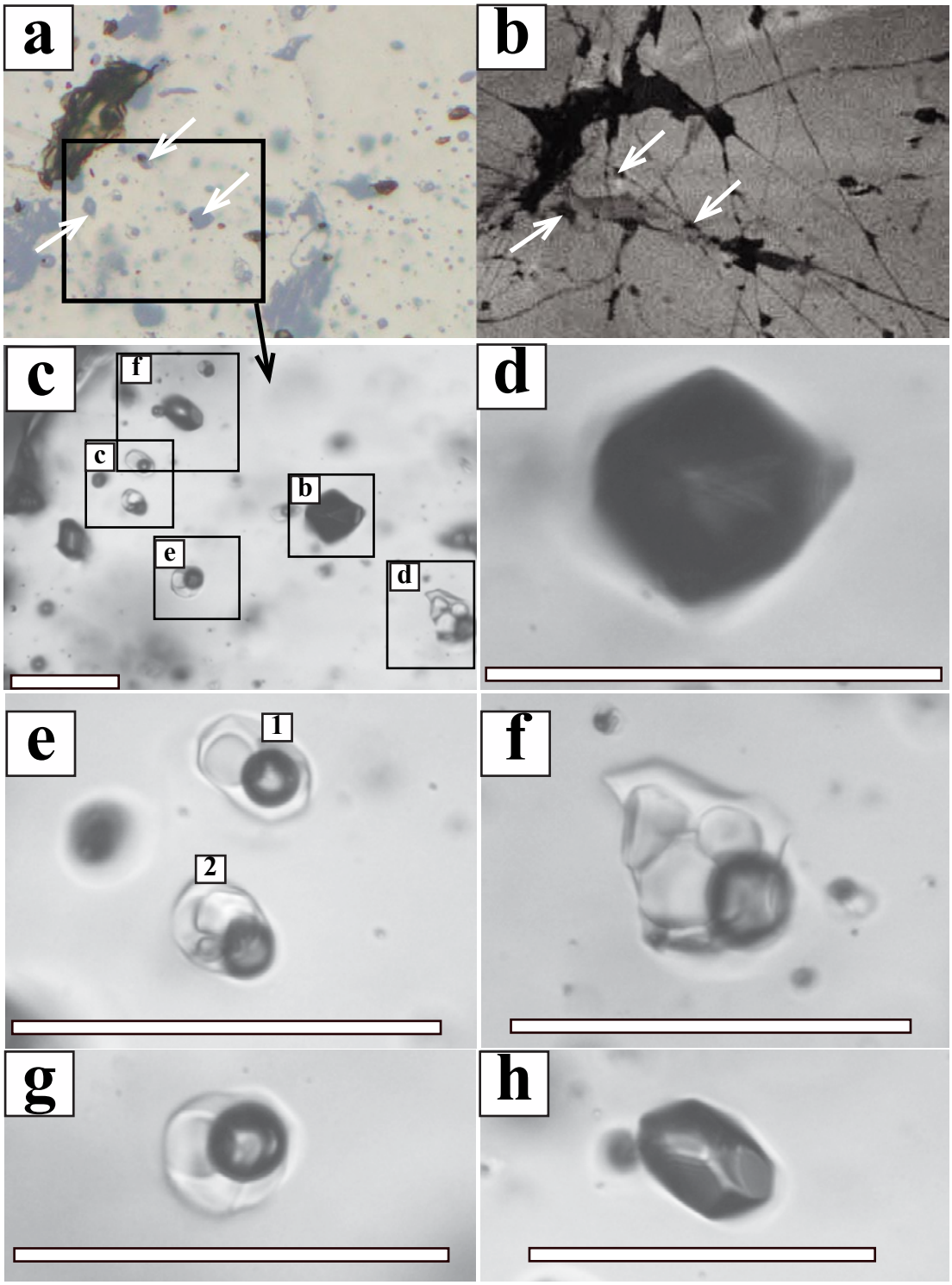

Figure 5-4 Distribution and diversity of fluid inclusions

Sample 138-2 from Batu Hijau. (a) - an optical image, partly crossed polars; dark areas are surface defects, such as exposed fluid inclusions, grey spots are fluid inclusions under the surface. The rectangle - area shown in (c). (b) - the same area as in (a), CL image. Arrows show vapour inclusions (a) and corresponding surface areas (b). (c) - a group of fluid inclusions, general view, rectangles are areas enlarged in (d-h). Inclusions are: (d, h) - vapour-rich, (e1) - two-phase, (g) - three-phase, (e2) - four-phase, (f) - multiphase. Scale bars are 20 µm.

and in three-dimensional clusters and often associate with fluid inclusions (Fig 5-3).

Type 6 Mineral inclusions (Fig 5-3f). They are often decorated with multiple gas bubbles and occupy the same trails with fluid inclusions. Amoeboid-shaped mineral inclusions with shrinkage bubbles (sometimes numerous) were observed in topaz (Fig 5-6) and sometimes in feldspar (Fig 5-7c). Topaz containing amoeboid inclusions is late: it often occupies interstitial spaces near vein walls (Fig 5-6c) or fills circular embayments in pyrite grains (Fig 5-6a) and fractures. EDS analyses showed inclusions in topaz are quartz or K-feldspar (Fig 5-6d). Amoeboid quartz inclusions in topaz are often associated with Type 2 inclusions (Fig 5-6d).

Most quartz eyes contain inclusions of different types (Table 5-1). Distribution patterns of inclusions are rather complicated: several types of inclusions are usually observed within a single group, or a healed fracture (coeval inclusions) and inclusions of the same type can occur both as three-dimension groups, along growth zones and healed fractures. Diversity of inclusions is illustrated in Figures 5-4 and 5-5. Figure 5-4 shows relationships between different types of fluid inclusion within sample 138-2 from Batu Hijau where vapour-rich inclusions (Fig 5-4b and f), two-phase (Fig 5-4c), three-phase (Fig 5-4e), four-phase (Fig 5-4c) and multiphase inclusions (Fig 5-4d) are observed in a single group. In most samples groups of mixed fluid and melt/mineral inclusions are common. Figure 5-5 shows common associations that were observed. Those associations usually include:

• Two-phase vapour- or liquid-rich inclusions with different gas/liquid ratios (Fig 5-5c, labelled ‘1’).

• Inclusions containing different solid phases and number of phases with varying gas bubble/solid phase ratios (Fig 5-5, labelled ‘2’). Some crystals are silicate phases and have very high birefringence, other phases have low birefringence and refractive indexes close to that of quartz (Fig 5-5a and b). Inclusions with spherical gas bubbles can be next to inclusions with a non-spherical vapour phase (Fig 5-5a). Shapes of mineral phases are often vermicular, adjusted to the shape of inclusion cavities (see a hematite shape in Fig 5-5a).

• Crystalline melt inclusion (Fig 5-5b) and mineral inclusions (Fig 5-5c) with different Al/K/Si ratios (Fig 5-5, labelled ‘3’).

Feldspar-hosted inclusions are strikingly different from quartz eyes-hosted

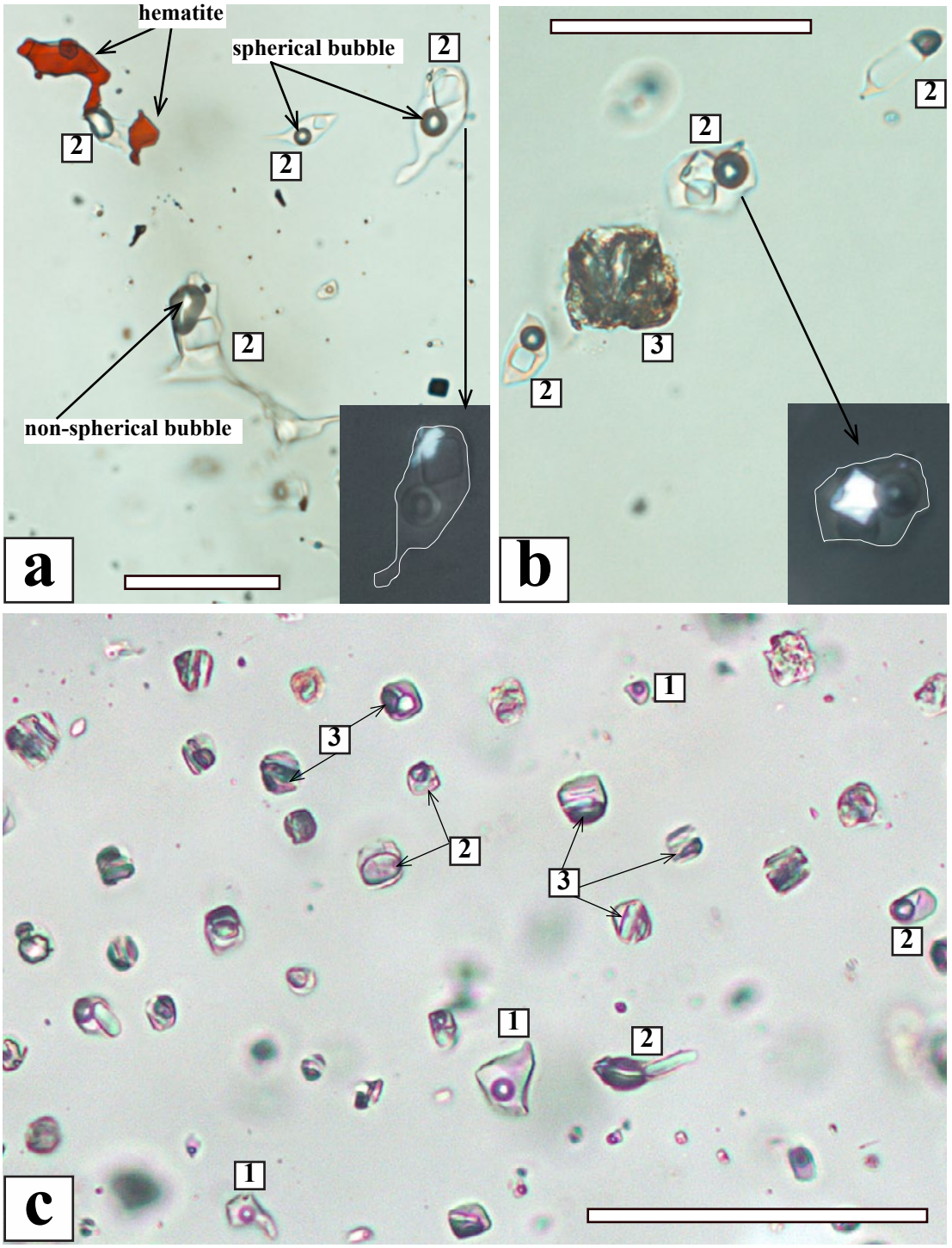

Figure 5-5 Diversity of fluid and melt inclusions within a single quartz eye
(a, b) - inclusions from CA6 (Rio Blanco); (a) – a group of fluid inclusions with different daughter minerals and their numbers. Note that hematite crystals (arrowed) have inclusion cavity shape, which points out to in-situ crystallisation. (b) - fluid inclusions of different composition coexisting with crystalline melt inclusion. (c) - sample 109646 (Climax): silicate inclusions with different Al/K/Si ratios (EDS analyses) coexisting with fluid inclusions containing different phases and varying phase ratios. All photographs are in transmitted light except for the insets in (a) and (b) which are in crossed polars. 1-3 - types of inclusions, see text. Scale bars are 20 µm.

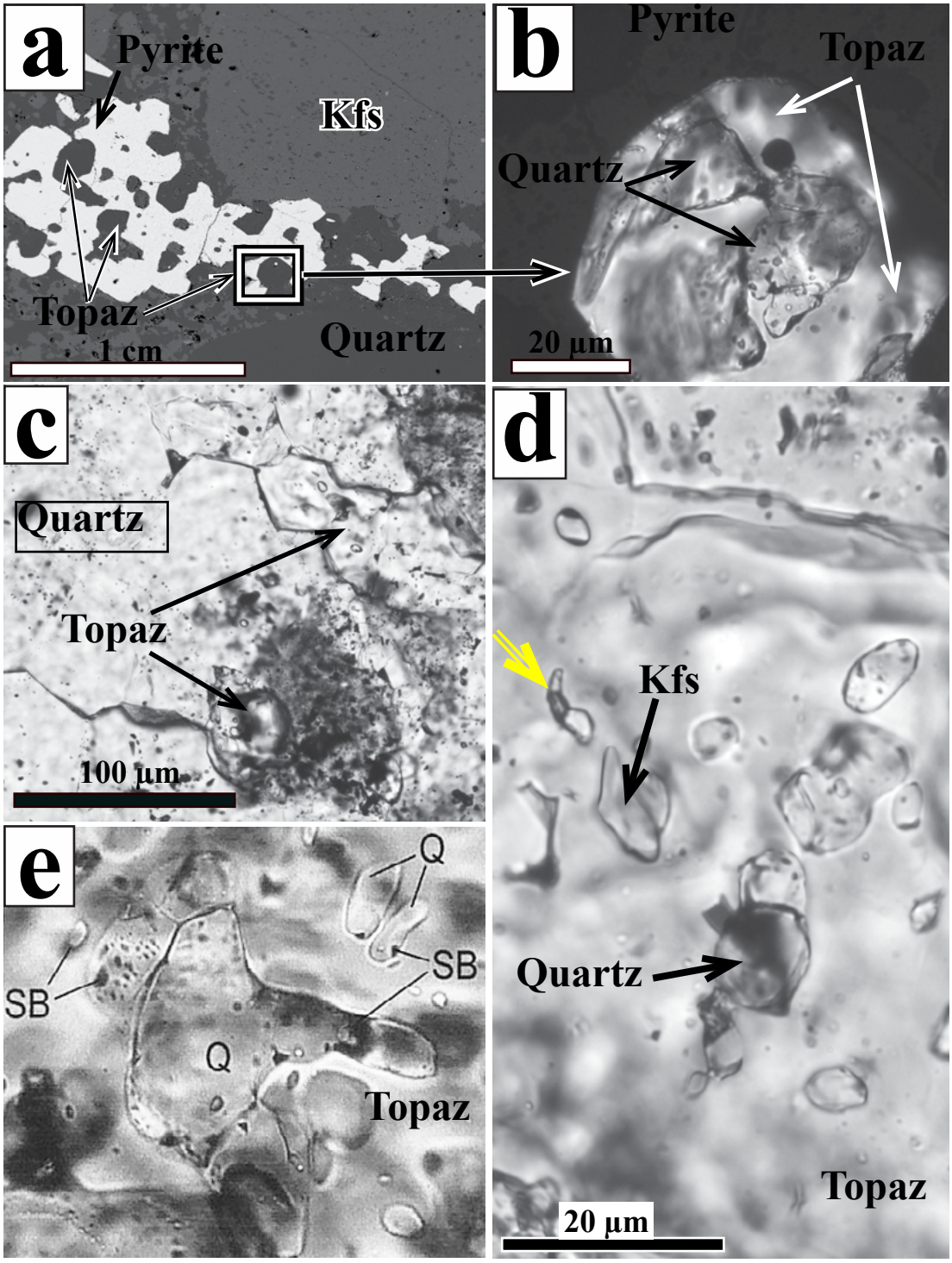

Figure 5-6 Relationships between sulphides, topaz and quartz and inclusions of quartz in topaz

(a) - amoeboid pyrite grain betweeen K-feldspar phenocryst and quartz eye with topaz within its embayments; those topaz grains contain inclusions of quartz (b), samples 109646 from Climax. (c) - Topaz is secondary relatively to quartz occupying interstitial space, sample 109646 from Climax. (d) - quartz and K-feldspar inclusions in topaz, sample 109645. Note that mineral inclusions are sometimes associated with Type 2 fluid inclusions (shown by the yellow arrow). (e) - inclusions of quartz (Q) with multiple shrinkage bubbles (SB) in topaz from Hensbarrow greisen (from Williamson, 1997).

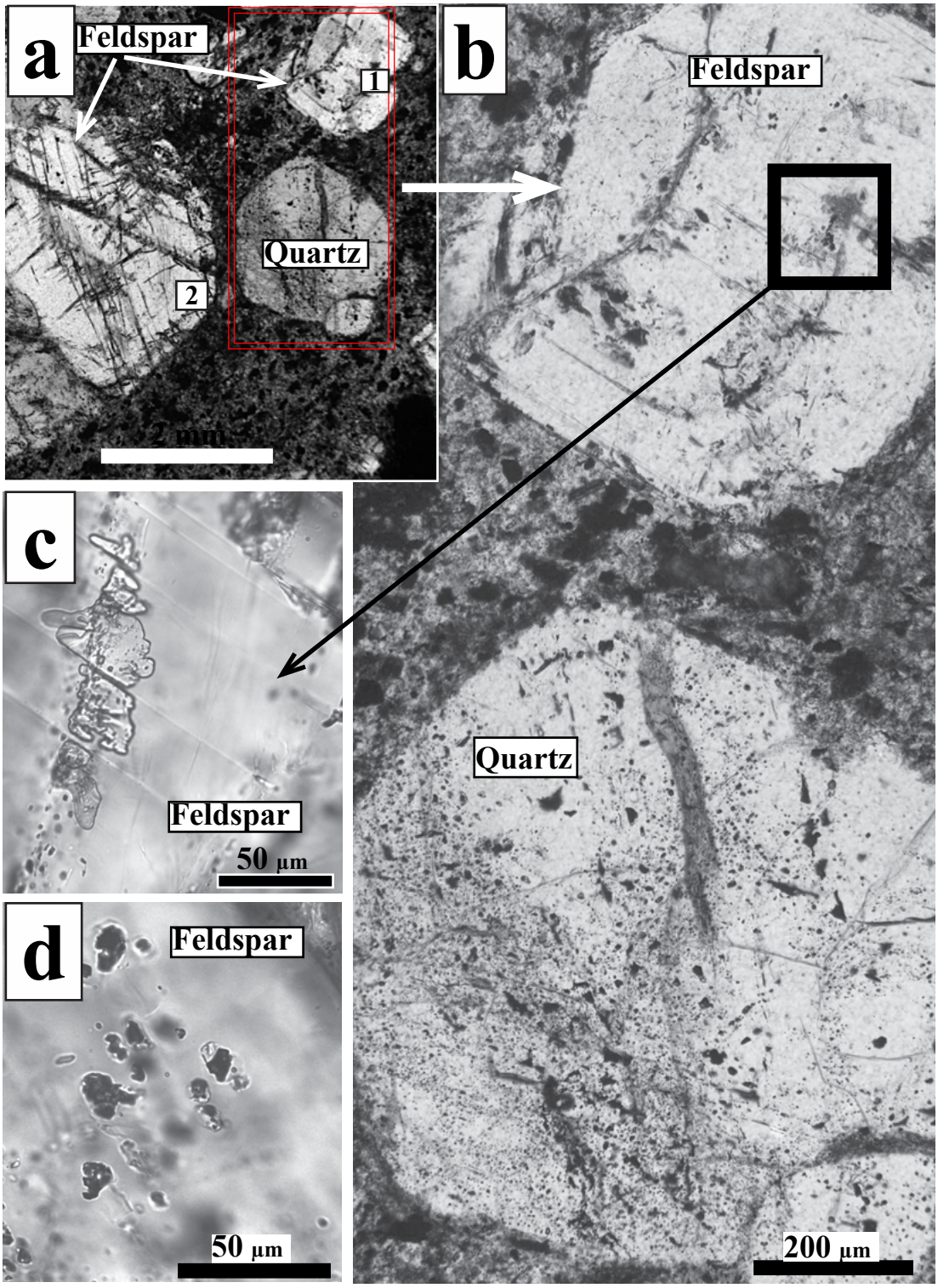

Figure 5-7 Inclusions in quartz and feldspar

Sample SBD-69, Batu Hijau, showing two feldspar grains (1 and 2) and a quartz eye (a). The inset in (a) is enlarged in (b), note that quartz grain is sponge-textured because of the abundance of inclusions whereas feldspars are almost inclusion-free, there are only secondary bleb-like inclusions (1) shown in details in (c). Feldspar (2) contains only melt inclusions both primary localised as a group, and secondary localised along a fracture (d).

inclusions (Fig 5-7). Quartz is often sponge-textured due to the abundance of fluid inclusions, whereas adjacent feldspar crystals contain primary and secondary melt inclusions and in some cases amoeboid mineral inclusions (Fig 5-7). Primary melt inclusions are localised as a group; secondary inclusions are distributed along fractures (Fig 5-7d).

5.4. Melt inclusions

Melt inclusions are crystalline except for samples 9902 and CA33 where crystalline melt inclusions are randomly mixed with glassy inclusions (Fig 5-3e). Samples 9902 and CA33 were studied in detail by Davidson (2005, 2001), who found three types of melt inclusions:

• Silicate glass inclusions. They were glassy and negative crystal-shaped (<80 μm) with one or several shrinkage bubbles. The glass contained rare daughter quartz, amphibole crystals, sometimes unidentified crystals and amorphous phases within bubbles. The glass compositions were rhyodacitic-rhyolitic (Table 5-2) and more evolved (higher SiO_2 and K_2O and lower in all other major elements) than the whole-rock compositions.

• Crystalline inclusions (volatile-rich silicate melt) contained translucent crystalline and amorphous aggregates and aqueous fluid. They had similar size and shape to glassy inclusions and coexisted with them in growth planes (Fig 5-8). Crystalline inclusions contained crystals of feldspars, mica, and quartz, with accessory sphalerite, chalcopyrite, Fe oxides and hydroxides, carbonates, and salts (e.g. halite). The feldspar-like daughter phases had a wide range of compositions varying in Ca/Na/K ratios (Table 5-2) on a micron scale. Interstitial liquid and vapour phases within the inclusions of the type were found to be H_2O-rich (darker areas). The solid/liquid ratios appeared to be variable between trapping planes, though they were relatively uniform within a given plane (Fig 5-8). Inclusions of the type often had halos of aqueous vapour-dominated bubbles (<5 μm). Homogenisation experiments with crystalline inclusions failed due to their decrepitation at temperatures around 600°C. Smaller inclusions showed melting at 750° to 800°C, although complete homogenisation was not achieved even at higher temperatures. A composition of partly homogenised silicate glass and representative silicate phases within unheated crystalline inclusions are presented in Table 5-2. Qualitative laser ablation LA-ICP-MS analysis on individual crystalline inclusions revealed the presence of metals (e.g. Cu, Zn, Pb, Sb, Ag, see Figure 5-9). Copper was attributed to interstitial aqueous phase. Boron concentrations were well above the detection limits and correlated well

Table 5-1 Main characteristics of fluid and melt inclusions in the studied samples

Locality	Sample	Abundancy of inclusions	Distribution of inclusions within quartz eyes	Types of inclusions	Coeval inclusions	Inclusion size, μm
Antapacay	334-53250	abundant	Healed fractures, three-dimension groups	1-5	1+2+4+5, 1+2+3	5-25
	092-29700	very abundant*	Three-dimension groups, growth zones, healed fractures	1-5	2+3+4, 3+4, 1+2, 2+4, 1+4, 1+2+5	5-25
Rio Blanco	CA6	common	MI along growth zones, FI along healed fractures	2-5	2+3+4+5	10-40
	CA8	common	MI along growth zones, FI along healed fractures and in three-dimension groups	2-6	2, 2+5	5-30
	CA33	common	MI in three-dimension groups	5	5	40-80
	9902	common	MI in three-dimension groups and along growth zones	5, 1	5, 1	15-50
	G1	very abundant*	Three-dimension groups and healed fractures	1-5	1+2+ 3+4+5	5-40
	G2	abundant	MI in three-dimension groups and along growth zones FI along healed fractures	1, 2, 5	1,2,5	5-40
	599-2	common	MI in three-dimension groups and along healed fractures, FI along healed fractures	1-3, 5, 6	1+2, 1+2+3, 3+5, 6	10-40
	599-5	common	FI and MI along healed fractures	1-6	1+2+3, 3+4, 5, 6	10-40
Climax	109643	Abundant, some areas within grains are very abundant*	FI and MI along healed fractures, rare in three-dimension groups	1-3, 5, 6	1+2+3+5, 6+1	5-25
	109644	abundant	FI and MI along healed fractures, rare in three-dimension groups	1, 2, 5, 6	1+2+5, 6	5-25
	109645	Abundant, some areas are very abundant*	FI in three-dimension groups and along healed fractures	2,3,6	2+3, 6+2	5-15
Climax	109646	Abundant, some areas are very abundant*	FI and MI along healed fractures	2, 3, 5, 6	2+3+5, 6+2	5-25
Panguna	109607	common	MI along growth zones and in three-dimension groups, FI along healed fractures	2, 3, 4, 5	2+3+4, 5	10-20
	109611	common	Healed fractures and three-dimension groups	1-5	1+2+3 +4+5	5-25

Locality	Sample	Abundancy of inclusions	Distribution of inclusions within quartz eyes	Types of inclusions	Coeval inclusions	Inclusion size, µm
Batu Hijau	138.2	very abundant*	Three-dimension groups and along healed fractures	1-5	1+2+3 +4+5	10-50
	SBD-69	very abundant*	Healed fractures, three-dimension groups, growth zones	1-5	1+2+3+4, 1+4+5	10-25
	SRD-02	abundant	Healed fractures	1, 3, 4	1+3+4	5-15

FI – fluid inclusions
MI – melt inclusions
1 – halite undersaturated one-phase (vapour) inclusions
2 – halite undersaturated two-phase inclusions (liquid + vapour with different volume fractions)
3 – halite-saturated inclusions (±hematite)
4 – multiphase liquid-rich inclusions (with a shrinkage bubble)
5 – silicate melt inclusions
6 – mineral inclusions often with a gas bubble
* - sponge-textured quartz grains.

Table 5-2 Chemical analyses of Rio Blanco rhyolites and inclusions hosted in quartz, after Davidson (2001)

	9902,whole rock analyses	Glass type 1	Glass type 2	Glass type 3	Individual silicate phases in type 2 inclisions		
SiO_2	70.48	73.67	65.29	74.01	64.19	69.98	68.61
TiO_2	0.19	0.06	0.13	0.05	0.00	0.00	0.02
Al_2O_3	15.79	13.41	18.52	13.33	18.34	18.04	18.97
FeO	1.25	0.16	0.47	0.06	0.04	0.10	0.03
MnO	0.05	0.03	0.07	0.04	0.01	0.05	0.00
MgO	0.47	0.01	0.16	0.01	0.00	0.01	0.00
CaO	2.03	0.50	1.14	0.58	0.00	4.20	0.46
Na_2O	4.79	3.56	5.07	4.47	0.82	2.46	10.46
K_2O	2.98	4.50	5.53	3.67	15.87	3.39	0.15
P_2O_5	0.07	0.02	0.00	0.01	n.d.	n.d.	n.d.
Cl	n.d.	0.05	0.15	0.10	n.d.	n.d.	n.d.
Total	95.13	96.27	96.53	96.33	99.27	98.23	98.70

Table 5-3 Microprobe analyses of melt inclusions from sample SBD-69 (Batu Hijau)

	MI-2-1	MI-2-2	MI-1-1	MI-1-2	MI-3-1	MI-3-2	MI-4-12
SiO_2	70.9	69.54	73.69	64.71	75.06	75.53	73.55
TiO_2	0.17	0.18	0.11	0.11	0.19	0.21	0.24
Al_2O_3	16.75	17.51	13.73	25.41	14.49	14.28	13
FeO	0.65	0.43	0.39	0.27	0.24	0.22	0.43
MnO	0.07	0.07	0.03	0.08	0.05	0.00	0.06
MgO	0.25	0.23	0.13	0.19	0.11	0.19	0.06
CaO	0.74	0.8	0.34	0.38	0.14	0.1	0.77
Na_2O	3.61	3.35	4.52	2.98	5.42	4.74	4.94
K_2O	4.4	3.54	3.63	2.97	3.65	4.03	3.81
P_2O_5	0.00	0.07	0.00	0.00	0.01	0.03	0.01
Cl	0.22	0.26	0.25	0.19	0.24	0.24	0.22
Total	97.78	95.98	96.81	97.28	99.61	99.58	97.08

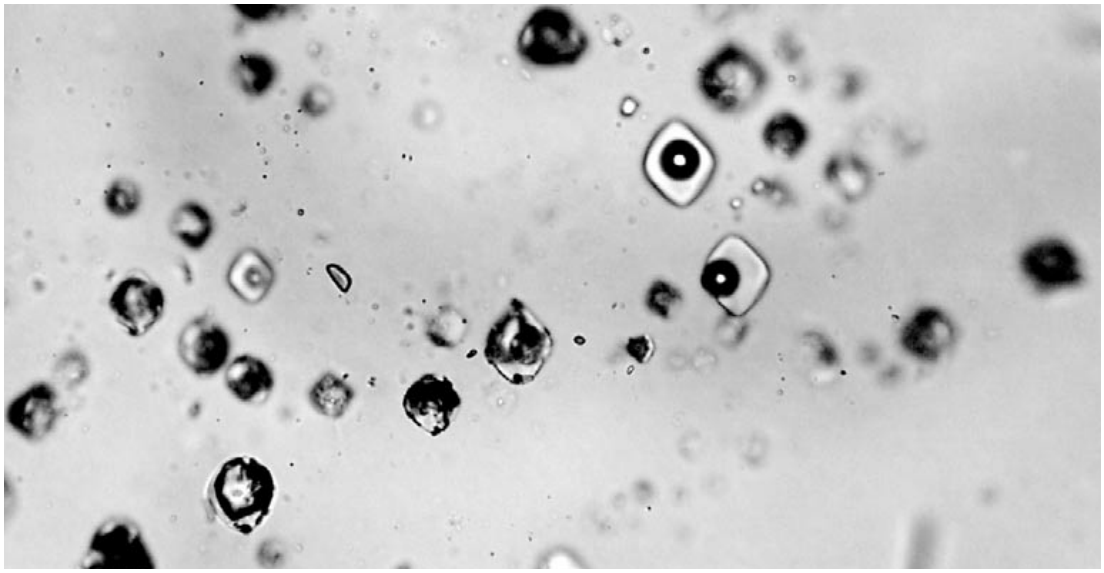

Figure 5-8 Silicate glass, crystallised volatile-rich and composite inclusions coexisting in a single growth planes quartz.
After Davidson (2001). Scale bars are 50 µm.

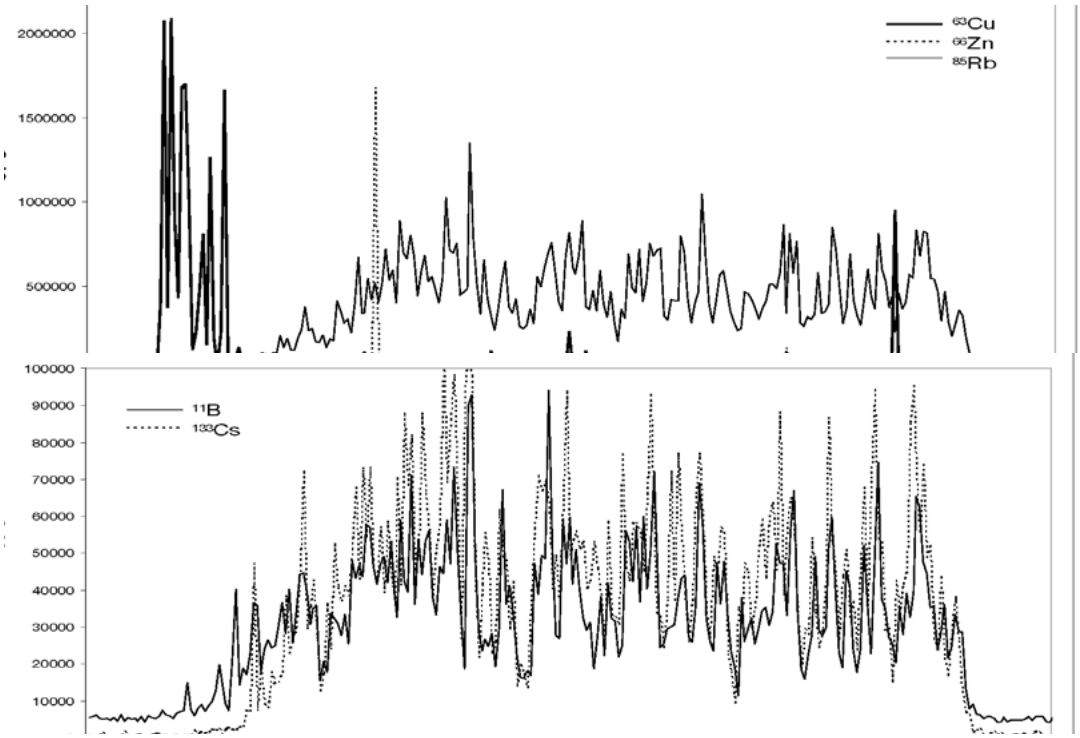

Figure 5-9 Selected LA-ICP-MS data (^{11}B, ^{63}Cu, ^{66}Zn, ^{85}Rb, and ^{133}Cs) from a crystalline inclusion in quartz
This Figure is taken from Davidson (2001): the X-axis shows elapsed time from the beginning of ablation, while the Y-axis shows the spectrometer signal for each mass in counts per second. At ~6 s this particular inclusion was breached by the laser, from ~6 to 75 s material within the inclusion was ablated, at ~75 s the laser burned through the inclusion. Note the correlation between Rb, B, and Cs, the explosive release of Cu as soon as the inclusion was breached, and the presence of minor Zn and Cu spikes possibly corresponding to single micron-sized daughter sulfides.

with the lithophile element abundances (Fig 5-9).

• Composite inclusions contained silicate glass of similar to type 1 inclusions (Table 5-2) and a globular mass of crystalline and amorphous aggregates with aqueous fluid (similar to type 2 inclusions).

Melt inclusions of type 2 were found in sample SBD-69 from Batu Hijau. Quartz crystals containing inclusions were heated at 750°C for 24 hours and then inclusions were analysed by electron microprobe. Large inclusions homogenised partially, small inclusions homogenised completely. Glass compositions of four typical inclusions (MI-2, MI-1, MI-3 and MI-12) are shown in Table 5-3. The average melt composition of type 2 inclusions from Batu Hijau is very similar to that of type 2 inclusions from Rio Blanco (Table 5-2). Analyses also showed that glass composition may vary between different inclusions within a sample.

5.5. Microthermometry

Fluid inclusions from quartz eyes and veins from samples 138-2 (Batu Hijau) and sample G1 (Rio Blanco) were studied by microthermometry. Results are shown in Table 5-4. Microthermometry experiments included temperature measurements, at which phase transitions occurred, not only during heating but also during cooling. Temperatures of phase transitions upon heating are believed to characterise fluid

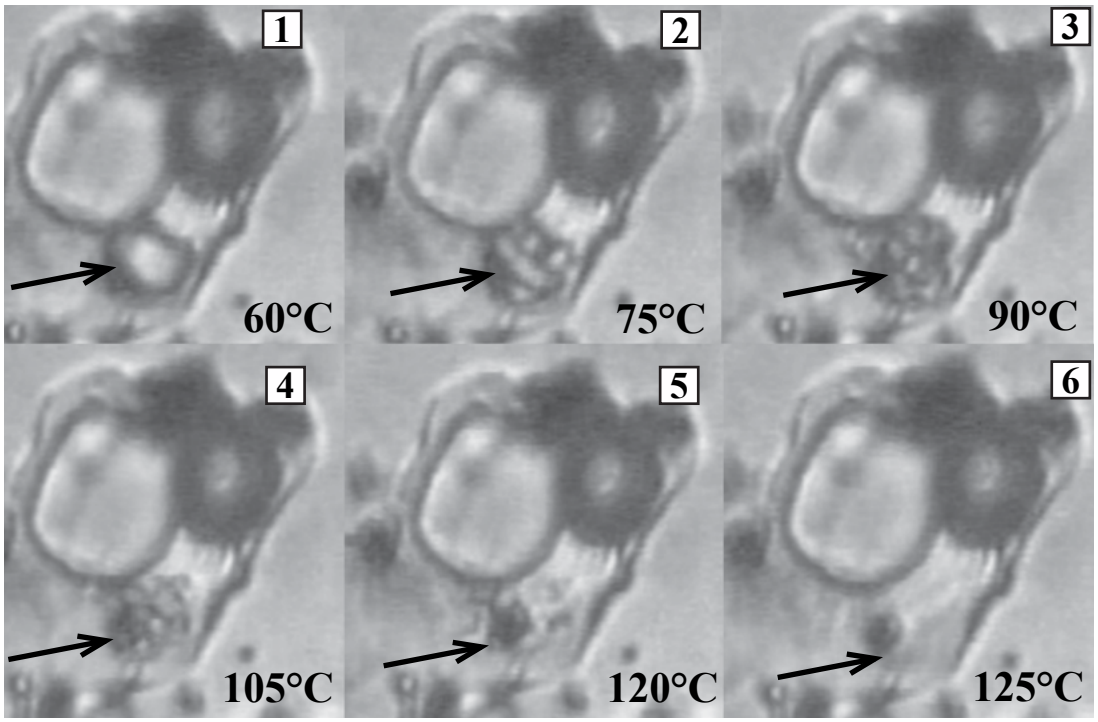

Figure 5-10 Swirling and disappearing of a phase in fluid inclusions Sample 138-2, quartz vein (the phase is shown by an arrow).

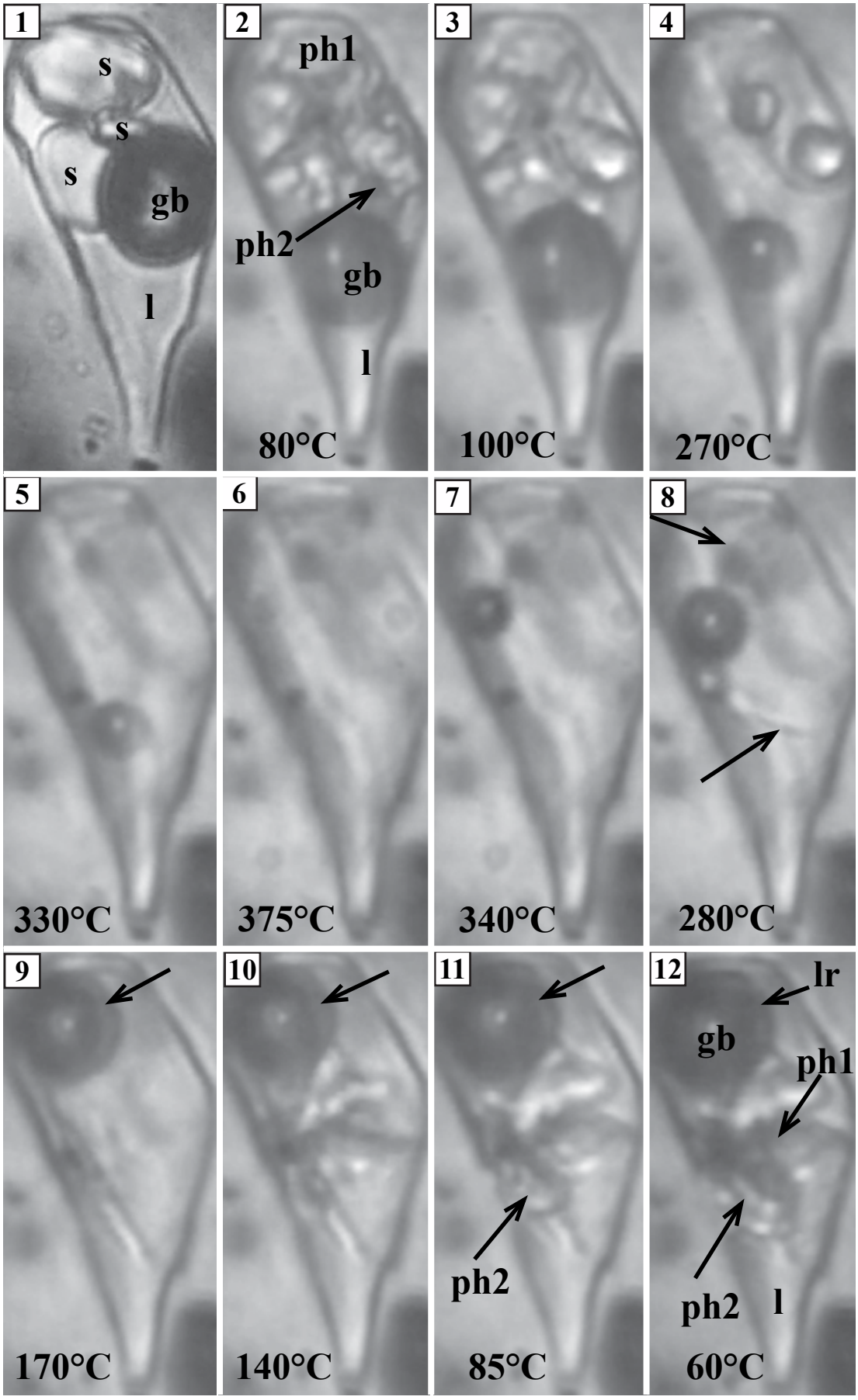
1
s
s
s
gb
l
2
ph1
ph2
gb
l
80°C
3
100°C
4
270°C
5
330°C
6
375°C
7
340°C
8
280°C
9
170°C
10
140°C
11
ph2
85°C
12
lr
gb
ph1
ph2
l
60°C

Figure 5-11 Typical behaviour of fluid inclusions during heating-cooling experiments Sample 138-2, quartz eye, inclusion 2
1 - before heating, 2-6 - heating: 2 - first melting starts (ph2, shown by an arrow), 3 - phase 2 disappears, 4-5 - phase 1 melting, 6 - bubble disappearance. 7-12 - cooling: 7 - bubble appearance, 8 - the first episode of immiscibility occurs, 9 - a liquid rim around bubble appears, 10 - the second episode of immiscibility, 11 - the third episode of immiscibility, 12 - after cooling, the inclusion contains a gas bubble (gb), a liquid rim around gb (lr), a liquid phase (1) and two dense phases (ph2 and ph3) immiscible with the liquid and represented by anhedral mass.

properties, such as temperatures and pressures of entrapment. Temperatures of phase transformations during cooling are not usually measured; fluid phases are often metastable upon cooling, and thus, temperatures of phase transitions are not replicable. However, in natural environments exsolution, transport of ore-forming fluid, and precipitation from it occur during cooling. Thus, our knowledge about fluid behaviour upon decreasing temperatures may contribute significantly to our understanding of ore-forming processes.

5.5.1. Typical fluid behaviour during heating-cooling experiments

Detailed description of two typical experiments on heating and cooling of fluid inclusions from Batu Hijau can be found in the SUPPLEMENTARY section. Four videos of typical behaviour of inclusions from Batu Hijau (sample 138-2) are also in the SUPPLEMENTARY section. In this chapter a summary of all experiments is given.

The first changes during heating typically occurred at low temperatures (60-100 °C) and related to nucleation, growth, swirling and disappearing of one of the phases, which appeared to be solid before heating (Figs 5-10-5-12, see video files 'BH_138-2_vein_inclusion1' and 'BH_138-2_vein_inclusion5' in SUPPLEMENTARY section). Nucleation and growth of this phase was observed in several cases at 20-70°C (Table

Figure 5-12 Typical behaviour of fluid inclusions during heating-cooling experiments Sample 138-2, quartz vein, inclusion 4
1 - before heating, 2-8 - heating: 2 - a gas bubble seems to be surrounded by a liquid (l?), 3 - phase 2 starts melting, 4 - phase 2 disappears, 5 - all the phases are shrinking, 6 - the bubble disappeared, 7 - further shrinking of the phase 1, 8 - phase 1 disappeared. 9-20: cooling. 9 - nothing happened, 10 - first immiscibility episode, 11-15 - recrystallisation of the phase 1 and growth of the bubble, 16-19 - second immiscibility episode due to which the phase 2 appeared, 20 - after cooling, the inclusion contains a gas bubble (gb), liquid phase (l), two immiscible phases (ph2 and ph3) and hematite (h).

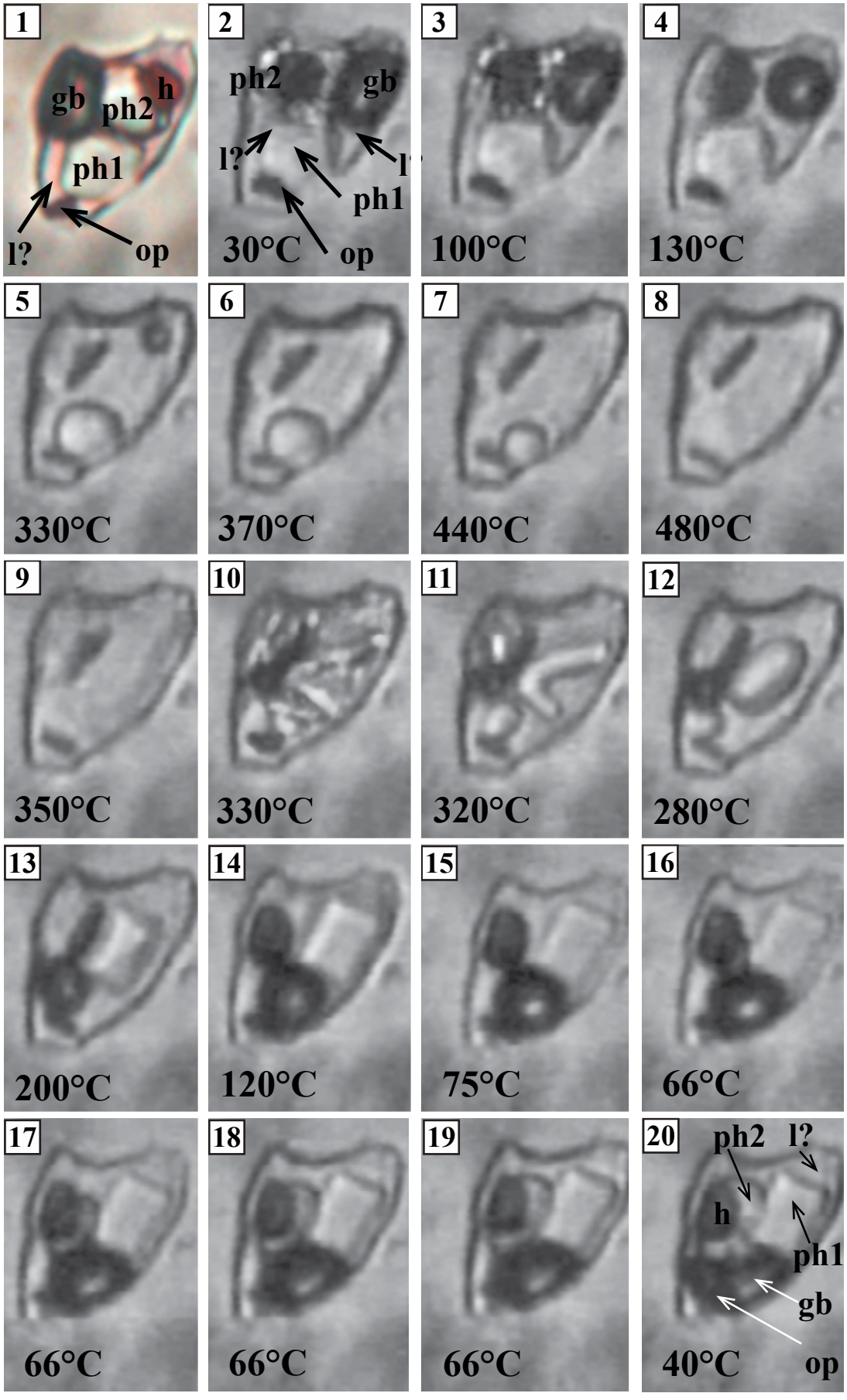
1
gb
ph2
h
ph1
l?
op
2
ph2
gb
l?
ph1
30°C
op
3
100°C
4
130°C
5
330°C
6
370°C
7
440°C
8
480°C
9
350°C
10
330°C
11
320°C
12
280°C
13
200°C
14
120°C
15
75°C
16
66°C
17
66°C
18
66°C
19
66°C
20
ph2
l?
h
ph1
gb
40°C
op

Table 5-4 Results on microthermometry

sample	inclusion	run	heating			cooling			
			T_{hs1}	T_{hsf}	T_{hb}	T_{het_bubble}	T_{imm1}	T_{imm2}	T_{imm3}
G1 quartz eyes	1	1	80-100[7]	330	440	430	240		
	2	1		430	390	340	210		
	3-1	1		>460	250	-	-		
	3-2	1		340	>460	-	170		
	3-2	2		-	-	-	155		
	3-2	3		-	560	530[1]	150		
	4	1		330	460	440	150		
	5	1		460	365	340	300		
	5	2		-	-	350	240		
	6	1		415	>460	-	210		
	7	1		435	400	360	280		
	9	1		410	>600	-	210		
	10	1		390	>500	-	190		
	11	1	80-100	400	>500	-	190		
G1 quartz vein	1	1	70-100[7]	420	>460	-	270		
	2	1		-	>425	-	257		
	3	1		330	330	280[2]	150		
	4	1		270	330	280	110		
	5	1			>350	-	270		
	7	1		450	380	340	220		
	8	1		385	260		220		
	9	1		345	300	280	110		
	10	1		350[3]	360	340	160		
	11	1		>400	>400		210		
	13	1	100-130[7]	>400	300	280			
		2			320	280			
	14	1			350	310			
	15-1	1		>415	330	280			
		2		400	230	150[2]	80		
		3		270	215		105		
	15-2	1		>415	370[4]	290[2]			
		2		430		150[2]	350		
		3		390	200	200	250		
		4		430	270	105	300		
	15-3	1		>415	350	290[2]			
		3		460			300		
		4		440	200	-	-		
	16	1		>460	270	240	-		
	17	1		370	>460	-	150		

sample	inclusion	run	heating			cooling			
			T_{hs1}	T_{hsf}	T_{hb}	T_{het_bubble}	T_{imm1}	T_{imm2}	T_{imm3}
138-2 quartz eye	1	1	70-110	340	430	427	180	80	
	2	1	80-100	330	375	340	280[6]	140	85
	3	1	-	320	340	310	160		
	4	1	70[5]: 80-100	340	385	360	280[6]	180	
	6	1	80-100	330	395	380	150	70	
	12	1	70-90	340	340	265	265	140	75
	13	1	110-140	420	310	260	260	82	
	14	1	70-120	336	>430	-	176		
	15	1	80-100	340	380	350	140		
	16	1	90-110	380	420	390	280	160	
138-2 vein quartz	1	1	20[5]:80-125	>480	390	390	415	80	
	2	1		420			250		
	3	1	35-95	>430	400	370	66		
	4	1	60-130	480	370	330	330	66	
	5	1	50[5]:70-115	320	150	380	140		
	5	2	50[5]: 70-110	290	180	97	210		
	5	4	125	500	415	380	325		
	6	1	70-135	<510	>510	-	85		
		2	135	-	-	-	85		
	8	1	60[5]: 100	480	>535	-	300		

T_{hs1} – temperature of the first solid phase disappearance
T_{hsf} – temperature of the last solid phase disappearance
T_{hb} – temperature of a gas bubble disappearance
T_{het_bubble} – temperature of a gas bubble appearance
T_{imm1} (T_{imm2}, T_{imm3}) – temperatures of immiscible episodes (the second, the third)
T^1 – gas bubble is deformed from the beginning of the experiments
T^2 – simultaneous separation of several gas bubbles
T^3 – temperature at which solid phase disappears after liquid-like behaviour (when it changes its shape as though it is liquid)
T^4 - bubble jerks unexpectedly before it disappears
T^5: - a phase appears during heating
T^6 - formation of an immiscible phase that appears film-like
T^7 – temperature of disappearing of a phase that reappeared only after a significant period of time (for example, the next day after experiments).

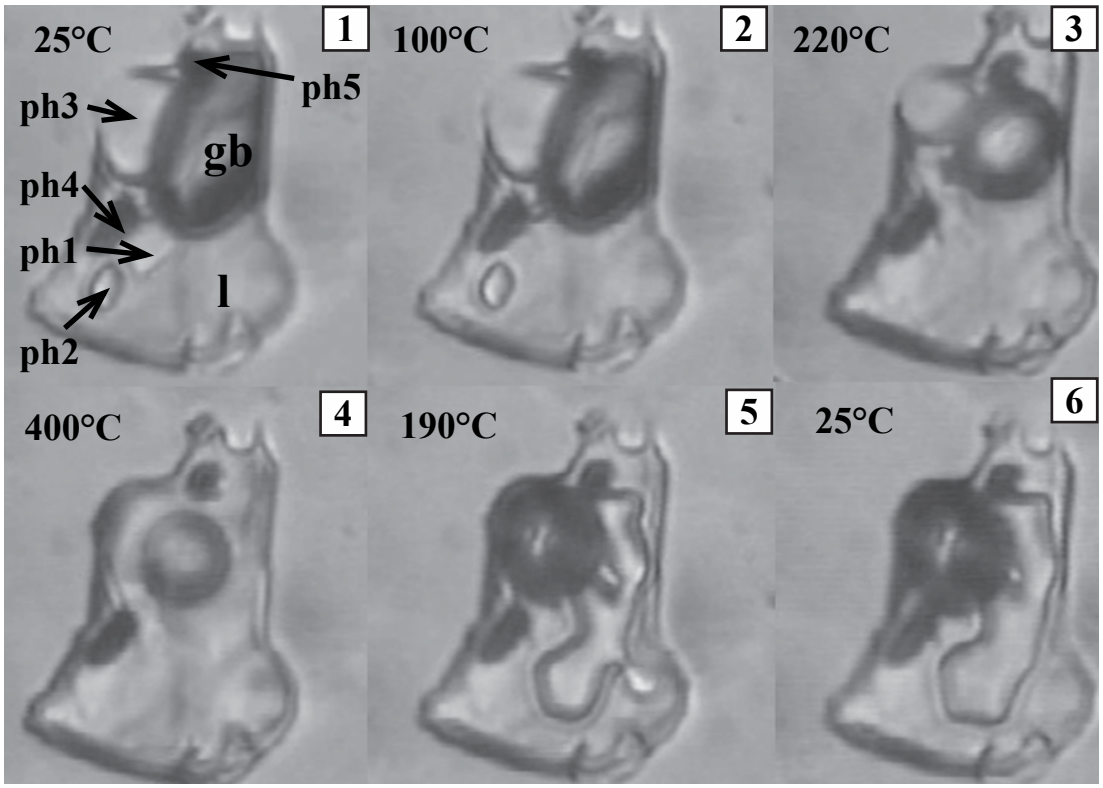

Figure 5-13 Typical behaviour of fluid inclusions during heating-cooling experiments Sample G1, Rio Blanco, quartz eye

1-4 - heating: 1 - inclusion at room temperature, 1-3 - transparent solid phases of different shapes and sizes; 4, 5 - opaque phases, gb - gas bubble, l - liquid. During heating (1-4) phase 1 disappeared first (2), then phase 2 (3) and phase 3 dissolved (4). Gas bubble and opaque phases did not homogenise at 500°C, to preclude decrepitation the inclusion was not heated further. 5, 6 - cooling: 5 - at 190°C an episode of immiscibility occures, a single anhedral phase appears and does not changes during further cooling even to room temperature (6).

5-4); in other cases significantly lower temperatures (below room temperature) were needed for the nucleation. As soon as the phase has grown, it begins swirling and then breaks up into multiple rounded bodies that finally disappears at 100-125°C (Fig 5-10 and video file BH_138-2_vein_inclusion1 in SUPPLEMENTARY section). I use the term 'swirling' to describe a complex behaviour of a phase upon heating or cooling during which a phase that appeared to be a crystal before experiments begins changing its shape in a way more typical for immiscible liquids than for crystals, rapidly shrinking in some parts while growing and coalescing in others without general changes in a size of this phase (see video file BH_138-2_vein_inclusion1 in SUPPLEMENTARY section). Such behaviour (swirling) upon heating is either atypical, or has not been mentioned in the literature. In sample 138-2 such atypical phases reappeared again during cooling at rather low temperatures (about 60-80°C) as a result of the last immiscibility episode (see below); in sample G1 such phases reappeared only on the

day after experiments so that the phase could be observed only during the very first heating run.

Further heating causes the disappearance of other phases and a vapour bubble (Figs 5-11 and 5-12). Homogenisation of two types was observed. Some inclusions homogenise by bubble disappearance and others by solid phase dissolution (see Table 5-4). Almost all inclusions contained one or more insoluble opaque solid phases (at least insoluble at the temperatures of the experiments), so in some cases homogenisation might be considered as partial. Some inclusions decrepitated before homogenisation. Because of that problem heating was often stopped before homogenisation to prevent decrepitation. In the Table 5-3 such instances are indicated by '>' mark: '>500' means that an inclusion did not homogenise at 500°C but was not heated further to prevent decrepitation. Temperatures of homogenisation (even within inclusions of one type) vary in a very wide range: from 250 to higher than 600°C for inclusions from quartz eyes (G1), from 200 to higher than 460°C for inclusions from the quartz vein (G1), from 340 to higher than 430°C for inclusions from quartz eyes (138-2), from 320 to higher than 535°C for inclusions from quartz vein (138-2).

During cooling a vapour bubble appeared first if the inclusion homogenised by bubble disappearance was usually the first phase to exsolve (see Table 5-4, the column T_{het_bubble}). Further cooling caused immiscibility (usually one to three subsequent episodes); in rare cases, bubble separation was simultaneous with the first immiscible episode ($T_{imm1,}$ see Table 5-4). I use the term 'immiscibility' instead of 'crystallisation' to emphasise that the phases appeared to behave as liquids rather than solids. When immiscibility occurred two immiscible phases form instantly (both of them appear liquid-like), after that one of them usually reshapes to form crystals. In sample 138-2 the number of immiscibility episodes was related to the number of solid phases, which were present before experiments. The same number of phases (as was before heating) formed after cooling to room temperature. Their shapes, however, differed significantly from initial ones (Fig 5-12). In sample G1, though, most inclusions after cooling showed a single anhedral phase instead of several small phases of different shapes (Fig 5-13).

5.6. Results of LA-ICP-MS

Inclusions from sample 138-2 (Batu Hijau) and sample G1 (Rio Blanco) were analysed by LA-ICP-MS technique. Unfortunately, the quartz host always cracked at the initiation of ablation when impacted by the laser beam, which precluded representative quantitative analytical results on individual inclusions. Analyses on

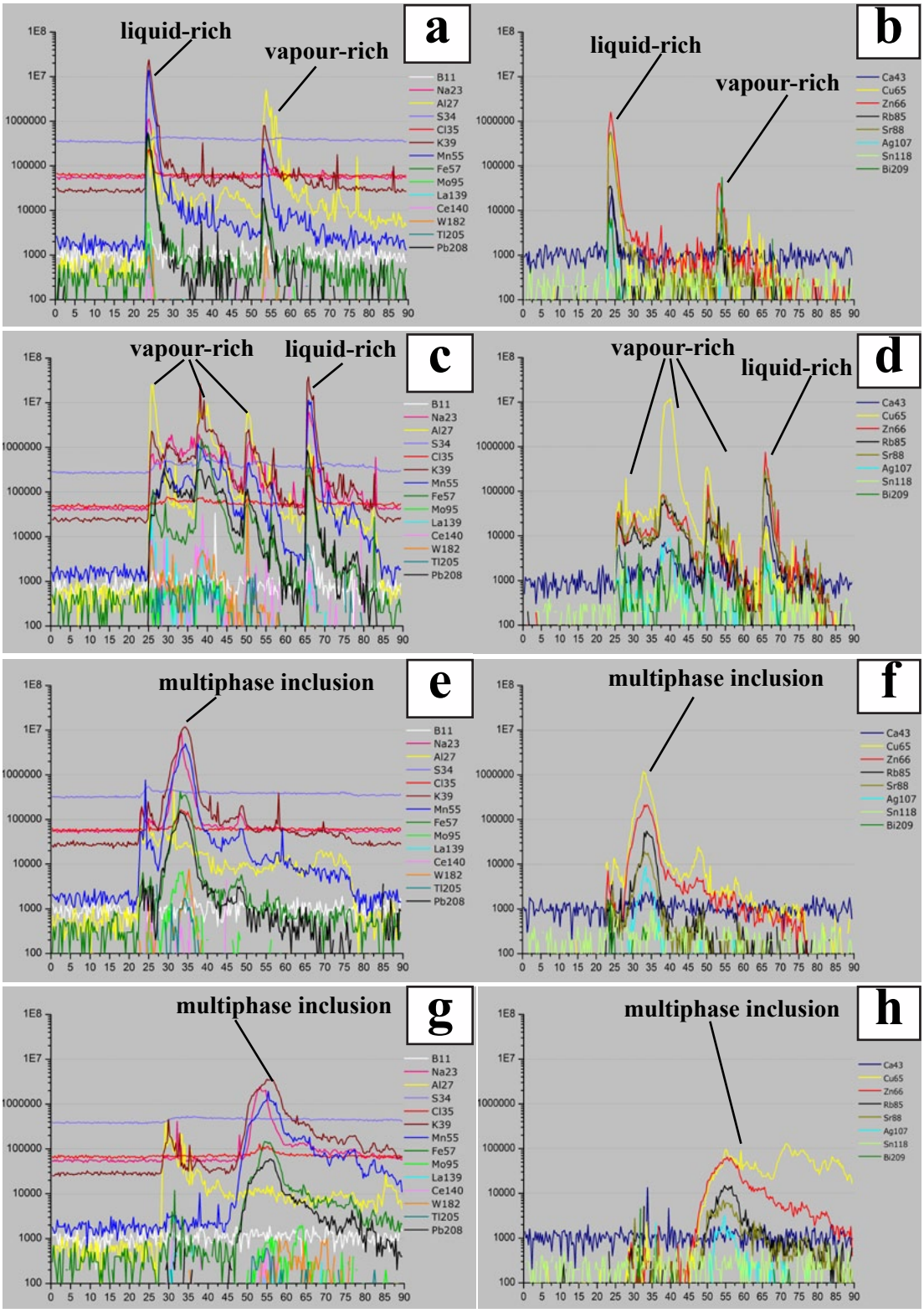

Figure 5-14 Typical LA-ICP-MS analytical trace of a group of fluid inclusions (a-d) or individual inclusions (e-h) in sample 138-2 and G1

All peaks correspond to fluid inclusions. (a, c, e, g) - signals of B, Na, Al, S, Cl, K, Mn, Fe, Mo, La, W, Tl, Pb; (b, d, f, h) - signals of Ca, Cu, Zn, Rb, Sr, Ag, Sn, Bi. Vertical scales are the same.

groups of inclusions were performed instead, which could provide only qualitative results. Eighty nine inclusions and inclusion groups were analysed from these two samples. Figure 5-14 illustrates typical spectra in samples from Rio Blanco and Batu Hijau. All peaks correspond to fluid inclusions. Signals for B, Na, Al, S, Cl, K, Mn, Fe, Mo, La, W, Tl, Pb are shown in Figure 5-14 (a, c, e, g) signals of Ca, Cu, Zn, Rb, Sr, Ag, Sn, Bi are shown in Figure 5-14 (b, d, f, h) with the same vertical scales. Since absolute concentrations depend on matrix composition and volume of the ablated inclusion, it is difficult to compare the absolute concentrations between different inclusions. Moreover, we cannot actually correlate spectral peaks with individual inclusions. However, we still can distinguish type of inclusions and compare element ratios in different inclusions. Inclusions showing sharp narrow peak and absence of chlorine are considered as vapour. Chlorine-rich inclusions with the narrow peak are considered as liquid-rich. Finally, chlorine-bearing inclusions showing broad peaks are believed to be multi-phase inclusions. The following features of these spectra were particularly notable:

► Fluid inclusions contain Al, Na, K, Fe, Mn, Cl, S, W, Pb, Cu, Zn, Ca, Ag, Sn, Bi and Rb well above their detection limits.

► Liquid-rich inclusions are chlorine-rich, and sometimes B-rich (Fig 5-14c). Liquid-rich inclusion often show higher Zn/Cu, Rb/Cu and Sr/Cu ratios than vapour-rich inclusions (Fig 5-14d).

► Vapour-rich inclusions are usually aluminium-rich, so that Al/K, Al/Mn and Al/Na ratios are higher than in liquid-rich inclusions (Fig 5-14c). Zn/Cu, Rb/Cu and Sr/Cu ratios in vapour-rich inclusions are usually much lower than in liquid-rich inclusions (Fig 5-14d).

► Unlike liquid-rich and multiphase inclusions, vapour-rich inclusions are often sulphur-bearing (Fig 5-14c).

► Multiphase inclusions generally demonstrate the same set of the major elements as in vapour- and liquid-rich inclusions except Al (very low relative the other elements, see Fig 5-14e and g).

► Maximal peaks of K, Mn, Na, Fe and Cl are often related (Fig 5-14a, c, e, g).

5.7. Summary

Fluid inclusions are distributed along healed fractures visible in CL and often have halos of secondary quartz around them. Sometimes different parts of a grain or adjacent grains show distinctly different distribution of fluid inclusions. Inclusion assemblages in quartz are significantly different from those in adjacent feldspar phenocrysts. Coeval fluid inclusions show extreme compositional diversity. In most cases fluid assemblages included a continuous range between two or even three end-members with different gas/liquid/solid ratios. Multiphase inclusions always contain various number of solid phases, and crystalline melt inclusions often have different gas/melt ratios. In most samples inclusions of all the types are associated with each other. Bleb-like inclusions of quartz and K-feldspar were found in late topaz, which often found associated with sulphides.

Inclusions demonstrate very complex behaviour upon heating and cooling; upon heating some phases nucleation, grow, swirl and disappear. Temperatures of homogenisation vary in a wide range from about 300°C to about 600°C. Transitions upon cooling are often related to immiscibility episodes. Generally, the number of immiscibility events upon cooling correlates with number of solid phases initially present in an inclusion.

LA-ICPMS data indicate that the composition of inclusions is distinctly different from model fluid (usually NaCl-H_2O system). They contain Al, Na, K, Fe, Mn, Cl, S, W, Pb, Cu, Zn, Ca, Ag, Sn, Bi, Rb and Sr well above their detection limits. Vapour inclusions are often Al- and S-bearing with higher Cu/Zn, Cu/Rb and Cu/Sr ratios than in liquid-rich and multiphase inclusions.

Chapter 6. Composition and distribution patterns of metal-bearing phases

It is believed that in most cases metal-bearing phases precipitate simulteneously with quartz during hydrothermal ore formation (Wilkinson et al., 2009). If quartz and metal-bearing phases are coeval then we can study quartz to determine conditions of ore precipitation. This chapter is our results on the composition and distribution patterns of metal-bearing phases. The study was conducted to determine relationships between quartz and other non-metal phases with metal-bearing phases.

Several different metal-bearing phases were found in the studied samples, including sulphides (mostly pyrite and chalcopyrite), oxides (such as cassiterite, magnetite or rutile) and fluorides and phosphates (often of Rare Earth Elements, i.e. REE). Metal-bearing minerals were found within the groundmass, as separate grains or aggregates (or blebs), as grains or aggregates within veins and veinlets and also as inclusions (often bleb-like) in quartz eyes. Metal-bearing phases within the groundmass, blebs, veins and quartz eyes are usually the same phases, but vary in size. Major characteristic of metal-bearing phases in the studied samples are listed in Table 6-1.

6.1. Metal-bearing phases within groundmass

Metal-bearing phases within groundmass are usually magnetite, pyrite, chalcopyrite or rutile grains, and commonly 10 to 70 μm. They are often angular and fill interstitial spaces between other groundmass minerals; in other cases they are globular or vermicular, and very rarely subhedral (Fig 6-1). Metal-bearing phases in the groundmass are often spatially associated with non-metal minerals such as apatite, chlorite, biotite, calcite, anhydride and K-feldspar (Table 6-1).

6.2. Metal-bearing mineral aggregates

Metal-bearing mineral aggregates are often globular, and sponge-textured. They usually contain magnetite, pyrite, chalcopyrite and sometimes rutile, together with non-metal bearing minerals, such as quartz, apatite, sericite and fluorite (Figs 6-2 and 6-4). Metal-bearing blebs are commonly of 0.2 to 1.3 mm (rarely up to 2 mm) and often vermicular, spherical or amoeboid; rutile aggregates are botryoidal (Fig 6-4). Non-metal bearing minerals often define the aggregate forms, since non-metal bearing minerals have their own morphology, and a metal-bearing phase typically fills

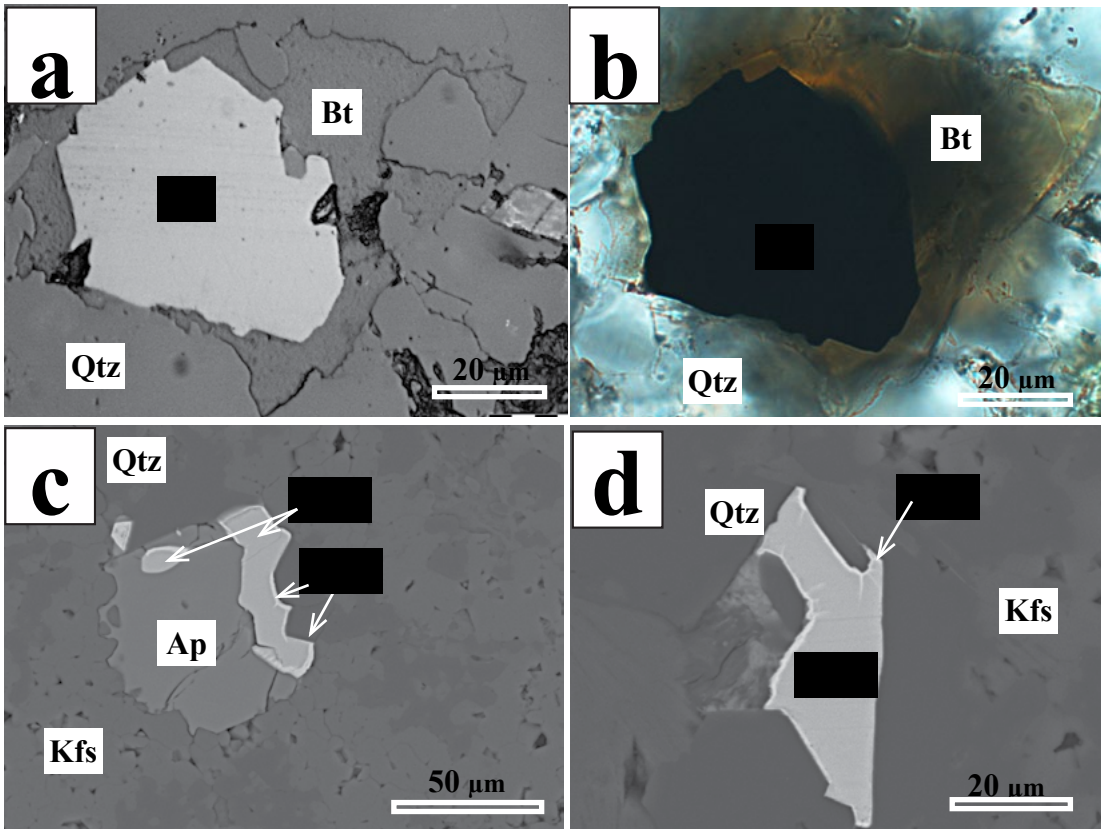

Figure 6-1 Metal-bearing phases in groundmass
(a-b) - SBD-69, Batu Hijau, magnetite (Mt) is associated with biotite (Bt); (a) - reflected light, (b) - transmitted light. (c, d) - DC-DLP-1, Rio Blanco, BSE images: chalcopyrite grains have bornite rims and are associated with apatite (Ap) and biotite (Bt), and often fill interstitial spaces between groundmass quartz (Qtz) and K-feldspar (Kfs).

the interstices (Fig 6-4). In some cases such aggregates are deformed between large grains of quartz, albite or K-feldspar (Figs 6-2 and 6-3).

Metal-bearing aggregates sometimes contain zones of multi-mineral assemblages (Figs 6-2, 6-4 and 6-5), which commonly show extreme compositional heterogeneity: up to fifteen minerals can be observed within a single bleb including HREE phosphates, galena, zircon (often zoned), W-Nb-Mn and Ti-Nb oxides, sphalerite, cassiterite, chalcopyrite, manganese phosphate (probably reddingite), Th-HREE fluorite, U and Y carbonates and U-Ti oxides (Figs 6-2, 6-4 and 6-5). There is no clear distribution pattern of such zones within aggregates: they can be banded around a pure pyrite core in some blebs, located strictly within no-metal phase, or distribute rather chaotically (Figs 6-2 and 6-5).

Metal-bearing aggregate shape, size and composition usually varies dramatically within a single thin section. In some cases homogeneous pyrite grains were found

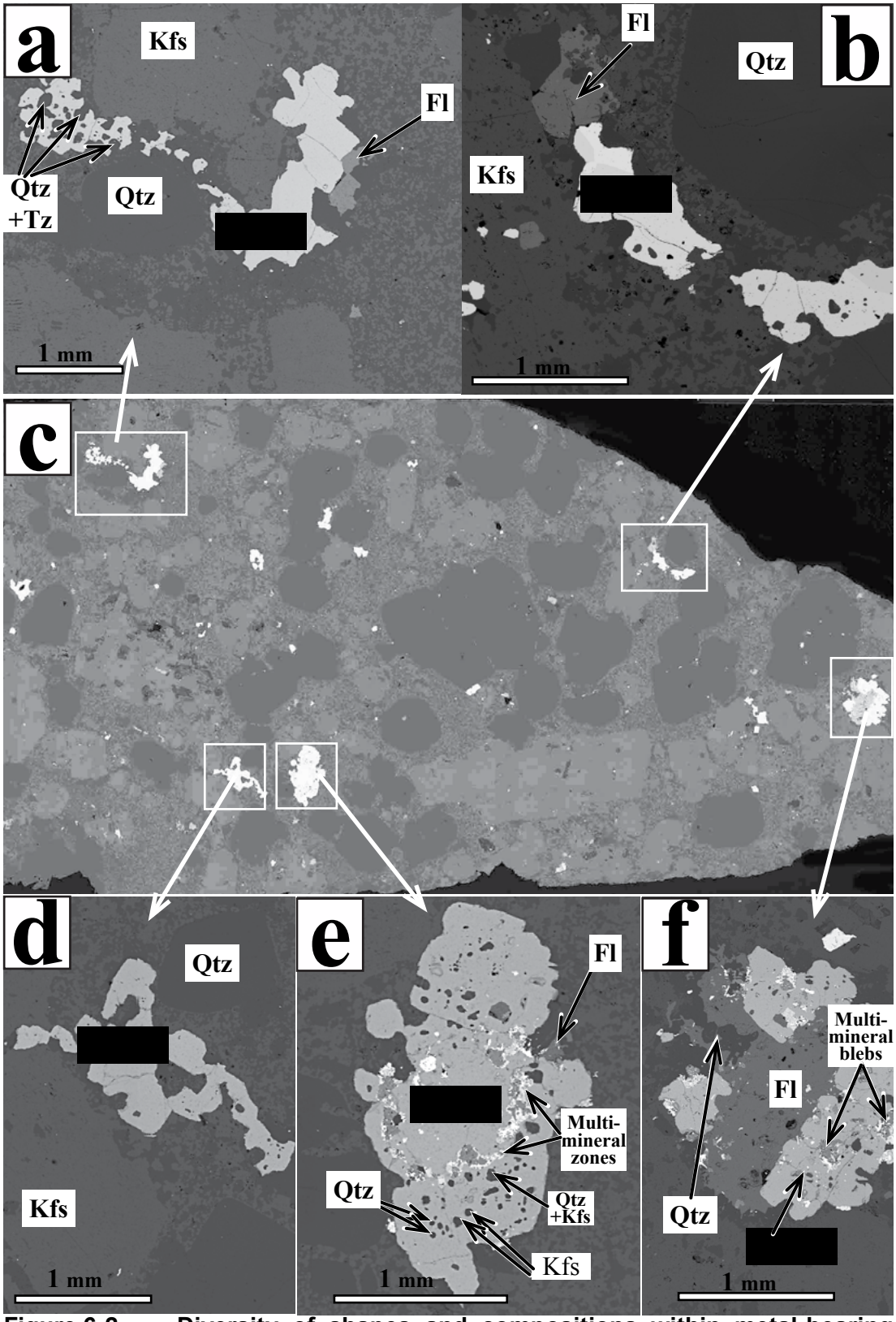

Figure 6-2 Diversity of shapes and compositions within metal-bearing blebs in sample 109646, Climax, USA

BSE images. (c) - the whole thin section, (a, b, d-f) - enlarged areas from (c), showing vermicular pyrite blebs with various amount of fluorite, (e, f) - blebs containing multi-mineral zones. Qtz -quartz, Kfs - K-feldspar, Fl - fluorite, Tz - topaz.

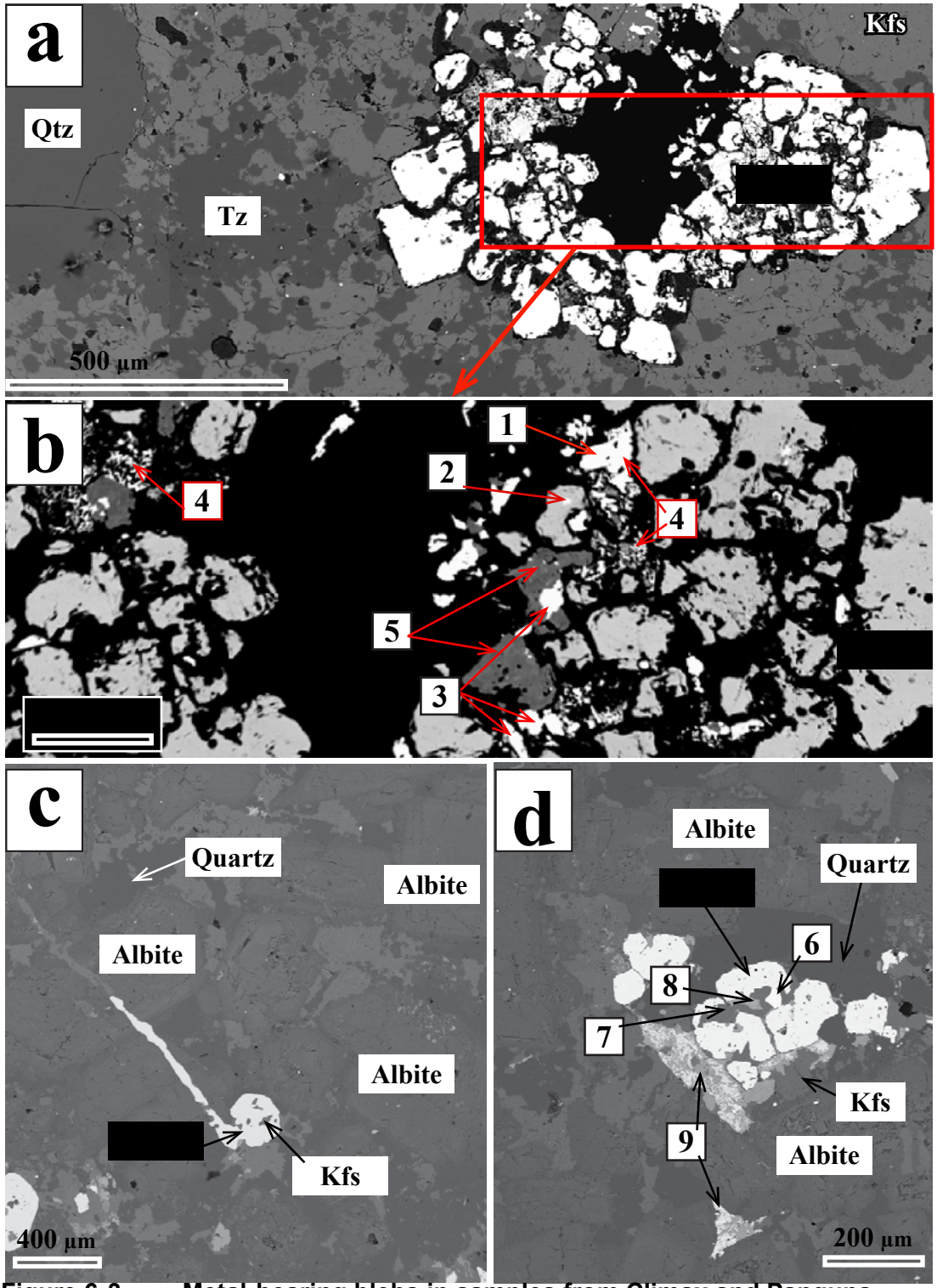

Figure 6-3 Metal-bearing blebs in samples from Climax and Panguna

(a, b) - 109644 (Climax), (a) - general view of pyrite bleb, b - enlarged area from (a) with less contrast. (c, d) - 109611 (Panguna); (c) - a pyrite grain appeared to be squeezed between large albite grains, (d) - multi-mineral assemblage deformed between large albite grains. 1-9 - minerals determined with EDS: 1 - REE phosphate, 2 - zircon (often zoned), 3 - W, Nb, Mn oxide sometimes with Ti, 4 - cassiterite, 5 - Nb-Ti oxide, 6 - chalcopyrite, 7 - chlorite, 8 - titanite, 9 - Fe-Ti oxide.

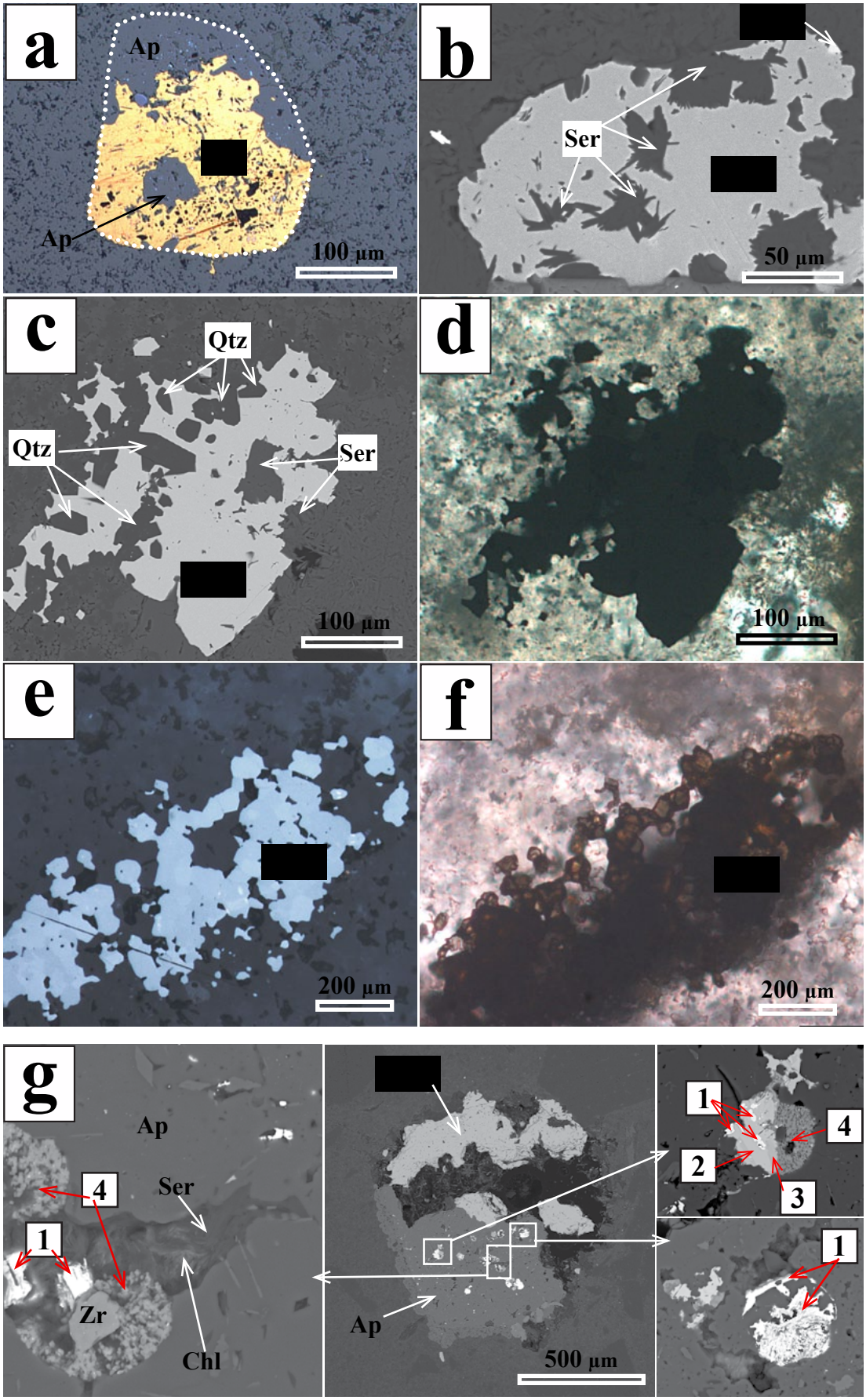
a
Ap
Ap
100 µm
b
Ser
50 µm
c
Qtz
Qtz
Ser
100 µm
d
100 µm
e
200 µm
f
200 µm
g
Ap
Ser
4
1
Zr
Chl
Ap
500 µm
1
4
2
3
1

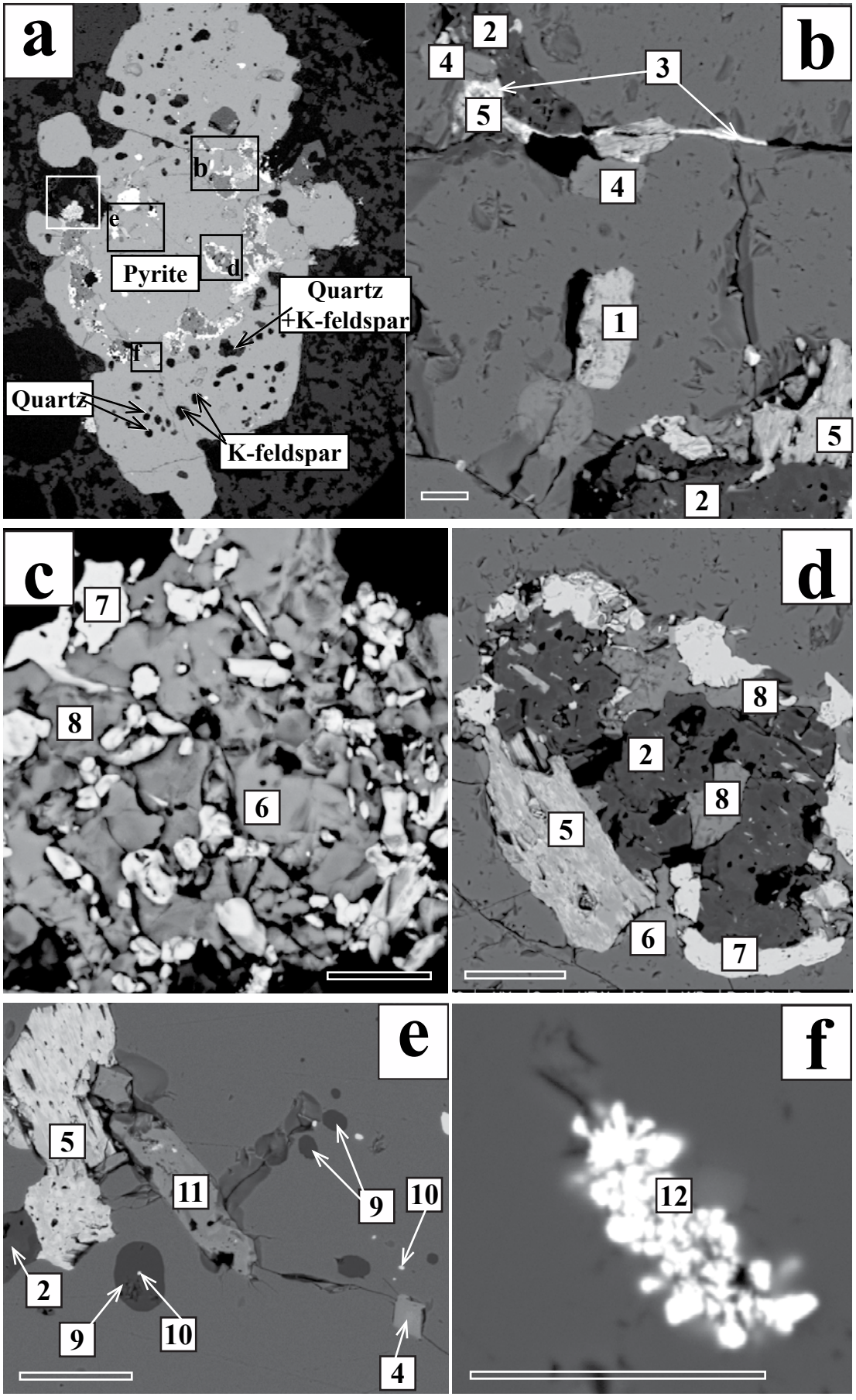
a
b
e
Pyrite
d
Quartz
+K-feldspar
f
Quartz
K-feldspar
b
2
4
3
5
4
1
5
2
c
7
8
6
d
8
2
8
5
6
7
e
5
11
9
10
2
9
10
4
f
12

Figure 6-4 Metal-bearing blebs from samples 599-2, 599-5, CA6 and DC-DLP-1 from Rio Blanco
(a) - chalcopyrite-apatite aggregate (599-2). (b) - fragment of the pyrite-chalcopyrite aggregate (599-2) containing needle-shaped sericite inclusions. (c, d) - vermicular chalcopyrite bleb from 599-2 containing euhedral quartz inclusions. Note, that sericite and quartz shapes determine chalcopyrite morphology. (g) - chalcopyrite-apatite aggregate from CA6 containing inclusions of U and Y carbonates (1 and 4) and U-Ti-oxides (2 and 3). (e, f) - botryoidal rutile bleb, (a, e) - reflected light, (b, c, g) - BSE images, (d, f) - transmitted light. Py - pyrite, Cpy - chalcopyrite, Bor - bornite, Ap - apatite, Ser - sericite, Qtz - quartz, Rt - rutile, Zr - zircon.

Figure 6-5 Composition of one of the sulphide blebs in sample 109646
(a) - general view of pyrite grain, with a pyrite core, surrounded by a ring of bright multi-mineral zones, and an outer rim containing numerous quartz and K-feldspar inclusions. b-f - detailed areas from (a). 1-12 - minerals determined with EDS: 1 - REE phosphate, 2 - rutile (sometimes with Nb component), 3 - galena, 4 - zircon (often zoned), 5 - W, Nb, Mn oxide sometimes with Ti, 6 - sphalerite, 7 - cassiterite, 8 - chalcopyrite, 9 - manganese phosphate (probably reddingite), 10 - REE fluoride, 11 - Nb-Ti oxide, 12 - U-rich mineral. Scale bar is 20 µm.

next to heterogeneous aggregates, which can contain many other minerals (Figs 6-2 - 6-5). Some aggregates are sponge-textured because they contain abundant inclusions; other blebs within a single thin section are massive or contain only a few of inclusions.

Different aggregates within a single thin section also contain different amount of non-metal bearing minerals. An example of a diversity of shapes and compositions of blebs within a single thin section is shown in Figure 6-2. It displays several varieties of metal-bearing blebs within sample 109646 from Climax (USA):

► Vermicular pure pyrite blebs with various amount of fluorite (compare Figs 6-2a, b and d). Pyrite within such blebs can be both euhedral and anhedral and contain numerous inclusions of quartz, topaz or K-feldspar.

► Vermicular blebs with a pyrite core banded with zones of highly heterogeneous composition and an outer rim containing pyrite with numerous quartz, quartz+K-feldspar and K-feldspar inclusions (Fig 6-2e).

► Almost spherical fluorite-pyrite blebs with randomly distributed multi-mineral blebs both within pyrite and fluorite (Fig 6-2f).

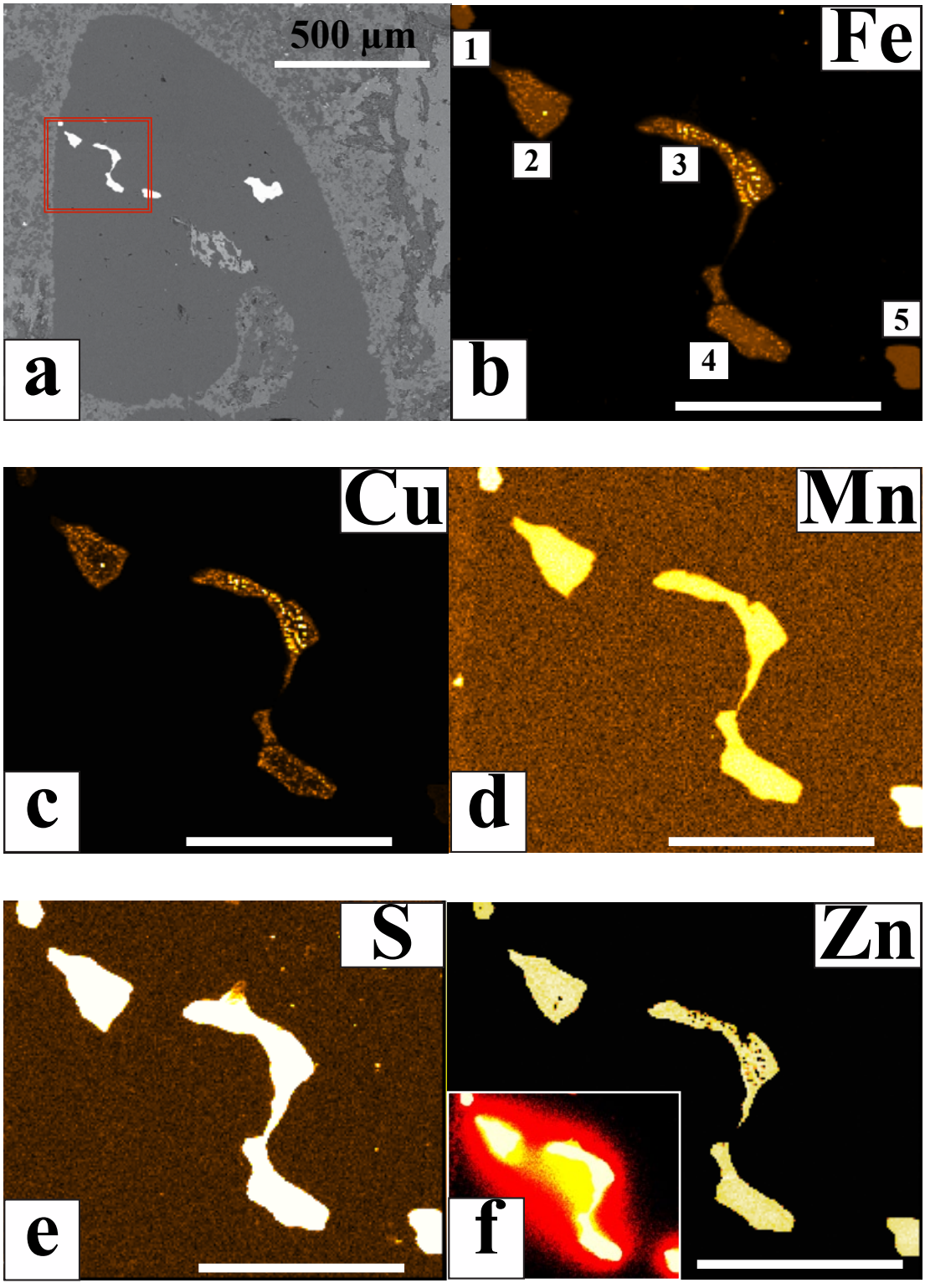

Figure 6-6 Composition of sulphide blebs within a quartz eye, sample 092-29700, Antapacay

(a) - BSE image of a quartz eye showing sulphide blebs distributed along a fracture. Note that sulphides localise strictly within the quartz eye. (b-f) - Fe, Cu, Mn, S, Zn distribution maps of an area from (a) marked with a red dashed rectangle. The inset in (f) is the Zn map of lower concentration showing diffusional distribution pattern. 1-5 - numbered sulphide grains. Scale bar is 200 µm.

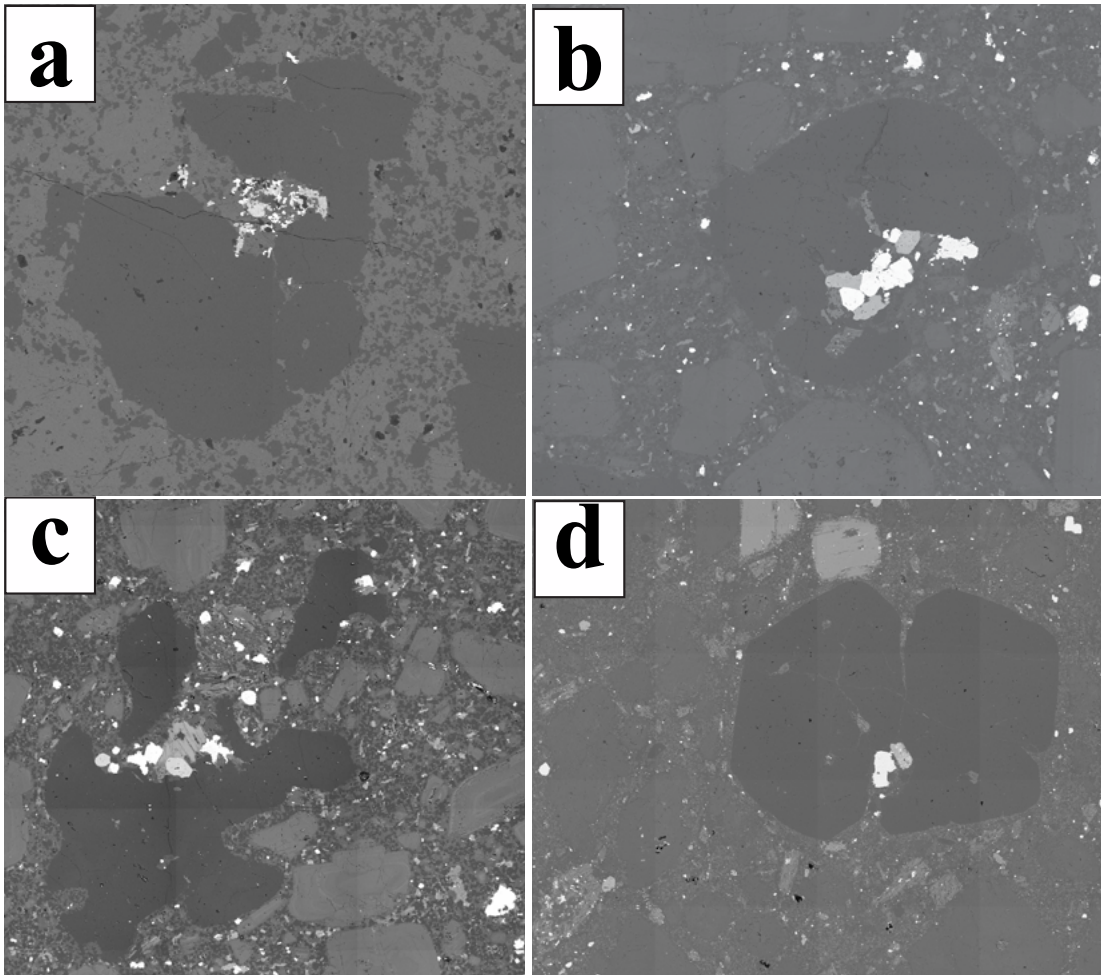

Figure 6-7 Oxide assemblages associated with a damage of quartz eyes
BSE images. (a) - sample 109644, Climax. Metal-bearing assemblage contains REE fluorides and phosphates, zircon (with some zones rich in REE), rutile, Nb-Ti-Fe oxides. (b) - sample 138.2, Batu Hijau. Oxide assemblage contains magnetite, apatite, ilmenite, rutile, chlorite and calcite. (c) - sample SBD-69, Batu Hijau. Damage of quartz eye is associated with magnetite, apatite, ilmenite, rutile and chlorite. (d) - sample 334-53250, Antapacay, quartz eye with magnetite and apatite.

6.3. Metal-bearing minerals within quartz eyes

Metal-bearing minerals within quartz eyes are commonly related to late quartz (dark in CL) that fills fractures (Fig 4-24) and like the late quartz they are distributed strictly within quartz eyes (Fig 6-6). They are usually sulphides of 0.01-0.15 mm, and often associated with calcite, apatite, K-feldspar and epidote (Fig 6-8 and Table 6-1), which, except for K-feldspar (which is abundant in groundmass surrounding the quartz eye) are also distributed only within quartz eyes. Sulphides in quartz eyes are often globular in shape and often heterogeneous in composition. In sample G1 from Rio Blanco a pyrite bleb within secondary quartz in a quartz eye contains chalcopyrite

and gold (Fig 6-8). Element mapping (Fe, Cu, Mn, S and Zn) of a quartz eye in sample 092-29700 from Antapacay (Peru) that contain bleb-like sulphide inclusions showed significant compositional heterogeneity within sulphide blebs. Figure 6-6 illustrates Fe, Cu, Mn, S and Zn distribution within analysed areas, where grains 1 to 5 are sulphide blebs exposed at the surface (and grains 2-4 are different parts of a single sulphide bleb). Sulphur is the only element which is distributed evenly throughout the blebs. Both copper and iron are localised in the centre of grain 3, and at margins of grains 2 and 4; copper is almost absent in grains 1 and 5, and centres of grains 2 and 4 are also lacking in copper. Iron content in grains 1 and 5 are lower than in the other grains. On the contrary, concentration of manganese is highest in grains 1 and 5; centres of grains 2, 3 and 4 are also high in manganese and their margins are less manganese-rich. Zn mostly concentrates in the centres of the grains, but lacking in the grain 1, margins of grains 2-5 and within the grains 2 and 3 in the spots, which are rich in iron and copper. Zn distribution pattern is diffusional (see inset in Fig 6-6); its traces are found in both secondary and primary quartz surrounding the sulphides (Fig 4-24).

Metal-bearing mineral assemblages are often related to damage to quartz eyes and embayments (Fig 6-7). Such assemblages usually contain magnetite, apatite, ilmenite, rutile, and often associate with non-metal bearing minerals, such as chlorite, calcite and sometimes REE fluorides and phosphates (Fig 6-7).

6.4. Metal-bearing phases in veins

Metal-bearing phases in quartz veins are most commonly chalcopyrite and pyrite, sometimes with magnetite (Figs 6-9, 6-10 and 6-11). Vein sulphides are apparently late and fill interstitial spaces between quartz crystals within veins (Figs 6-9, 6-10 and 6-11). In sample 138-2 there are two types of veins; their relationships are not clear. Vein A contains mostly chalcopyrite with lesser amount of pyrite; chalcopyrite grains are angular and mostly concentrated in the centre of the vein, interstitial between quartz grains (Fig 6-9). Pyrite grains are much smaller and occur mostly in the selvages, often with magnetite and apatite. Chlorite and sericite together with late quartz are closely associated with vein sulphides in this sample; they are also interstitial (Fig 6-9). This late chlorite-sulphide-quartz assemblage cuts an earlier generation of quartz (Fig 6-9). Vein B contains mostly chalcopyrite, sometimes with pyrite. They are 0.05-4 mm in size, sponge-textured, dendritic or globular and associated with calcite, apatite, chlorite and K-feldspar (Table 6-1).

In sample G1 there are also two different veins (Fig 6-10). One of them is earlier

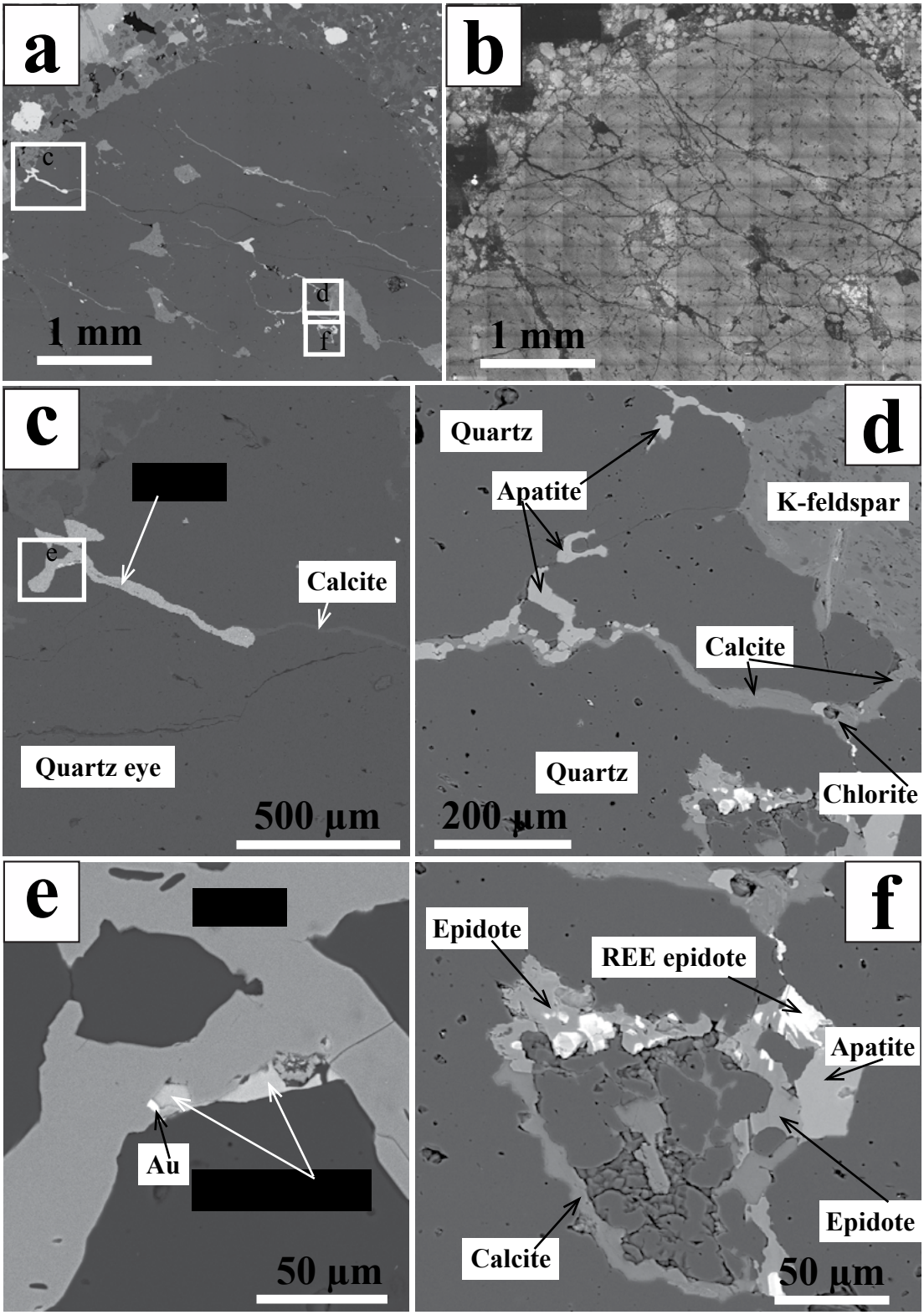

Figure 6-8 Quartz eye from sample G1

(a) - Quartz eye, general view, BSE image, rectangles are areas enlarged in images in (c-f). (b) - the same view, cathodoluminescence image. (c-f) - BSE images. (c, e) - pyrite bleb with chalcopyrite and gold. The quartz eye contains secondary minerals along a fracture including sulphide blebs and apatite, epidote (sometimes with REE), calcite and chlorite and K-feldspar inclusions.

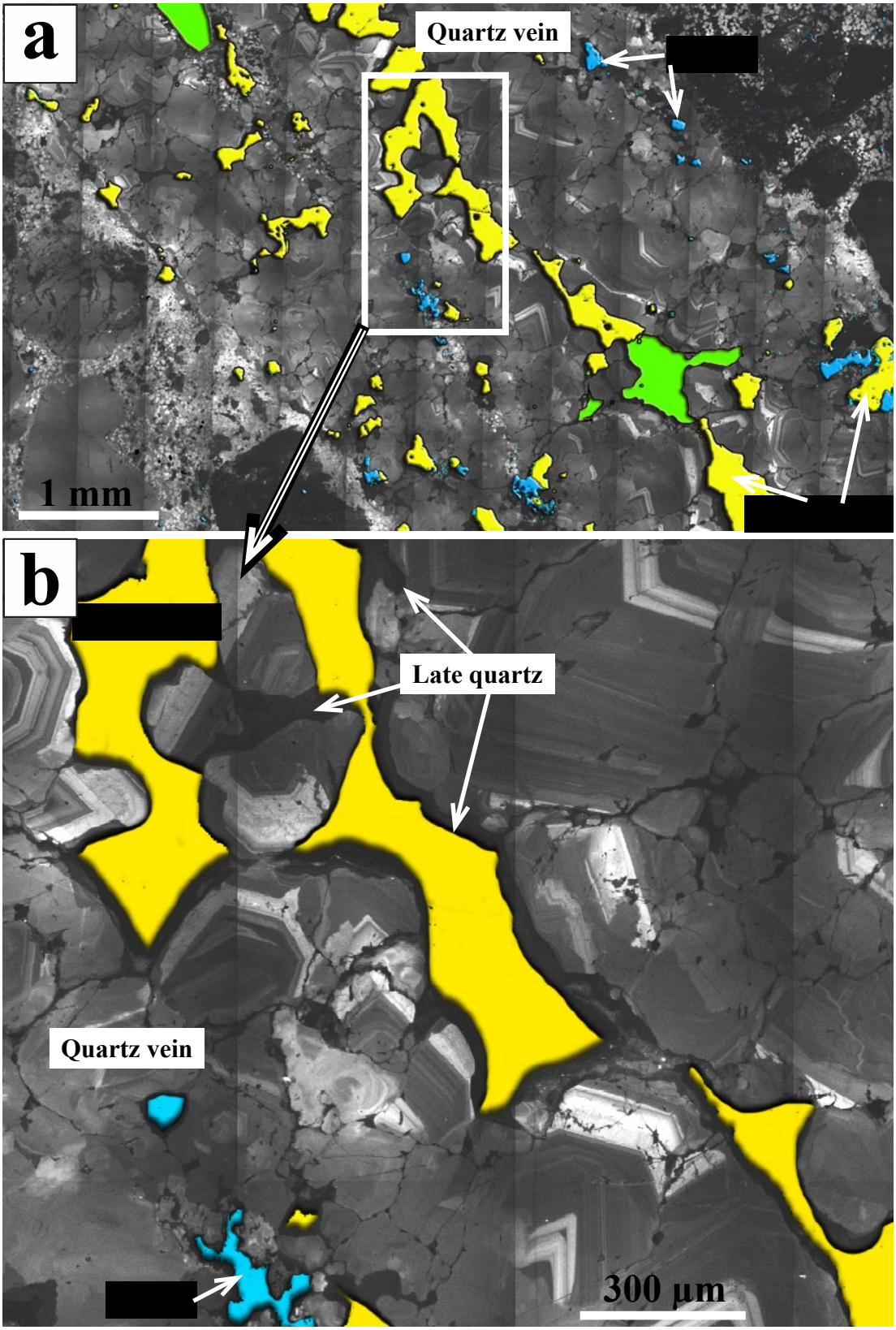

Figure 6-9 Cathodoluminescence images of the quartz vein, sample 138-2 from Batu Hijau with superimposed mineral map

(a) - general view, rectangle is the are enlarged in (b). Coloured areas represent pyrite (blue), chalcopyrite (yellow) and chlorite + sericite (green).

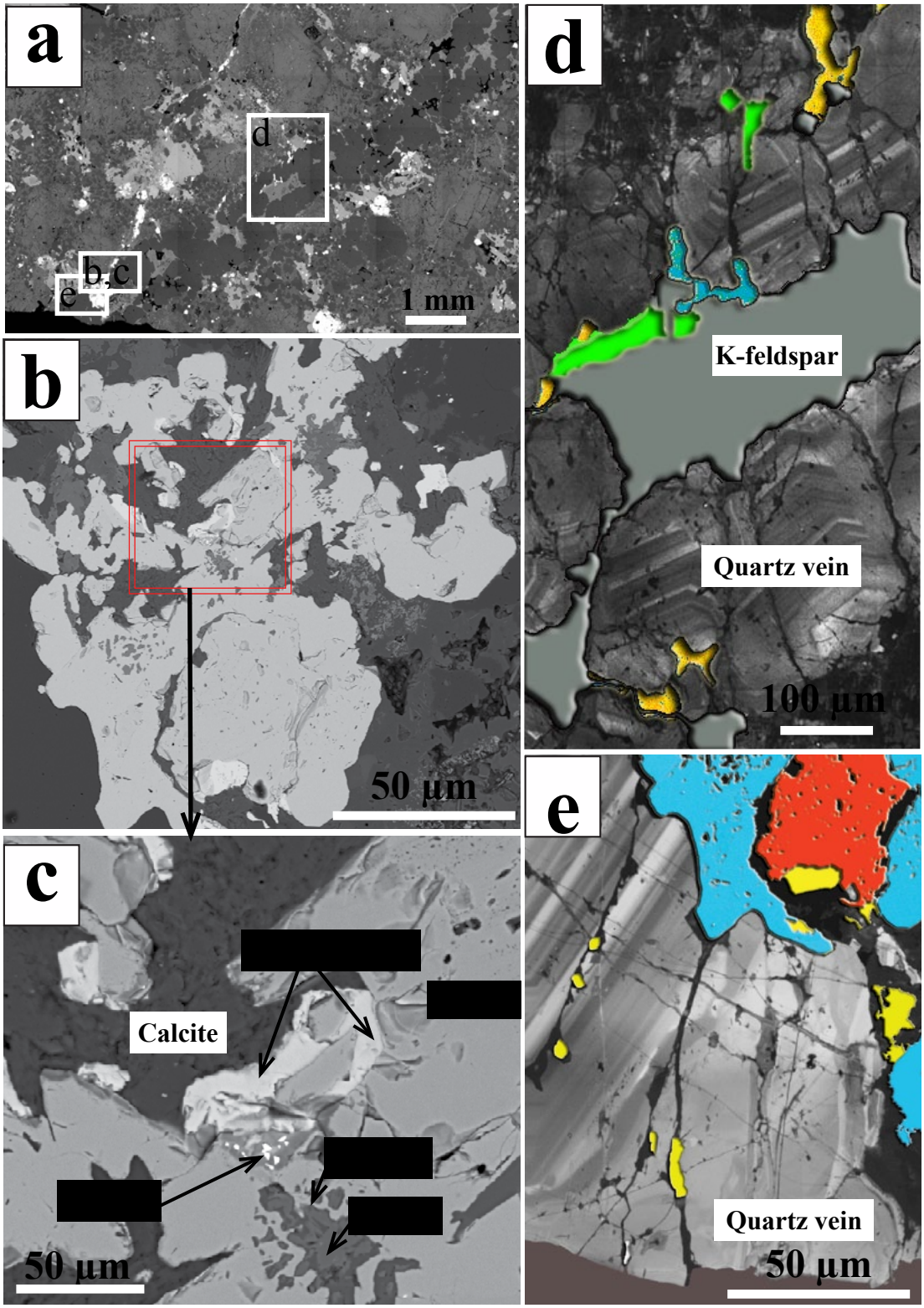

Figure 6-10 Composition of vein sulphides and their relationships with other vein minerals, sample G1 from Rio Blanco

(a-c) - BSE images: (a) - general view of the thin section, squares are areas showing enlarged in (b-e). (b & c) - sulphide assemblages in the late vein, (c) - enlarged area from (b). (d, e) - CL images showing internal zoning in early vein quartz; coloured minerals are pyrite (blue), chalcopyrite (yellow), chlorite (green) and K-feldspar (grey).

and contains quartz and scarce sulphides with associated magnetite, K-feldspar, and chlorite, with very rare apatite and epidote and calcite (vein A, Fig 6-10d). Sulphides within this vein are interstitial; they are globular pyrite and chalcopyrite of 0.01-0.1 mm, which are distributed mostly in the selvages of the vein (Fig 6-10). K-feldspar and chlorite fill the rest of interstitial space between quartz grains. The late interstitial mineral assemblage cut zonation of early quartz (Fig 6-10d). The other vein (vein B) is later and contains almost no quartz, but a sulphide assemblage with associated calcite, K-feldspar and chlorite. Sulphides are pyrite, chalcopyrite and sometimes galena (Fig 6-10); the grains are commonly 0.1-0.5 mm, bigger than in the vein A, and are often associated with magnetite and Ti minerals (rutile and titanite, see Fig 6-10).

In samples 109643, 109644 and 109645 from Climax sulphides are mostly pyrite and molybdenite. Pyrite is amoeboid-shaped, molybdenite is bladed-shaped (Fig 6-11). Molybdenite in most cases associates with chlorite (Fig 6-11b, c), whereas pyrite is often associates with interstitial topaz (Fig 6-11d, e), which contains numerous bleb-like inclusions of quartz and K-feldspar described in the previous chapter (Fig 5-4).

Thus, sulphides in veins are always associated with late quartz and several other non-metal bearing phases, which are:

1. Sericite and chlorite within the vein A and calcite, apatite, chlorite and K-feldspar in vein B in sample 138-2 from Batu Hijau,

2. K-feldspar with minor chlorite in the early quartz-sulphide vein A, and calcite, K-feldspar and chlorite in the late vein B in sample G1 from Rio Blanco,

3. Chlorite, fluorite and topaz in samples 109643, 109644 and 109645 from Climax.

4. Late quartz associated with sulphides in veins is always of minor amount and usually embedded between vein quartz and interstitial mineral assemblages.

If we compare sulphide assemblages and associated minerals in sample G1 in quartz eyes and veins several very important observations can be made. Sulphides are always related to the latest mineral assemblages. Moreover, the mineral composition of those late mineral assemblages in healed fractures within the quartz eyes, and in quartz veins are very similar; they are quartz, K-feldspar, calcite, chlorite, biotite and apatite. The amounts of those minerals in veins and quartz eyes, however, are different. For example, pyrite, chalcopyrite and calcite are in minor amount in interstitial spaces in the vein A, but abundant in the quartz eyes and the vein B, in

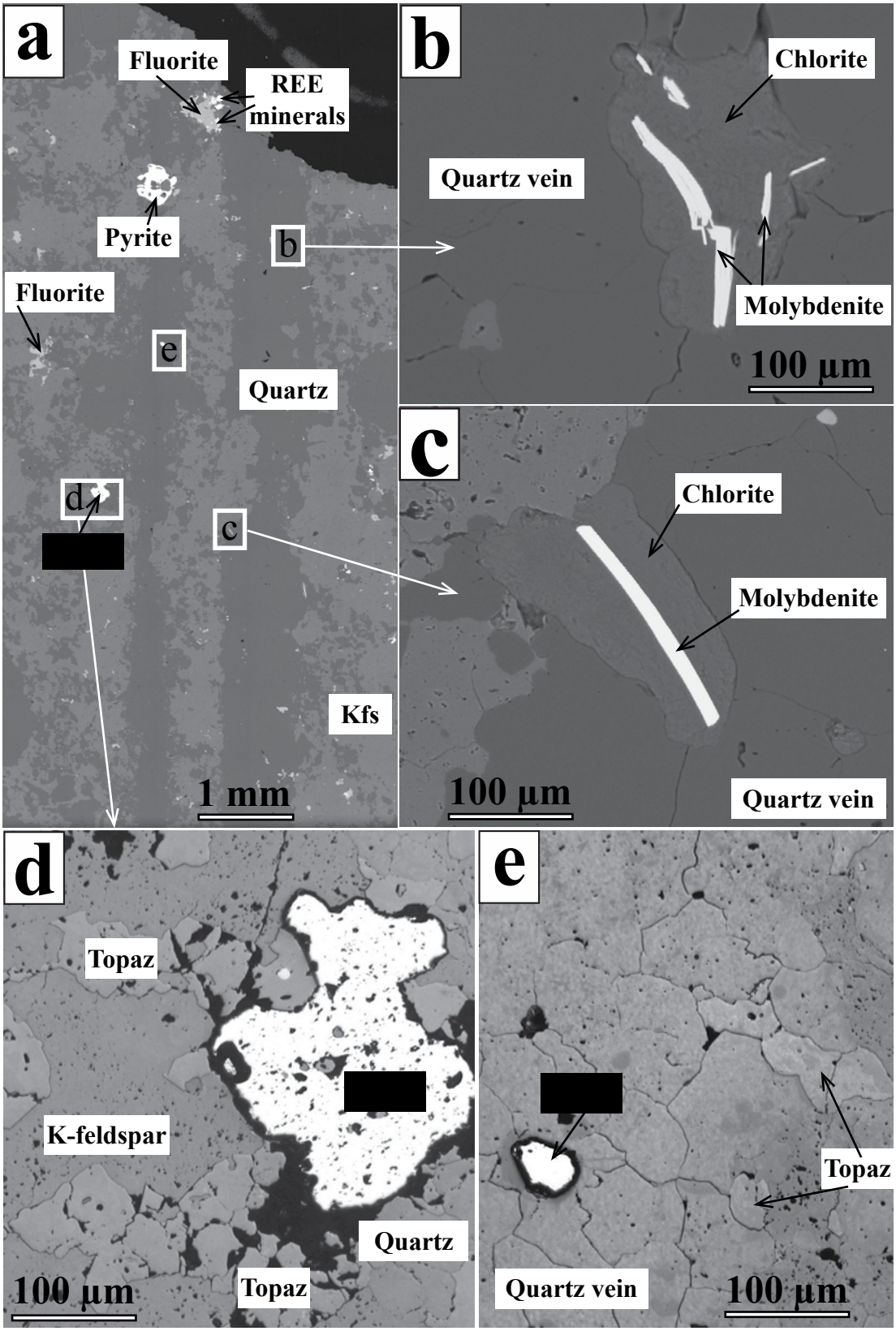

Figure 6-11 Distribution of sulphides within quartz veins in sample 109645 from Climax

(a-c) - BSE images: (a) - general view of the thin section. (b) and (c) are enlarged areas from (a). (d, e) - association of pyrite with topaz, reflected light.

which sulphides are more abundant than calcite, whereas in quartz eyes calcite is more abundant than sulphides.

6.5. Sulphides in quartz crystals from miarolitic cavities

Quartz from miarolitic cavities from Yaogangxian tungsten mine (Hunan Province, China) was studied in order to compare properties of quartz from quartz eyes and quartz veins with those of quartz from miarolitic cavities, as well as to compare distribution and composition of sulphides related to quartz of different origin. The data obtained showed that sulphides in quartz from miarolitic cavities are blebs of 0.01-0.08 mm and always related to late quartz (see cathodoluminescence image in Fig 6-12a). Different blebs within a single quartz grain are commonly heterogenious in composition (Figure 6-12). They are:

1. Sphalerite with stannite and chalcopyrite inclusions,
2. Cassiterite, sometimes with sphalerite inclusions,
3. Stannite with chalcopyrite and sphalerite inclusions.

Thus, sulphides from miarolitic quartz are very similar to sulphides obtained in quartz eyes as bleb-like inclusions and in quartz veins.

6.6. Summary

Study of metal-bearing phases revealed significant diversity in their shapes and compositions within a single thin section. Similar diversity was found within hydrothermal quartz from miarolitic cavities from Yaogangxian tungsten mine. Metal-bearing aggregates often contain multi-mineral blebs, which are composed from up to fifteen different minerals. The aggregates, as well as metal-bearing phases within veins and groundmass are associated with the latest minerals, such as K-feldsar, chlorite, late quartz, topaz and calcite. They fill interstitial spaces between the earlier minerals.

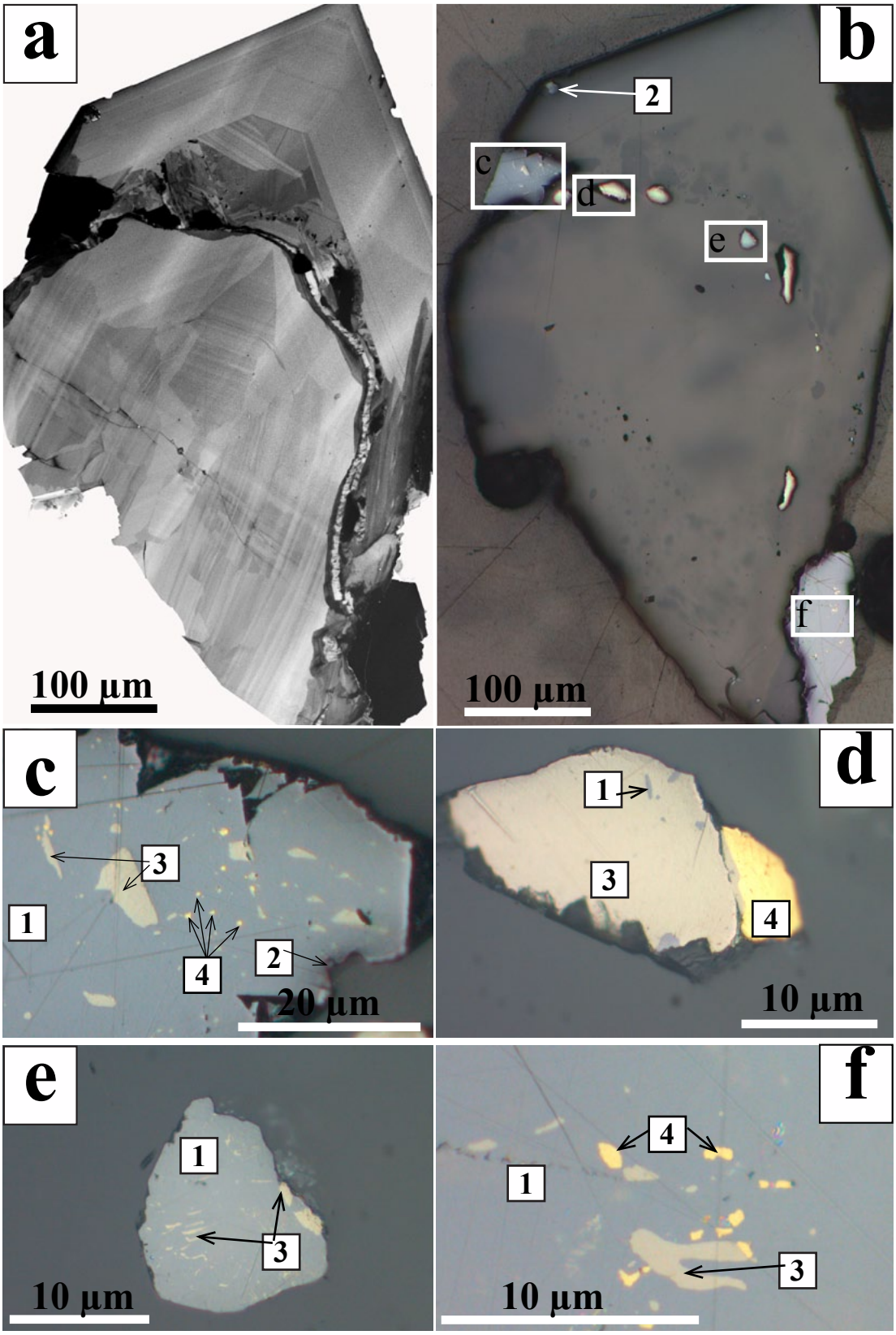

Figure 6-12 Bleb-like Sn-Zn-Fe-Cu-bearing inclusions in quartz from Yaogangxian Mine

(a) - CL image, (b) - reflected light image. (c-f) - enlarged areas from (b), reflected light. 1 - sphalerite, 2 - casseterite, 3 - stannite, 4 - chalcopyrite.

Table 6-1 Composition and distribution pattern of metal-bearing phases in studied samples

Locality	Sample	Metal-bearing phases in groundmass				Metal-bearing phases as aggregates or blebs				Metal-bearing phases in veins				Metal-bearing phases as inclusions in quartz eyes			
		Compo-sition	Shape	Size, mm	Non-metal associ-ation	Compo-sition	Shape	Size, mm	Non-metal associ-ation	Compo-sition	Shape	Size, mm	Non-metal associ-ation	Compo-sition	Shape	Size, mm	Non-metal associ-ation
Antapacay	334-53250	Mt, Il	Globular, angular	0.02-0.05	Ahd, Act	Mt,Il, Tit,Rt and Cpy,Bor	Subhedral, spongy, amoeboid, sulphides are often interstitial	0.2-1	Cc, Ahd, Qtz, Kfs	Mt,Il,Rt	Subhedral, globular	0.04-0.06					
	092-29700					Py, Cpy, Bor	Angular, vermicular	0.2-0.4	Cc, Ahd	Bor, Cpy	Bleb-like	0.02-0.15					
	133 - 19920	Mt, Il	Globular, angular	0.02-0.05	Ahd, Cc					Mt,Il,Rt	Interstitial	0.05-0.1					
Rio Blanco	CA 6	Py	Amoeboid, vermicular	0.02-0.07	Bt	Py, Cpy, Bor, Cov	Vermicular	0.2-0.9	Ap, Si, Ahd								
	CA 8	Cpy, Py	Vermicular	0.02-0.05		Cpy, Py	Vermicular	0.2-0.9	Si, Bt	Mt, Cpy	Bleb-like	0.02-0.05	Ap				
	CA 33	rare Mt	Angular	0.02-0.05	rare Ap	rare Mt	Subhedral	0.2-0.4	rare Ap	Mt	Euhedral	0.02-o.04					
	9902					Mt, Il	Subhedral, amoeboid	0.2-0.5	Ap								

Locality	Sample	Metal-bearing phases in groundmass			Metal-bearing phases as aggregates or blebs				Metal-bearing phases in veins					Metal-bearing phases as inclusions in quartz eyes			
		Composition	Shape	Size, mm	Non-metal association	Composition	Shape	Size, mm	Composition	Shape	Size, mm	Non-metal association		Composition	Shape	Size, mm	Non-metal association
Rio Blanco	**DC-DLP-1**	Cpy, Rt	Rt-botryoidal, Cpy - subhedral or angular	0.025 -0.05	Bt, Chl	Cpy, Bor, Ht and Rt	Globular, Rt and Ht - botryoidal	0.2-0.4	Cpy, Bor, Ht, Py	Py - angular, interstitial, Ht - colloform	0.05-0.2	Qtz		Rt, Cpy, Ht	Rt-botryoidal, Cpy - angular	0.02-0.06	
	G1	Mt	Globular, angular	0.1-0.2	Ap, Bt, Chl	Mt	Spheric, amoeboid	0.5-1.3	Mt, Ap, Py, Cpy	Globular, vermicular	0.01-0.1	Ap, Qtz, Kfs, Chl		Py, Cpy, Au	Vermicular	0.01-0.05	Cc, Ap, Kfs
									Py, Cpy	Vermicular	0.1-0.5	Cc, Chl, Kfs					
	G2	Mt, Il	Globular, angular	0.01-0.05	Ap, Chl, Bt, Kfs	Mt, Il	Subhedral, amoeboid	0.2-1	Ap, Chl, Bt					Mt, Il	Subhedral	0.01-0.05	Ap, Kfs, Chl
	599-2	Py, Rt	Rt-botryoidal, Py - subhedral or angular	0.02-0.05	Ap, Qtz, Bt	Cpy, Py, Rt	Amoeboid, Cpy-interstitial	0.2-0.7	Ap, Qtz, Bt								
	599-5	Py, Rt	Rt-botryoidal, Py - subhedral or angular	0.02-0.05	Bt	Cpy, Py and Rt	Amoeboid, Cpy-interstitial	0.4-0.7	Ap, Bt								

Locality	Sample	Metal-bearing phases in groundmass				Metal-bearing phases as aggregates or blebs				Metal-bearing phases in veins				Metal-bearing phases as inclusions in quartz eyes			
		Composition	Shape	Size, mm	Non-metal association	Composition	Shape	Size, mm	Non-metal association	Composition	Shape	Size, mm	Non-metal association	Compo-sition	Shape	Size, mm	Non-metal association
Climax	**109 643**	Mt	Vermicular	0.02-0.05						Py	Subhedral	0.2-0.6	Fl, Cc, Tz				
	109 644	Rt	Angular	0.01-0.03		Py	Botryoidal	0.4-1	Chl	Py	Euhedral, subheral, Amoeboid	0.05-0.4	Qtz, Tz	Rt, Ree minerals	Globular	0.05-0.06	Qtz, Kfs
	109 645					Py	Globular	0.3-1	Fl, Qtz, Kfs	Py, Mo	Py - Amoeboid, Mo - needles	0.01-0.2	Qtz, Tz				
	109 646					Py, Cpy	Subhedral, vermicular, amoeboid	1-2	Chl, Fl, Tz, Qtz					Py	Anhedral, vermicular	0.1-0.15	Chl, Tz
	109 647	Mt	Subhedral	0.01-0.03	Bt	Mt, Py	Globular	0.1-0.6	Ap								
Pangua	**109 607**	Mt	Interstitial	0.02-0.06	Bt	Mt, Ap, Il	Subhedral, spongy, amoeboid	0.2-0.5	Ap					Mt	Bleb-like	0.1-0.2	Ap
	109 611					Py, Cpy, Mt Il	Spongy, amoeboid	0.6-1.5	Bt, Chl, Ap								

Locality	Sample	Metal-bearing phases in groundmass			Metal-bearing phases as aggregates or blebs				Metal-bearing phases in veins				Metal-bearing phases as inclusions in quartz eyes			
		Composition	Shape	Size, mm	Non-metal association	Composition	Shape	Size, mm	Non-metal association	Composition	Shape	Size, mm	Non-metal association	Composition	Shape	Size, mm	Non-metal association
SEP	P 13	Mt, Cpy	Interstitial	0.02-0.065		Mt, Il	Subhedral, spongy, amoeboid	0.5-1.2	Ap								
Batu Hijau	138.2	Mt, Cpy	Interstitial	0.02-0.07	Bt	Mt, Ap, Il	Spheric, amoeboid	0.9-1.5	Chl	Cpy, Py, Mt	Angular, fills interstitials	1-4	Qtz, Chl, Ser	Mt, Ap, Il, Rt	Amoeboid	0.05-0.1	Chl, Cc
										Cpy, Py	Spongy, dendritic, globular	0.2-1	Cc, Ap, Chl, Kfs				
	SBD-69	Mt, Il	Interstitial	0.02-0.07	Bt	Mt, Ap, Il	Spheric, amoeboid	0.2-1	Bt					Mt, Ap, Il, Rt	Amoeboid, star-like	0.05-0.1	Chl, Cc
	SRD-02	Mt, Il, rare Cpy	Interstitial	0.02-0.07	Bt, Kfs	Mt, Ap, Il	Spheric, amoeboid	0.3-1	Bt					Py	Bleb-like	0.05	Chl

Chapter 7. Discussion

The orthomagmatic model for formation of porphyry deposits is currently the most accepted one. It includes subvolcanic intrusion of magma, its crystallisation, exsolution of a magmatic vapour phase (MVP), its accumulation, and precipitation of ore minerals around the intrusion. Conditions that are known to favour formation of porphyry-type deposits are numerous, and sometimes are contradictory. For example, conditions that favour exsolution of a metal-rich fluid (about 60% crystallised magma) reduce the potential for effective fluid transport (optimally less than 20-25% crystallised magma). Favourable conditions for the partitioning of metals into a fluid imply the pressure about 2 kbar or higher; at those depths exsolved fluids have high metal-carrying capacity, but as soon as fluid rises it can lose most of the load due to melt-fluid re-equilibration.

Mass-balance considerations showed that at least 20-90 km^3 of parent magma would be sufficient to supply copper and other metals for economic porphyry mineralisation (Cline and Bodnar, 1991; Hattori and Keith, 2001). However, such magma volume is not enough to supply sulphur for a deposit: *'the total sulphur contained in the Bingham Canyon deposit would require at least 4,800 km^3 of felsic melt' (Hattori and Keith, 2001)*. Injections of mafic magmas in felsic magma reservoirs were suggested to supply most of S, Cu and other metals (Hattori, 1993; Hattori and Keith, 2001; Maughan et al., 2002; Pasteris, 1996; Wallace and Carmichael, 1992; Wallace and Gerlach, 1994). Although such mafic magma injections contribute to sulphur, copper and other metals supplies, they are believed to be the main cause of eruptions, which destroy porphyry systems (Cloos, 2001). Detailed analysis of the current model of porphyry formation showed that it has many mutual contradictions. There is still no convincing explanation for co-precipitation of sulphides and silica. It is still unclear what makes the difference between barren and mineralised plutons. All models are a work in progress, however the number of internal contradictions suggest that something must be missing in the model. It is my intention in this study to add another, alternative, piece of the puzzle in the hope of removing some of those contradictions.

Porphyry-related intrusions are typically characterised by porphyritic textures, which is typically defined by feldspar and quartz crystals, quartz eyes in the terminology of this study. Both feldspar phenocrysts and quartz eyes are believed to crystallise at depth within convecting magma (Burnham and Ohmoto, 1980; Cloos, 2001). However, magmas of intermediate composition are silica undersaturated and thus,

in such systems quartz should be the last phenocrystic phase to crystallise, because the silica saturation necessary to trigger quartz crystallisation occurs relatively late. Therefore, at least some of quartz eyes should crystallise in-situ after magma emplacement. If so, then crystallisation of quartz eyes should be related to formation of mineralising fluid in porphyry systems since both are latest stage crystallisation phenomena. In this case study of quartz eyes textures can provide us with valuable information about origin of quartz eyes, and fluid inclusions in them. This data may be crucial to understand how the deposits of this type form.

7.1. Are quartz eyes 'true phenocrysts'?

Quartz eyes from porphyry intrusions are usually assumed to crystallise within convecting magma prior an intrusion, i.e. to be phenocrysts. According to 'Collins Dictionary Of Geology' by Lapidus (1990) *'phenocryst is a crystal in a igneous rock, larger than other crystals in the matrix, and formed during early stages of crystal development'.*

In rare cases though, quartz eyes were suggested to be of other origins (Harris et al., 2004; Wiebe et al., 2007). For example, Wiebe (2007) suggested that quartz crystals from a felsic porphyry of the Vinal Cove intrusive complex formed by '*remelting crystal-rich granitic mush when a large basaltic dike intruded through it*'. That means that quartz cores crystallised in granitic magma prior or during its emplacement, and quartz rims formed in-situ after magma emplacement under the influence of heat from the intruded basaltic dyke. Harris (2004) found two types of quartz crystals at the Bajo de la Alumbrera Cu-Au porphyry deposit, NW Argentina: typical quartz phenocrysts that show euhedral shapes and are often resorbed to a different extent, and sugary quartz aggregates interpreted to be miarolitic pods.

Quartz eyes from porphyries in the studied samples differ significantly from typical quartz phenocrysts. In our study quartz phenocrysts in the samples from Taupo Volcanic Zone, and an extrusive sample from Rio Blanco, i.e. CA33 (Davidson, 2004) are used as reference samples of phenocrysts described above.

7.1.1. Inclusions

Unlike quartz phenocrysts, which typically contain melt inclusions of rhyolitic composition (Tables 5-2 and 5-3, see also Dunbar and Hervig, 1992), quartz eyes contain abundant fluid inclusions; they may even have spongy textures due to the abundance of fluid inclusions (Fig 5-7b). Crystals adjacent to quartz phenocrysts, such as sanidine, plagioclase and clinopyroxene crystals, typically contain melt

inclusions of the same composition (Dunbar and Hervig, 1992; Wardell et al., 2001) which proves their crystallisation from the same magma. In distinct contrast, quartz eyes and adjacent feldspar crystals contain different inclusions: sponge-textured quartz eyes full of fluid inclusions occur next to 'clear' feldspar crystals containing only melt inclusions (Fig 5-7b).

7.1.2. Shapes

True quartz phenocrysts typically occur either as fragments of clusters or discrete euhedral crystals (Fig 4-19, see also Nakada et al., 1994; Shane et al., 2008). However, quartz eyes are often preserved as intact clusters, which consist of two to six, and occasionally more quartz grains (Fig 4-1). Quartz eyes also show variety of shapes within a single thin section, i.e. from euhedral to rounded and amoeboid (Table 41), which is atypical for true quartz phenocrysts.

7.1.3. Internal CL patterns

Quartz eyes from porphyries in this study show internal CL patterns distinctly different from the patterns of quartz phenocrysts: the former show high contrast compositional zoning often with core-and-rim patterns, whereas the latter display only subtle oscillatory zoning (compare Figs 4-5 and 4-6 with 4-16). Similar CL patterns were observed by other researches in lava samples from Taupo and other volcanic zones (Peppard et al., 2001; Shane et al., 2008; Watt et al., 1997). Moreover, unlike volcanic quartz, which display abundant open fractures (Fig 4-16), quartz eyes show networks of randomly oriented healed fractures and fluid inclusion halos (dark in CL, Figs 5-1, 5-2) typical for granitic quartz (Müller, 2000; Shaw, 2006; Van den Kerkhof and Hein, 2001; Wiebe et al., 2007). Unlike open cracks within quartz phenocrysts, healed fractures in quartz eyes from porphyries are often associated with inflections or/and smudging of growth layers (Fig 4-12e). Embayments and inclusions in quartz eyes are also often related to disturbance of CL banding (Figs 4-13 and 4-14), whereas in quartz phenocrysts embayments and inclusions typically cut CL zoning (Fig 4-19).

Published studies (Müller, 2000; Müller et al., 2002a; Müller et al., 2002b; Van den Kerkhof et al., 2004) suggest that formation of secondary CL-dark quartz occurs as a two stage process (see Fig 7-1). The first stage includes simultaneous massive decrepitation of fluid inclusions, which can be caused by cooling-induced thermal stress, for example, during incoherent α/β-transition or up-lift. During the second stage defect-poor quartz grows at the cost of the host quartz and releases or replaces defect centres. However, true quartz phenocrysts also undergo cooling-induced thermal stress during up-lift and α/β-transition, but do not show three dimensional networks

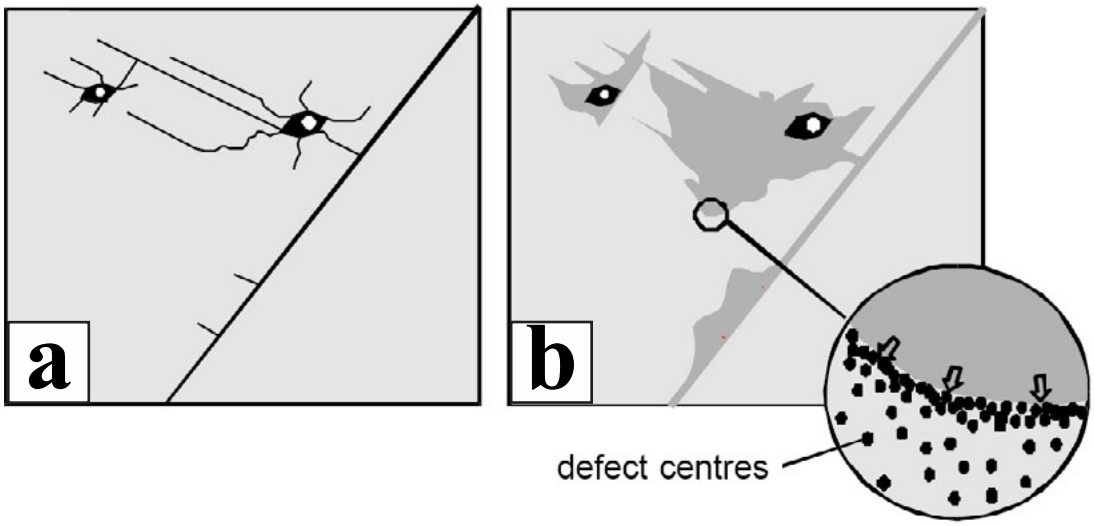

Figure 7-1 Model of formation of halos of secondary quartz around fluid inclusions

This Figure is taken from Müller (2000); (a) – first stage: mass decrepitation of fluid inclusions (micro-crack formation). (b) – second stage: defect-poor quartz grows at the cost of the host quartz and releases or replaces defect centres.

of secondary quartz. In order to form 3D network of secondary CL-dark quartz by the suggested mechanism quartz eyes must initially contain abundant primary fluid inclusions, i.e. crystallise from extremely fluid-rich melt. According to our LA-ICP-MS analyses of fluid inclusions, this melt must dominated by silica, water and alkalis, and be also metal-rich. This is inconsistent with conditions under which crystallisation of true quartz phenocrysts is implied. For instance, Müller (2000) suggested that crystallisation of quartz phenocrysts starts from depth around 21 km.

7.1.4. Crystal structure

True phenocrysts and quartz eyes are damaged by electron beam in different ways. Quartz phenocrysts appeared to be less damaged; they show shallow silica outgrowths with smooth surfaces (Fig 4-21a), whereas quartz eyes have higher outgrows with shagreen-like surfaces (Fig 4-21b). Outgrowths from the Taupo sample show homogeneous dark CL (Figs 4-21e), whereas silica outgrowth from quartz eyes are brighter, and have even brighter rims (Figs 4-21f). Different responses on damage from electron beam may indicate differences in the lattice structure and thus their origins.

7.1.5. Do quartz eyes and quartz phenocrysts have a different origin?

Differences between quartz eyes from porphyries and quartz phenocrysts from volcanic rocks implies different crystallisation conditions. The most significant difference between intrusive and extrusive rocks is that the former originate from slowly cooling magmas, whereas the latter are products of quenched magmas. We infer that quartz phenocrysts may reflect conditions of crystallisation in magma chamber prior to eruption, and quartz eyes from porphyries characterise magma evolution during prolonged cooling after magma emplacement. Taking into account felsic to intermediate composition of mineralised porphyry stocks, it may be further assumed that quartz eyes are likely to crystallise after significant fractional crystallisation (at least for stocks of intermediate composition), which is necessary to produce more silica-saturated melts to trigger crystallisation of quartz. Thus, it is probable that quartz eyes crystallise in-situ after magma emplacement from evolved magmas. Abundance of well-preserved quartz clusters and silica rims around them, which have the same optical extinction (Fig 4-3), are in a good agreement with in-situ crystallisation of quartz eyes.

7.2. What are quartz eyes?

7.2.1. Diversity of quartz eye shapes

Quartz eyes within a single thin section show different morphologies and CL patterns. Variety of shapes are usually attributed to magmatic resorption. For example, Vernon (1977) believed that '*the rounded and embayed shapes must have been formed at the magmatic stage, regardless of their exact mechanism of origin*' and explained variety of shapes by magmatic resorption, which is '*typically capricious*' and can result in '*rounding and embaying some phenocrysts in preference to others and even selecting parts and corners of individual phenocrysts'*. However, the CL textures of quartz eyes in this study show that CL bands are parallel to grain surfaces even around embayments (Figs 4-5 and 4-6), and that excludes resorption as a cause of variety of crystal shapes.

Another explanation for variety of quartz eye shapes is different origin of adjacent grains. For example, some of quartz eyes can crystallise as syn- or post-tectonic porphyroblasts, whereas others can form during hydrothermal alteration (Hopwood, 1976; Lentz and Goodfellow, 1993). However, absence of typical metamorphic assemblages, and the fact that the samples are fresh and unaltered rule out this assumption.

We assume that development of different shapes could occur in-situ during prolonged crystallisation within evolving melt. This is consistent with experimental data of MacLellan (1991), who observed several quartz morphologies within run products of experiments on crystallisation of quartz from haplogranodiorite melt at 597-850°C and 1 kbar. In their experiments quartz crystallised 'as euhedral hexagonal dipyramids, skeletal crystals, anhedral crystals, granophyric intergrowths, micropoikilitic quartz, and as a component of spherulites' depending on initial degree of undercooling and duration of the experiments. The authors concluded that several quartz morphologies can form in a single environment under conditions of continuous non-equilibrium cooling, and that the sequences of the formation depend on cooling rates.

7.2.2. Diversity of CL patterns

Diversity of CL textures within a single thin section is usually assigned to multi-cycle crystallisation, when every cycle includes a period of resorption and regrowth. Such conditions may accompany multi-stage magma ascent (Müller, 2000) or associated with magma rejuvenation (Shane et al., 2008; Wark et al., 2007; Wiebe et al., 2007). However, we proposed that in-situ prolonged crystallisation from magmas being gradually enriched in volatiles, silica and metals with time, may produce such diversity of CL patterns within adjacent quartz eyes. The mechanism of formation of such diversity will be described later in section 7.5.1.

In a similar way to the internal textures of separate quartz eyes, internal patterns of clusters can also be different within a thin section: e.g. a cluster with high Ti rim can be adjacent to a cluster without the high Ti rim (Fig 4-11). A mechanism for formation of quartz clusters in porphyries was suggested by Wiebe (2007). The mechanism includes:

- Clustering of grains crystallised in different environments.
- Reduction of porosity by further crystallisation from interstitial melt.
- Dissolution along a cluster boundary (dissolution along established quartz-quartz contacts is hindered).
- Crystallisation of high in Ti rims at higher temperatures.

However, CL patterns of quartz clusters in our study are inconsistent with suggested mechanism. In many cases attached grains within a cluster have identical patterns, often with CL layers continued from one grain to another (Figs 4-7b and 4-11d, f and g). Such patterns indicate that quartz grains were attached during their growth, rather than attaching after crystallisation in different environments. Other

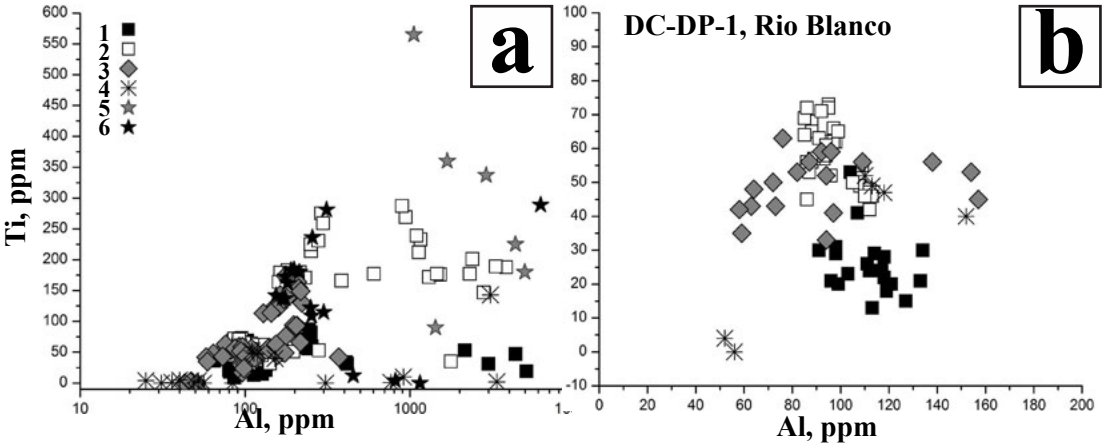

1 - CL-dark cores
2 - CL-bright rims
3 - grains with no core-rim pattern
4 - secondary quartz
5 - outmost and CL-brighest spots within rims
6 - groundmass quartz

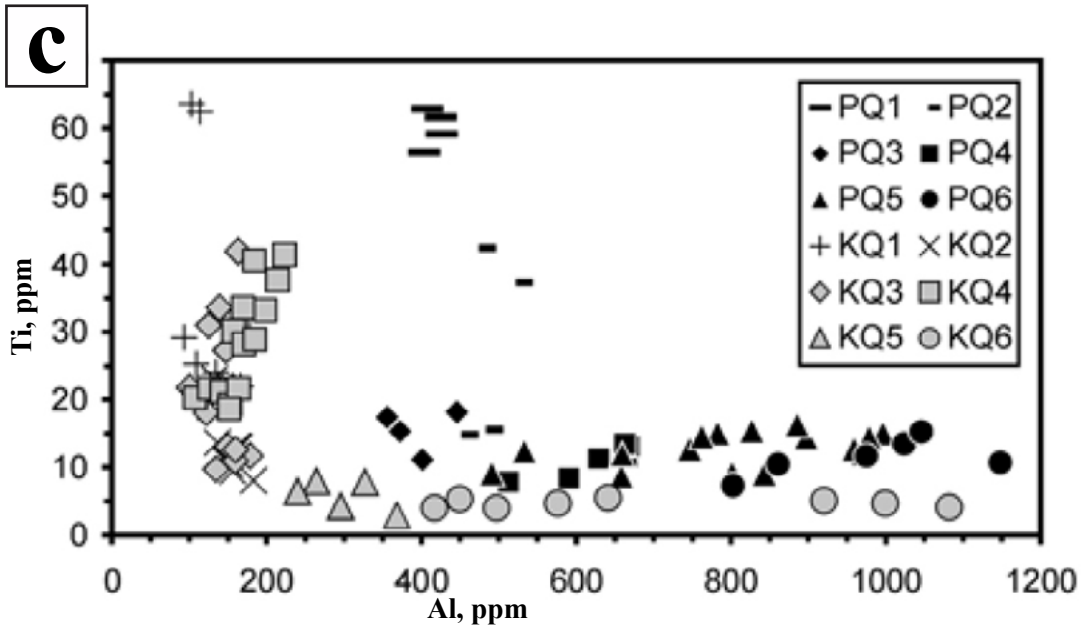

PQ1	Sub-euhedral quartz phenocrysts (1–5 mm); fine-grained groundmass quartz (0.1–2 mm)
PQ2	
PQ3	Interstitial pegmatitic quartz (0.5–5 cm)
PQ4	Snowball quartz (0.2–1.5 mm)
PQ5	Late comb quartz in UST layers (0.5–2 cm)
PQ6	Comb quartz (1–5 mm) growing around granite clasts
KQ1	Drop-like quartz phenocrysts (0.5–2 mm)
KQ2	Anhedral groundmass quartz (0.2–3 mm)
KQ3a	Euhedral quartz phenocrysts (1–3 mm)
KQ3b	Broken sub-euhedral quartz xenocryst (> 3 cm)
KQ4	Early comb quartz in UST layers (0.5–3 mm)
KQ4	Early comb quartz in UST layers (0.5–10 mm)
KQ5	Drop-like groundmass quartz (0.2–1 mm)
KQ6	Late comb quartz in UST layers (0.3–2 cm)

Figure 7-2 Al vs Ti concentrations in the studied samples compared with published data (Breiter and Müller**, 2009)**
(a) - Ti vs Al in all studied samples, (b) - Ti vs Al in sample DC-PD-1, Rio Blanco, (c) - data from (Breiter and Müller, 2009)

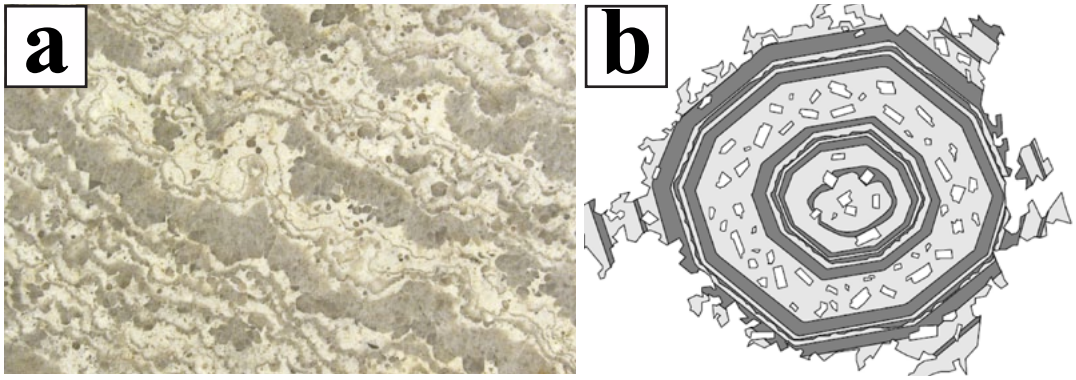

Figure 7-3 Examples of comb and snowball quartz
z(a) - photograph of comb quartz from Sinclair (2007), (b) - snowball quartz, a sketch from Müller (2002).

clusters have the attached grains with different patterns but they form a single shape and show no sign of dissolution (Fig 4-11b, e) that indicates that they grew being attached.

7.2.3. Composition of quartz eyes

Trace element data showed that quartz eyes contain Ti, Al, Fe and Li well above their detection limits. CL internal zoning is well correlated to Ti content: the higher the Ti concentration, the brighter quartz in CL. This is consistent with other published data (D'Lemos et al., 1997; Götze, 2009; Müller, 2000; Penniston-Dorland, 2001; Peppard et al., 2001; Rusk et al., 2008; Rusk et al., 2006; Wark and Spear, 2005).

Low CL intensity zones (CL-dark) are usually restricted to cores, although in some cases, dark zones occur in irregular areas or discrete layers (Fig 4-6). Dark zones are often characterised by extremely low Ti concentrations (9-30 ppm, Fig 7-2). Such low CL intensity and low Ti content are unusual for magmatic quartz; Ti concentrations higher than 40 ppm are usually mentioned for magmatic quartz (Allan and Yardley, 2007; Müller, 2000; Rusk et al., 2006; Wark et al., 2007; Wiebe et al., 2007). Rarely, Ti content in magmatic quartz is less than 40 ppm, for example, average Ti content in drop-like quartz phenocrysts in Hora Svatéť Kateřiny granite, Czech Republic (Fig 7-2) is 37.7 ppm, and it is even lower in other types of quartz, which crystallised from more evolved melt: 26-32 ppm in comb-quartz and 13 ppm in groundmass quartz (Fig 7-2). Hydrothermal quartz usually shows very low CL intensity and Ti concentration below detection limit (Allan and Yardley, 2007; Breiter and Muller, 2009; Lehmann et al., 2009; Müller, 2000; Rusk et al., 2006).

Titanium-in-quartz geothermometer (Wark and Watson, 2006) allowed estimation temperatures of quartz crystallisation, which are as low as 560-670°C for

quartz cores with Ti content from 9 to 30 ppm (at activity of Ti equal to 0.6).

Dark CL cores sometimes show higher Al concentrations than bright rims (Fig 7-2b). Some dark cores in our study contain thousands ppm of aluminium (Fig 4-23, sample DC-DLP-1, Rio Blanco). Increased Al is characteristic of quartz from highly evolved and flux-enriched magma batches (Breiter and Muller, 2009). For instance, comb and snowball quartz (Fig 7-3) show higher Al content than quartz phenocrysts (Fig 7-2c). Both comb and snowball quartz types are widespread in highly evolved granites and believed to be textural indicators for fluid-saturated melts (Lowenstern and Sinclair, 1996; Müller, 2000). Comb quartz crystallises within Unidirectional Solidification Textures (UST) in magma carapaces (Harris et al., 2004). Snowball quartz is 'characterises by zonal arrangement of entrapped matrix minerals' and crystallises within 'a nearly non-convecting and fluid-saturated crystal mush at a temperature of <600°C' (Müller et al., 2002a).

In many cases dark cores show sector zoning (Fig 7-6). Observed sector zoning is mostly determined by variations in Ti content and to a less extent Al concentrations. FT-IR spectroscopy showed that quartz eye cores with sector zoning are also rich in Al-OH and Li-OH defects (Fig 4-34). Sector zoning has never been observed in magmatic quartz phenocrysts (Müller, 2000), but it is a common feature in hydrothermal quartz (Allan and Yardley, 2007; Ihinger and Zink, 2000; Müller, 2000) and agates (Götze et al., 2009). Sector zoning is an indicator of rapid growth under non-equilibrium conditions (Götze et al., 2009; Ihinger and Zink, 2000). '*If the fluid and crystal were to grow under equilibrium conditions, the loosely bound impurities would be rejected by the advancing solid ± fluid interface. However, when the crystal grows at a rate too fast to maintain equilibrium, impurity concentrations will increase with increasing growth rate and result in chemically distinguishable sector zones' (Ihinger and Zink, 2000).*

Sector zoning in hydrothermal quartz can be caused by different uptake of trace elements along different faces due to different growth rates; faces that grow rapidly have higher concentrations of trace elements than faces that grow slow (Allan and Yardley, 2007). Some faces can be more reactive than others because of the higher number of free bonds; at such faces foreign ions are preferably adsorbed (Müller, 2000). However, at high temperatures (close to the temperatures of magmatic crystallisation) all faces take up foreign ions in similar proportions, and development of sector zoning becomes unlikely (Müller, 2000).

Thus, sector zoning together with trace element (high Al and OH^-, low Ti)

distribution in quartz eye cores show that they have more similarities with hydrothermal quartz than with magmatic phenocrysts. However, their hydrothermal origin seems improbable. If quartz eyes were hydrothermal then CL mapping would show veinlets or healed fractures in their closest vicinity, which could provide a path for a hydrothermal fluid at the time of quartz precipitation from a fluid.

Quartz eye cores with sector zoning are overgrown by Ti-high rims often with pronounced oscillatory zoning, which is believed to be an indicator of magmatic conditions (Müller, 2000; Wiebe et al., 2007). Estimation of crystallisation temperatures of quartz by titanium-in-quartz geothermometer (Wark and Watson, 2006) showed that quartz rims crystallised at very high temperatures: up to 970^{o}C (269 ppm, sample DC-DLP-1, at activity of Ti equal to 0.6). Oscillatory zoning is caused by self-organised diffusion-controlled mechanism on the crystal-melt boundary layer (Müller, 2000). Formation of CL-bright rims around CL-dark cores is usually explained by crystallisation at higher temperature due to magma rejuvenation, or remelting of crystal mush caused by an injection of hot mafic dykes (Wark et al., 2007; Wiebe et al., 2007). However, rejuvenation or remelting must have an effect on all quartz grains so that adjacent crystals should have similar rims. On the contrary, quartz eyes within a single thin section often show different rims (Figs 4-5 and 4-6).

Titanium distribution in the studied samples is inconsistent with Ti pattern from other published studies. For example, Breiter (2009) showed that in two different granite suites Ti concentrations in quartz phenocrysts always exceed that in groundmass. An opposite pattern was observed in our samples: groundmass quartz has always higher Ti content (brighter CL) than quartz eyes (Figs 4-25 and 4-26), and within quartz eyes Ti is often higher in rims than in cores (Fig 4-27). High Ti content (bright CL) usually indicates crystallisation at higher temperatures (Wark and Spear, 2005; Wark and Watson, 2006). In our study the distribution of Ti, Al, Li and OH^- within some of the quartz eyes implies that quartz eye cores crystallised at lower temperatures conditions and from more evolved melts (they are richer in Al, Li and H_2O) than quartz eye rims. Our data on trace element distribution within groundmass quartz can imply that it crystallised at higher temperatures than both quartz eye cores and rims. It appears that the grains with high Ti rims and high Al cores had an inverse thermal evolution trend. If quartz eyes crystallised at deeper conditions at higher temperatures than groundmass quartz, then Ti distribution would show different patterns, e.g. patterns of Ti distribution obtained by Breiter (2009). Crystallisation at higher temperatures due to injection of hot mafic magmas was suggested by many authors to explain CL-bright rims (Müller, 2000; Rusk et al., 2006; Wark et al., 2007; Watt et al., 1997; Wiebe et al.,

2007), however, it is inconsistent with the observed CL patterns, which showed that not all the quartz eyes have high Ti rims (Fig 4-6).

7.2.4. Similarities of textures with agates

Cathodoluminescence mapping (SEM-CL) shows that the observed internal textures of quartz eyes are similar to internal patterns of agates (Figs 7-4 and 7-5). For example, quartz eyes and agates sometimes show multiple crystallisation centres on their boundaries (Fig 7-4 a and a'). Small crystals grown on quartz eye boundaries often have the CL pattern, which may indicate growth inwards (Fig 7-4 a', white arrows); growth patterns within the quartz eyes next to the small boundary crystals show similar growth direction (black arrows in Fig 7-4 a').

Double zoning is often observed in both agates and quartz eyes (Fig 7-5). Double zoning is a pattern, which includes crosscutting relationships of two different zones. For example, the purple zone in the agate in the Figure 7-5 (a) has crescent-like shape and localises only within the left half of the agate, whereas thin white layers continue from the purple zone into the pink zone (Fig 7-5c, shown by an arrow). Similar crosscutting relationships are observed in quartz eyes (Fig 7-5b, d).

Lobe-like shape of clusters is characteristic for both quartz eyes and agates (see Fig 7-4 c and c'). Deep tubular embayments typical for quartz eyes are also observed in agates (see Fig 7-4 d and d'). In agates such channels are called 'outburst' channels (Elliston, 2005). Unlike tubular embayments in quartz eyes, 'outburst' channels in agates point outwards (Fig 7-4).

There is interplay between primary growth zones and fractures in the both quartz eyes and agates (see Fig 7-4 b and 'b'). Such interplay was described in details in section 4.2.2.3. There is similar influence of fractures on banding in agates: fractures change the geometry of layers (Fig 7-4). Unlike layers in quartz eyes, layers in agates inflect outwards (Fig 7-4).

A number of quartz grains with CL pattern of type 1 show a sector growth in cores. Examples of sector growth in quartz are shown in Figure 7-6 in the quartz grains from samples DC-DP-1 (Fig 7-6a) and CA6 (Fig 7-6b, c), Rio Blanco. They also display fine concentric oscillatory zones, which crosscut the sector growth zones (Fig 7-6a-c). Sector growth is also very common in hydrothermal quartz (Fig 7-6e) and agates (Fig 7-6d, f).

There is a number of suggested hypotheses for formation of agates, which involve different sources for silica and mechanisms of deposition, such as precipitation

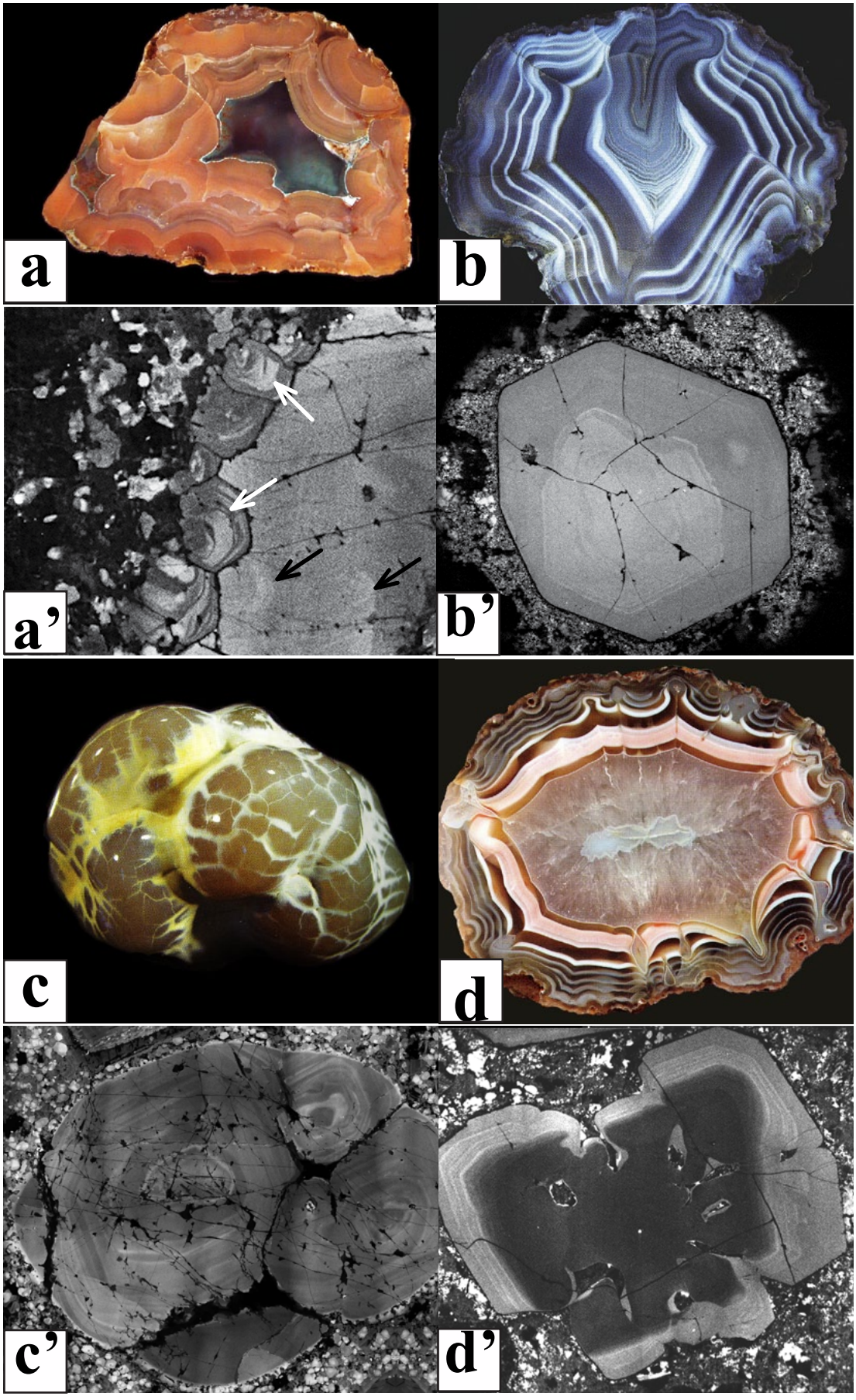
a
b
a'
b'
c
d
c'
d'

Figure 7-4 Similarity between the CL pattern shown by quartz eyes and internal textures of agates
(a-e) images of agates from 'Agates' by Zenz (2005). (a'-e') - CL images of quartz eyes: a' - sample 109644 from Climax, b' - sample DP-DLP-1 from Rio Blanco, c' - sample SBD-69 from Batu Hijau, d' and e' - DC-DP-1 and CA6 from Rio Blanco.

from true solutions, recrystallisation from silica glasses or silica gels (Moxon, 1996). However, it can only be safely stated that agates form as a result of nucleation and growth of microcrystalline silica within cavities in volcanic rocks. Such growth occurs inward, from vug walls towards centres. The silica sources, mechanisms of its transport and deposition largely remain unanswered (Moxon, 2002). It is widely accepted that temperatures of agate formation are usually lower that 100 °C (Heaney and Davis, 1995; Moxon et al., 2006), though in some cases temperatures higher than 375 °C were proposed (Moxon, 2002). Although temperatures of crystallisation of quartz eyes

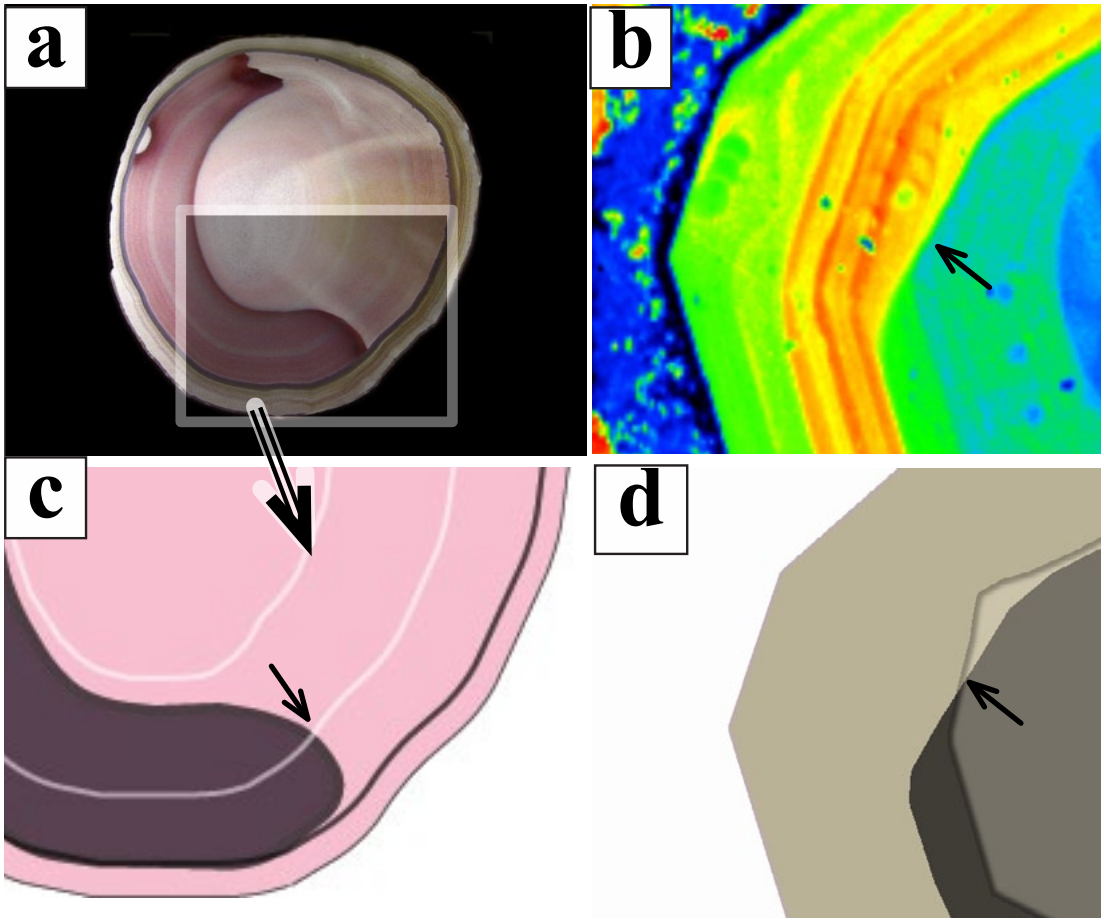

Figure 7-5 Double zoning in agates and quartz eyes
(a) - photograph of an agate from 'Agates' by Zenz (2005), (b) - hyperspectral CL map of the grain DP-DC-1 (Rio Blanco). (c, d) - simplified sketches of (a, b) showing crosscuting of CL layers (see arrows).

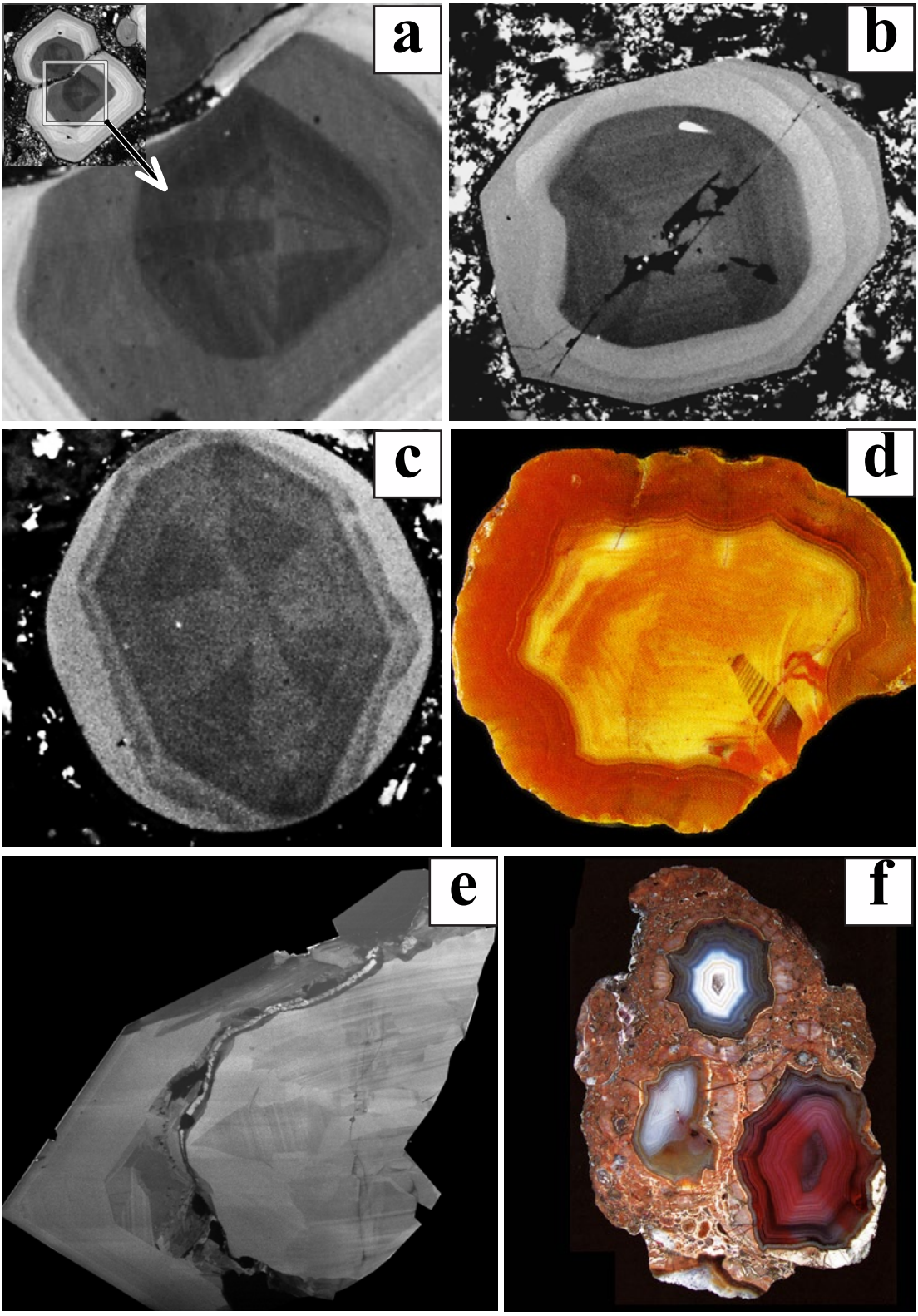

Figure 7-6 Sector zoning in quartz eyes, hydrothermal quartz and agates
(a-c) - quartz eyes: (a) - DC-DP-1, Rio Blanco, (b, c) - CA 6, Rio Blanco. (e) - hydrothermal quartz from Yaogangxian Mine. (d, f) - agates. Images of agates are from the book 'Agates' by Zenz (2005).

are significantly higher, and crystallisation environments are different, the similarities in internal textures may indicate that some of the processes, which led to formation of agates and quartz eyes are similar.

7.2.5. Summary on conditions of crystallisation of quartz eyes

Thus, internal textures of quartz eyes are only partially consistent with magmatic origin. They are distinctly different from quartz phenocrysts crystallised within convecting magma at deep levels. Quartz eyes contain different inclusion assemblages, show different CL patterns and trace element distributions, which are often inconsistent with normal thermal evolution trend. Such differences in inclusions and internal textures imply different origin. Unlike quartz phenocrysts, quartz eyes crystallise in-situ after magma emplacement from the residual melt, which is significantly enriched in water, alkalis and silica. Crystallisation of quartz eyes in a water-rich environment is consistent with the observed CL textures and distribution of trace elements; it can also be implied from the similarities of the textures between in agates and quartz of hydrothermal origin.

7.3. What are fluid inclusions in quartz eyes?

7.3.1. Primary or secondary?

This study demonstrated that inclusions in quartz eyes are distributed along healed fractures. On the other hand, healed fractures, which are associated with fluid inclusions and sometimes sulphides (Fig 6-6), do not extend beyond quartz eye boundaries. Minerals associated with sulphides within healed fractures (calcite, apatite and epidote) are also distributed in quartz eyes only, e.g. they are absent in the groundmass immediately surrounding quartz eyes. Significant amount of fluid must circulate through fractures in order to precipitate secondary quartz and associated minerals. In this case, though, fractures and their content would be distributed through the whole rock, not restricted to quartz eyes. Distribution of secondary quartz, sulphides and associated minerals strictly within quartz eyes indicate that either the processes, which led to formation of those secondary textures, occurred only within quartz eyes, or quartz eyes were transported from the environment in which they crystallised. The latter possibility is unlikely because it is inconsistent with well-preserved clusters and the other evidences (described earlier) in favour of in-situ crystallisation.

7.3.2. Post-entrapment modifications

It was proposed that CL-dark secondary quartz forms as a result of a two-stage process (Fig 7-1): firstly, massive decrepitation of fluid inclusions occurs, and secondly, recrystallisation of host quartz and release or replacement of defect centres takes place (see Fig 7-1, Müller, 2000; Müller et al., 2002a; Müller et al., 2002b; Van den Kerkhof et al., 2004). Such mechanism is in a good agreement with the obtained data: it explains why fluid inclusions have halos and are distributed along healed fractures. It also explains why fractures are distributed within quartz only.

However, if this mechanism operates in porphyry environments it indicates that fluid inclusions in quartz eyes are partially decrepitated. Moreover, since the mechanism involves inevitable massive decrepitation (e.g. as a result of α/β-transition or up-lift) and subsequent recrystallisation of host quartz, there is a little chance that the initial composition of inclusions is preserved. Thus, fluid inclusions in quartz eyes underwent post-entrapment modifications, and therefore, the fundamental assumption that fluid inclusions behave as compositionally and volumetrically closed systems after the entrapment is invalid. This means that we cannot interpret the 'messages' from fluid inclusion 'bottles' (Clemens, 2009) correctly, and hence, fluid inclusions from quartz eyes cannot be used for proxies for fluid compositions or for P-T estimations of conditions for crystallisation of the host quartz eyes.

On the other hand, suggested mechanism for formation of secondary quartz implies that quartz contained abundant fluid inclusions before the decrepitation, and thus, the inclusions could be primary. Therefore, fluid inclusions still provide some useful constraints on the composition of the primary fluid, or at least on the conditions of precipitation of secondary quartz.

7.3.3. Fluid composition

It is generally assumed that fluid inclusions are trapped aliquotes of aqueous solutions that transport metals as chloride complexes (Roedder, 1984; Skinner, 1979). Although natural fluids are in most cases multi-component, their properties are assumed to be similar to those of a simple NaCl-H_2O system (Roedder, 1984). This assumption is fundamental for the existing models of formation of porphyry-type deposits (Candela and Piccoli, 1995; Cline and Bodnar, 1991; Cloos, 2001; Eastoe, 1978; Shinohara et al., 1995).

Our data showed that the composition of fluid inclusions from quartz eyes is significantly different from the model fluid. LA-ICP-MS analyses demonstrated that

studied fluid inclusions contain Al, Na, K, Fe, Mn, Cl, S, W, Pb, Cu, Zn, Ca, Ag, Sn, Bi and Rb above their detection limits. The element ratios varied significantly within adjacent inclusions (Fig 5-14). Liquid-rich inclusions are usually chlorine-rich, and sometimes are B-rich (Fig 5-14a, c). Inclusions often contain high concentrations of Zn, Rb and Sr. Vapour-rich inclusions are often S- and Al-rich and Cl-poor, and sometimes with higher Cu/Zn, Cu/Rb and Cu/Sr ratios than in liquid-rich and multiphase inclusions. Multiphase inclusions demonstrate very broad peaks (Fig 5-14 e-h), with the same set of the major elements except Al (very low).

7.3.4. Fluid behaviour

If the studied fluid had similar properties to the model one, and thus could be described by simple NaCl-H_2O system, then we should observe similar behaviour to NaCl-H_2O fluid upon heating and cooling. However, our microthermometry results demonstrated atypical behaviour of the fluid. For instance, swirling of phases upon heating and multiple immiscibility episodes upon cooling (Figs 5-10 - 5-12) were observed. Swirling took place at rather low temperatures, 80-120°C, within the phases that appeared to be solid before heating (Figs 5-10 - 5-12). Swirling may indicate that those phases are immiscible liquids rather than solids. Every immiscibility episode led to separation of a phase, which appeared to be initially liquid-like and later could gradually reshape to form crystals.

7.3.5. How can we use fluid inclusions from quartz eyes?

Fluid inclusion study showed that inclusions are partially decrepitated; they contain multi-component fluid of varying composition, and show extremely complex fluid behaviour upon heating and cooling. In this case the fundamental assumption that inclusion compositions and volumes did not change after entrapment is invalid. Moreover, composition of fluid inclusions are extremely complex, and fluid properties cannot be described by the simple NaCl-H_2O system. Apparently, interpretation of the data based on the knowledge of the properties of NaCl-H_2O or other simplified system would lead to erroneous results, and thus inappropriate.

If we cannot use fluid inclusion in traditional way a question about how can we use the data arises. Although it is impossible to model fluid properties with the data we obtained, we believe that we can at least partially model the fluid behaviour upon cooling. Precipitation of ore minerals can occur by many mechanisms, such as boiling, chemical reactions with host rocks, etc., but in most cases all those processes are accompanied by general cooling of host rocks, and thus the knowledge on how fluid behaves at decreasing temperatures may be very important.

7.4. Heavy fluid

Microthermometry experiments showed that upon cooling fluids undergo a series of immiscibility episodes and several immiscible non-crystalline phases can be in equilibrium in inclusions. Similar phenomena were observed by Kotel'nikova (2010a, b) within fluid inclusions synthesised in H_2O-Na_2SO_4-SiO_2 and H_2O-NaF-SiO_2 systems at 700-800°C and 1-3 kbar. They observed formation of a non-crystalline phase contained substantial amount of silica (a heavy fluid) upon heating, when heterogeneous sulphate or fluoride fluids reacted with silicate materials and form sodium hydrosilicates (Kotel'nikova and Kotel'nikov, 2010a, b). From the behaviour of the heavy fluid they concluded that at decreasing temperatures the fluid can undergo fractional crystallisation or can be subjected to a series of immiscibility events, which can lead to formation of a highly mineralised phase at low temperatures. Since the heavy fluid phase is enriched in both silicate and metals, its formation provides a mechanism to transport both ore and gangue components (Kotel'nikova and Kotel'nikov, 2010b).

A number of other published studies have shown the existence of silica-, water- and alkali-rich phase at a wide range of temperatures (250-800°C), pressures (0.5-2.5 kbar and >15 kbar) and within different systems in natural environments and in experiments (Ganeev, 1971; Peretyazhko et al., 2010; Peretyazhko et al., 2004; Sirbescu and Nabelek, 2003; Taylor, 2005; Taylor et al., 2004; Thomas and Davidson, 2008; Thomas et al., 2000; Thomas et al., 2010; Tuttle, 1953; Tuttle and Friedman, 1948; Wilkinson et al., 1996; Williamson et al., 1997; Williamson et al., 2002).

Thomas (2008; 2000) showed that during cooling of highly fractionated residual melts, melt-melt immiscibility may occur, and relatively H_2O-poor peraluminous type A melt may coexist immiscibly with extremely H_2O-rich peralkaline type B melt. After separation, each phase evolves independently during further cooling, and multiple exsolution events are possible within every phase (Thomas and Davidson, 2008; Thomas et al., 2000). These two melts have extremely divergent properties, such as density, viscosity, wetting behaviour and melt structure, and can separate easily under gravity or filter pressing (Thomas and Davidson, 2008). Unlike type A melt, type B melt (30 wt% SiO_2, 12 wt% Na_2O and up to 50 wt% H_2O) is highly mobile, and migrates easily (Thomas and Davidson, 2008). In pegmatite systems type B melt can migrate inwards and forms a quartz pegmatite core. Thomas (2008) hypothesised that further evolution of type B melt can lead to formation of silica gel, which forms the quartz cores in pegmatites where giant rare minerals crystallise.

During experiments by Ganeev (1971) a vitreous phase containing different proportions of H_2O, SiO_2 and Na_2O (called '*heavy phase*') formed as a result of immiscibility in experiments at 250-350°C and pressures 200-1400 bar in H_2O-SiO_2-NaOH system and at 300-400°C in H_2O-SiO_2-Na_2CO_3 system. The author concluded that this phase is a coagulated silica gel formed from a silica saturated solution due to its polymerisation.

A clear water-soluble glassy phase was obtained in the experiments on quartz solubility in the systems H_2O-Na_2O-SiO_2 by Tuttle (1948). The authors concluded that this glassy phase is liquid at the temperatures of the experiments, immiscible with alumosilicate melt and/or supercritical fluid, and quenches into clear glass (Tuttle and Friedman, 1948). This phase can contain 10-55 wt% SiO_2, 5-20 wt% Na_2O and 25-85 wt% H_2O and change its properties dramatically from highly soluble phase with a hardness of about 2.5 at 250 °C to brittle and barely soluble with a hardness of approximately 5 at 350 °C. The viscosity of the quenched heavy phase changed continuously from a glass to a liquid (Tuttle and Friedman, 1948).

Formation of a '*melt-like gel*' phase was established as a result of experiments with the system Na_2O-SiO_2-B_2O_3-H_2O at 500-650°C and 1.5-2 kbar (Peretyazhko et al., 2004). The phase contained 53-62 wt% SiO_2, 14-17 wt% Na_2O and up to 15 wt% H_2O) and quenches to a transparent glass. The authors suggested that this phase is an alkali silica gel, and emphasised that high-temperature gels are the perfect media for metal transport and crystal growth. They concluded that high-temperature gels can form in hydrothermal systems '*as a result of successive polymerisation and further gelling of dissolved silica, alumina and other components*'. They also suggested colloid origin for the natural inclusions in quartz from pegmatites, which show abnormal concentrations of major oxides and high concentrations of trace and ore components (Peretyazhko et al., 2004).

'Silicothermal' fluid (Wilkinson et al., 1996) similar to the fluids described above, formed during synthesis of fluid inclusions in K_2O-CO_2-SiO_2-H_2O system at 300-750°C and 1-2 kbar. The 'silicothermal' fluid is a glassy potassic- and silica-rich (up to 90 wt% SiO_2+K_2O) phase that can coexist with supercritical fluid at the parameters of the experiments (Wilkinson et al., 1996). The authors believed that such fluid may be highly efficient in metal transport, especially for lithopile elements, such as K, Cs, Ba and metals of economic significance, such as Au.

Formation of a hydrosilicate liquid (HSL) was observed in experiments in the systems Na_2O-SiO_2-H_2O and rare-element granite-H_2O at 600°C and 1.5 kbar (Thomas

et al., 2010). As a result of the experiments alkaline fluid reacted with SiO_2 and Al_2O_3 and polymerised forming drops of HSL. During rapid cooling (50°/hr) skeletal quartz and albite grew within HSL. The authors noted that '*crystal growth in HSL has much in common with crystal growth in gels (Henisch, 1996)*'. During further cooling the nucleation of a subsequent generation of HSL droplets was observed.

Thus, type B melt, 'heavy phase', 'melt-like gel', 'silicothermal' fluid or 'hydrosilicate' liquid are different names for phases enriched in silica, alkalis and volatiles, which may coexist with a melt and aqueous fluid, and may have gel-like structure (Ganeev, 1971; Peretyazhko et al., 2004; Wilkinson et al., 1996) or convert into gel during cooling (Thomas and Davidson, 2008). Having H_2O concentrations from 5 wt% to more than 50 wt% such phases do not strongly resemble melts, but with silica concentrations sometimes greater than their H_2O concentrations they have little resemblance to solutions. In the absence of a widely accepted term such phases will be called 'heavy fluid' hereafter.

Formation of heavy fluid is a well-known phenomenon described by many researches (see references above). Heavy fluid can form as a result of melt-melt immiscibility in silica-, water- and alkali-rich melts during late magmatic – early hydrothermal (=transitional) stages. Moreover, '*immiscibility need not be a single event; multiple exsolution events are possible as long as the alumosilicate melts are H_2O rich, since each new immiscible phase has a distinct composition, and will evolve independently down-temperature*' (Thomas and Davidson, 2008). Quartz is the main product of crystallisation of the B-melt, because silica is one of the main constituents. Therefore, upon cooling heavy fluid crystallises to quartz, which contains fluid inclusions, i.e. water, metals and alkalis expelled during crystallisation of quartz. We believe that at least some of quartz eyes formed as a result of formation and evolution of the heavy fluid. Such origin of the quartz eyes is more consistent with fluid inclusion data and internal textures observed in this study.

7.5. Formation of quartz eyes: the alternative model

We propose that after magma emplacement as a result of fractional crystallisation the residual melt is enriched in silica, alkalis, metals and volatiles. According to Veksler (2004) crystallisation and immiscibility are competitive processes; liquid immiscibility is enhanced in peralkaline systems and in the presence of non-silicate anions such as F^-, Cl^-, CO_3^{2-} and BO_3^{3-}. Thus, immiscibility is enhanced in the residual melt in porphyry systems.

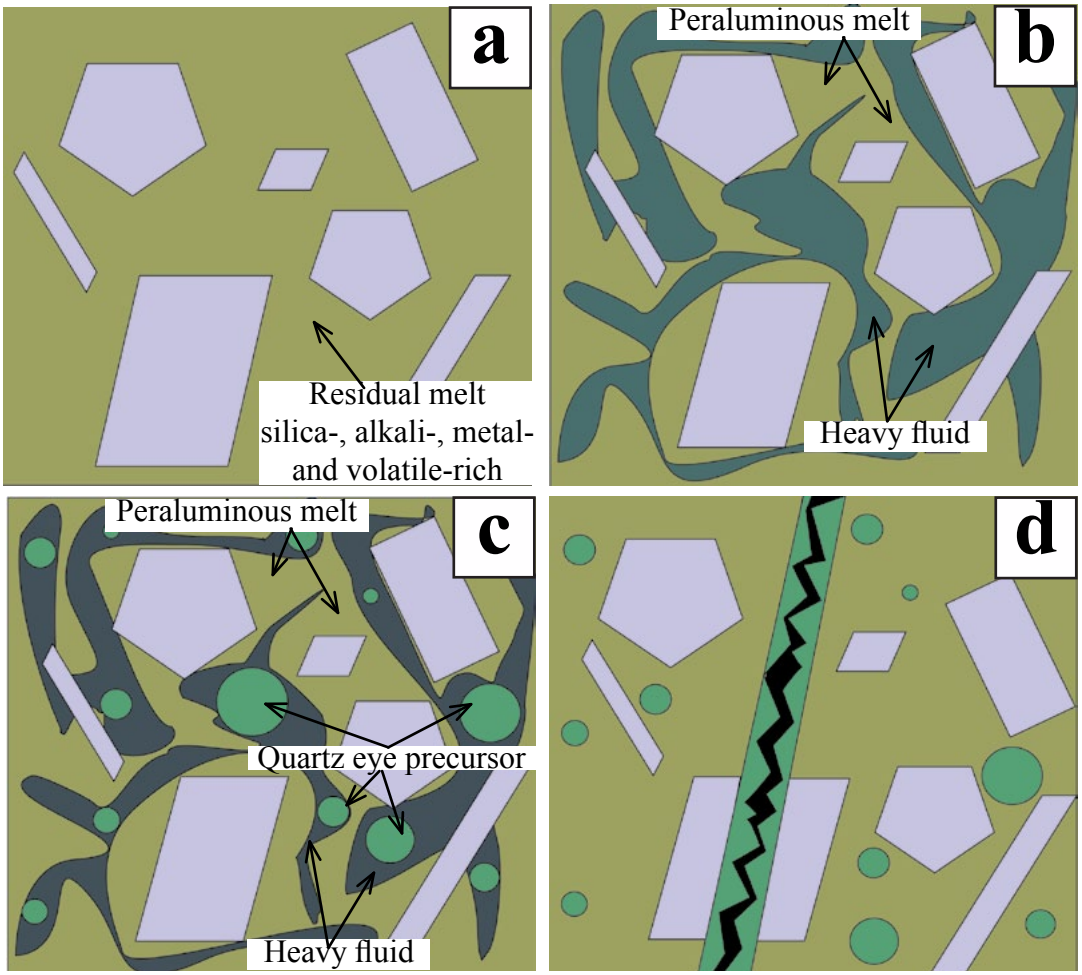

Figure 7-7 The alternative model for crystallisation of quartz eyes and formation of mineralising fluid

(a) - as a result of fractional crystallisation residual melt is enriched in silica, alkalis, metals and volatiles, (b) - the first immiscibility occurs separating peraluminous melt and heavy fluid, (c) - next immiscibility provokes formation of quartz eyes, (d) - the rest of the heavy fluid moves to fractures and forms stockwork quartz and aqueous fluids.

As a result of the early immiscibility event silica-, water- and alkali-rich substance, a heavy fluid, can form and coexist with the silicate melt (Fig 7-7a, b). Further cooling causes silica oversaturation and since crystallisation within heavy fluid is hindered (because of high concentrations of non-silicate anions) next immiscibility can occur, which leads to the separation of the excess of the silica within the heavy fluid. The newly formed phase can contain up to 90wt% of silica as was observed in experiments of Wilkinson (1996). From this phase quartz eyes form (Fig 7-7c), whereas the rest of the heavy fluid undergoes other immiscibility events; each of them can lead to separation of silica-rich phase and its subsequent crystallisation into quartz. Due to the removal of silica access concentration of alkalis, volatiles and metals within heavy fluid increases. Moreover, it becomes less viscous, more mobile, and migrates readily.

We suggest it moves into fractures, where during further cooling and subsequent silica oversaturation it may undergo further immiscibility and form stockwork quartz and aqueous fluids (Fig 7-7d).

7.5.1. Crystallisation from a heavy fluid

Melts are characterised by interactions between atoms or molecules (often with short distance order); gels are defined as a network of particles of one phase suspended in another liquid phase. During early stages of its formation heavy fluid most likely has a melt-like structure (Thomas and Davidson, 2008; Thomas et al., 2009; Thomas et al., 2000; Thomas et al., 2010). However, it was also assumed that the heavy fluid can be gel-like (Ganeev, 1971; Peretyazhko et al., 2004; Wilkinson et al., 1996)structure, or convert into a gel during cooling (Thomas and Davidson, 2008). Indeed, oversaturation will inevitably occur upon cooling, and multiple centres of crystallisation may form. Since that moment the heavy fluid would behave as multiphase system, with particles of one or more phases suspended in a liquid phase, i.e. as colloidal system (a sol). Sols are unstable under most of the upper crustal conditions (Roedder, 1968) and will coagulate, transforming into a gel, and crystallising later. A residual aqueous fluid carries the amount of silica according to the silica solubility in the fluid of this composition under the conditions. Such fluid is very mobile and migrates further until next oversaturation occurs. Since temperature, pressure and composition of the fluid changes rapidly due to reaction with cold host rocks we can assume that it will be under non-equilibrium conditions most of the time, which may imply that this cycle is multiple.

As described by Elliston (2005), when crystallisation of quartz takes place in gel media, ‘close-packing’ (e.g. gathering of similar particles) occurs first, that allows reduction in total surface energy for denser clusters. Close-packing allows van der Vaal’s forces to take effect and crystallisation (syneresis) occurs. During syneresis surface water and electrolytes are expelled from crystallising gel and form brine inclusions (Elliston, 2005). Crystallisation of quartz from silica gel may occur rapidly either without any transient phases, or through very short-lived intermediate phases (such as opal) (Oehler, 1976), especially in multi-component systems (Okamoto et al., 2010), so that in most cases there are no textural evidences preserved for a former colloidal precursor (Williamson et al., 1997). Only in extremely rare cases such evidences were reported. For example, abundant spheroidal inclusion-rich quartz cores were believed to be an evidence of crystallisation of mesothermal quartz veins from an amorphous silica gel (Herrington and Wilkinson, 1993). Other textural evidences for colloidal precursors include spongy texture and tubular embayments

(Elliston, 2005), which are very common in quartz eyes. Elliston (2005) also assumed that in cases of colloidal origin adjoining ovoids can be different in size, embayment patterns, content of impurities and inclusions and that is also consistent with our data.

Crystallisation from colloid precursor was suggested for quartz from inclusions in greisen topaz (Williamson et al., 1997). Similar inclusions of quartz in topaz were also observed in this study (Fig 5-6). This suggests that at least during late stages of vein formation (topaz is interstitial in quartz veins and fills fractures in quartz eyes) fluids could be gel-like.

7.5.2. Application for formation of internal textures of quartz eyes

The phase, which separates from the heavy fluid during the early immiscibility event, forms droplets, which will evolve independently. Droplets in close proximity may start with different bulk compositions, and they may crystallise in different ways or at different points in the melt evolution, which can explain the diversity of internal textures of quartz eyes without invoking crystallisation in different environments. For example, drops of heavy fluid enriched in Ti will crystallise at high temperatures into quartz with euhedral shapes, whereas drops enriched in water, alkalis and aluminium will crystallise at lower temperatures (later) into quartz showing anhedral shapes.

We suggest that formation of quartz eyes may occur in four steps. The first step is formation of separate drops of heavy fluid (Figs 7-8, stage I). The second step is redistribution of trace element within drops driven by self-organising processes. Such redistribution leads to formation of compositional (or step) zoning within a soft globule (Fig 7-8, stage II). Next stage is partial solidification and deformation of semi-solid droplets (Fig 7-8, stage III). Plasticity of silica-rich material on this stage is consistent with the observed internal textures, such as interplay of CL layers with embayments and mineral inclusions (Figs 4-13 - 4-15). In some cases deformation of droplets can lead to formation of clusters (Fig 7-9). When solidification proceeds fractures may form. Our data showed that fracturing can occur within semi-solid material; in this case cut layers on one side of a fracture and inflecting layers on the other side are observed (Fig 4-12). Finally, deformed globules crystallise, and as a result of crystallisation oscillatory zoning forms (Fig 7-8, stage IV). Such mechanism of crystallisation is more consistent with the observed features, such as asymmetric internal pattern observed in sample DC-DLP-1 (Figs 7-8b) and double zoning observed in the quartz eyes from Climax and Rio Blanco described in the chapter 4 (Fig 4-23). Formation of double zoning by magmatic crystallisation seems unlikely, but it is consistent with the idea of crystallisation from a heavy fluid. In this case two different type of zoning

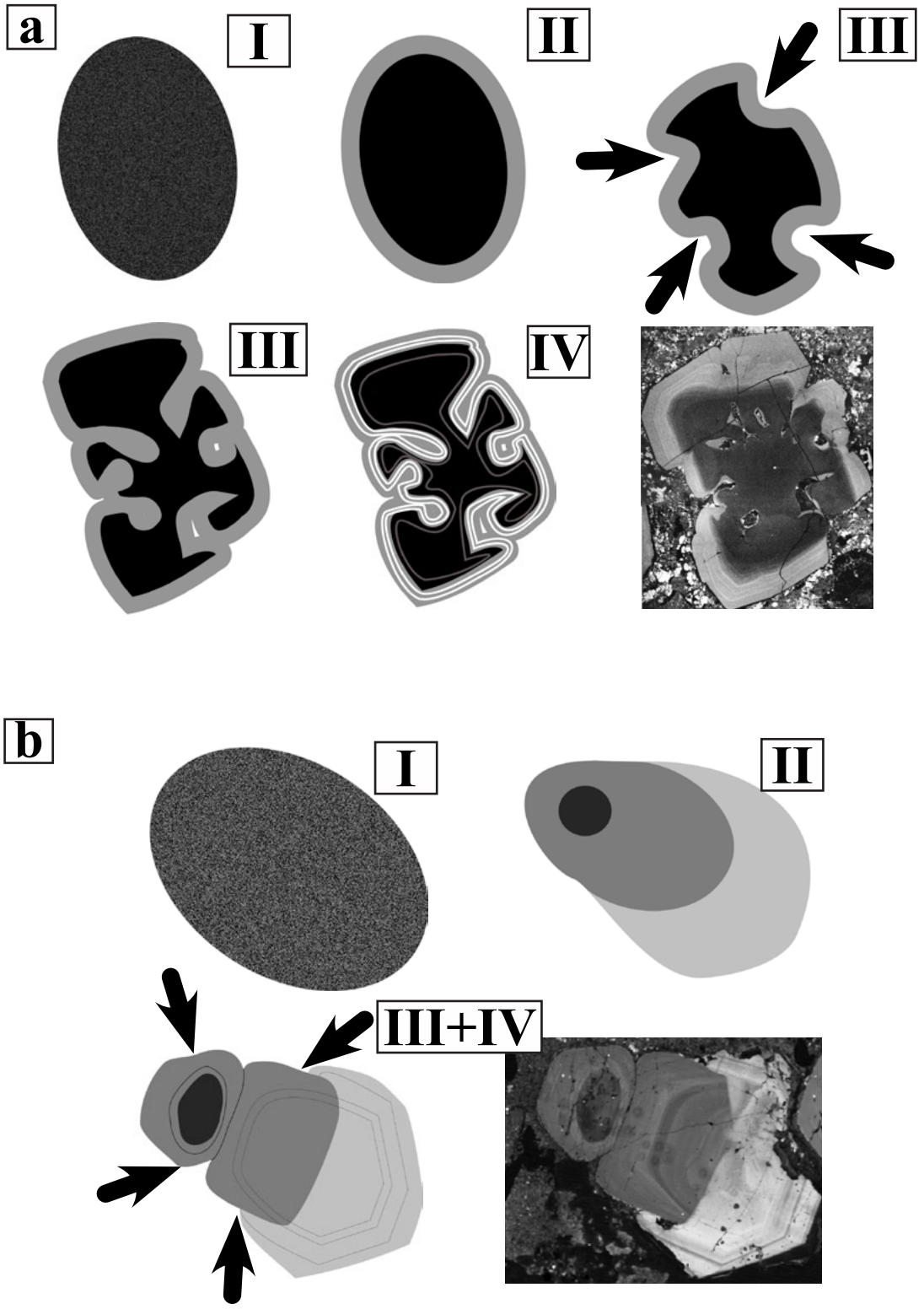

Figure 7-8 The alternative model for formation of quartz eyes

I - IV - stages of formation of quartz eyes from immiscible silica-rich globules, modelled for quartz eyes from samples DC-DP-1 (a) and DC-DLP-1 (b). Stage I - separation of silica-rich droplets from heavy fluid. Stage II - redistribution of trace element within droplets. Stage III - partial solidification and deformation of droplets. Stage IV - crystallisation of deformed droplets.

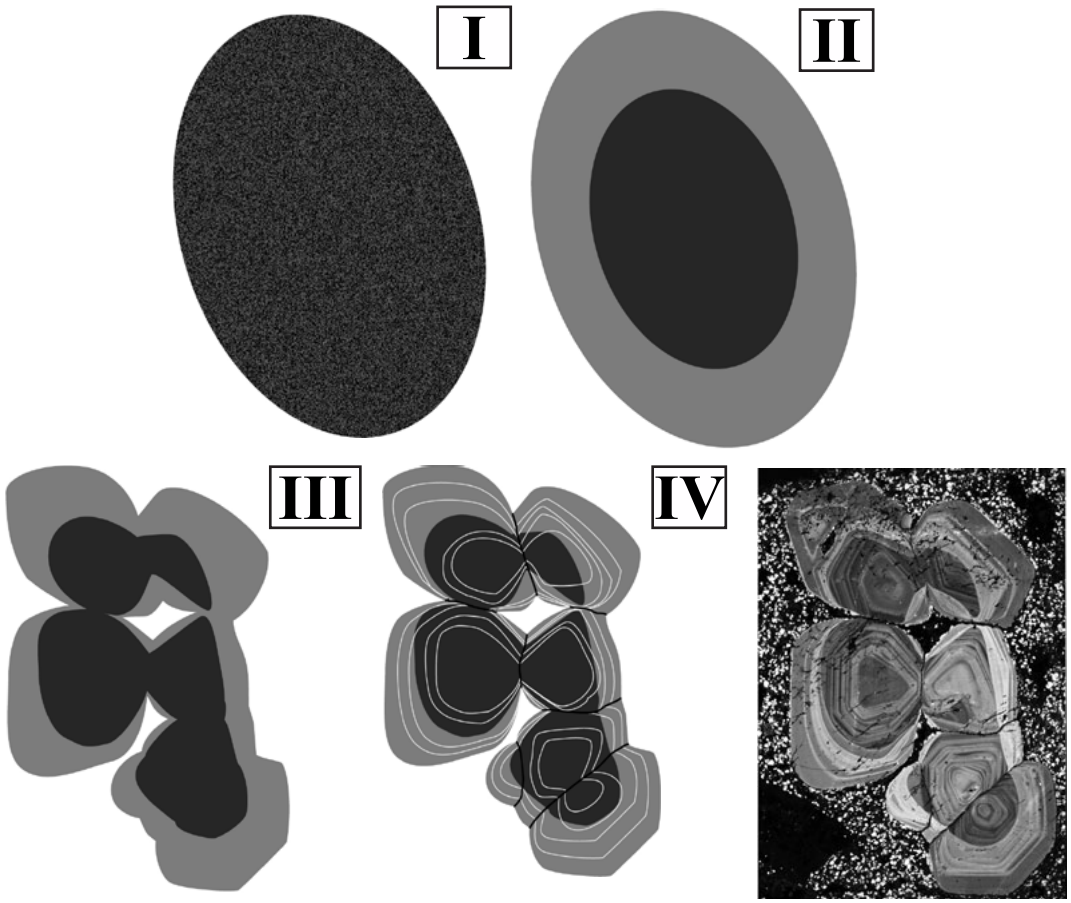

Figure 7-9 The alternative model for formation of quartz eye clusters
I - IV - stages of formation of quartz eyes from immiscible silica-rich globules, the same as in Figure 7-8), modelled for quartz eyes from sample 109647 from Climax.

are determined by two different processes, i.e. self-organising on the earlier stage is responsible for formation of compositional zoning and crystallisation during the later stage forms oscillatory zoning.

Furthermore, inverse evolution observed in many of the studied quartz eyes is consistent with the suggested mechanism for formation of quartz eyes and indicates that crystallisation may begin in a rim zone and proceed inwards, so that rims crystallise at higher temperatures, and cores crystallise later at lower temperatures.

7.5.3. Application to the origin of fluid inclusions

The silica-rich material, the precursor of quartz eyes, can contain up to 90 wt% of silica as it was determined by Wilkinson (1996). The rest 10 wt% (or even more) is water, salt and metals, which upon cooling can be exsolved and trapped as fluid inclusions (Elliston, 2005). We suggest that this process can be prolong upon cooling and crystallisation of quartz from quartz precursor. This may be similar to exsolution

of aqueous fluid from the melt, when the latter is viscous enough and thus prevents coalescence of exsolved bubbles. Similar phenomena was observed in inclusions of the magmatic emulsion described by Davidson (2005).

Generally, depending on the conditions, exsolved fluid can be single-phase or two-phase. The coexistence of vapour-rich and aqueous, as well as salt undersaturated and salt saturated inclusions may indicate that trapped fluids were immiscible. On the other hand, compositional variety of fluid inclusions may also be explained by their prolonged formation, when gradual changes in temperature and pressure provide changes in composition of exsolved fluid. Due to the high viscosity of the silica-rich material and thus hindered diffusion, coalesce of trapped fluid bubbles is not likely, and thus, in this case coexistence of bubbles of different composition will be observed. Moreover, quartz precursor material can also trap small portions of surrounding heavy fluid; due to the slow diffusion inclusions of the heavy fluid will coexist with inclusions exsolved from silica-rich material later. Furthermore, partial decrepitation of inclusions can also contribute significantly to the compositional diversity of fluid inclusions: provided that decrepitation occurred before the crystallisation of daughter minerals, inclusions, which underwent the most significant fluid leakage, will be vapour-rich. This is consistent with our fluid inclusion and CL data showing that vapour inclusions are often located on an intersection of healed fractures (Fig 5-4).

Our fluid inclusion data showed that although temperatures of homogenisation vary significantly they are generally much lower than estimations of the crystallisation temperature calculated with titanium-in-quartz geothermometer (see chapter 7.3.3). Not only fluid inclusions trapped during magmatic crystallisation would show higher temperatures of homogenisation but partial decrepitation occurred later would also lead to an increase in homogenisation temperatures. Thus, suggested mechanism for formation of quartz eyes, i.e. their crystallisation from the silica-rich material at lower temperatures during magmatic-hydrothermal transition, is more consistent with our fluid inclusion data.

Abundance of fluid inclusions in quartz eyes is in a good agreement with their crystallisation in extremely fluid-rich environment. Moreover, the suggested origin of fluid inclusions is also in a good agreement with the observed relationships between CL intensity and abundance of fluid inclusions in adjacent zones (Fig 5-1). Such relationships can be related to initial variations in water content between different quartz grains or layers: the more water-rich the quartz precursor, the more abundant fluid inclusions it will contain.

It is most likely that exsolution of the fluid within quartz eyes occurred rather late, probably during stage IV, i.e. during crystallisation after deformation of silica-rich globules. It is consistent with the fact that fluid inclusions do not disturb primary CL layers. Such inclusions may be called ‘exsolution’ or ‘pseudoprimary’ inclusions, and were described earlier in a number of papers (Herrington and Wilkinson, 1993; McLaren and Phakey, 1966; Roedder, 1984; Sanders and Black, 1988).

7.5.4. Formation of healed fractures and halos of secondary quartz around inclusions

Absence of similar healed fractures in adjacent phenocrysts (plagioclase or K-feldspar) indicate that their formation were determined by processes occurred in quartz eyes only. According to the model suggested by Müller (2000) and Van den Kerkhof (2001) 3D network of healed fractures formed as a result of the two-stage process: firstly, simultaneous massive decrepitation of fluid inclusions occurred, which could be caused by cooling-induced thermal stress, such as α/β-transition or up-lift. Secondly, defect-poor quartz grew at the cost of the host quartz releasing or replacing defect centres. Observed temperatures of homogenisation of fluid inclusions vary from 340 to higher than 600°C indicating that decrepitation of inclusions and healing of fractures most likely occurred at temperatures lower than those of α/β-transition. Moreover, since fluid inclusions are most likely partially decrepitated, their initial temperatures of homogenisation could have been even lower. Multiple evidences were described earlier, which support the idea that crystallisation of quartz eyes occurred in-situ, therefore up-lift could not be the cause for the thermal stress. Moreover, several generation of the secondary quartz were often observed in many quartz eyes, which points out that fracturing and healing could be a repetitive process. Thus, it is unlikely that α/β-transition or up-lift caused fracturing of quartz eyes.

If secondary quartz halos formed as a result of dissolution-precipitation processes as was proposed by Van den Kerkhof (2001) then inclusions with negative shapes should form. However, only a few of the studied inclusions have negative crystal shape. That may indicate that dissolution-precipitation processes were not intense enough to be responsible for formation of thick halos around inclusions.

Another explanation for the formation of secondary quartz halos around inclusions in the literature is related to recrystallisation processes; secondary quartz grows at the cost of host quartz and releases or replaces defect centres and pushes the released trace elements into the host quartz or fluid inclusions (Müller, 2000; Van den Kerkhof and Hein, 2001). The mechanism would lead to increase in trace element

content in the host quartz next to secondary quartz, as was observed by (Müller, 2000). However, no elevation of trace element concentrations was observed in our samples.

Furthermore, neither dissolution-precipitation nor recrystallisation can explain several generations of secondary quartz. Every generation includes halos of secondary quartz and healed fractures of distinct CL intensity (Fig 5-2d), indicating that temperatures of formation were also different for every generation.

We suggest that fracturing events in quartz eyes could be related to the pressure release during fracturing of the pluton and host rocks as a result of crystallisations of the pluton. It was shown earlier (Bakker and Jansen, 1994; Vityk et al., 2000) that after entrapment fluid inclusions produce strain in the adjacent host quartz, and as a result multiple dislocations nucleate on inclusion walls. Therefore, zones around fluid inclusions are structurally weaker than inclusion-free areas and stress conditions will likely to cause formation of fractures through inclusions.

As was demonstrated previously (Kotel'nikova and Kotel'nikov, 2010a, b; Thomas and Davidson, 2008) an alkali-rich fluid is capable to carry significant amounts of silica. Thus, inclusions in quartz can precipitate significant amount of silica upon cooling or pressure release. We envisage that decrepitation of fluid inclusions can cause fast silica oversaturation, and as a result its precipitation on inclusion walls and along fractures within quartz eyes. Stockwork systems in porphyry deposits are characterised by multiple generations of veinlets indicating repetitive fracturing. If formation of healed fractures in quartz eyes is related to the fracturing of the pluton then several generation of healed fractures observed in studied quartz eyes is in a good agreement with suggested mechanism of their formation (Figs 5-2 and 7-1).

7.5.5. Application for formation of metal-bearing phases

The suggested mechanism for the formation of quartz eyes implies that their crystallisation may be the beginning of the formation of mineralising fluids. Heavy fluid is the residual substance, which forms as a result of prolonged fractional crystallisation and separation of silicate melt, and contains silica and incompatible elements (water, alkalis and metals). Upon cooling heavy fluid undergoes several episodes of immiscibility. Each subsequent immiscibility event removes excess of silica and therefore, enriches the remaining fluid in metals and alkalis, which crystallises later within interstitial spaces between quartz grains or migrates and forms metal-rich veinlets. This is in a good agreement with the observed data on distribution of metal-bearing phases. For example, sulphide minerals and other metal-bearing phases in

veins from the studied samples are interstitial and associated with alkali-rich non-metal phases, such as K-feldspar or sericite (Figs 6-9 and 6-10).

Typical sequences of porphyry veins includes early porphyry veins are barren ptygmatic and disjointed A style (quartz veins), which are overprinted by locally wormy A style (quartz-sulphide), or M style (quartz-magnetite-sulphide) veins (Corbett, 2009). Next vein generations are characterised by centrally terminated comb quartz in-filled by later sulphides (B veins) and finally, development of D veins (sulphides) occurs (Corbett, 2009). Such evolution shows gradual enrichment of the fluid in ore material and depletion in silica component, which is consistent with suggested mechanism of formation of mineralised fluid.

In our study metal-bearing phases were also found as aggregates (or blebs) where they associated with non-metal phases, such as quartz, fluorite or apatite (Fig 6-4). In many cases the blebs are multi-mineral, and adjacent blebs often differ significantly in mineral compositions and their ratios (Fig 6-2). This suggests that metal-bearing phases may also crystallise as a result of an immiscibility event, which caused the formation (separation) of metal-rich blebs during earlier stages and their crystallisation later.

7.5.6. Heavy fluid vs light (aqueous) fluid: contribution to mineralisation

Formation of a deposit is all about the extraction of metals from large magma volumes and their spatial concentration. In the orthomagmatic model concentration of metals starts in residual melts, then metals are scavenged from melts by fluids, transported and deposited along fractures around intrusion carapace. High efficiency of concentration of metals in a melt is provided by fractional crystallisation. Indeed, it is an excellent mechanism for enrichment of residual melts in metals. However, efficiency of metal extraction drops dramatically during the next stage, i.e. scavenging of metals from melts by fluids. This happens because ability of a fluid to carry metals is pressure dependant; metals readily partition into a fluid if confining pressure is high, e.g. 2 kbar or more, and partition back into a melt when pressure drops (Cline and Bodnar, 1991; Cloos, 2001). It is believed that pressure quenching is important in porphyry environments, and that it is responsible for porphyry textures, which are so characteristic for deposits of the type (Cline and Bodnar, 1991). If it takes place, then efficiency of metal extraction decreases significantly, because as soon as pressure drops fluid-melt re-equilibration occurs, and metals partition back to a melt. Boiling of a fluid also causes significant reduction of metal-carrying capacity of a fluid (Cline and Bodnar, 1991). With low efficiency of metal extraction more fluid is required to form a

deposit, and since the amount of fluid generated by magmas is limited, extra volumes of magmas are needed. As a result magma reservoirs up to 150 times larger than porphyry stocks are invoked to explain formation of economically significant deposits (Cloos, 2001; Lowenstern, 1994; Shinohara et al., 1995).

The proposed evolution of residual melt via formation of the heavy fluid is much more efficient in extraction and transport of metals. The heavy fluid forms as a result of immiscibility event and contains elements that are incompatible with silicate melt. Due to its structure heavy fluid has extremely high metal-carrying capacity (Thomas and Davidson, 2008; Thomas et al., 2009; Thomas et al., 2000; Thomas et al., 2010; Wilkinson et al., 1996; Williamson et al., 1997; Williamson et al., 2002). For example, Thomas (2010) compared the distribution of F, Ta, Sn, Zn, Mo and W between supercritical alkaline aqueous fluid and the heavy fluid. He showed that:

► F, Ta, Sn and Zn partition specifically to the heavy fluid.

► Concentrations of Sn and Zn in the heavy fluid are 20 to 50 times as much as those in aqueous fluid.

► Concentrations of W and Mo in the heavy fluid are 5.1 and 3.6 times as much as those in aqueous fluid.

► Ta behaves similarly to Sn and Zn showing strong partitioning to the heavy fluid. It also shows inhomogeneous distribution within the heavy fluid, suggesting that diffusion coefficients for Ta in the heavy fluid are much higher than in aqueous solutions.

Thus, altough light (aqueous) fluid can also coexist with the heavy fluid it has much more limited capacity to extract metals.

The mechanism of further evolution of the heavy fluid is similar to fractional crystallisation, and can operate during late magmatic, magmatic-hydrothermal and hydrothermal stages. Similar to fractional crystallisation, immiscibility episodes provide efficient enrichment of the residual fluid in incompatible elements, such as volatiles, alkalis and metals. Formation of the heavy fluid as intermediate stage between magma and light fluid, makes the transition smoother and reduces losses of economically significant components.

Due to high efficiency of metal extraction there is no need to accumulate heavy fluid from the magma reservoirs of batholitic size; the amount of the heavy fluid sufficient for formation of a deposit may form within a small porphyry stock if residual melt was rich enough in volatiles, alkalis and metals. It may be squeezed (filter pressing) from crystallising pluton and accumulated under a carapace to form

unidirectional textures, or remain in magma until an immiscibility episode occurs and more aggressive and mobile alkali-rich aqueous phase forms, which is able to move upwards. Furthermore, precipitation from heavy fluid is more consistent with co-deposition of quartz and sulphides so typical for porphyry-type deposits.

The coexistence of quartz and sulphides may also point to the important role of sulphur in the melt-to-fluid evolution in porphyry systems. However, due to the lack of data on the behaviour of sulphur in heavy fluids it is difficult to make conclusions about how sulphur affects the system. Apparently, sufficient amount of sulphur is needed to precipitate sulphides, but whether sulphur enhances immiscibility and formation of the heavy fluid is unknown. It was shown that at near-magmatic conditions (>750°C) concentrated NaCl fluid can dissolve significant amount of anhydrite (Newton and Manning, 2005) and silica (Kotel'nikova, 2010a, b). Thus, it is possible that heavy fluid can be not only silica- but also sulphur-rich. It was suggested recently that speciation of sulphur can differ from what is usually believed; Pokrovski and Dubrovinsky (2011) suggested that at temperatures higher than 300°C and pressures higher than 0.5 GPa trisulphur ion S_3^- accounts for >50 to 95% of dissolved sulphur. How S_3^- behaves in residual melts and heavy fluids is yet to be astablished; however, due to the similarity of S–S–S bond angle to that of H–O–H (Pokrovski and Dubrovinsky, 2011) it can be suggested that significant amount of sulphur can be incorporated in water-rich heavy fluid at the conditions of ore formation.

Existing models for formation of porphyry deposits consider immiscibility as crucial for metal extraction and its transport. Two major immiscibility events are believed to play the most important role: the exsolution of fluid from magma and fluid boiling. Generally, the former is the beginning of the magmatic-hydrothermal transition, and the latter is its final period. We know that hydrothermal fluid in porphyry systems are derived from porphyry magmas, and thus, the deposit-specific geochemical signatures are inherited from the magmatic stage of system evolution (Audetat et al., 2008), but what is happening during the magmatic-hydrothermal transition is generally obscure for us (Audetat et al., 2008). The suggested mechanism of evolution of residual melt to aqueous fluid through a series of immiscibility events may provide a missing link between magmatic and ore deposition stages.

7.5.7. Formation of the heavy fluid in mineralized vs barren intrusions

Our data indicate that there are no any principle differences between studied quartz eyes from different localities or between those from barren vs mineralised plutons. For example, sample SRD-02 from the barren intrusion and sample 138.2

from the mineralised zone (both from Batu Hijau) contain similar quartz eyes with similar internal textures and inclusion assemblages, which are distributed along healed fractures. Therefore, it can be assumed that formation of the heavy fluid is the stage of magma evolution, which occurs in both potentially mineralised and barren plutons.

We assume that as soon as concentration of non-silicate anions (such as F^-, Cl^-, BO_3^{3-} or PO_4^{2}) in residual melt occurs, a series of immiscibility events may be triggered. Formation of the heavy fluid may be a prerequisite for development of mineralisation because this mechanism provides the most effective metal concentration; however, formation of the heavy fluid does not necessarily leads to formation of a deposit. Whether mineralisation is developed or not will be a function of initial composition of parental magmas, conditions of crystallisation and the efficiency of accumulation of incompatible elements within residual melt, as well as the further evolution of immiscible phases. However, provided that sufficient amount of ore metals is accumulated in residual melt the chance of formation of an ore deposit is higher in a system, which evolves through formation of the heavy fluid.

We appreciate the speculative element in our hypothesis of the formation of heavy fluid, and the important role it may play in formation of economic porphyry deposits. However, we suggest that it is possible that some sort of silica-, water- and metal-rich heavy fluid is the missing point in the orthomagmatic model of porphyry deposit formation. Although it diverges from conventional models, it does have the virtue that it can overcome some of the problems and contradictions in the existing models. Over the decades since C. W. Burnham's pioneering work (1979) on genesis of porphyry ore deposits, there has been continuous 'tweaking' as new data and experimental work has been acquired, and more examples explored, without a final consensus on all of the details being achieved. However, if such a mechanism as we propose operates in porphyry environments, we may need to reconsider some aspect of the model that describes formation of ore deposits of the type. We do not ask for a leap of faith, but rather tolerance in allowing alternative hypotheses to be examined on their merits, and developed as they may warrant.

Conclusions

Quartz eyes from seven porphyry deposits showed features distinctly different from those of quartz phenocrysts from lava samples:

► Clusters of quartz eyes are usually preserved, whereas quartz phenocrysts are in most cases fragments of crystals.

► Quartz eyes usually show strongly contrasted cathodoluminescence (CL) patterns, often with distinct core and rim zones, whereas quartz phenocrysts usually display dull oscillatory luminescence.

► Quartz eyes and quartz phenocrysts response differently to the surface damage caused by electron beam.

► Quartz eyes typically show dense network of healed fractures, which are visible only in CL maps, and which are absent in quartz phenocrysts.

► Quartz eyes are often sponge-textured because of the abundance of fluid inclusions in them, whereas quartz phenocrysts contain primarily melt inclusions.

Difference in internal textures and inclusion assemblages implies different origin. More detailed study of quartz eye internal textures showed:

► There is a significant diversity of internal patterns within quartz eyes or quartz clusters within a single thin section. Grains with normal zoning (CL-bright cores and CL-dark rims) may be next to grains with reverse zoning or grains showing irregular or no zonation.

► CL-dark cores are often enriched in Al, Li and OH-, depleted in Ti and show sector zoning. Quartz eye rims are Ti-rich, contain variable Al and show oscillatory zoning.

► There are three main contributors to CL emission centred at 1.93 eV, 2.05 eV and 2.72 eV. The first two emissions are intrinsic, i.e. caused by host Si and O atoms; the 2.72 eV peak is caused by Ti impurities. Aluminium does not cause any intensive luminescence, but significantly suppresses 1.93 eV emission.

► Al distribution pattern does not correlate with Ti distribution pattern within a single quartz grain: Ti enriched zones cross Al-rich zones; tiny fractures healed by quartz depleted in Al are not reflected in Ti distribution maps. Al shows diffusional distribution, whereas transitions between different Ti zones are extremely narrow.

Our evidence suggest that quartz eyes were likely to crystallise in-situ after

magma emplacement, and thus diversity of internal patterns must be related to prolonged crystallisation from residual magmas enriched in volatiles, silica and metals. Different distributions of Ti and Al within quartz eyes point to different processes or conditions that control Si substitutions by those elements. Substitution of Si by Ti is temperature dependant: the higher crystallisation temperature the higher the Ti content in quartz. Factors controlling Al content in quartz are not fully understood yet, nor are the variations of Al content within a single quartz grain, or its correlation with Ti concentrations. Generally, Al concentrations in quartz increases during evolution of a melt, for instance, Al content in quartz eyes is lower than that in comb quartz, which is in turn lower than Al content in quartz veins. In many cases quartz eyes have high Ti rims and low Ti cores; the latter are often high in Al, Li and OH- and sometimes show sector zoning. This may indicate to inverse evolution of magma or crystallisation inwards from rims to cores.

Fluid inclusions (FI) in quartz eyes are abundant and unique; no other minerals in a given sample contain similar inclusions. Their characteristic features are:

► FI are distributed along healed fractures and have halos of secondary quartz around them. Fractures do not extend to groundmass.

► FI show extreme diversity in composition.

► FI contain Al, Na, K, Fe, Mn, Cl, S, W, Pb, Cu, Zn, Ca, Ag, Sn, Bi and Rb with varying element and phase ratios within adjacent inclusions. Liquid-rich inclusions are usually Cl-rich with B, Zn, Rb and Sr. Vapour-rich inclusions are Al- and S-bearing with higher Cu/Zn, Cu/Rb and Cu/Sr ratios than in liquid-rich and multiphase inclusions. Multiphase inclusions are metal-rich (Cu, Zn, Rb, Sr, Ag, Pb, Mo and W).

► FI demonstrate atypical behaviour upon heating and cooling; swirling upon heating and multiple episodes of immiscibility upon cooling are observed.

Fluid composition and its behaviour upon heating and cooling indicate that such complex fluid is significantly different from the NaCl-aqueous system, which is usually used for modelling of porphyry deposit formation. Moreover, CL mapping showed that fluid inclusions are likely to be partially decrepitated (distribution along healed fractures and secondary quartz halos); partial decrepitation can also be responsible for the inclusion diversity. Thus, using the NaCl-aqueous fluid system for reconstruction of the conditions of formation of porphyry deposits can lead to erroneous results.

The evidence presented shows that quartz eyes are distinctly different from

quartz phenocrysts. They crystallised in-situ after magma emplacement within the unique fluid-rich environment, and show distribution of trace elements that may indicate inverse crystallisation. On the basis of these observations, and the data on fluid behaviour upon cooling, a model for crystallisation of quartz eyes is proposed. Residual magma enriched in silica, alkalis, volatiles and metals may undergo a liquid-liquid immiscibility and silica-alkali-volatile-rich phase (heavy fluid) separates from peraluminous water-poor melt. The further evolution of the phases occurs independently and may include a series of immiscibility episodes. Liquid-liquid immiscibility within heavy fluid separates silica-rich globules (up to 90 wt% of SiO_2) from the alkali- and water-rich phase. From silica globules quartz eyes crystallise; during the crystallisation all foreign components (Na (K, Li, Al)$_2$O, H_2O and Me) are expelled from the crystal lattice. When the expelled elements are not able to migrate out from the quartz they form fluid inclusions. Crystallisation within globules can occur either from the centre outwards or from the outside inwards, in the latter case Ti-rich rims (high temperature) form first and Al-, Li- and OH-rich cores with sector zoning crystallise later. External stress induced by final stages of crystallisation of the pluton leads massive decrepitation (partial) of fluid inclusions and healing of multiple fractures with the released fluid.

The residual phase left after segregation of silica-rich globules is extremely mobile and unstable; it moves along fractures and may undergo rapid oversaturation. That leads to precipitating of residual silica first and alkali- and metal-bearing phases later in the interstitial spaces between quartz grains or in new fractures. This scenario implies that the heavy fluid is a precursor for the mineralising fluid. Provided that the magma contains sufficient metals and volatiles and that evolution of the residual melt leads to formation of heavy fluid, a series of further immiscibility episodes provide extremely effective enrichment of the residual fluid in metals by removal of gangue phases from it. Without formation of heavy fluid the efficiency of metal concentration is much lower: metals partition from melt into fluid according their partitioning coefficients which are pressure dependable; shallow fluids have low metal-carrying capacities and significant amount of metals remain in melts. Furthermore, transport of fluid bubbles within magma is hindered after it is more than 30% crystallised, which means fluid cannot be accumulated under a carapace for the focused fluid flow, which is a prerequisite for formation of a deposit. The mechanism that involves formation of heavy fluid does not require fluid accumulation under a carapace; heavy phase does not need to scavenge metals; as residual phase it already contains all metals and other elements that are left from crystallisation of rock forming minerals. Its further evolution during cooling occurs by removal of oversaturated phases.

Although the study was focused on porphyry deposits we would suggest that the principles involved may be related to several other geologically important processes such as the formation of pegmatites. In this study we have advanced a hypothesis to explain the observed data, and discrepancies in existing models. In some respects this hypothesis is a large step from the comfort of earlier models, but we have shown other works, both observational and experimental, which imply the existence of immiscible water- and silica-rich phase, somewhere between melts and solutions, which resembles the heavy fluid. We are confident that further work will join up these disparate phases, and the studies which demonstrated them.

Supplementary

Diversity of CL patterns

Antapacay (334-53250)

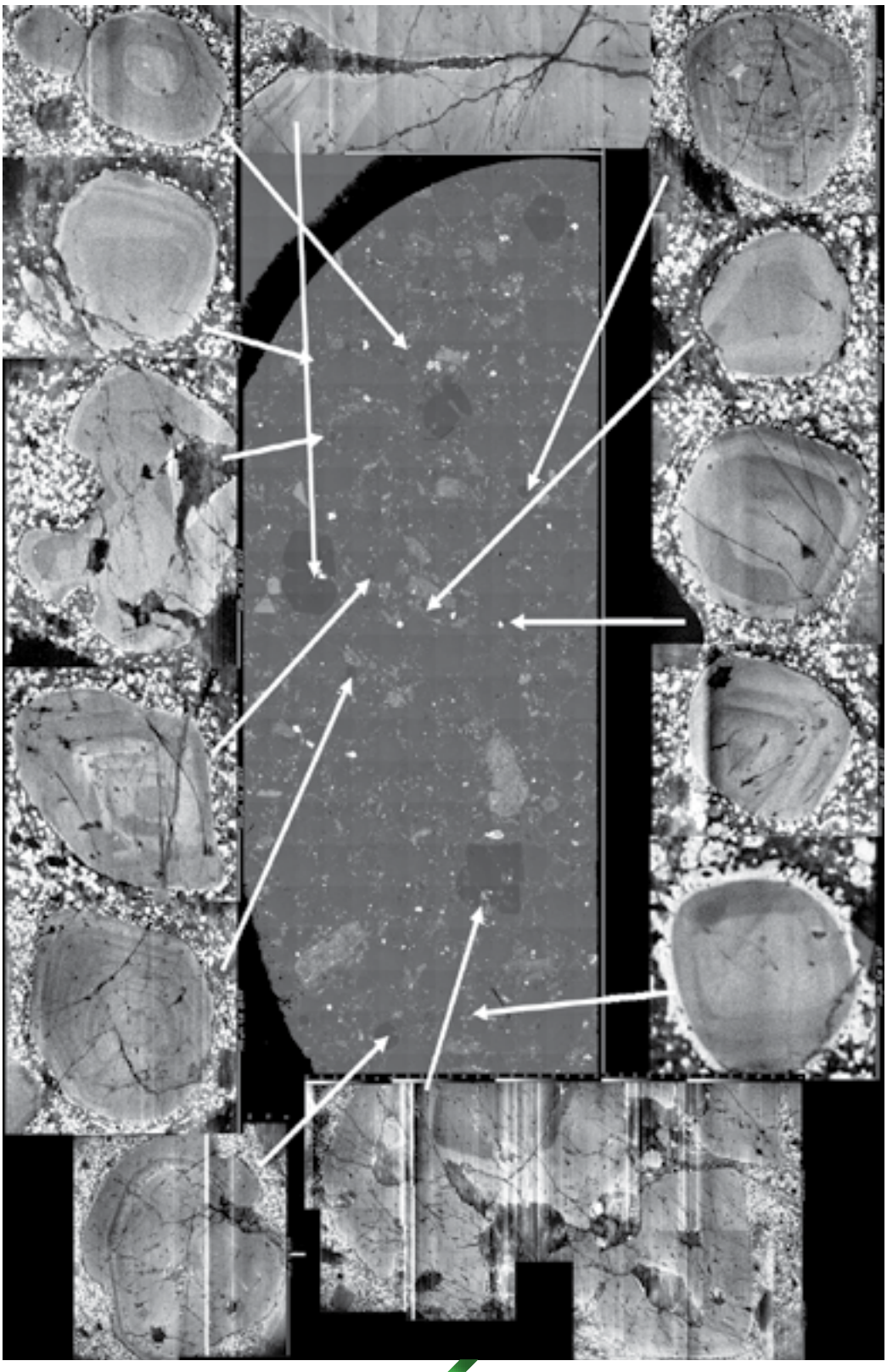

Antapacay (092-29700)

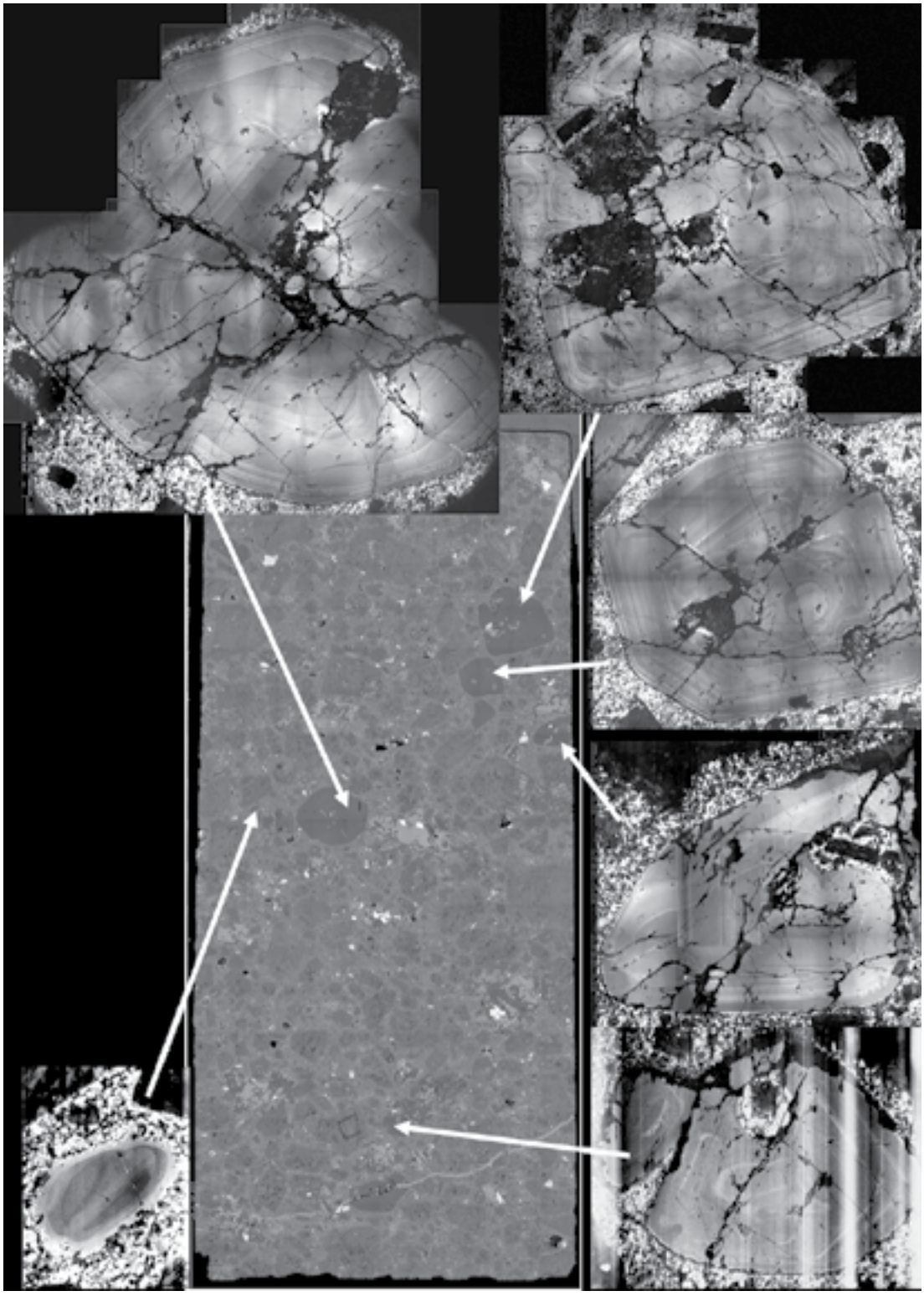

Antapacay (133-19920)

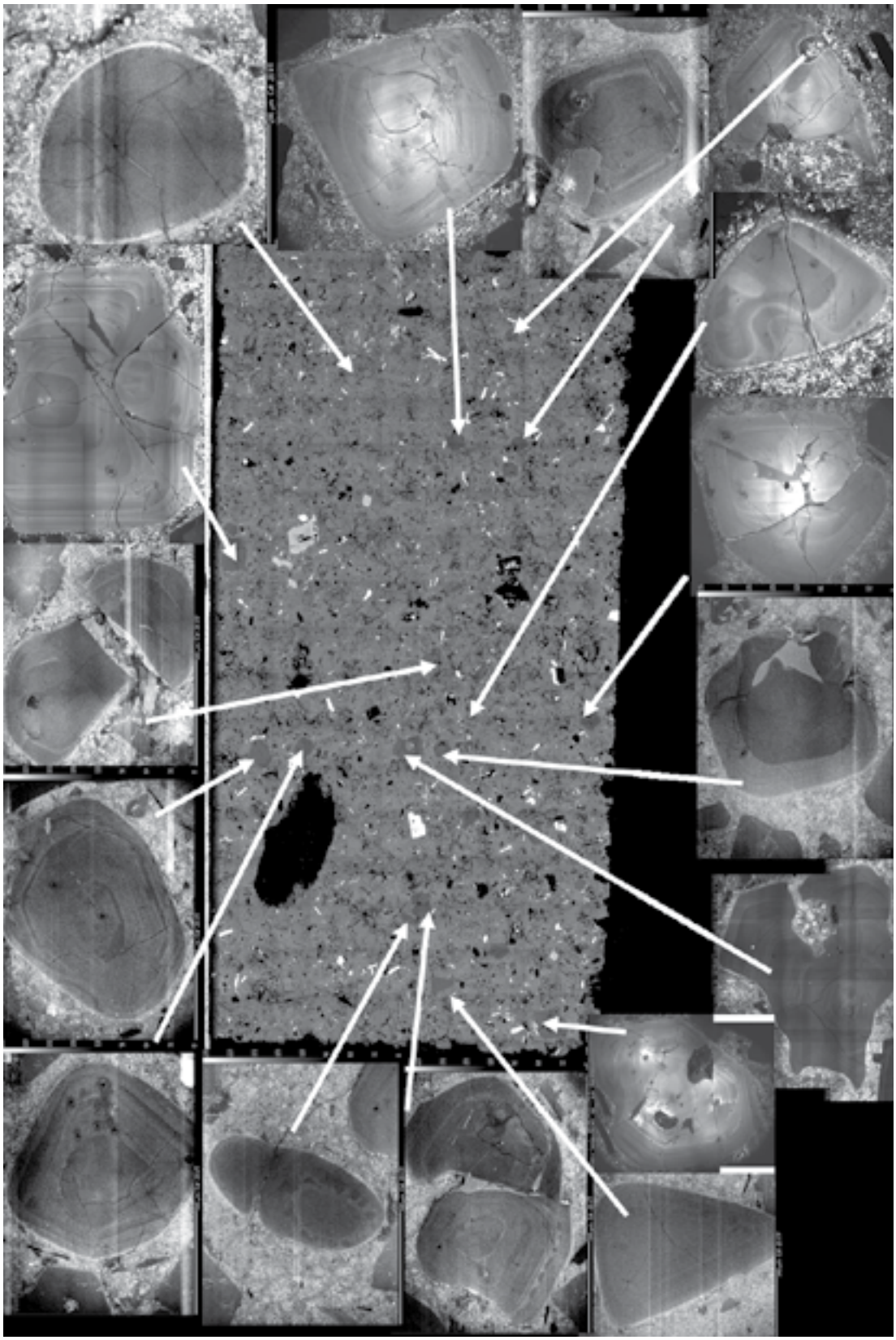

Rio Blanco (CA6)

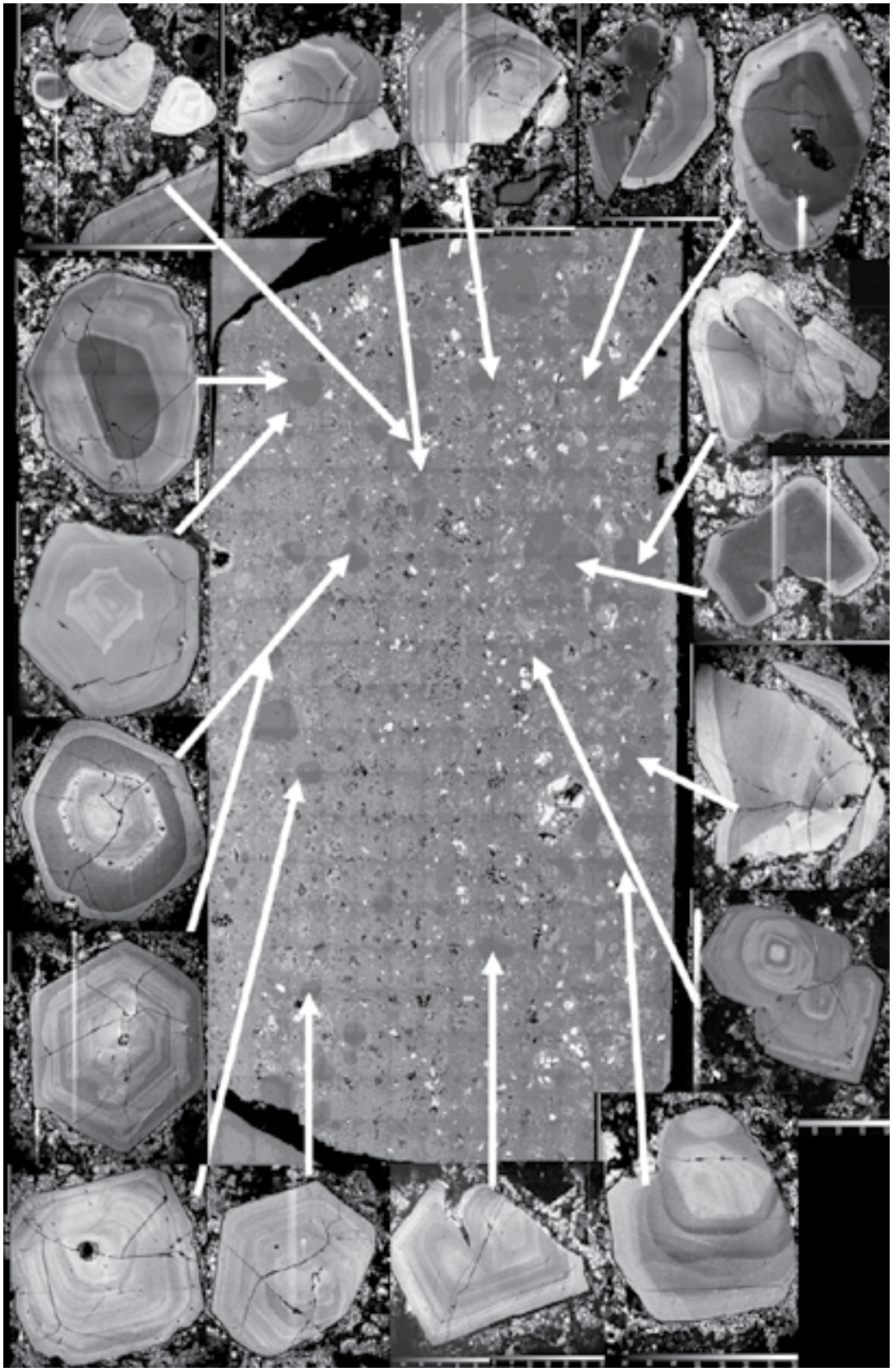

Rio Blanco (CA8)

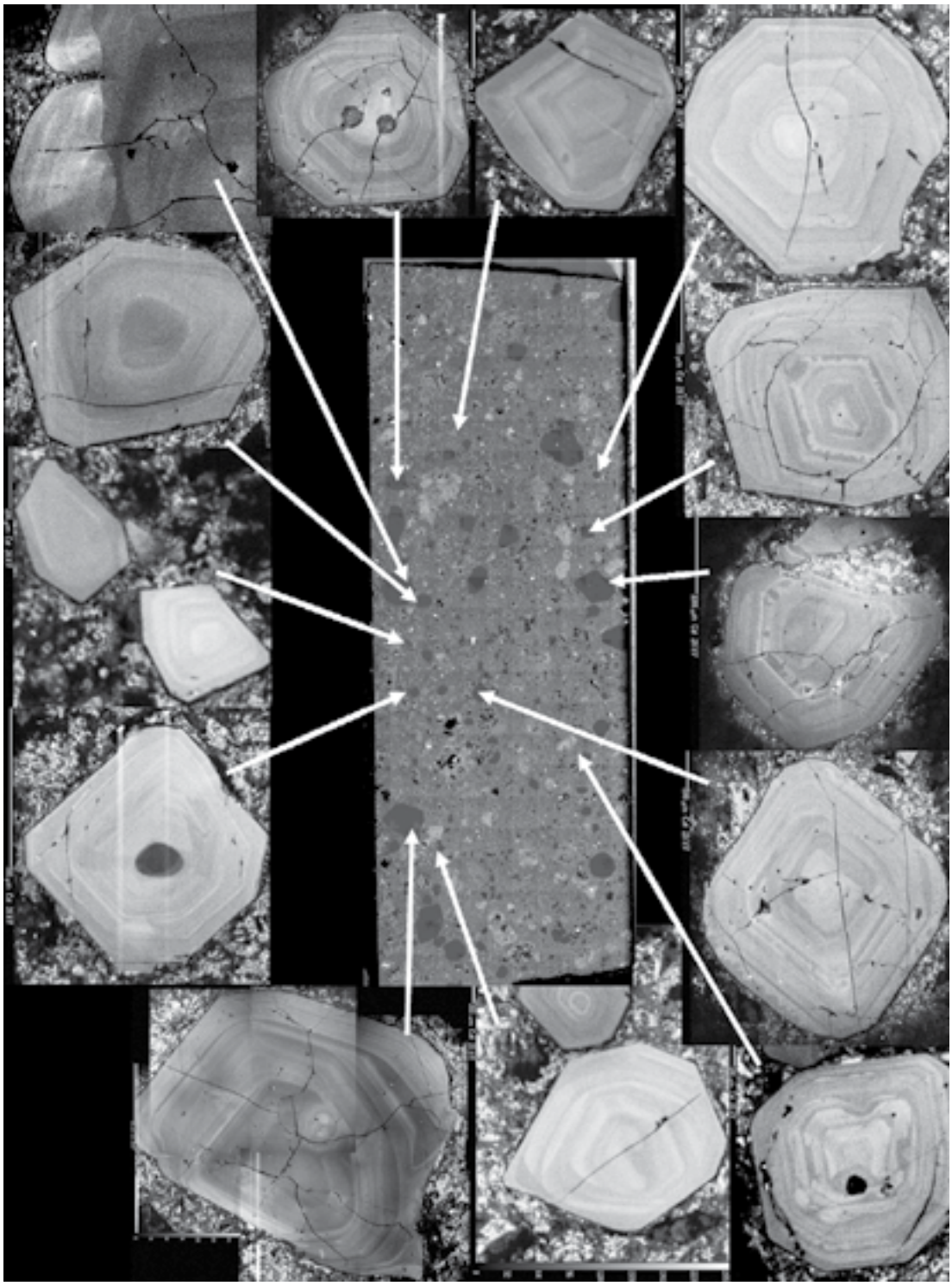

Rio Blanco (9902)

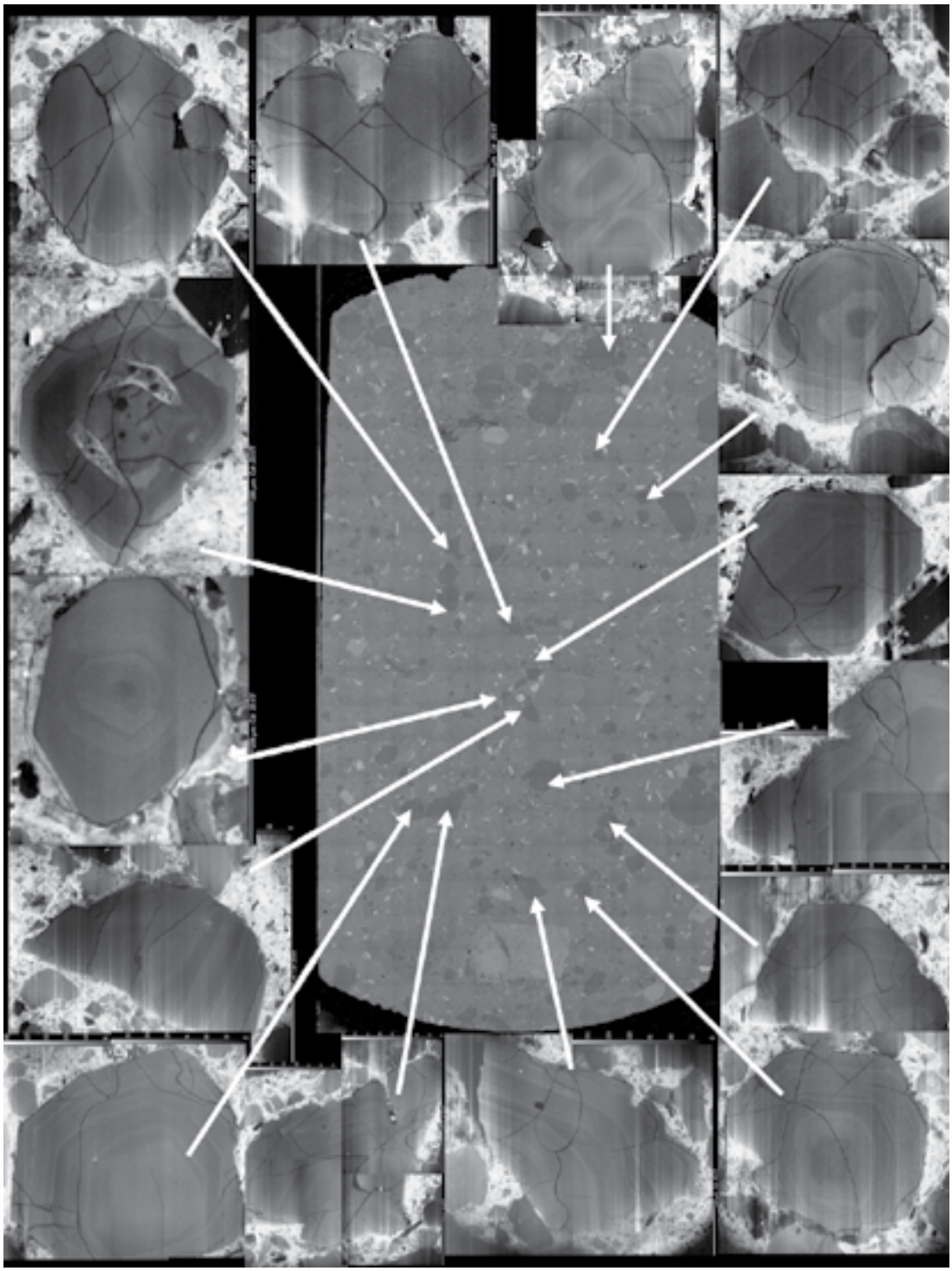

Rio Blanco (DC-DP-1)

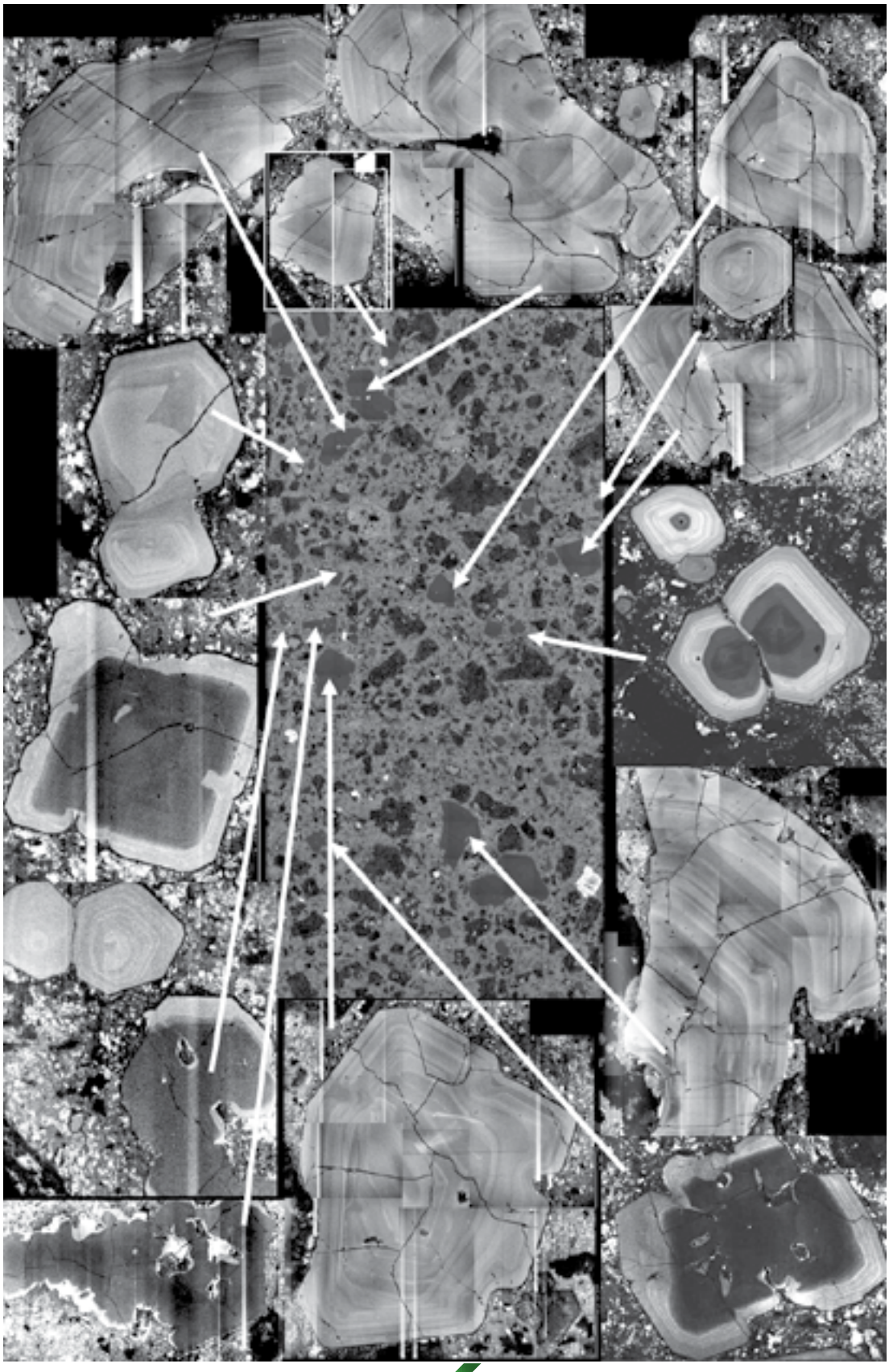

Rio Blanco (DC-DLP-1)

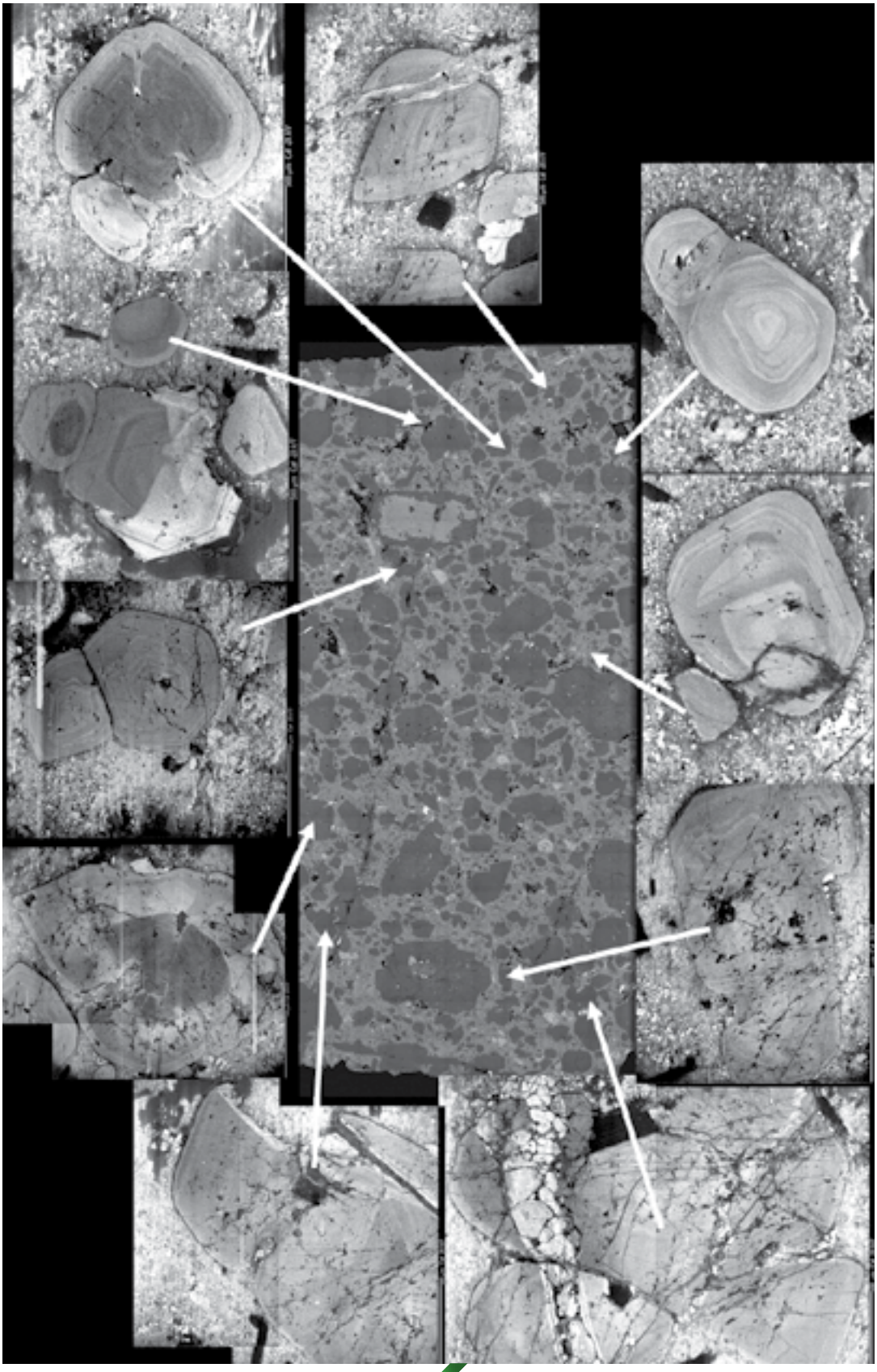

Rio Blanco (G1)

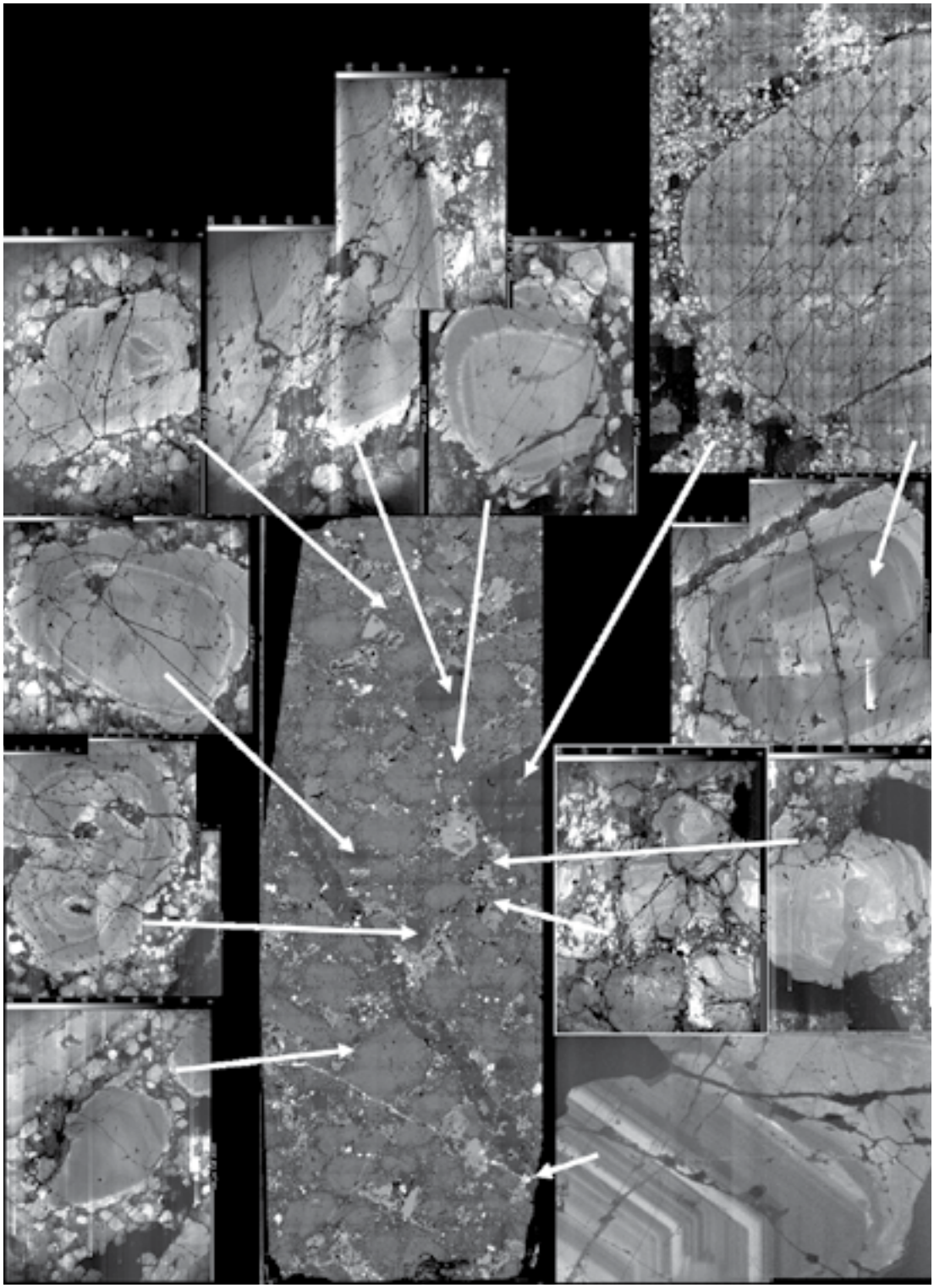

Rio Blanco (G2)

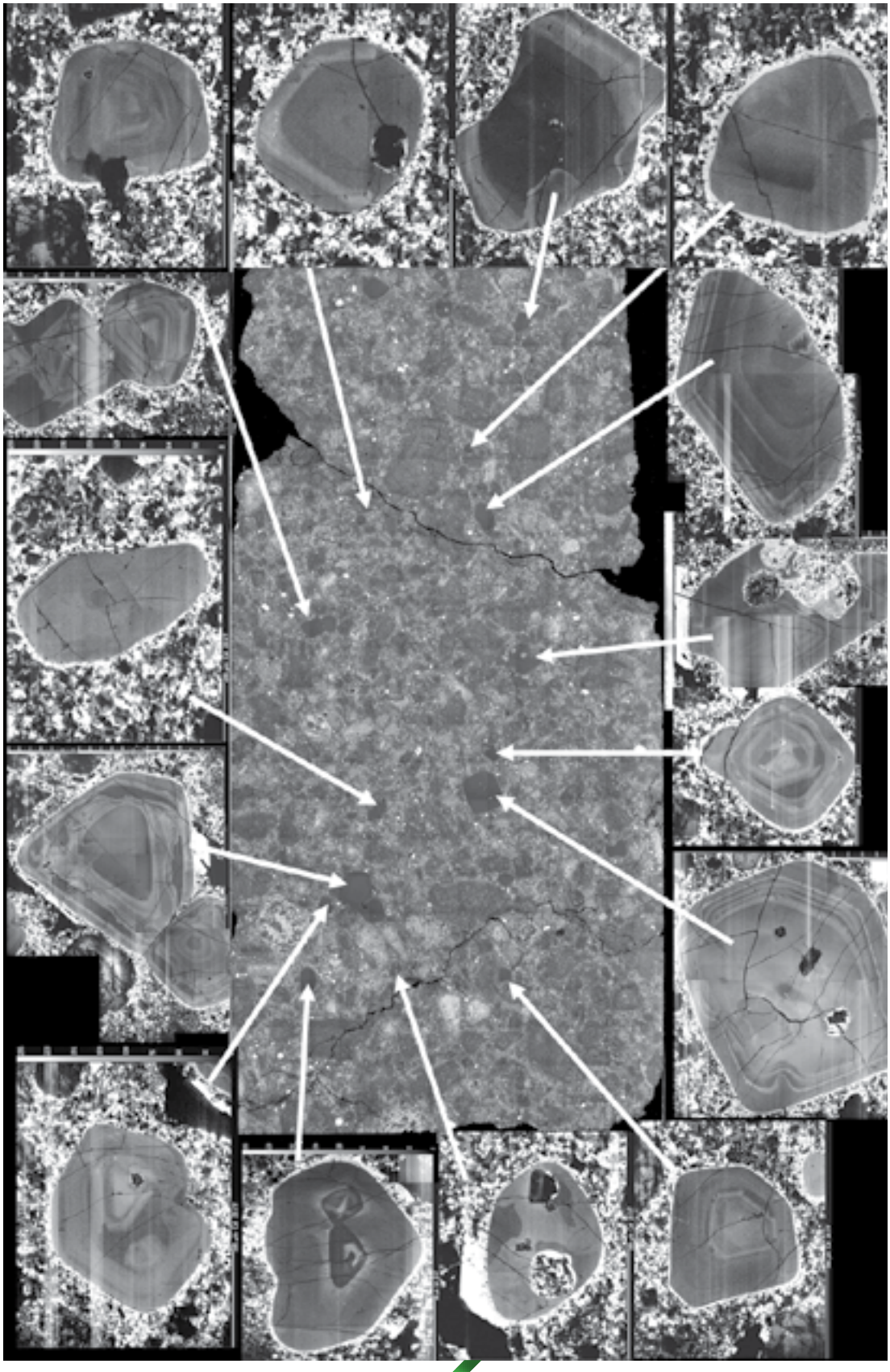

Rio Blanco (599-2)

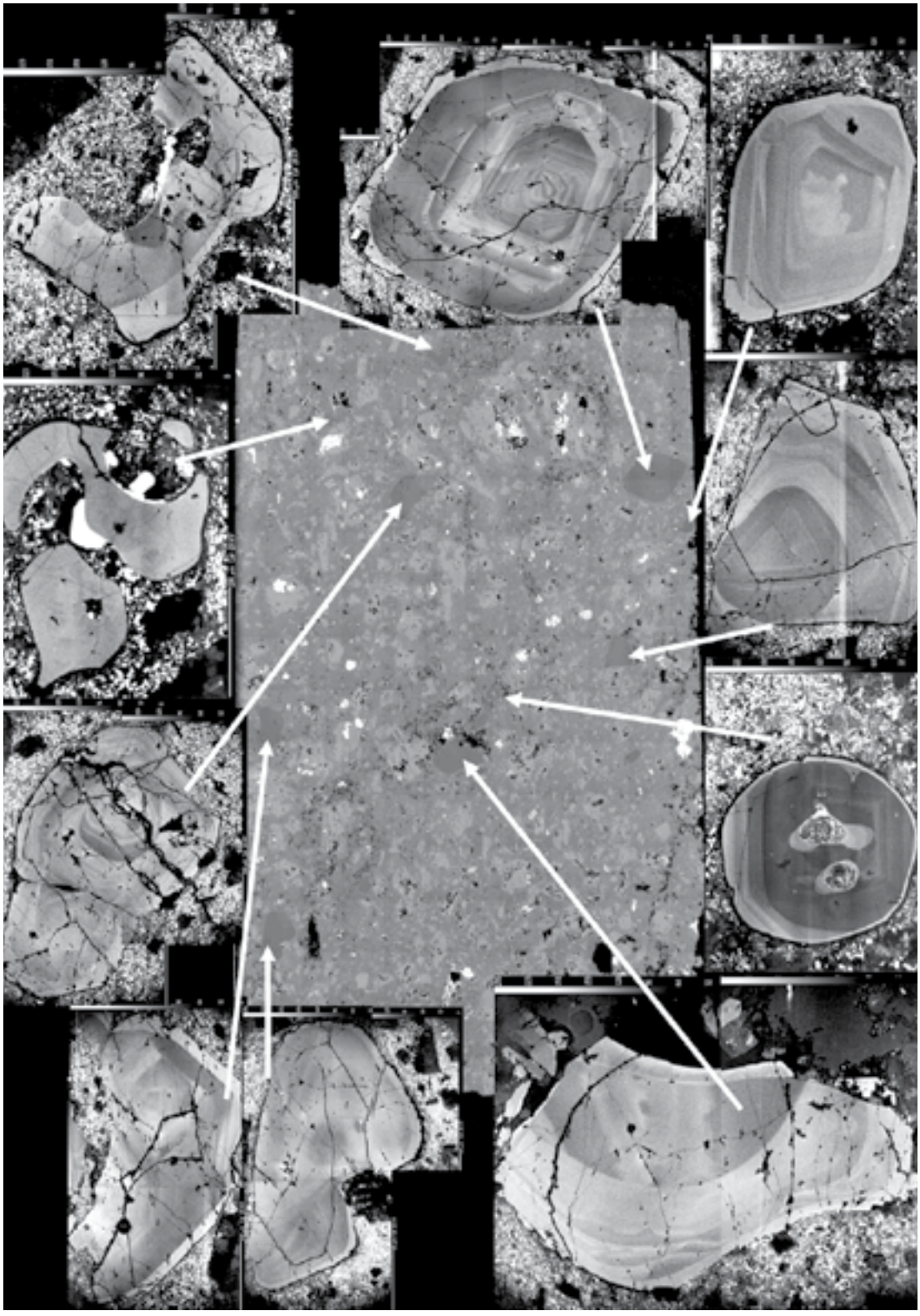

Rio Blanco (599-5)

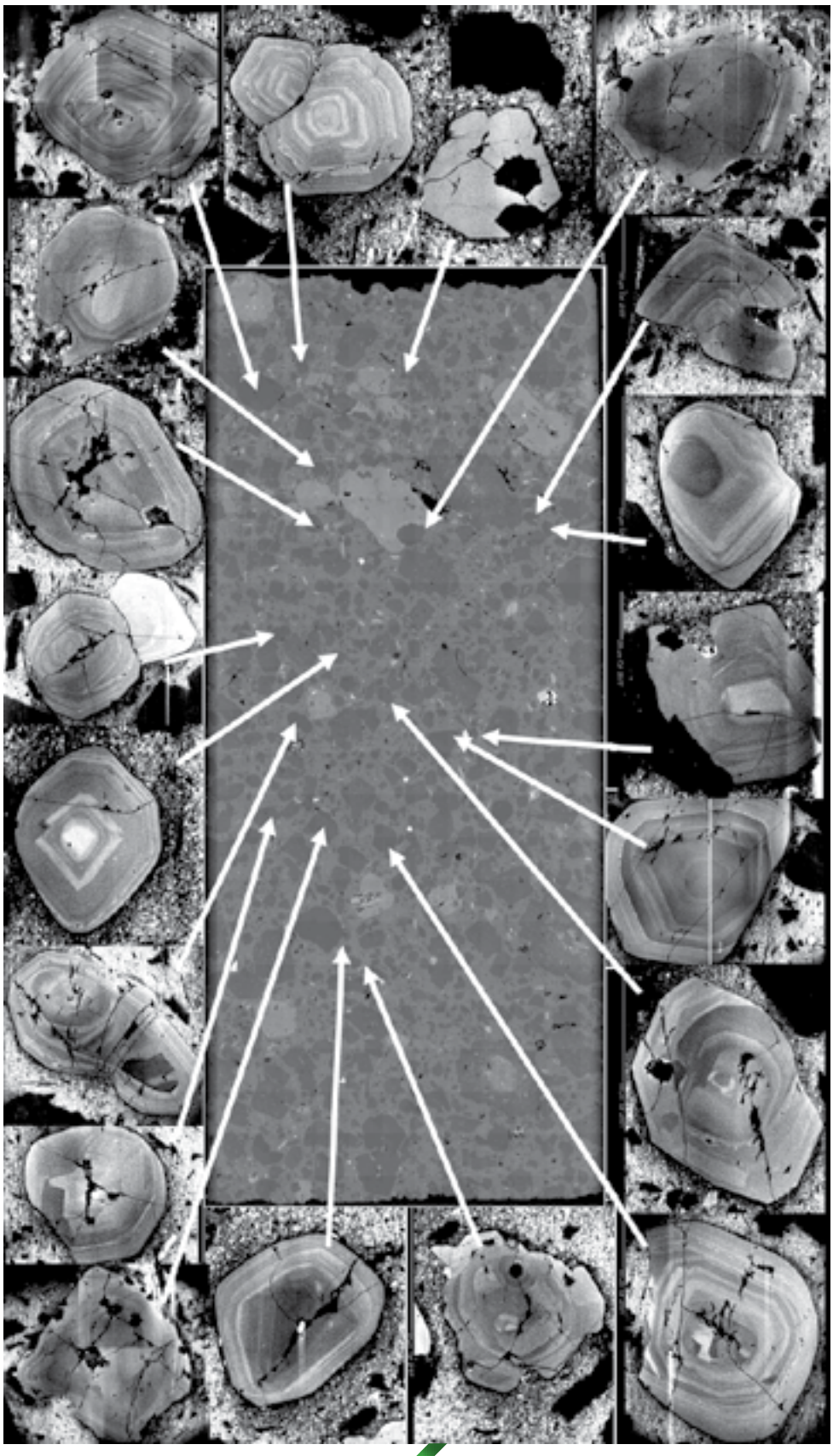

Climax (109644)

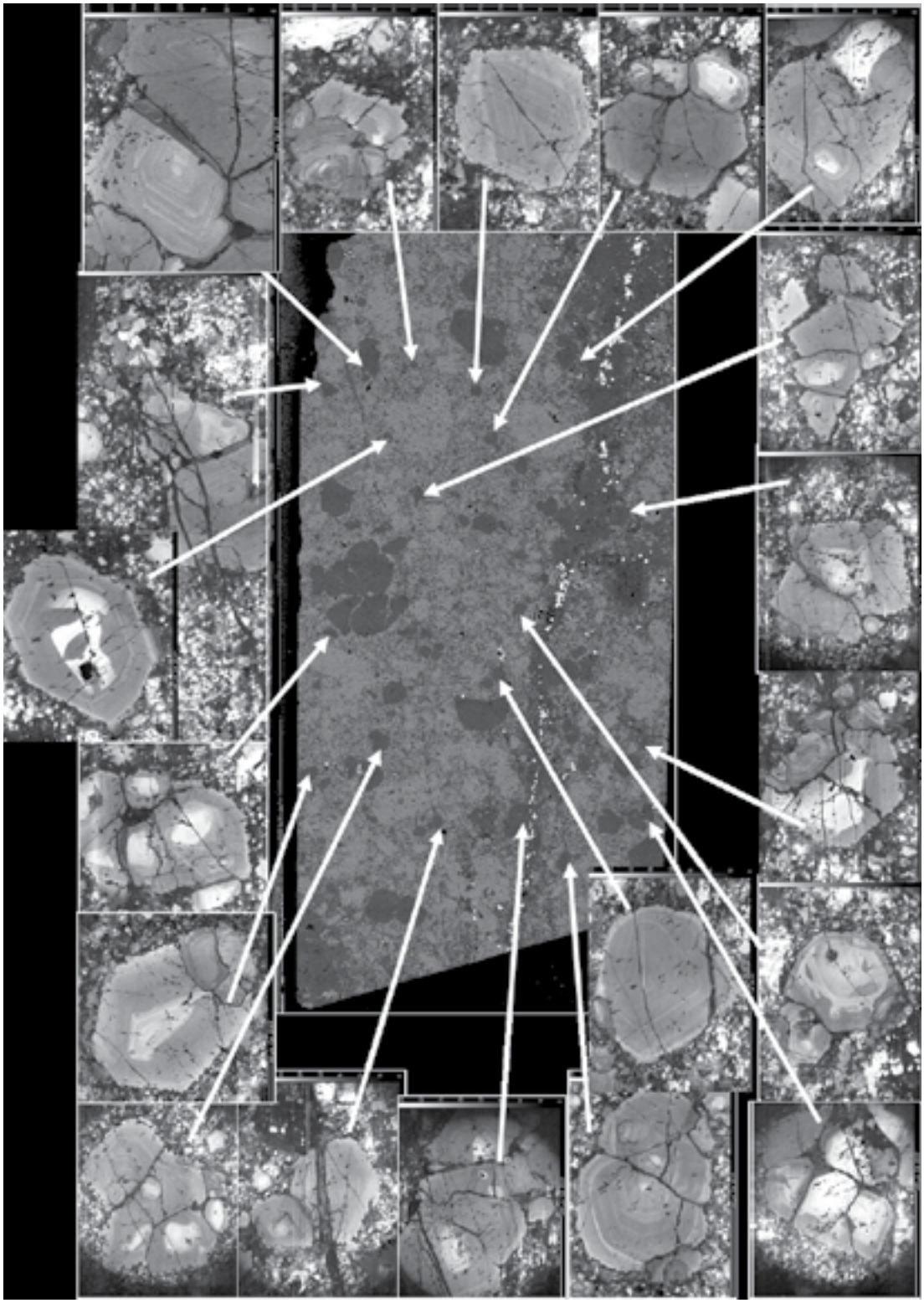

Climax (109646)

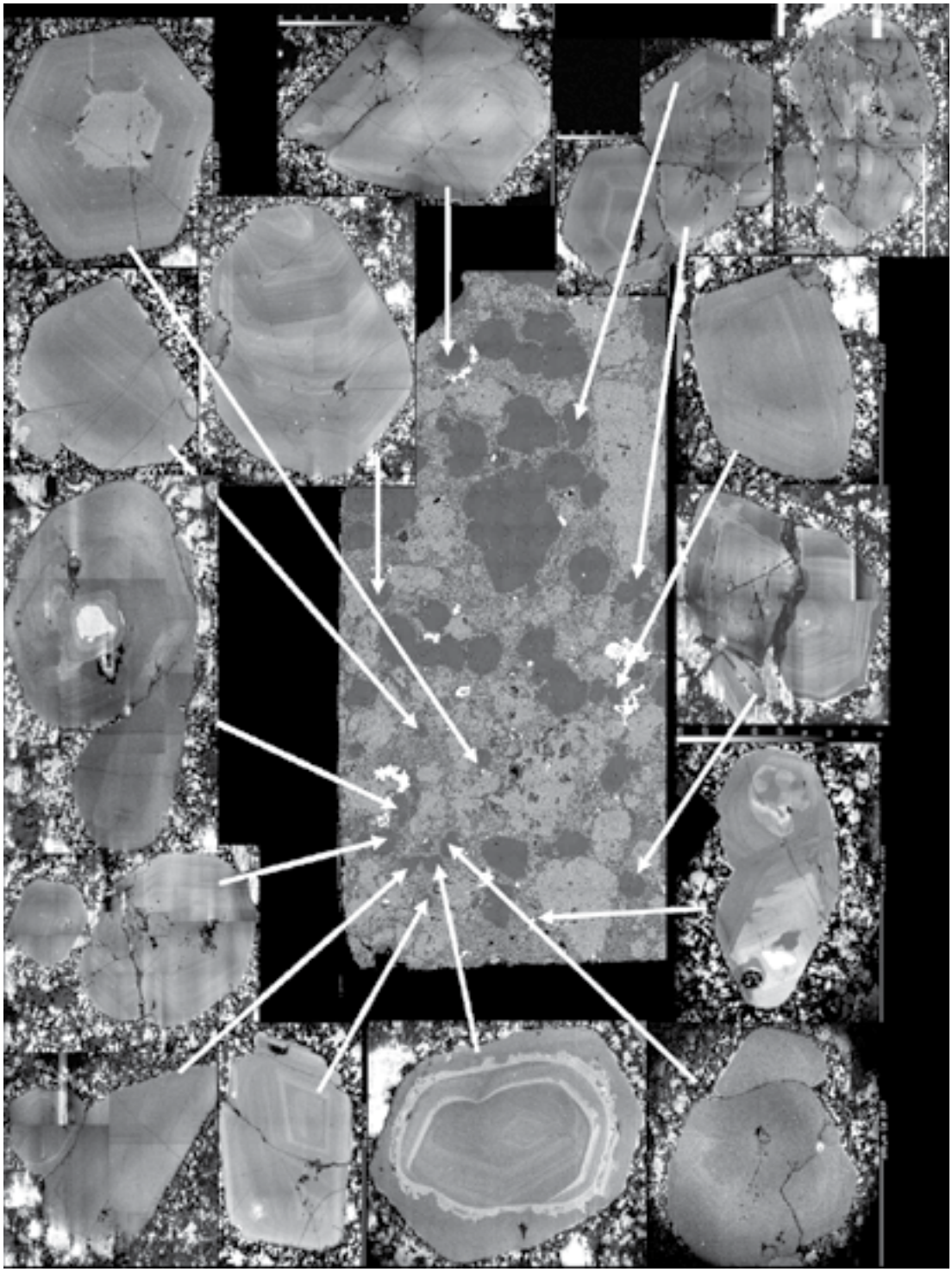

Climax (109647)

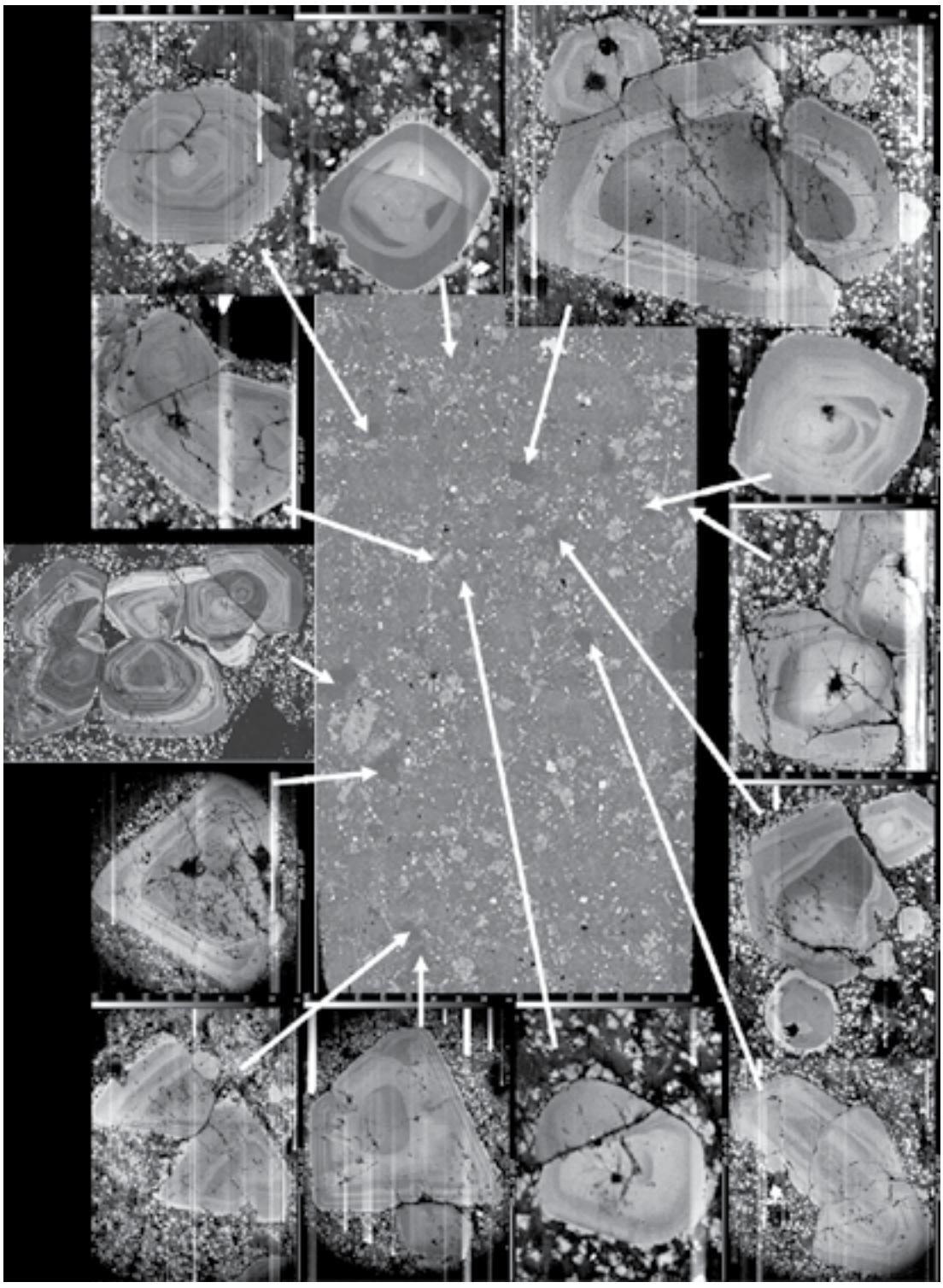

Panguna (109607)

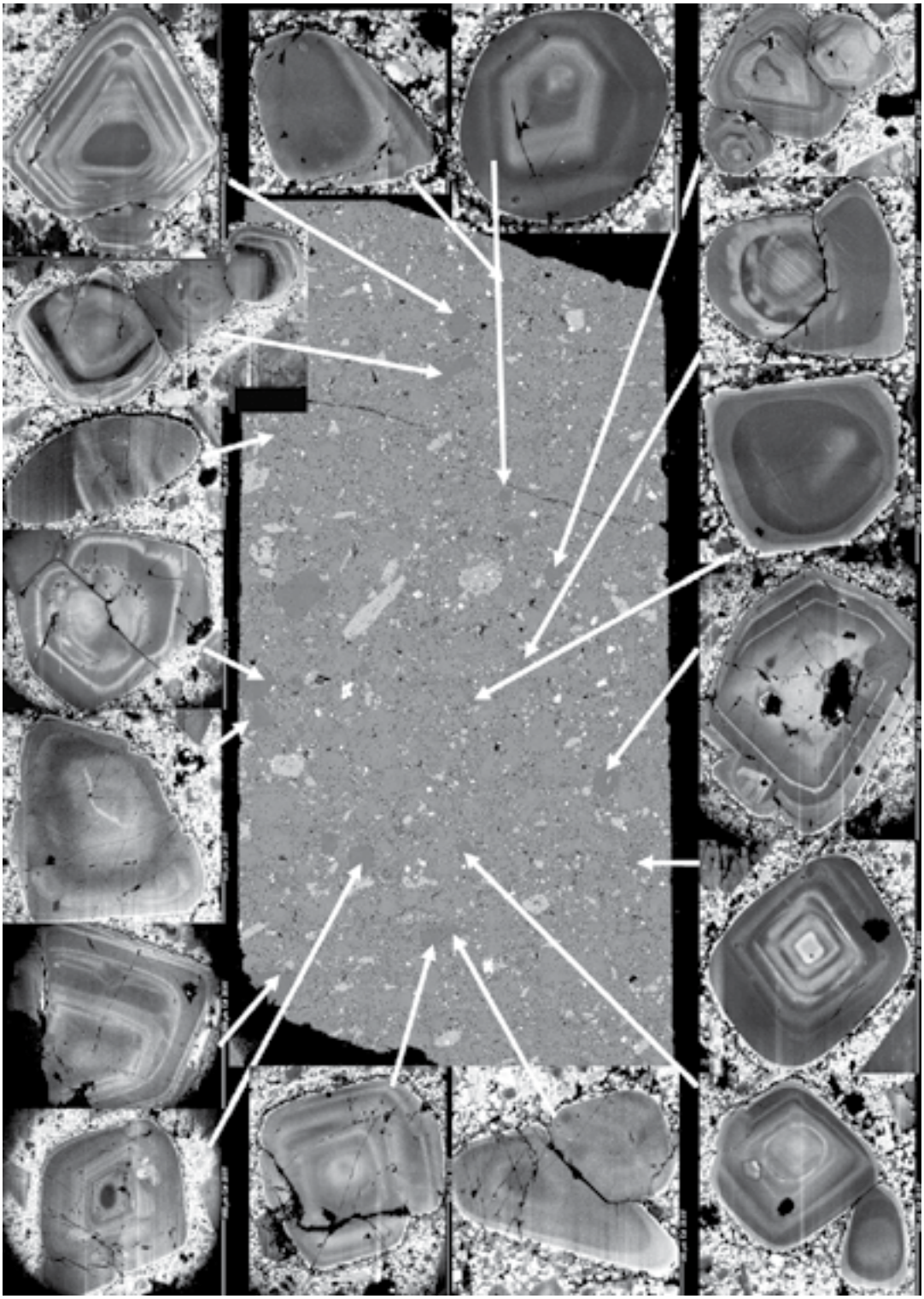

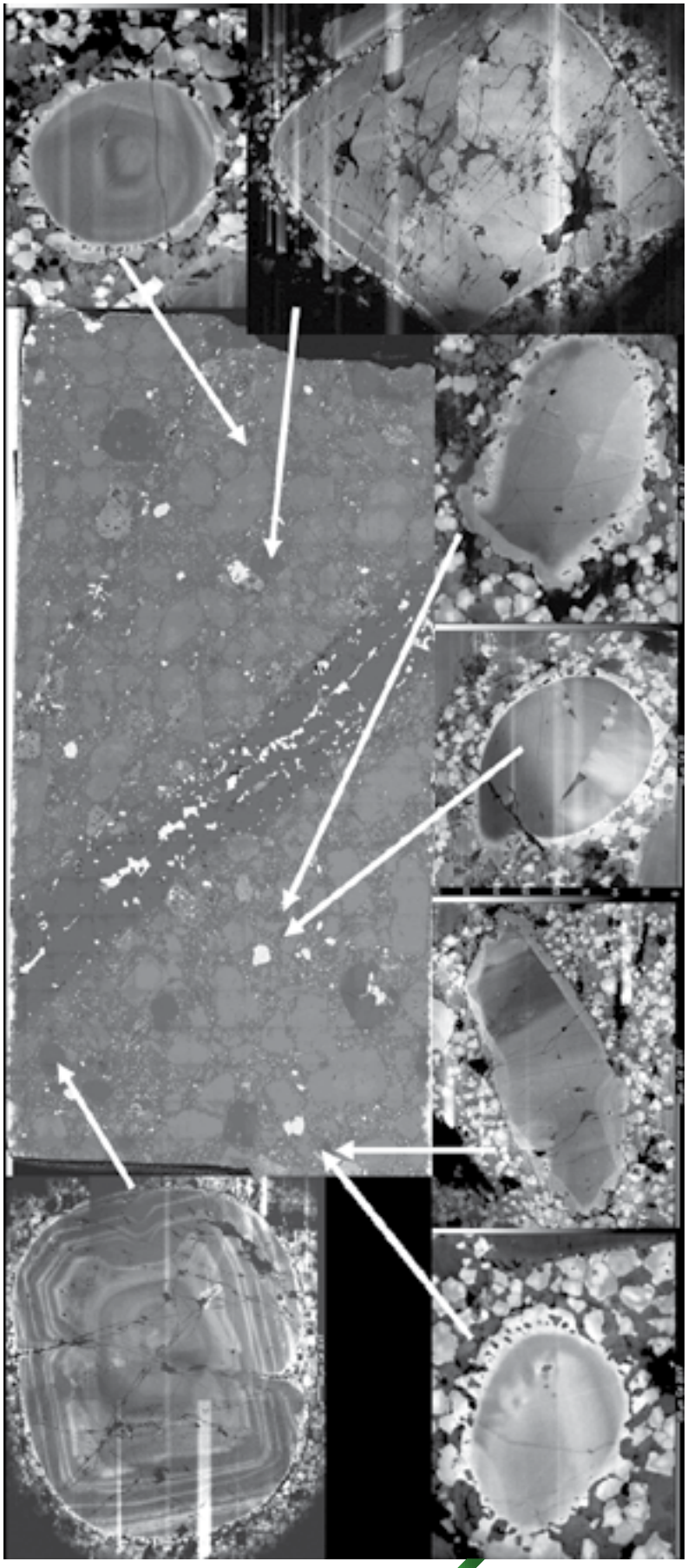

Batu Hijau (138-2)

Batu Hijau (SBD-69)

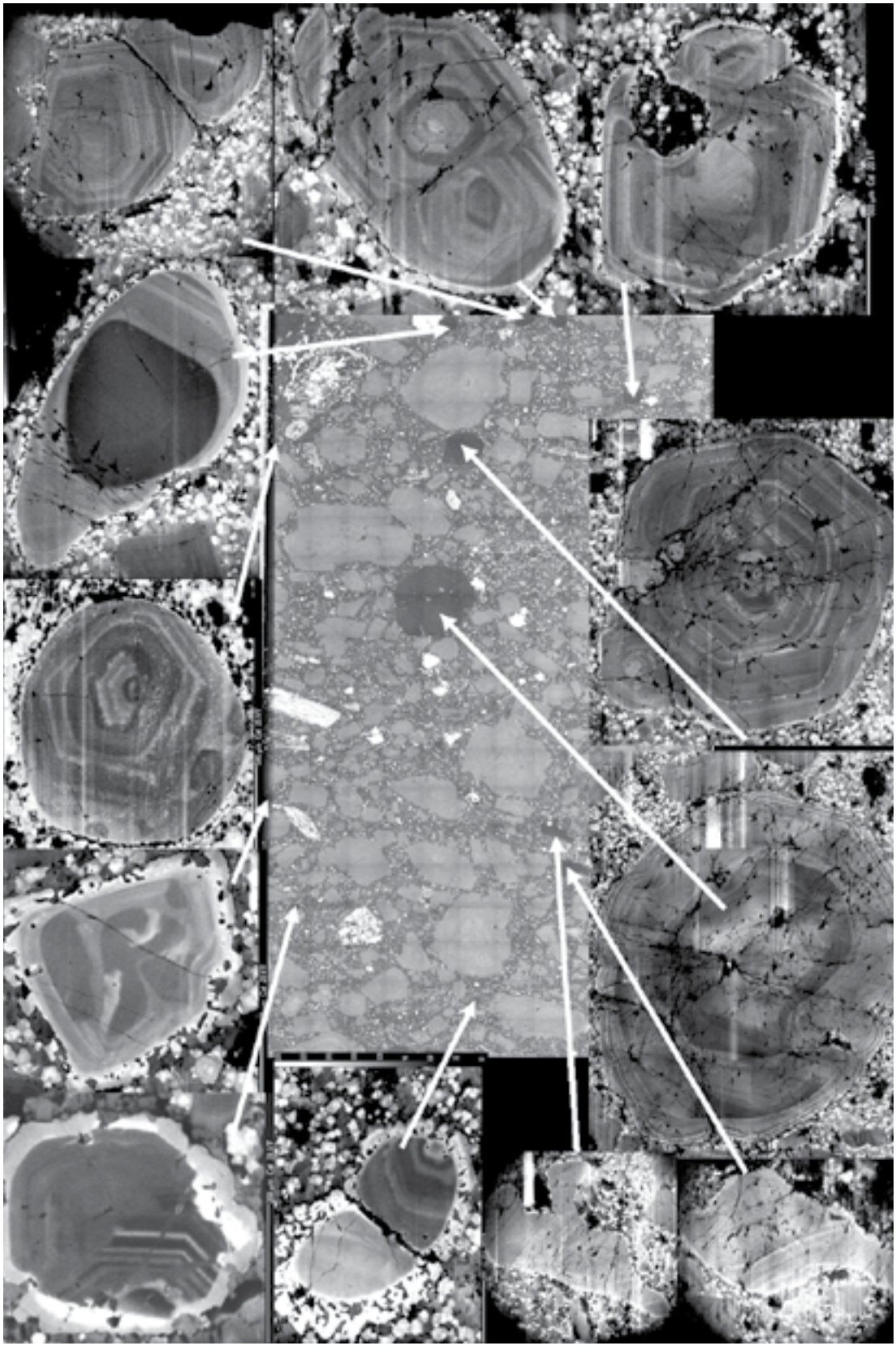

Batu Hijau (SRD-02)

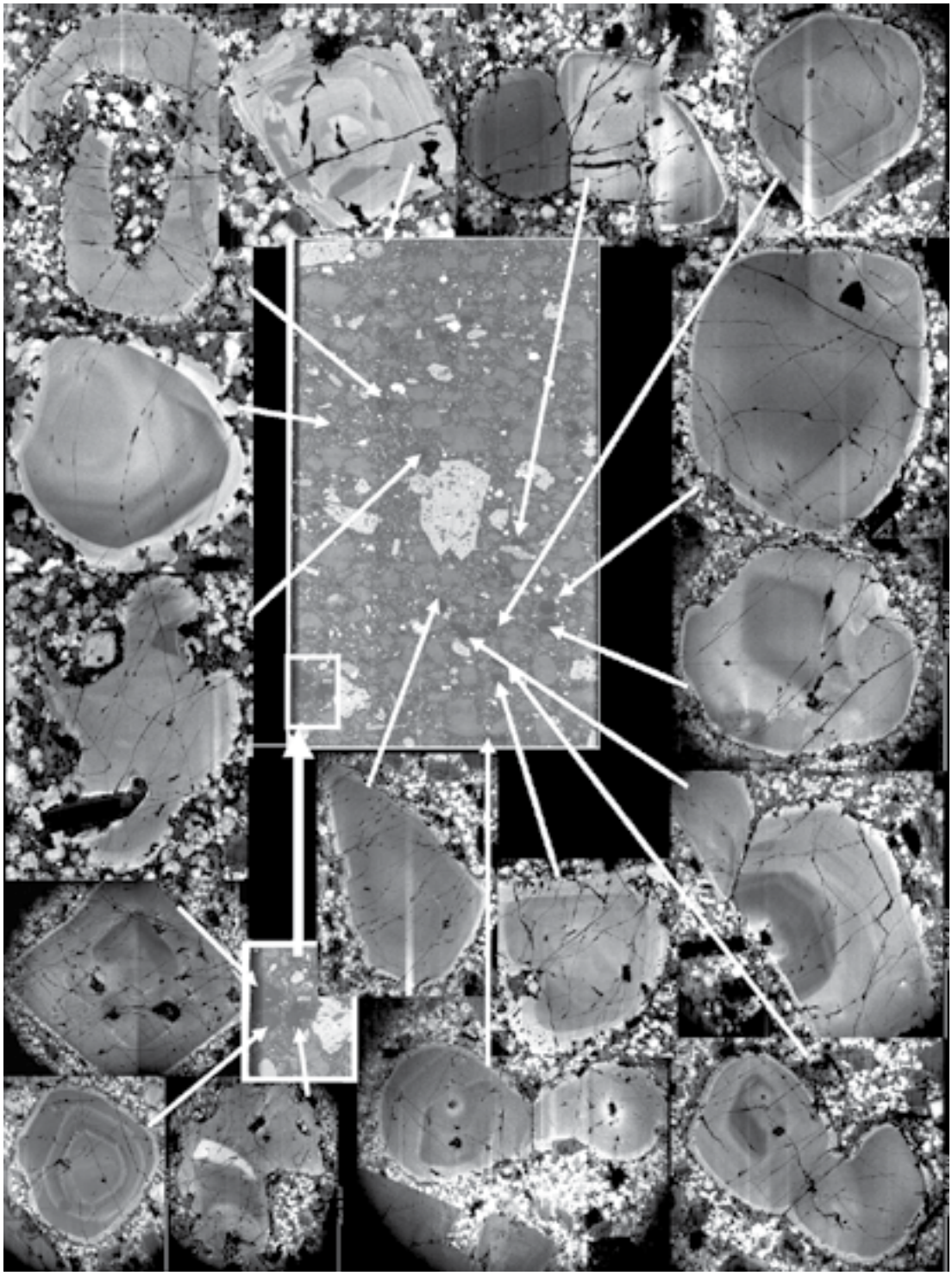

South East Porphyry (P13)

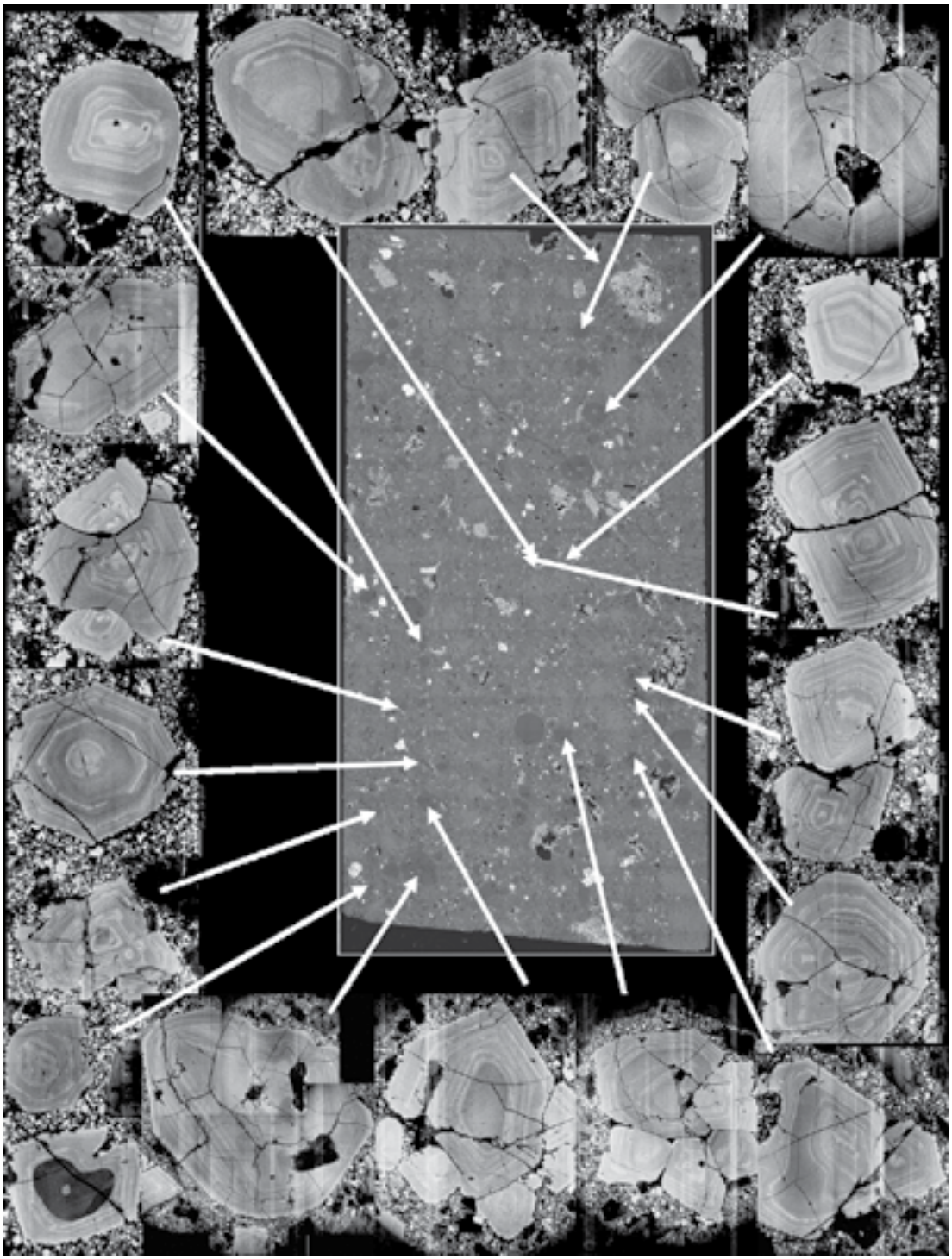

Trace elements in quartz

Sample	Al	Fe	Ti
Climax (109647)	110	38	12
	109	34	6
	184	53	30
	159	67	47
	170	114	17
	155	151	30
	135	223	17
	190	354	30
	131	19	17
	125	33	16
	110	23	3
	197	44	37
	176	59	43
	145	135	22
	146	203	29
	1797	318	20
	225	496	36
	115	21	1
	157	44	35
	148	26	15
	309	22	38
Rio Blanco (DC-DLP-1)	2825	99	132
	972	37	254
	1333	56	157
	1187	83	218
	1550	63	161
	3340	216	174
	1483	98	162
	121	17	45
	112	9	49
	118	1	31
	132	6	54
	112	12	43
	282	16	45
	4387	65	32
	3025	235	16
	2175	41	38
	146	52	44
	633	30	162
	922	39	272
	3858	71	173
	1125	63	224
	1158	61	197
	2417	169	186
	126	10	48
	112	14	41
	107	14	24
	132	6	51

Sample	Al	Fe	Ti
Rio Blanco (DC-DLP-1)	122	246	43
	148	17	30
	152	14	18
	5110	81	4
	125	35	36
	134	37	39
	138	12	49
	158	16	29
	438	19	19
	105	20	34
	140	14	47
	160	16	31
	128	10	26
	94	19	21
Batu Hijau (SBD-69)	239	23	58
	240	39	56
	227	34	58
	244	39	87
	250	42	82
	221	37	71
	251	35	214
	250	47	225
	278	45	231
	214	20	179
	207	60	177
	215	41	180
	384	63	166
	231	56	171
	209	45	175
	197	28	167
	181	58	183
	164	111	179
	4967	1246	180
	3167	1048	522
	289	63	275
	160	75	164
	297	71	259
	25	3	4
	3071	72	143
Rio Blanco (DC-DP-1, Qtz-2)	121	13	20
	118	15	22
	118	19	28
	96	14	21
	112	18	24
	99	10	20
	88	22	68
	88	6	65
	95	11	62

Sample	Al	Fe	Ti
Rio Blanco (DC-DP-1, Qtz-2)	88	20	56
	85	28	69
	94	28	58
	108	88	49
	112	103	48
	113	103	46
	104	0	53
	107	33	41
	110	32	48
	93	29	57
	87	16	53
	89	34	57
	86	25	45
	96	2	52
	105	0	50
	1055	97	565
	1681	103	360
	2894	163	337
Rio Blanco (DC-DP-1, Qtz-10&10a)	119	0	18
	103	6	23
	113	2	13
	134	35	30
	133	8	21
	127	13	15
	91	22	30
	98	20	31
	98	15	29
	86	49	56
	85	69	64
	98	46	62
	86	49	72
	95	70	73
	95	63	72
	110	174	46
	109	164	55
	112	191	42
	114	49	29
	117	33	24
	111	15	26
	118	47	47
	97	39	65
	97	47	66
	94	35	62
	91	38	63
	93	24	58
	97	50	62
	99	57	65
	92	57	71
	94	54	61

Sample	Al	Fe	Ti
Rio Blanco (DC-DP-1, Qtz-11)	52	0	4
	56	19	0
	152	32	40
	113	6	49
	110	5	52
	72	27	50
	63	5	43
	92	10	59
	64	0	48
	58	1	42
	59	0	35
	82	22	53
	76	19	63
	87	11	56
	73	25	43
	97	42	41
	94	65	33
	157	190	45
	154	174	53
	138	187	56
	109	30	56
	96	33	59
	94	48	52
Rio Blanco (CA6)	1156	58	351
	139	21	35
	86	23	29
	91	23	30
	97	27	27
	99	17	21
	91	26	15
	95	29	48
	90	34	47
	90	37	50
	95	39	34
	105	40	28
	104	52	28
	115	96	43
	111	113	49
	124	128	55
	101	69	58
	96	75	55
	112	57	61

Sample	Al	Fe	Ti	Zn
Batu Hijau (SRD-02)	153	442	125	5
	159	450	123	10
	129	337	113	42
	766	386	1	47
	176	144	174	59
	84665	169	0	20
	190	462	183	6
	175	343	172	10
	154	410	142	34
	6197	744	289	17
	213	505	180	19
	256	247	236	34
	181	140	162	33
	14712	263	154	0
	312	246	281	10
	172	215	136	0
	207	269	93	29
	207	175	164	52
	84	88	0	0
	211	28	154	9
	221	31	130	63
	31	23	0	14
	198	155	184	39
	175	142	137	9
	118039	1962	97	6
	250	140	122	26
	197	117	94	56
	36	53	1	7
	144	112	114	13
	217	67	149	20
	204	170	93	0
	163	515	143	25
	179	284	138	0
	176	153	76	17
	4359	182	225	27
	168	237	137	25
	300	95	115	0
	453	403	12	18

Sample	Al	Fe	Ti	Zn
Antapacay (092-29700)	96	19	17	1342
	95	27	30	1661
	43	14	0	2538
	47	36	3	4304
	51	46	0	5691
	370	10	42	3278
	216	21	66	2637
	153	11	61	2217
	100	16	31	1364
	117	15	40	928
	154	22	63	740
	1427	63	90	547
	253	38	109	176
	1148	33	0	256
	816	36	4	417
	3361	51	2	3048
	911	39	10	3908
	49	69	0	5852
	40	41	5	3984
	307	40	0	3885
	101	15	44	1417
	114	0	41	2078
	98	11	24	1551
	174	30	49	855

Typical fluid behaviour during heating-cooling experiments

This section includes detailed description of two characteristic experiments BH_138-2_eye_inclusion2 and BH_138-2_vein_inclusion4) distinguishing typical fluid behaviour within the studied samples and emphasising some unusual features. The experiments chosen to be described in details here were carried out with samples from Batu Hijau (138-2) from quartz eye (inclusion 2) and quartz vein (inclusion 4) and seemed to be representative of the fluid behaviour in studied samples. Some features occurred in other experiments are also pointed out both in the description.

138-2 Quartz eye, inclusion 2

Heating from 40 to 380°C

This was the second run with the sample, so the phase appearances in the inclusion in the beginning of heating were distinct from initial ones that were observed before the first run. Before heating the inclusion contained an undeformed gas bubble (gb), liquid phase (l) and three solid phases (s). After the first heating run, at the beginning of the second run four phases were observed in the inclusion at 40°C: an undeformed gas bubble (gb), a liquid phase (l), an aggregate of anhedral transparent mass (ph1) and a darker less transparent phase with a high relief.

The earliest phase transitions began at 80°C. One of the phases (ph2) began swirling changing its volume and shape, separating into small spherical parts and dissolving gradually at the same time. It dissolved completely at 100°C. There were no more changes observed until 150°C. Further heating from 150°C led to gradual dissolution of the second phase. At 280°C two small round crystals were observed and the last of them dissolved at 315°C. Active movement and disappearance of film-textured transparent substance was observed at about 300°C to 330°C, followed by dissolution of ph1. A gas bubble disappeared at 375°C.

Cooling from 380 to 40°C

At 340°C a gas bubble appeared and started growing. At 280°C the bubble jerked and the first episode of immiscibility occurred when the thin film appeared in the centre of the inclusion and expanded rapidly towards the walls becaming almost invisible. Further cooling from 280°C was accompanied by growth of the gas bubble, and at about 170°C a thin rim of liquid phase appeared around the gas bubble. The second episode of immiscibility occurred at 140°C, when another phase appeared suddenly in the centre of the inclusion in a form of skeletal crystalline mass. It seemed that the new phase formed inside the film phase, which appeared earlier at 280°C.

The new phase did not change during further cooling. About the same time the liquid rim around the gas bubble got deformed. At 85°C the third episode of immiscibility was observed: another phase grew rapidly within a couple of seconds. No further changes were observed during cooling to room temperature. At 60°C the inclusion contained five phases: a gas bubble (gb), a liquid rim around gas bubble (lr), a liquid phase (l), an aggregate of anhedral transparent mass (ph1) and a darker and less transparent phase with a high relief (ph2). Phases ph1 and ph2 that observed at 60°C after cooling are presumably corresponded to phases ph1 and ph2 before heating.

138-2 Quartz vein, inclusion 4

Heating from 30 to 490°C

Before heating the inclusion contained a gas bubble (gb), liquid phase (l), two solid phases (s), hematite (h) and an unidentified opaque phase (op). Since the sample was previously heated (to observe inclusions 1, 2 and 3) phases in the inclusion before an experiment differed from those observed earlier. The phases before the experiment were deformed gas bubble (gb, surrounded by a liquid?), a liquid phase (l), a transparent cubic phase (ph1) and an aggregate of anhedral transparent mass (ph2) around hematite (h).

At 80°C phases 2 decreases in volume, swirling in the beginning and then separating into small spherical parts and dissolving gradually at the same time. This phase together with a liquid phase surrounding the bubble dissolved completely at 130°C. When phase 2 disappeared the bubble became spherical. There were no changes observed until 220°C when hematite crystal rotated. Further heating led to disappearing of the bubble at 370°C and finally, dissolution of the second phase (ph1) at 480°C. Neither hematite nor the other opaque phase dissolved during heating.

Cooling from 490 to 40°C

There were no changes observed in the inclusion during cooling to 330°C when the first episode of immiscibility occurred. Two immiscible transparent phases and a gas bubble formed as a result of this event and then one of the phases recrystallised rapidly to form three anhedral phases. Further cooling led to further recrystallisation; two transparent phases were observed at 280°C and only one transparent phase at 200°C. Further cooling to 66°C caused only minor changes: the bubble grew slightly, phase 2 became cubic with nice faces and a liquid phase changes its refractive properties so that optic boundary between inclusion and host quartz becomes darker. At 66°C the second episode of immiscibility was observed: another phase (ph2) grew

rapidly within a couple of seconds. During following cooling to about 40°C the gas bubble expanded and gradually got deformed.

At 40°C the inclusion contained five phases: a deformed gas bubble (gb), a liquid phase (l), a hematite (h) and an unidentified opaque phase (op), a transparent cubic phase (ph1) and a transparent round phase with higher diffraction index (ph2).

Video files

BH_138-2_vein_inclusion1

BH_138-2_vein_inclusion5

BH_138-2_vein_inclusion4

BH_138-2_eye_inclusion2

List of acronyms

Qtz - quartz
Qtz eye - quartz eye
Qtz vein - quartz vein
Kfs - K-feldspar
Pl - plagioclase
Ap - apatite
Fl - fluorite
Rt - rutile
Bt - biotite
Cpy - chalcopyrite
Bor - bornite
Pyr - pyrite
Ser - sericite
Chl - chlorite
Mt - magnetite
Tz - topaz

h - hematite
gb - gas bubble
ph - phase
s - solid phase
l - liquid
lr - liquid rim
op - opaque
Ma - Million years ago
FI - fluid inclusions
LA-ICP-MS - Laser ablation-inductively coupled plasma-mass spectrometry
BSE - Backscattered Electrons
SE - Secondary Electrons
CL - cathodoluminescence
SEM-CL- Scanning Electron Microscope based cathodoluminescence

References

Akinfiev, N. N., and Diamond, L. W., 2009, A simple predictive model of quartz solubility in water–salt–CO2 systems at temperatures up to 1000oC and pressures up to 1000 MPa: Geochimica et Cosmochimica Acta, v. 73, p. 1597-1608.

Allan, M. M., and Yardley, B. W. D., 2007, Tracking meteoric infiltration into a magmatic-hydrothermal system: A cathodoluminescence, oxygen isotope and trace element study of quartz from Mt. Leyshon, Australia: Chemical Geology, v. 240, p. 343–360.

Ancey, M. F., Microanalysis and scanning electron microscopy, St-Martin-d'Heres, France, 1978, Proceedings of Summer School

Andres, R. J., Rose, W. I., Kyle, P. R., Desilva, S., Francis, P., Gardeweg, M., and Roa, H. M., 1991, Excessive Sulfur-Dioxide Emissions from Chilean Volcanos: Journal of Volcanology and Geothermal Research, v. 46, no. 3-4, p. 323-329.

Audetat, A., and Gunther, D., 1999, Mobility and H_2O loss from fluid inclusions in natural quartz crystals: Contributions to Mineralogy and Petrology, v. 137, p. 1-14.

Audetat, A., Pettke, T., Heinrich, C. A., and Bodnar, R. J., 2008, The Composition of Magmatic-Hydrothermal Fluids in Barren and Mineralized Intrusions: Economic Geology, v. 103, no. 5, p. 877-908.

Bakker, R. J., and Jansen, J. B., 1994, A Mechanism for Preferential H_2O Leakage from Fluid Inclusions in Quartz, Based on Tem Observations: Contributions to Mineralogy and Petrology, v. 116, no. 1-2, p. 7-20.

Bodnar, R. J., 1995, Fluid inclusion evidence for a magmatic source for metals in porphyry copper deposits, in Thompson, J. F. H., ed., Magmas, Fluids and Ore Deposits, Volume 23, Mineralogical Association of Canada Short Course, p. 139-152.

Borisenko, A. S., 1977, Studying of salt composition of fluid inclusions in minerals a method cryometry: Geology and geophysics (in Russia), v. 8, p. 16-27.

Breiter, K., and Muller, A., 2009, Evolution of rare-metal granitic magmas documented by quartz chemistry: European Journal of Mineralogy, v. 21, no. 2, p. 335-346.

Burnham, C. W., 1979, Magmas and hydrothermal fluids, in Barnes, H. L., ed., Geochemistry of Hydrothermal Ore Deposits: New York, J.Wiley & Sons, p. 63-123.

Burnham, C. W., and Ohmoto, H., 1980, Late-stage processes of felsic magmatism: Mining Geology Special Issue, v. 8, p. 1-11.

Candela, P. A., 1991, Physics of Aqueous Phase Evolution in Plutonic Environments: American Mineralogist, v. 76, no. 7-8, p. 1081-1091.

Candela, P. A., and Holland, H. D., 1984, The Partitioning of Copper and Molybdenum between Silicate Melts and Aqueous Fluids: Geochimica Et Cosmochimica Acta, v. 48, no. 2, p. 373-380.

Candela, P. A., and Piccoli, M. P., 1995, Model ore-metal partitioning into vapor and vapor/brine mixtures, in Thompson, J. F. H., ed., Magmas, Fluids and Ore Deposits, Volume 23: Victoria, B.C., Mineralogical Association of Canada Short Course Series, p. 101-127.

Carten, R. B., Geraghty, E. P., and Walker, B. M., 1988, Cyclic Development of Igneous Features and Their Relationship to High-Temperature Hydrothermal Features in the Henderson Porphyry Molybdenum Deposit, Colorado: Economic Geology, v. 83, no. 2, p. 266-296.

Chang, Z. S., and Meinert, L. D., 2004, The magmatic-hydrothermal transition - evidence from quartz phenocryst textures and endoskarn abundance in Cu-Zn skarns at the Empire Mine, Idaho, USA: Chemical Geology, v. 210, no. 1-4, p. 149-171.

Clemens, J. D., 2009, The message in the bottle: "Melt" inclusions in migmatitic garnets: Geology, v. 37, no. 7, p. 671-672.

Cline, J. S., and Bodnar, R. J., 1991, Can Economic Porphyry Copper Mineralization Be Generated by a Typical Calc-Alkaline Melt: Journal of Geophysical Research-Solid Earth and Planets, v. 96, no. B5, p. 8113-8126.

Cloos, M., 2001, Bubbling magma chambers, cupolas, and porphyry copper deposits: International Geology Review, v. 43, no. 4, p. 285-311.

Corbett, G., 2009, Geological Models in Epithermal-Porphyry Exploration: Terry Leach's Legacy: SGEG Newsletter, no. 1-2, p. 3-14.

D'Lemos, R. S., Kearsley, A. T., Pembroke, J. W., Watt, G. R., and Wright, P., 1997, Complex quartz growth histories in granite revealed by scanning cathodoluminescence techniques: Geology Magazine, v. 134, no. 4, p. 549–552.

Davidson, P., 2004, A new methodology for the study of the magmatichydrothermal transition in felsic magmas: applications to barren and mineralised systems: University of Tasmania, 289 p.

Davidson, P., and Crawford, A. J., 2006, Coexisting melt and fluid inclusions at Batu Hijau: Evidence for primary magmatic aqueous fluids and their relationship to mineralisation: Geochimica Et Cosmochimica Acta, v. 70, no. 18, p. A131-A131.

Davidson, P., Kamenetsky, V., Cooke, D. R., Frikken, P., Hollings, P., Ryan, C., Van Achterbergh, E., Mernagh, T., Skarmeta, J., Serrano, L., and Vargas, R., 2005,

Magmatic precursors of hydrothermal fluids at the Rio Blanco Cu-Mo deposit, Chile: Links to silicate magmas and metal transport: Economic Geology, v. 100, no. 5, p. 963-978.

Davidson, P., and Kamenetsky, V. S., 2001, Immiscibility and continuous felsic melt-fluid evolution within the Rio Blanco porphyry system, Chile: Evidence from inclusions in magmatic quartz: Economic Geology and the Bulletin of the Society of Economic Geologists, v. 96, no. 8, p. 1921-1929.

Dunbar, N. W., and Hervig, R. L., 1992, Petrogenesis and Volatile Stratigraphy of the Bishop Tuff - Evidence from Melt Inclusion Analysis: Journal of Geophysical Research-Solid Earth, v. 97, no. B11, p. 15129-15150.

Eastoe, C. J., 1978, Fluid Inclusion Study of Panguna-Porphyry-Copper-Deposit, Bougainville, Papua-New-Guinea: Economic Geology, v. 73, no. 5, p. 721-748.

Elliston, J., 2005, The origin of rocks and mineral deposits - using current physical chemistry of small particle systems, ELLISTON RESEARCH ASSOCIATES PTY LTD.

Ganeev, I. G., 1971, Unmixing in the system H_2O-SiO_2-NaOH under the high temperatures and pressures: Inorganic Materials, v. 7, no. 12, p. 2191-2194.

Gerlach, T. M., Westrich, H. R., Casadevall, T. J., and Finnegan, D. L., 1994, Vapor Saturation and Accumulation in Magmas of the 1989-1990 Eruption of Redoubt Volcano, Alaska, Journal of Volcanology and Geothermal Research, Volume 62, p. 317-337.

Götze, J., 2009, Chemistry, textures and physical properties of quartz - geological interpretation and technical application: Mineralogical Magazine, v. 73, no. 4, p. 645-671.

Götze, J., Mockel, R., Kempe, U., Kapitonov, I., and Vennemann, T., 2009, Characteristics and origin of agates in sedimentary rocks from the Dryhead area, Montana, USA: Mineralogical Magazine, v. 73, no. 4, p. 673-690.

Götze, J., Plötze, M., and Habermann, D., 2001, Origin, spectral characteristics and practical applications of the cathodoluminescence (CL) of quartz - a review: Mineralogy and Petrology, v. 71, p. 225-250.

Götze, J., Plötze, M., and Trautmann, T., 2005, Structure and luminescence characteristics of quartz from pegmatites: American Mineralogist, v. 90, p. 13-21.

Gustafson, L. B., 1978, Some Major Factors of Porphyry Copper Genesis: Economic Geology, v. 73, no. 5, p. 600-607.

Halter, W. E., Pettke, T., and Heinrich, C. A., 2002, The origin of Cu/Au ratios in porphyry-type ore deposits: Science, v. 296, no. 5574, p. 1844-1846.

Harris, A. C., Kamenetsky, V. S., White, N. C., and Steele, D. A., 2004, Volatile phase separation in silicic magmas at Bajo de la Alumbrera porphyry Cu-Au deposit, NW Argentina: Resource Geology, v. 54, no. 3, p. 341-356.

Harrowfield, I. R., MacRae, C. M., and Wilson, N. C., 1993, Chemical imaging in electron microprobes, Proceedings of the 27th Annual MAS meeting 1993, Microbeam Analysis Society, p. 547-548.

Hattori, K., 1993, High-Sulfur Magma, a Product of Fluid Discharge from Underlying Mafic Magma - Evidence from Mount-Pinatubo, Philippines: Geology, v. 21, no. 12, p. 1083-1086.

Hattori, K. H., and Keith, J. D., 2001, Contribution of mafic melt to porphyry copper mineralization: evidence from Mount Pinatubo, Philippines, and Bingham Canyon, Utah, USA: Mineralium Deposita, v. 36, no. 8, p. 799-806.

Heaney, P. J., and Davis, A. M., 1995, Observation and Origin of Self-Organized Textures in Agates: Science, v. 269, no. 5230, p. 1562-1565.

Hedenquist, J. W., Arribas, A., and Reynolds, T. J., 1998, Evolution of an intrusion-centered hydrothermal system: Far Southeast-Lepanto porphyry and epithermal Cu-Au deposits, Philippines: Economic Geology and the Bulletin of the Society of Economic Geologists, v. 93, no. 4, p. 373-404.

Hedenquist, J. W., and Lowenstern, J. B., 1994, The Role of Magmas in the Formation of Hydrothermal Ore-Deposits: Nature, v. 370, no. 6490, p. 519-527.

Heinrich, C. A., 2007, Fluid-fluid interactions in magmatic-hydrothermal ore formation: Fluid-Fluid Interactions, v. 65, p. 363-387.

Henisch, H. K., 1996, Crystal Growth in Gels, New York, Dover Publications, INC, 111 p.:

Herrington, R. J., and Wilkinson, J. J., 1993, Colloidal Gold and Silica in Mesothermal Vein Systems: Geology, v. 21, no. 6, p. 539-542.

Holland, H. D., 1965, Some application of thermochemical data to problems of ore deposits, II. Mineral assembledges and the composition of oreforming fluids: Economic Geology, v. 60, p. 1101-1166.

Hopwood, T. P., 1976, Quartz-Eye-Bearing Porphyroidal Rocks and Volcanogenic Massive Sulfide Deposits: Economic Geology, v. 71, no. 3, p. 589-612.

Hu, X. Y., Bi, X. W., Hu, R. Z., Shang, L. B., and Fan, W. L., 2008, Experimental study on tin partition between granitic silicate melt and coexisting aqueous fluid: Geochemical Journal, v. 42, no. 2, p. 141-150.

Ihinger, P. D., and Zink, S. I., 2000, Determination of relative growth rates of natural quartz crystals: Nature, v. 404, no. 6780, p. 865-869.

Ingerson, E., 1954, Nature of the ore-forming fluids at various stages - a suggested approuch: Economic Geology and the Bulletin of the Society of Economic Geologists, v. 49, p. 727-733.

Jones, B. M., 2006, The Abancay Batholith, late eocene crustal thickening, multiple mixing-differentiation cycles, and porphyry Cu-Au mineralisation on the Altiplano at Antapaccay, Southern Peru: Geochimica Et Cosmochimica Acta, v. 70, no. 18, p. A297-A297.

Kamenetsky, V. S., 2006, Melt inclusion record of magmatic immiscibility in crustal and mantle magmas, Mineralogical Association of Canada Short Course Series, p. 81-98.

Kamenetsky, V. S., and Kamenetsky, M. B., 2010, Magmatic fluids immiscible with silicate melts: examples from inclusions in phenocrysts and glasses, and implications for magma evolution and metal transport: Geofluids, v. 10, no. 1-2, p. 293-311.

Kamenetsky, V. S., Naumov, V. B., Davidson, P., van Achterbergh, E., and Ryan, C. G., 2004, Immiscibility between silicate magmas and aqueous fluids: a melt inclusion pursuit into the magmatic-hydrothermal transition in the Omsukchan Granite (NE Russia): Chemical Geology, v. 210, no. 1-4, p. 73-90.

Keith, J. D., Whitney, J. A., Hattori, K., Ballantyne, G. H., Christiansen, E. H., Barr, D. L., Cannan, T. M., and Hook, C. J., 1997, The role of magmatic sulfides and mafic alkaline magmas in the Bingham and Tintic mining districts, Utah: Journal of Petrology, v. 38, no. 12, p. 1679-1690.

Kennedy, G. C., 1950, A portion of the system silica-water: Economic Geology, v. 45, p. 629-653.

Kilinc, I. A., and Burnham, C. W., 1972, Partitioning of chloride between a silicate melt and coexisting aqueous phase from 2 to 8 kilobars: Economic Geology, v. 76, no. 2, p. 231-235.

Kotel'nikova, Z. A., and Kotel'nikov, A. R., 2010a, Experimental study of heterogeneous fluid equilibria in silicate-salt-water systems: Geology of Ore Deposits, v. 52, no. 2, p. 154-166.

-, 2010b, Immiscibility in sulfate-bearing fluid systems at high temperatures and pressures: Geochemistry International, v. 48, no. 4, p. 381-389.

Landtwing, M. R., and Pettke, T., 2005, Relationships between SEM-cathodoluminescence response and trace-element composition of hydrothermal vein quartz: American Mineralogist, v. 90, no. 1, p. 122-131.

Lapidus, D. F., 1990, Collins Dictionary Of Geology HarperCollins Publishers, p. 480.

Leeman, W. P., Vicenzi, E. P., MacRae, C. M. M., Wilson, N. C., Torpy, A., and Lee,

C.-T. A., 2008, Systematics of Cathodoluminescence and Trace Element Compositional Zoning in Natural Quartz from Volcanic Rocks: Ti mapping in Quartz: Microscopy and Microanalysis, v. 14, no. Supplement S2.

Lehmann, K., Berger, A., Gotte, T., Ramseyer, K., and Wiedenbeck, M., 2009, Growth related zonations in authigenic and hydrothermal quartz characterized by SIMS-, EPMA-, SEM-CL- and SEM-CC-imaging: Mineralogical Magazine, v. 73, no. 4, p. 633-643.

Lentz, D. R., and Goodfellow, W. D., 1993, Petrography and mass-balance constrains on the origin of quartz-augen shcist associated with Brunswick massive sulfide deposits, Bathurst New Brunswick: Canadian Mineralogist, v. 31, p. 877-903.

Lowell, J. D., and Guilbert, J. M., 1970, Lateral and Vertical Alteration-Mineralization Zoning in Porphyry Ore Deposits: Economic Geology, v. 65, no. 4, p. 373-408.

Lowenstern, J. B., 1994, Dissolved volatile concentrations in an ore-forming magma: Geology, v. 22, p. 893-896.

Lowenstern, J. B., and Sinclair, W. D., 1996, Exsolved magmatic fluid and its role in the formation of comb-layered quartz at the cretaceous logtung W-Mo deposit, Yukon territory, Canada: Transactions of the Royal Society of Edinburgh-Earth Sciences, v. 87, p. 291-303.

MacLellan, H. E., and Trembath, L. T., 1991, The Role of Quartz Crystallization in the Development and Preservation of Igneous Texture in Granitic-Rocks - Experimental-Evidence at 1-Kbar: American Mineralogist, v. 76, no. 7-8, p. 1291-1305.

MacRae, C. M., Wilson, N. C., Johnson, S. A., Phillips, P. L., and Otsuki, M., 2005, Hyperspectral mapping - Combining cathodoluminescence and X-ray collection in an electron microprobe: Microscopy Research and Technique, v. 67, no. 5, p. 271-277.

Maughan, D. T., Keith, J. D., Christiansen, E. H., Pulsipher, T., Hattori, K., and Evans, N. J., 2002, Contributions from mafic alkaline magmas to the Bingham porphyry Cu-Au-Mo deposit, Utah, USA: Mineralium Deposita, v. 37, no. 1, p. 14-37.

McLaren, A. C., and Phakey, P. P., 1966, Transmission Electron Microscope Study of Bubbles and Dislocations in Amethyst and Citrine Quartz: Australian Journal of Physics, v. 19, no. 1, p. 19-&.

Monecke, T., Kempe, U., and Götze, J., 2002, Genetic significance of the trace element content in metamorphic and hydrothermal quartz: a reconnaissance study: Earth and Planetary Science Letters, v. 202, p. 709-724.

Moxon, T., 1996, Agate: Microstructure and Possible Origin, Terra, Doncaster, UK.

-, 2002, Agate: a study of ageing: European Journal of Mineralogy, v. 14, no. 6, p.

1109-1118.

Moxon, T., Nelson, D. R., and Zhang, M., 2006, Agate recrystallisation: evidence from samples found in Archaean and Proterozoic host rocks, Western Australia: Australian Journal of Earth Sciences, v. 53, no. 2, p. 235-248.

Müller, A., 2000, Cathodoluminescence and characterisation of defect structures in quartz with applications to the study of granitic rocks: Georg August University, 228 p.

Müller, A., Kronz, A., and Breiter, K., 2002a, Trace elements and growth patterns in quartz: a fingerprint of the evolution of the subvolcanic Podlesi Granite System(Krusne hory Mts., Czech Republic): Bulletin of the Czech Geological Survey, v. 77, no. 2, p. 135–145.

Müller, A., Lennox, P., and Trzebski, R., 2002b, Cathodoluminescence and micro-structural evidence for crystallisation and deformation processes of granites in the Eastern Lachlan Fold Belt (SE Australia): Contributions to Mineralogy and Petrology, v. 143, p. 510–524.

Nadeau, O., Williams-Jones, A. E., and Stix, J., 2010, Sulphide magma as a source of metals in arc-related magmatic hydrothermal ore fluids: Nature Geoscience, v. 3, no. 7, p. 501-505.

Nakada, S., Bacon, C. R., and Gartner, A. E., 1994, Origin of Phenocrysts and Compositional Diversity in Pre-Mazama Rhyodacite Lavas, Crater Lake, Oregon: Journal of Petrology, v. 35, no. 1, p. 127-162.

Newton, R. C., and Manning, C. E., 2005, Solubility of anhydrite, CaSO4, in NaCl-H_2O solutions at high pressures and temperatures: Applications to fluid-rock interaction: Journal of Petrology, v. 46, no. 4, p. 701-716.

Oehler, J. H., 1976, Hydrothermal Crystallization of Silica-Gel: Geological Society of America Bulletin, v. 87, no. 8, p. 1143-1152.

Okamoto, A., Saishu, H., Hirano, N., and Tsuchiya, N., 2010, Mineralogical and textural variation of silica minerals in hydrothermal flow-through experiments: Implications for quartz vein formation: Geochimica Et Cosmochimica Acta, v. 74, no. 13, p. 3692-3706.

Pasteris, J. D., 1996, Mount Pinatubo volcano and ‘‘negative” porphyry copper deposits: GEOLOGY, v. 24, no. 12, p. 1075-1078

Penniston-Dorland, S., 2001, Illumination of vein quartz textures in a porphyry copper ore deposit using scanned cathodoluminescence: Grasberg Igneous Complex, Irian Jaya, Indonesia: American Mineralogist, v. 86, p. 652–666.

Peppard, B. T., Steele, L. M., Davis, A. M., Wallace, P. J., and Anderson, A. T., 2001, Zoned quartz phenocrysts from the rhyolitic Bishop Tuff: American Mineralogist,

v. 86, p. 1034–1052.

Peretyazhko, I. S., Smirnov, S. Z., Kotel'nikov, A. R., and Kotel'nikova, Z. A., 2010, Experimental study of the system H_3BO_3-NaF-SiO_2-H_2O at 350-800 degrees C and 1-2 kbar by the method of synthetic fluid inclusions: Russian Geology and Geophysics, v. 51, no. 4, p. 349-368.

Peretyazhko, I. S., Smirnov, S. Z., Thomas, V. G., and Ye., Z. V., Gels and melt-like gels in high-temperature endogeneous mineral formation, in Proceedings The Interim IAGOD conference on "Metallogeny of the Pacific Northwest: Tectonics, Magmatism and Metallogeny of Active Continental Margins, Vladivostok, 1-20 September 2004 2004, Vladivostok Dalnauka.

Pokrovski, G. S., and Dubrovinsky, L. A., 2009, Sulfur speciation in aqueous solution and its consequencies for metal transport by hydrothermal fluids: Geochimica Et Cosmochimica Acta, v. 73, no. 13, p. A1037-A1037.

Pokrovski, G. S., and Dubrovinsky, L. S., 2011, The S(3)(-) Ion Is Stable in Geological Fluids at Elevated Temperatures and Pressures: Science, v. 331, no. 6020, p. 1052-1054.

Preusser, F., Chithambo, M. L., Gotte, T., Martini, M., Ramseyer, K., Sendezera, E. J., Susino, G. J., and Wintle, A. G., 2009, Quartz as a natural luminescence dosimeter: Earth-Science Reviews, v. 97, no. 1-4, p. 184-214.

Proffett, J. M., 2009, High Cu grades in porphyry Cu deposits and their relationship to emplacement depth of magmatic sources: Geology, v. 37, no. 8, p. 675-678.

Qin, Z. W., Lu, F. Q., and Anderson, A. T., 1992, Diffusive Reequilibration of Melt and Fluid Inclusions: American Mineralogist, v. 77, no. 5-6, p. 565-576.

Rimstidt, J. D., 1997, Gangue mineral transport and deposit, in Barnes, H. L., ed., Geochemistry of hydrothermal ore deposits: New York, John Wiley & Sons, p. 487-515.

Roedder, E., 1968, Noncolloidal Origin of Colloform Textures in Sphalerite Ores: Economic Geology, v. 63, no. 5, p. 451-&.

-, 1971, Fluid inclusion studies on the porphyry-type ore deposits at Bingham, Utah, Butte, Montana, and Climax, Colorado: Economic Geology, v. 66, p. 98-120.

-, 1984, Fluid Inclusions, Reviews in Mineralogy, 1-644 p.:

-, 1992, Fluid inclusion evidence for immiscibility in magmatic differentiation: Geochimica et Cosmochimica Acta, v. 56, p. 5-20.

Rusk, B. G., Lowers, H. A., and Reed, M. H., 2008a, Trace elements in hydrothermal quartz: Relationships to cathodoluminescent textures and insights into vein formation: Geology, v. 36, no. 7, p. 547-550.

Rusk, B. G., and Reed, M. H., 2002, Scanning electron microscope–cathodoluminescence analysis of quartz reveals complex growth histories in veins from the Butte porphyry copper deposit, Montana: Geology, v. 30, no. 8, p. 727–730.

Rusk, B. G., Reed, M. H., and Dilles, J. H., 2008b, Fluid inclusion evidence for magmatic-hydrothermal fluid evolution in the porphyry copper-molybdenum deposit at Butte, Montana: Economic Geology, v. 103, no. 2, p. 307-334.

Rusk, B. G., Reed, M. H., Dilles, J. H., and Kent, A. J. R., 2006, Intensity of quartz cathodoluminescence and trace-element content in quartz from the porphyry copper deposit at Butte, Montana: American Mineralogist, v. 91, p. 1300-1312.

Sanders, M. V., and Black, J. E., 1988, Crystallization and Recrystallization of Growth-Zoned Vein Quartz Crystals from Epithermal Systems - Implications for Fluid Inclusion Studies: Economic Geology, v. 83, no. 5, p. 1052-1060.

Shane, P., Smith, V. C., and Nairn, I., 2008, Millennial timescale resolution of rhyolite magma recharge at Tarawera volcano: insights from quartz chemistry and melt inclusions: Contributions to Mineralogy and Petrology, v. 156, no. 3, p. 397-411.

Shaw, C. S. J., 2006, Effects of melt viscosity and silica activity on the rate and mechanism of quartz dissolution in melts of the CMAS and CAS systems: Contributions to Mineralogy and Petrology, v. 151, p. 665–680.

Shinohara, H., Iiyama, J. T., and Matsuo, S., 1989, Partition of Chlorine Compounds between Silicate Melt and Hydrothermal Solutions .1. Partition of Nacl-Kcl: Geochimica Et Cosmochimica Acta, v. 53, no. 10, p. 2617-2630.

Shinohara, H., Kazahaya, K., and Lowenstern, J. B., 1995, Volatile transport in a convecting magma column: implications for porphyry Mo mineralization: Geology, v. 23, no. 12, p. 1091-1094.

Shmulovich, K. I., Yardley, B. W. D., and Graham, C. M., 2006, Solubility of quartz in crustal fluids: experiments and general equations for salt solutions and H_2O-CO2 mixtures at 400-800 degrees C and 0.1-0.9 GPa: Geofluids, v. 6, no. 2, p. 154-167.

Sinclair, W. D., 2007, Porphyry deposits, in Goodfellow, W. D., ed., Mineral Deposits of Canada: A Synthesis of Major Deposit-Types, District Metallogeny, the Evolution of Geological Provinces, and Exploration Methods: Geological Association of Canada, Mineral Deposits Division, Volume Special Publication No. 5, p. 223-243.

Sirbescu, M.-L. C., and Nabelek, P. I., 2003, Crustal melts below 400oC: Geology, v. 31, no. 8, p. 685-688.

Skinner, B. J., 1979, The many origins of hydrothermal mineral deposits, in Barnes, H.

L., ed., Geochemistry of Hydrothermal Ore Deposits, Volume 2nd edition: New York, NY, Wiley & Sons, p. 1-21.

Skinner, B. J., and Barton, P. B., 1973, Genesis of Mineral-Deposits: Annual Review of Earth and Planetary Sciences, v. 1, p. 183-211.

Spear, F. S., and Wark, D. A., 2009, Cathodoluminescence imaging and titanium thermometry in metamorphic quartz: Journal of Metamorphic Geology, v. 27, no. 3, p. 187-205.

Taylor, M. C., 2005, The Sol-Gel Nature of Pegmatites.

Taylor, M. C., Sheppard, J. B., Walker, J. N., Kleck, W. D., and Humiston, L. E., 2004, Magmatic hydrogels and hydrosols in the petrogenesis of rare-element pegmatites and other ore deposits: Geol. Assoc. Can. - Mineral.Assoc. Can. Program Abstr, v. 29, no. 198.

Thomas, R., and Davidson, P., 2008, Water and melt-melt immiscibility, the essencial component in the formation of pegmatities; evidence from melt inclusions Z. geol. Wiss, v. 36, no. 6, p. 347-364.

Thomas, R., Davidson, P., and Badanina, E., 2009, A melt and fluid inclusion assemblage in beryl from pegmatite in the Orlovka amazonite granite, East Transbaikalia, Russia: implications for pegmatite-forming melt systems: Mineralogy and Petrology, v. 96, no. 3-4, p. 129-140.

Thomas, R., Webster, J. D., and Heinrich, W., 2000, Melt inclusions in pegmatite quartz: complete miscibility between silicate melts and hydrous fluids at low pressure: Contributions to Mineralogy and Petrology, v. 139, no. 4, p. 394-401.

Thomas, V. G., Smirnov, S. Z., Kamenetsky, V. S., and A., K. O., 2010, Formation of hydrosilicate liquids in the system Na_2O ($\pm K_2O$) – SiO_2 ($\pm Al_2O_3$)–H_2O and their ability to concentrate some elements (on the basis of experimental data), Asian Current Research On Fluid Inclusions, Volume 52: Novosibirsk, Russia, Russian Geology and Geophysics.

Tuttle, O. F., 1953, Continuity between Hydrous Granite Magmas and Hydrothermal Solutions: Geological Society of America Bulletin, v. 64, no. 12, p. 1484-1485.

Tuttle, O. F., and Friedman, I. I., 1948, Liquid Immiscibility in the System H20-Na20-SiO_2 Journal of the American Chemical Society, v. 70, no. 3, p. 919-926.

Van den Kerkhof, A. M., and Hein, U. F., 2001, Fluid inclusion petrography: Lithos, v. 55, p. 27-47.

Van den Kerkhof, A. M., Kronz, A., Simon, K., and Scherer, T., 2004, Fluid-controlled quartz recovery in granulite as revealed by cathodoluminescence and trace element analysis (Bamble sector, Norway): Contributions to Mineralogy and Petrology, v. 146, p. 637–652.

Vasyukova, O. V., and Fonarev, V. I., 2006, Experimental modeling of the transformation of H_2O-CO_2-CH_4 inclusions during isobaric cooling and isothermal compression: Geochemistry International, v. 44, no. 12, p. 1170-1180.

Veksler, I. V., 2004, Liquid immiscibility and its role at the magmatic-hydrothermal transition: a summary of experimental studies: Chemical Geology, v. 210, no. 1-4, p. 7-31.

Veksler, I. V., Dorfman, A. M., Dulski, P., and Dingwell, D. B., 2004, Element partitioning between immiscible melts and geochemical anomalies in igneous rocks: Geochimica et Cosmochimica Acta, v. 68, no. 11, p. A639-A639.

Vernon, R. H., and Flood, R. H., 1977, Quartz-Eye-Bearing Porphyroidal Rocks and Volcanogenic Massive Sulfide Deposits - Discussion: Economic Geology, v. 72, no. 4, p. 698-701.

Vityk, M. O., and Bodnar, R. J., 1995, Textural Evolution of Synthetic Fluid Inclusions in Quartz During Reequilibration, with Applications to Tectonic Reconstruction: Contributions to Mineralogy and Petrology, v. 121, no. 3, p. 309-323.

Vityk, M. O., Bodnar, R. J., and Doukhan, J. C., 2000, Synthetic fluid inclusions. XV. TEM investigation of plastic flow associated with reequilibration of fluid inclusions in natural quartz: Contributions to Mineralogy and Petrology, v. 139, no. 3, p. 285-297.

Vityk, M. O., Bodnar, R. J., and Dudok, I. V., 1995, Natural and Synthetic Re-Equilibration Textures of Fluid Inclusions in Quartz (Marmarosh Diamonds) - Evidence for Refilling under Conditions of Compressive Loading: European Journal of Mineralogy, v. 7, no. 5, p. 1071-1087.

Wallace, P., and Carmichael, I. S. E., 1992, Sulfur in Basaltic Magmas: Geochimica Et Cosmochimica Acta, v. 56, no. 5, p. 1863-1874.

Wallace, P. J., and Gerlach, T. M., 1994, Magmatic Vapor Source for Sulfur-Dioxide Released during Volcanic-Eruptions - Evidence from Mount-Pinatubo: Science, v. 265, no. 5171, p. 497-499.

Wallace, S. R., Muncaster, N. K., Jonson, D. C., Mackenzie, W. B., Bookstrom, A. A., and Surface, V. A., 1968, Multiple intrusion and mineralization at Climax, Colorado, New York, American Institute of Mining, Metallurgical, and Petroleum Engineers, Ore Deposits of the United States, 1933-1967 (Graton-Sales Volume), 605-640 p.:

Wardell, L. J., Kyle, P. R., Dunbar, N., and Christenson, B., 2001, White Island volcano, New Zealand: carbon dioxide and sulfur dioxide emission rates and melt inclusion studies: Chemical Geology, v. 177, no. 1-2, p. 187-200.

Wark, D. A., and Spear, F. S., 2005, Ti in quartz: Cathodoluminescence and

thermometry, The 15th Annual Goldschmidt Conference: Moscow, Idaho, USA, p. A592.

Wark, D. A., Spear, F. S., Cherniak, D. J., and Watson, E. B., 2007, Pre-eruption recharge of the Bishop magma system: Geology, v. 35, no. 3, p. 235–238.

Wark, D. A., and Watson, E. B., 2006, TitaniQ: a titanium-in-quartz geothermometer: Contributions to Mineralogy and Petrology, v. 152, p. 743–754.

Watt, G. R., Wright, P., Galloway, S., and McLean, C., 1997, Cathodoluminescence and trace element zoning in quartz phenocrysts and xenocrysts: Geochimica et Cosmochimica Acta, v. 61, no. 20, p. 4337-4348.

Webster, J. D., 1992a, Fluid-Melt Interactions Involving Cl-Rich Granites - Experimental-Study from 2 to 8 Kbar: Geochimica Et Cosmochimica Acta, v. 56, no. 2, p. 659-678.

-, 1992b, Water Solubility and Chlorine Partitioning in Cl-Rich Granitic Systems - Effects of Melt Composition at 2 Kbar and 800-Degrees-C: Geochimica Et Cosmochimica Acta, v. 56, no. 2, p. 679-687.

-, 1997, Exsolution of magmatic volatile phases from Cl-enriched mineralizing granitic magmas and implications for ore metal transport: Geochimica Et Cosmochimica Acta, v. 61, no. 5, p. 1017-1029.

Webster, J. D., and Mandeville, C. W., 2007, Fluid immiscibility in volcanic environments: Fluid-Fluid Interactions, v. 65, p. 313-362.

White, D. E., Muffler, L. J. P., and Truesdel, A. H., 1971, Vapor-Dominated Hydrothermal Systems Compared with Hot-Water Systems: Economic Geology, v. 66, no. 1, p. 75-&.

Whitney, J. A., 1975, Vapor Generation in a Quartz Monzonite Magma - Synthetic Model with Application to Porphyry Copper-Deposits: Economic Geology, v. 70, no. 2, p. 346-358.

Wiebe, R. A., Wark, D. A., and Hawkins, D. P., 2007, Insights from quartz cathodoluminescence zoning into crystallization of the Vinalhaven granite, coastal Maine: Contributions to Mineralogy and Petrology, v. 154, p. 439-453.

Wilkinson, J. J., 2001, Fluid inclusions in hydrothermal ore deposits: Lithos, v. 55, no. 1-4, p. 229-272.

Wilkinson, J. J., Nolan, J., and Rankin, A. H., 1996, Silicothermal fluid: A novel medium for mass transport in the lithosphere: Geology, v. 24, no. 12, p. 1059-1062.

Williams-Jones, A. E., and Heinrich, C. A., 2005, 100th Anniversary special paper: Vapor transport of metals and the formation of magmatic-hydrothermal ore deposits: Economic Geology, v. 100, no. 7, p. 1287-1312.

Williams-Jones, A. E., Heinrich, C. A., and Migdisov, A. A., 2005, Vapor as a medium for the transport of metals: Implications for ore deposit modeling: Geochimica et Cosmochimica Acta, v. 69, no. 10, p. A733-A733.

Williamson, B. J., Stanley, C. J., and Wilkinson, J. J., 1997, Implications from inclusions in topaz for greisenisation and mineralisation in the Hensbarrow topaz granite, Cornwall, England: Contributions to Mineralogy and Petrology, v. 127, p. 119-128.

Williamson, B. J., Wilkinson, J. J., Luckham, P. F., and Stanley, C. J., 2002, Formation of coagulated colloidal silica in high-temperature mineralizing fluids: Mineralogical Magazine, v. 66, no. 4, p. 574-553.

Zajacz, Z., Halter, W. E., Pettke, T., and Guillong, M., 2008, Determination of fluid/melt partition coefficients by LA-ICPMS analysis of co-existing fluid and silicate melt inclusions: Controls on element partitioning: Geochimica Et Cosmochimica Acta, v. 72, no. 8, p. 2169-2197.

Publications

Conference presentations:

Gömann K., Vasyukova O.V. and Kamenetsky V.S. The source and fate of silica in mineralized porphyries revealed by SEM-CL textures of quartz. Materials of reports of Goldschmidt Conference 2007 - "atoms to planets" August 19-24, 2007 Cologne, Germany, 2007, A334.

Kamenetsky V.S. and Vasyukova O.V. Fluid inclusions in quartz: parental solutions or residual gels? Materials of reports of "Syntaphral Tectonics and Diagenesis - 44 years on" symposium, Hobart, 2007,

Kamenetsky V. and Vasyukova O. Quartz and fluid inclusions from porphyry deposits: were hydrosilicate liquids involved? Geophysical Research Abstracts, Vol. 10, EGU2008-A-01466, 2008

Vasyukova O.V., Kamenetsky V.S. and Gömann K., Origin of "quartz eyes" and fluid inclusions in mineralized porphyries. Materials of reports of Goldschmidt Conference 2008 - "from Sea to Sky" July 13- 8 Vancouver, Canada, 2008, 955.

Kamenetsky V.S. and Vasyukova O.V. Quartz and fluid inclusions from porphyry deposits – were Hydrosilicate liquids involved? Materials of reports of Pacific Rim Congress, November 24-28, Gold Coast, 2008

Vasyukova, O., Gömann, K., MacRae, C.M., and Kamenetsky V.S. Origin of Quartz-eyes from porphyry-type deposits, Geochimica et Cosmochimica Acta, Volume 74, Issue 11 Supplement 1 (June 2010), A1076

Vasyukova O., Kamenetsky V. Origin of Fluid Inclusions in Quartz Eyes from Porphyry Deposits, proceedings from Society of Economic Geologists 2010 Conference, Keystone Resort, Colorado, September 30 – October 9, 2010